National Science Foundation
Under grant ATM-9900929

RAPID DEVELOPMENT OF TORNADO-LIKE VORTICES BY SIMULATED SUPERCELLS

by Brian Gaudet

William R. Cotton, P.I.

Colorado State University

DEPARTMENT OF ATMOSPHERIC SCIENCE

PAPER NO. 717

RAPID DEVELOPMENT OF TORNADO-LIKE VORTICES BY SIMULATED SUPERCELLS

by

Brian Gaudet
Department of Atmospheric Science
Colorado State University
Fort Collins, Colorado 80523

Research Supported by
National Science Foundation
under Grant ATM9900929

February 15, 2002

Atmospheric Science Paper No. 717

ABSTRACT

RAPID DEVELOPMENT OF TORNADO-LIKE VORTICES BY SIMULATED SUPERCELLS

The Regional Atmospheric Modeling System (RAMS) is used to examine the evolution of low-level vorticity beneath a modeled supercell thunderstorm. The simulations are performed using seven-species bulk microphysics in a horizontally-homogeneous domain, and are initialized through the use of a warm bubble. A mesocyclonic circulation becomes apparent a kilometer above the ground after 45 minutes of simulation time, and vertical vorticity of similar magnitude develops along the gust front near the surface by 55 minutes. Approximately five minutes later a transition occurs; the maximum vorticity beneath cloud base becomes vertically co-located, and translates with nearly constant grid-relative velocity. The vorticity increases by a factor of five during the five minutes following the co-location of the vorticity. An intense pressure deficit develops within the region of closed streamlines.

It is shown that the concentration of vorticity is not dynamically forced by vertical pressure gradients or buoyancy, but occurs in a quasi-horizontal framework. The process is similar to models of non-supercell tornadogenesis in the literature that invoke the non-linear pooling of vorticity by barotropic processes, but with modification due to the presence of large-scale plane convergence. Specifically, the plane convergence allows the vorticity to concentrate at much faster time scales and without need of the coalescence of several discrete vorticity centers. The relevance to observed tornadic vortices and the implications for future modeling work are discussed.

Brian Gaudet
Department of Atmospheric Science
Colorado State University
Fort Collins, Colorado 80523
Spring 2002

ACKNOWLEDGMENTS

I would like to thank my adviser, Professor Bill Cotton, for all of his support, guidance, and suggestions during my time at Colorado State, and for granting me the latitude to conduct my scientific investigations. I also thank him for causing constant 'pundemonium' and for successfully returning me to ground in his glider. I would also like to thank Prof. Mike Montgomery for his many valuable discussions during this study and Prof. Wayne Schubert for his good advice and suggestions for research. The guidance of my outside committee member, Prof. Bob Meroney from the Department of Civil Engineering, is also appreciated.

Lewis Grasso is thanked for first introducing me to and challenging me with the problems of supercell modeling, as well as providing the technical knowledge to help me begin my initial simulations. Bob Walko provided answers to numerous questions about the behavior and structure of the RAMS code itself.

I would also like to thank Dave Nolan in particular for sharing his knowledge of vortices with me and providing crucial insights into their behavior. Jim Kossin's assistance in running the pseudo-spectral barotropic model for this study is appreciated. Lou Wicker is thanked for his advice and for sharing his supercell modeling experience.

I greatly appreciate the help, suggestions, and friendship of Sue van den Heever, Chris Golaz, and Travis Ashby over the years. In particular I would like to thank Chris Golaz for abundant help in making this manuscript, and Will Cheng, Hongli Jiang, and Cory Wolf for their recommendations about the defense. There are many, many other Cotton group members, past and present, who have given me counsel and support during my academic career. Last but not least, I would like to thank Brenda Thompson for the innumerable times that she has assisted me over the years when I have turned to her for help.

On a personal level I would like to thank my parents John and Sandra Gaudet for encouraging my academic interests, and for their unfailing love. And I would like to acknowledge the constant support and love of my wonderful wife, Deborah, without whom I would not have been able to complete this study, and without whom I would be much poorer today.

Finally, I acknowledge God, who has been the ultimate source of strength in my weakness.

This research was supported by the National Science Foundation under grant #ATM9900929.

TABLE OF CONTENTS

LIST OF SYMBOLS

A_i	projected area in x-direction
A_j	projected area in y-direction
A_k	projected area in z-direction
A_m	projected area in generalized direction
A_T	$(A_i^2 + A_j^2 + A_k^2)^{0.5}$
a	semimajor axis of ellipse
$\mathbf{a}$	generic vector
B	buoyancy
b	semiminor axis of ellipse
$\mathcal{C}$	circulation
CAPE	Convective Available Potential Energy
c_p	specific heat at constant pressure
c_{pd}	c_p for dry air
c_s	adiabatic speed of sound
c_v	specific heat at constant volume
$\mathcal{D}$	two-dimensional deformation: $(T^2 + H^2)^{0.5}$
e	2.71828...
$\boldsymbol{F}$	non-pressure gradient, non-gravitational force
$\boldsymbol{F_H}$	horizontal part of F (vector)
F_{vm}	viscous force
F_{sm}	subgrid momentum diffusive force
f	Coriolis force
G_1	vertical pressure forcing
G_2	horizontal pressure forcing
g	gravitational force per unit mass
H	shearing deformation: $\partial v/\partial x + \partial u/\partial y$
i	x-direction component (vectors)
i	grid index for x-direction (scalars)
j	y-direction component (vectors)
j	grid index for y-direction (scalars)
K	eddy diffusion coefficient
K_H	horizontal eddy diffusion coefficent
K_V	vertical eddy diffusion coefficent
k	z-direction component (vectors)
k	grid index for z-direction (scalars)
$\hat{\mathbf{k}}$	unit vector in z-direction

l	general component (vectors)
$\mathbf{l}$	position vector
m	general component (vectors)
$\hat{\mathbf{m}}$	unit vector in general direction
n	general component (vectors)
p	pressure
p_0	reference pressure for Exner function
R	specific gas constant
R_d	specific gas constant for dry air
R_v	specific gas constant for water vapor
r	radius
$\hat{\mathbf{r}}$	unit vector in radial direction
r_c	water condensate mixing ratio
r_{draw}	radius from which circulation is drawn
r_{max}	radius of maximum winds
r_v	water vapor mixing ratio
s	arc-length parameter
s_f	final value of arc-length parameter
T	absolute temperature
$\mathcal{T}$	stretching deformation: $\partial u/\partial x - \partial v/\partial y$
T_v	virtual temperature
U	wind speed perpendicular to shear line
u	x-direction velocity component
V	wind speed tangential to shear line
v	y-direction velocity component
v_{env}	one-half tangential wind shear at boundary
$\mathbf{v_H}$	horizontal velocity (vector)
v_{max}	maximum tangential wind speed
v_r	radial velocity component
v_Θ	tangential velocity component
w	z-direction velocity component
x	west-east direction
x_{fac}	x-direction weighting
y	south-north direction
y_{fac}	y-direction weighting
z	vertical direction
α	$-\partial u/\partial x$
β	$-\partial v/\partial y$
Γ	circulation
Γ_c	circulation excess
γ	$\partial w/\partial z$
γ'	$\partial v/\partial y$
γ_0	c_p/c_v for air parcel
δ	horizontal divergence: $\partial u/\partial x + \partial v/\partial y$
$\delta_{1/e}$	e-folding width of Burgers vortex sheet

ζ	vertical vorticity component
$\boldsymbol{\zeta}$	vertical vorticity (vector)
ζ_0	initial state vertical vorticity component
$\boldsymbol{\zeta_H}$	horizontal vorticity (vector)
ζ_z	vertical vorticity component
$\bar{\zeta}_z$	average vertical vorticity
ζ_{z0}	initial state vertical vorticity component
ζ_{zD}	discrete vertical vorticity
η	aspect ratio of ellipse (a/b)
Θ	angular displacement in cylindrical coordinates
$\hat{\boldsymbol{\Theta}}$	unit vector in tangential direction
Θ_0	rotation of maximum v_r from x-axis
Θ_{max}	angle at which ellipse rotation rate is zero
θ	potential temperature
θ_e	equivalent potential temperature
θ_{il}	ice-liquid potential temperature
θ_v	virtual potential temperature
θ_v'	perturbation virtual potential temperature
θ_{v0}	reference state virtual potential temperature
κ	R/c_p
κ_d	R/c_p for dry air = R_d/c_{pd}
ν	gamma distribution width parameter
ν	dynamic viscosity
ξ	transformed distance in integration
π	3.14159...
π	Exner function = $c_p(p/p_0)^{R/c_p}$
π'	perturbation Exner function
π_0	reference state Exner function
ρ	air density
ρ_0	reference state air density
ρ_c	air density due to condensate
ρ_d	air density due to dry air
σ	circulation per unit length
σ_z	vertical terrain-following coordinate
τ	transformed time in integration
ϕ	latitude
Ω	angular rotation rate of Earth
ω	transformed vertical vorticity in integration

Chapter 1

INTRODUCTION

'And I looked, and, behold, a whirlwind came out of the north, a great cloud, and a fire infolding itself, and a brightness was about it, and out of the midst thereof as the colour of amber, out of the midst of the fire.'

Ezekiel 1:4

Tornadoes are neither the most damaging, nor deadliest, nor most common of weather hazards today. Yet perhaps no weather phenomenon evokes such awe and wonder at the power of the atmosphere, or shear terror for those who are unfortunate enough to not have the luxury of casually observing from a distant vantage point. The extreme power of tornadoes coupled with their diminutive size (median diameter of 50 m)[1] and transient nature (few last as long as an hour) have made them extremely resistant to study until recently (Grazulis 1993).

In March 1948 Air Force Weather officers Ernest Fawbush and Robert Miller, having seen a tornado strike Tinker Air Force Base five days previously under similar weather conditions, issued the first modern tornado forecast, which proved remarkably prescient

---

[1] Strong tornadoes (Fujita scale F3 or higher) are a small subset of all tornadoes, but when they do occur tend to be associated with supercells. For these tornadoes the median diameter is closer to 200 m (Grazulis 1993).

(Grice et al. 1999). Soon the basic climatology of tornadoes was discovered (Fawbush and Miller 1954): they tend to occur in environments with very warm, moist air near the surface, capped beneath an inversion that separates it from a layer of very dry, nearly statically-neutral air. The low level winds are usually from near the southeast but veer sharply with height, and usually the upper level winds are quite strong (Darkow and McCann 1977).

With the aid of radar studies, Browning and Donaldson (1963) and Browning (1964) were able to deduce that a particular type of large, long-lived, and vigorous storm, the supercell, was associated with a large fraction of reported severe weather, including tornadoes. It was soon realized that the tornado climatology was essentially a climatology of the conditions which Browning had shown were favorable for supercells.

Soon after numerical modeling of storm-scale phenomena began in the 1970s, the models were applied to modeling the supercell. These models had great success in reproducing the features of supercells (Klemp and Wilhelmson 1978a; Weisman and Klemp 1982), and facilitated the creation of physical analytical models to explain their behavior (Rotunno and Klemp 1982). The observational data base also grew substantially through damage track studies (Fujita 1970), 'storm chasing' (Bluestein 1999), and Doppler radar (Donaldson 1970).

Eventually observational studies (Lemon and Doswell 1979) conceptual models (Davies-Jones 1982), and numerical models (Klemp and Rotunno 1983) all suggested that low-level rotation beneath supercells had different origins than the rotation of the supercell storm itself. It was increasingly suggested that the interaction between the updraft and the downdraft of the storm is critical to the formation of the low-level mesocyclone.

The actual process of tornadogenesis occurs at scales even smaller than the low-level mesocyclone. Recently observations of the tornadogenesis process and tornadoes have been obtained in detail not previously seen (Wakimoto and Liu 1998; Bluestein and Pazmany 2000). The collapse of the low-level mesocyclone into the tornado is still not well understood however. Tornadic-like vortices in modeled supercells have been documented in the literature and show intriguing similarities to real tornadoes (Wicker and Wilhelmson 1995; Grasso and Cotton 1995; Grasso 1996; Finley 1997), but because of the limits of model resolution are still generally too large to be equated with real tornadoes.

It also has been recognized in the past couple of decades that not all tornadoes derive from supercells (Brady and Szoke 1989; McCaul 1993), nor do all tornadoes form in the same manner (Burgess and Donaldson 1979; Trapp et al. 1999). Model studies also reflect this disparity; some studies point to upward pressure gradient forces as the trigger to forming intense 'tornado-like' vortices (Wicker and Wilhelmson 1995; Grasso and Cotton 1995), others portray the vortices as being surface based (Grasso 1996; Finley 1997), and others explicitly model non-supercell vortices (Lee and Wilhelmson 1997a-c).

In this study idealized supercells will be modeled using the Regional Atmospheric Modeling System (RAMS), and will be shown to develop low-level mesocyclones that can rapidly collapse to form concentrated vortices. This collapse process will be analyzed in some detail in order to suggest the physical mechanism of the collapse and from where it originates. Chapters 2 and 3 will present conceptual and historical background, respectively. Chapter 4 will contain an overall description of a supercell simulation that produced a particularly strong collapse of vorticity. Chapter 5 contains a qualitative and quantitative description of a model of the collapse process, and it is argued that the process is related to the conceptual models of Neu (1984a,b). The ultimate source of the low-level vorticity is investigated in Chapter 6, whereas some tests of the dependencies of the low-level vorticity are found in Chapter 7. Finally, conclusions and implications for future work follow.

Chapter 2

ANALYTICAL FOUNDATIONS

In this chapter there are a series of derivations that are used to provide some background for the discussion of supercell and tornadic research that follows.

2.1 Thermodynamic Variables

For gases that obey the ideal gas equation, the pressure, density, and temperature are related by:

$$p = \rho R T, \tag{2.1}$$

where p is pressure, ρ is density, T is absolute temperature, and R is the gas constant, which is essentially a function of the molecular weight of the gas. For a mixture of ideal gases, both the pressures (by Dalton's law of partial pressures) and the densities simply add, while it is assumed that the temperature of all gaseous components is identical.

For all components of air except water vapor, the relative proportions are nearly constant, so one can simply perform a weighted average and relate the total air pressure to an effective gas constant, R_d, and effective density, ρ_d, of air. The variability of the water vapor content of air introduces a natural variability to the density and effective gas constant of air. To take this into account one can write the total pressure of the mixture as:

$$p = p_{air} + p_{vapor} = \rho_d R_d T + \rho_v R_v T = \rho_d R_d T \left(r_v \frac{R_v}{R_d} + 1 \right), \tag{2.2}$$

where $r_v = \rho_v/\rho_d$ is defined as the mixing ratio of water vapor, $R_d = 287\ \mathrm{J\,K^{-1}\,kg^{-1}}$, and $R_v = 461\ \mathrm{J\,K^{-1}\,kg^{-1}}$.

Meanwhile $\rho_d = \rho - \rho_v = \rho - r_v\rho_d$, so $\rho_d = \rho/(1 + r_v)$ and

$$p = \rho R_d T \frac{1 + (R_v/R_d)r_v}{1 + r_v} \approx \rho R_d T \left[1 + \left(\frac{R_v}{R_d} - 1\right) r_v\right] \tag{2.3}$$

since r_v is small.

Moist air is seen to obey the ideal gas law using a dry air gas constant, but with a mixing-ratio dependent correction factor. For a given absolute temperature and pressure, the total density of moist air is less than that of dry air, because the molecular weight of water vapor (approximately 18 g mol^{-1}) is less than that of dry air (approximately 29 g mol^{-1}). Mathematically, we see that at a given temperature and pressure, the density of a mixture of air is inversely proportional to the factor $[1 + (R_v/R_d - 1)r_v]$, which is approximately $0.61r_v$. In practice it is assumed that the gas constant for air is always R_d, but that air behaves as if it had a *virtual temperature* $T_v = T(1 + 0.61r_v)$.

The equations of motion for the atmosphere can be expressed as:

$$\frac{d\mathbf{v}}{dt} = -\frac{1}{\rho}\boldsymbol{\nabla} p - g\hat{\mathbf{k}} + \mathbf{F}, \tag{2.4}$$

where the first term is the pressure gradient acceleration (or 'pressure gradient force' in typical terminology), and the second term is the gravitational force. The third term represents the presence of any non-conservative forces, such as viscosity, as well as other forces distinct from the first two (most importantly, the Coriolis force). Because of the size of the gravitational term, the pressure must drop rapidly with height for approximate balance (see Section 2), and it can be shown that both temperature and density also decrease rapidly with height as a consequence (Dutton 1995). It is therefore convenient to define the potential temperature, θ, as:

$$\theta = T\left(\frac{p_0}{p}\right)^{\frac{R}{c_p}}, \tag{2.5}$$

where p_0 is a reference pressure normally taken as 1000 mb, and R/c_p is the ratio of the gas constant to the specific heat at constant pressure. It can be shown that this variable is conserved for air during adiabatic processes – when there is an absence of phase changes, radiation, and diffusive processes (Cotton and Anthes 1989; Holton 1992; Dutton 1995).

Using (2.3) to substitute for T in (2.5) gives:

$$\theta_v = \frac{p}{\rho R_d}\left(\frac{p_0}{p}\right)^{\frac{R}{c_p}}, \tag{2.6}$$

with the virtual potential temperature $\theta_v = \theta(1 + 0.61r_v)$. This allows a substitution of θ_v for $1/\rho$ in the pressure gradient force, giving:

$$-\frac{1}{\rho}\nabla p = -\frac{\theta_v R_d}{p}\left(\frac{p}{p_0}\right)^{\frac{R}{c_p}}\nabla p = -\frac{\theta_v \kappa_d c_{pd}}{p}\left(\frac{p}{p_0}\right)^{\kappa}\nabla p, \tag{2.7}$$

where $\kappa = R/c_p$ and $\kappa_d = R_d/c_{pd}$ is the value of κ for dry air. The value of κ_d is approximately 0.286, whereas κ for pure water vapor is approximately 0.241 (Fleagle and Businger 1980). However, it is almost always assumed that the actual value of κ for an air mixture can be approximated as κ_d. When this is applied, κ is then a constant in space, and the resultant pressure gradient force may be rewritten in the form

$$-\frac{1}{\rho}\nabla p = -\theta_v \nabla \pi \tag{2.8}$$

with the Exner function π defined as $c_{pd}(p/p_0)^{\kappa_d}$, where $c_{pd} = 1004$ J K^{-1} kg^{-1}. There are advantages to using the RHS of (2.8) as opposed to the LHS for the pressure gradient term (Cotton and Anthes 1989, Sec. 2.3.2), and this is the form used in RAMS.

Finally, it should be noted that the virtual potential temperature takes into account water vapor but not condensed water species. These species can also be measured in terms of a mixing ratio $r_c = \rho_c/\rho_d$ where ρ_c is the mass of the species per unit volume of air. This density makes no contribution to the gaseous pressure nor the ideal gas law[1], but it does

---

[1] Condensate does however alter the net heat capacity of an air parcel. RAMS takes this effect into account by allowing certain condensed water species to possess a temperature distinct from the air temperature (Walko et al. 1995).

increase the density in the equations of motion. To take this into account (2.8) should be multiplied by $\rho/(\rho_{air} + \rho_c) \approx 1 - \rho_c/\rho$ when ρ_c is small compared to ρ. Approximating once more with $\rho \approx \rho_d$ gives a final momentum equation of:

$$\frac{d\mathbf{v}}{dt} = -\theta_v(1 - r_c)\boldsymbol{\nabla}\pi - g\hat{\mathbf{k}} + \mathbf{F}. \tag{2.9}$$

2.2 Momentum Equation and Hydrostaticity

As noted above, because gravity is the dominant force acting on the atmosphere, to first order the pressure gradient is directed vertically upwards to balance the gravitational force; when the vertical component of the pressure gradient force exactly balances gravity, hydrostatic balance is achieved. Keeping this in mind, the Exner function can be decomposed into a mean state, $\pi_0(z)$, and a horizontally-variable perturbation, π'. A mean state virtual temperature $\theta_{v0}(z)$ can then be defined as that which creates hydrostatic balance with π_0, i.e. $\theta_{v0}\partial\pi_0/\partial z = -g$ (it is assumed the mean state has no condensed water). The sum of the vertical pressure gradient force and the gravitational force becomes:

$$\frac{dw}{dt} = \left[-\theta_{v0}\frac{\partial\pi_0}{\partial z} - \theta_{v0}\frac{\partial\pi'}{\partial z} - \theta'_v\frac{\partial\pi_0}{\partial z} - \theta'_v\frac{\partial\pi'}{\partial z}\right](1 - r_c) - g. \tag{2.10}$$

Substituting $-g/\theta_{v0}$ for $\partial\pi_0/\partial z$ produces:

$$\frac{dw}{dt} = \left[g - \theta_{v0}\frac{\partial\pi'}{\partial z} + g\frac{\theta'_v}{\theta_{v0}} - \theta'_v\frac{\partial\pi'}{\partial z}\right](1 - r_c) - g.$$

$$= \left[\overbrace{-\theta_{v0}\frac{\partial\pi'}{\partial z}}^{I} + \overbrace{g\frac{\theta'_v}{\theta_{v0}}}^{II} - \overbrace{\theta'_v\frac{\partial\pi'}{\partial z}}^{III}\right](1 - r_c) - gr_c. \tag{2.11}$$

One assumption is normally made at this point: that g is much larger than both the terms I and II in (2.11). We can substantiate this assumption for term II by noting that $g \approx 9.8$ m s^{-2}; even for a 30 K temperature perturbation term II is ≈ 1 m s^{-2} for $\theta_{v0} = 300$ K.

Two consequences are: a) since g has been assumed to be much larger than $g\theta_v'/\theta_{v0}$, then θ_v'/θ_{v0} is much less than unity, so term III can be neglected in comparison with term I; and b) the term r_c multiplying the brackets can be neglected in comparison with gr_c. We are then permitted to approximate (2.11) by:

$$\frac{dw}{dt} = -\theta_{v0}\frac{\partial \pi'}{\partial z} + g\frac{\theta_v'}{\theta_{v0}} - gr_c = -\theta_{v0}\frac{\partial \pi'}{\partial z} + g\left(\frac{\theta_v'}{\theta_{v0}} - r_c\right) \tag{2.12}$$

Of the two terms that remain, the first is the vertical perturbation pressure gradient (VPPG) contribution to vertical acceleration (though here actually a π' gradient), whereas the second is the buoyancy contribution. Note that it is not possible uniquely to partition the vertical acceleration into the buoyancy and VPPG terms. The specification of π_0 and θ_{v0} is arbitrary as long as the base state is hydrostatic, to the extent that the perturbation π' and θ_v' are not such that terms I-III rival g in magnitude.

In the horizontal equations of motion only π' is relevant to the horizontal gradient. In RAMS the horizontal pressure gradient force is simplified to $\theta_{v0}\boldsymbol{\nabla}_{\boldsymbol{H}}\pi'$ to be consistent with the VPPG. RAMS can be said to be 'Boussinesq' in that the horizontal pressure gradient force is simply the horizontal gradient of the scalar $\theta_{v0}\pi'$. The modified momentum equation can now be written as:

$$\frac{d\mathbf{v}}{dt} = -\theta_{v0}\boldsymbol{\nabla}\pi' + B\hat{\mathbf{k}} + \mathbf{F}, \tag{2.13}$$

where $B = g(\theta_v'/\theta_{v0} - r_c)$ is the buoyancy term.

2.3 Vorticity Equation

Vorticity, $\boldsymbol{\zeta}$, is simply defined as the curl of the velocity. For air parcels there is both relative vorticity, which is a function of the air velocity relative to the earth, and planetary vorticity, which is due to the rotation of the earth. The planetary vorticity has a vertical component given by $f = 2\Omega \sin\phi$ where $\Omega = 7.27 \times 10^{-5}$ rad s^{-1} is the rotation rate of the earth and ϕ is the latitude. For midlatitudes f is around 1×10^{-4} s^{-1}, suggesting that it takes on the order of a few hours for its effects to become significant. Because the focus of this study is tornadogenesis, it will be assumed that planetary vorticity acts too slowly to play a major role in the process, so only relative vorticity will be considered in this chapter. In component form, the relative vorticity is given by $\boldsymbol{\nabla} \times \mathbf{v} = (\partial w/\partial y - \partial v/\partial z,\ \ \partial u/\partial z - \partial w/\partial x,\ \ \partial v/\partial x - \partial u/\partial y)$.

Let us return for the moment to the non-Boussinesq atmospheric momentum equation, (2.9). The vorticity tendency equation can be derived by taking the curl of (2.9). First, using a vector identity to expand the LHS of (2.9) gives:

$$\frac{d\mathbf{v}}{dt} = \frac{\partial \mathbf{v}}{\partial t} + \boldsymbol{\nabla}\left(\frac{\mathbf{v}\cdot\mathbf{v}}{2}\right) - \mathbf{v} \times \boldsymbol{\zeta} = -\theta_v(1 - r_c)\boldsymbol{\nabla}\pi - g\hat{\mathbf{k}} + \mathbf{F}. \tag{2.14}$$

Proceeding now with taking the curl gives:

$$\frac{d\boldsymbol{\zeta}}{dt} = -\boldsymbol{\zeta}(\boldsymbol{\nabla}\cdot\mathbf{v}) + (\boldsymbol{\zeta}\cdot\boldsymbol{\nabla})\mathbf{v} + \boldsymbol{\nabla}\pi \times \boldsymbol{\nabla}\theta_v(1 - r_c) + \boldsymbol{\nabla} \times \mathbf{F}. \tag{2.15}$$

The third term is called the baroclinic term because it is nonzero when surfaces of constant pressure and constant temperature (or other thermodynamic field) intersect, indicating that the two surfaces are inclined to each other (Holton 1992). The term represents, for example, the differential forcing of parcels with different values of θ_v in the direction of the negative π-gradient. The first two terms are referred to as the barotropic terms, and the last term is the non-conservative force contribution to the vorticity tendency (to be referred to as the diffusion term for brevity).

Lines in the fluid that are everywhere tangent to the vorticity vector are called *vortex lines*. It can be shown that in the absence of baroclinity or non-conservative forces, vortex lines must move with the fluid (Helmholtz 1858; Dutton 1995). In other words, if at some initial time a vortex line segment is composed of a set of fluid parcels, at all later times the set of fluid parcels will still be a vortex line segment if the fluid is always barotropic (i.e., there is no intersection of pressure and temperature surfaces) and there are no non-conservative forces acting.

We will now consider the Boussinesq modified momentum equation (2.13). Taking the curl gives:

$$\frac{d\boldsymbol{\zeta}}{dt} = -\boldsymbol{\zeta}(\boldsymbol{\nabla}\cdot\mathbf{v}) + (\boldsymbol{\zeta}\cdot\boldsymbol{\nabla})\mathbf{v} + \boldsymbol{\nabla}_H\pi' \times \frac{\partial\theta_{v0}}{\partial z}\hat{\mathbf{k}} + \boldsymbol{\nabla}_H B \times \hat{\mathbf{k}} + \boldsymbol{\nabla}\times\mathbf{F}. \qquad (2.16)$$

With respect to tornadogenesis, the vertical component of this equation is most relevant:

$$\frac{d\zeta_z}{dt} = -\zeta_z(\boldsymbol{\nabla}\cdot\mathbf{v}) + (\boldsymbol{\zeta}\cdot\boldsymbol{\nabla})w + \boldsymbol{\nabla}\times\mathbf{F}|_z. \qquad (2.17)$$

Because of the Boussinesq approximation, vertical vorticity cannot be generated directly from baroclinic effects. Remaining are the vertical component of the diffusive term and the barotropic terms. The quantity $-\zeta_z\partial w/\partial z$ in the first barotropic term cancels $\zeta_z\partial w/\partial z$ in the second, leaving:

$$\frac{d\zeta_z}{dt} = -\zeta_z(\boldsymbol{\nabla}\cdot\mathbf{v_H}) + (\boldsymbol{\zeta}_{\boldsymbol{H}}\cdot\boldsymbol{\nabla})w + \boldsymbol{\nabla}\times\mathbf{F}|_z. \qquad (2.18)$$

The first term can be referred to as the convergence term. When vertical vorticity is already present, horizontal convergence will lead to a further increase in vertical vorticity. When the horizontal convergence is constant following an air trajectory, the air parcel's vertical vorticity will increase exponentially. This is the most general and basic explanation for the rapid formation of extreme vorticity values in tornadoes (the details will be addressed in this study); what is not explained is how vertical vorticity is generated where none had existed previously. Also, because the derivative occurs in a parcel-following framework, it does not necessarily follow that the vertical vorticity at a fixed point will exponentially increase because of the presence of constant horizontal convergence at that fixed point.

The second term is referred to as the 'tilting' term. Essentially it shows that when horizontal vorticity exists in the presence of a horizontal gradient in w, the horizontal vorticity will be 'tilted' into the vertical direction. This term is the one generally invoked to explain tornadogenesis; it then becomes necessary to explain the presence of the updraft gradient and the horizontal vorticity. Once vertical vorticity is generated, the convergence term can explain the subsequent increase in vertical vorticity to tornadic values. It should be noted, however, that when the vorticity vector is neither completely vertical nor completely horizontal, the convergence term also contributes to changing the vorticity vector direction, and the tilting term contributes to changing the vorticity vector magnitude; thus care must be taken in the interpretation of these processes. (Davies-Jones 1982; Grasso 1996; Finley 1997).

The horizontal vorticity equation derived from the modified momentum equation (2.13) has the form:

$$\frac{d\boldsymbol{\zeta}_{\boldsymbol{H}}}{dt} = -\boldsymbol{\zeta}_{\boldsymbol{H}}(\boldsymbol{\nabla}\cdot\mathbf{v}) + (\boldsymbol{\zeta}\cdot\boldsymbol{\nabla})\mathbf{v_H} + \boldsymbol{\nabla}_{\boldsymbol{H}}\pi' \times \frac{\partial\theta_{v0}}{\partial z}\hat{\mathbf{k}} + \boldsymbol{\nabla}_H B \times \hat{\mathbf{k}} + \boldsymbol{\nabla}\times\mathbf{F}|_H. \tag{2.19}$$

The first two terms are the barotropic terms, and the last is the diffusion term. The third term becomes zero when a base state θ_{v0} is chosen to be independent of height, which is a valid option provided θ_v/θ_{v0} is not much different from unity. If θ_v/θ_{v0} is significantly different from unity, either a new reference state should be chosen, or the assumptions leading to the Boussinesq modified momentum equation (2.13) are questionable. The fourth term is the baroclinic contribution to horizontal vorticity; in the Boussinesq modified system, it acts in a direction perpendicular to and to the right of the buoyancy gradient.

2.4 Compressibility

If one assumes that the model is incompressible such that $\nabla \cdot \mathrm{v} = 0$, then the vertical vorticity equation (2.18) can be written as:

$$\frac{d\zeta_z}{dt} = \zeta_z \frac{\partial w}{\partial z} + (\boldsymbol{\zeta_H} \cdot \boldsymbol{\nabla})w + \boldsymbol{\nabla} \times \mathbf{F}|_z. \tag{2.20}$$

Thus the presence of vertical divergence, increasing w with height, can exponentially increase vertical vorticity. Hence the convergence term is usually referred to as the 'stretching' term.

RAMS is not an incompressible model, but generally the three-dimensional divergence of the motion field is small. To find out how RAMS treats three-dimensional divergence, one can take the divergence of the equations of motion (2.13):

$$\begin{aligned} \frac{d}{dt}(\boldsymbol{\nabla} \cdot \mathrm{v}) &= -\left(\frac{\partial u}{\partial x}\right)^2 - \left(\frac{\partial v}{\partial y}\right)^2 - \left(\frac{\partial w}{\partial z}\right)^2 - 2\left[\frac{\partial v}{\partial x}\frac{\partial u}{\partial y} + \frac{\partial w}{\partial x}\frac{\partial u}{\partial z} + \frac{\partial w}{\partial y}\frac{\partial v}{\partial z}\right] + \frac{\partial B}{\partial z} \\ & \quad -\boldsymbol{\nabla} \cdot (\theta_{v0} \boldsymbol{\nabla} \pi') + \boldsymbol{\nabla} \cdot \mathbf{F}. \end{aligned} \tag{2.21}$$

Even if one assumes that the three-dimensional divergence is zero at a particular time, the terms on the first line of the RHS show that the effects of advection and buoyancy can create three-dimensional divergence. It is also seen how π and diffusion can cause $\boldsymbol{\nabla} \cdot \mathrm{v}$ to become non-zero.

Meanwhile the three-dimensional divergence causes a change in the density through the continuity equation:

$$-\boldsymbol{\nabla} \cdot \mathrm{v} = \frac{D}{Dt}(\ln \rho) = \frac{c_v}{R}\frac{D}{Dt}(\ln \pi) - \frac{D}{Dt}(\ln \theta_v) \tag{2.22}$$

in terms of the conventional thermodynamic variables of RAMS (see Appendix A). The treatment of this equation is simplified in RAMS and other numerical models by neglecting the horizontal π' advective terms and the local θ_v' tendency term on the RHS, leaving

$c_v/(R\pi_0)\partial\pi'/\partial t$ as the most significant term (Klemp and Wilhelmson 1978).[2] A local π' tendency equation results, given by

$$\frac{\partial \pi'}{\partial t} = -\frac{c_s^2}{\theta_{v0}}(\boldsymbol{\nabla}\cdot\mathbf{v}), \tag{2.23}$$

where $c_s^2 = c_p R T_{v0}/c_v$ is the square of the adiabatic speed of sound, and $T_{v0} = \pi_0\theta_{v0}/c_p$. When the three-dimensional divergence in (2.23) is substituted into (2.21), the equation produced resembles a forced wave equation for π', with c_s as the wave speed.

In the limit as the speed of sound approaches infinity, the change in π' becomes arbitrarily large for any three-dimensional divergence over a given spatial and temporal scale. Acoustic waves rapidly propagate outward, and tend to eliminate both $\boldsymbol{\nabla}\cdot\mathbf{v}$ and its tendency over advective time scales. In this state the atmosphere behaves as an incompressible fluid, and π' satisfies the relation:

$$\boldsymbol{\nabla}\cdot(\theta_{v0}\boldsymbol{\nabla}\pi') = -\left(\frac{\partial u}{\partial x}\right)^2 - \left(\frac{\partial v}{\partial y}\right)^2 - \left(\frac{\partial w}{\partial z}\right)^2 - 2\left[\frac{\partial v}{\partial x}\frac{\partial u}{\partial y} + \frac{\partial w}{\partial x}\frac{\partial u}{\partial z} + \frac{\partial w}{\partial y}\frac{\partial v}{\partial z}\right] + \frac{\partial B}{\partial z} + \boldsymbol{\nabla}\cdot\mathbf{F}. \tag{2.24}$$

This is a Poisson partial differential equation that may be inverted for π' given the terms on the RHS and the appropriate boundary conditions. This equation is useful for explaining the formation of strong pressure gradients by supercells. While it is not an exact relation for a compressible fluid, it will be approximately true when the terms on the RHS of (2.24) exist for long timescales compared to the time required for sound waves to propagate from the region. For computational efficiency purposes c_s is artificially reduced by RAMS, but is still generally over 150 m s^{-1} in these simulations.[3]

---

[2] When there is a vertical variation in the density and θ_{v0} basic states, another term is retained in numerical models, relating to the vertical advection of these basic states (Grasso, personal communication)

[3] Like Klemp and Wilhelmson (1978), RAMS also uses a time-splitting technique to maintain stability in the horizontal dimensions, discussed in later chapters. Even with these modifications stability in the vertical direction is not assured and often violated, so an implicit scheme is used to update the pressure from the vertical velocities.

If one assumes heuristically that the π' Laplacian term is proportional but opposite in sign to π' itself (normally true for localized disturbances away from the boundaries), then positive terms on the RHS of (2.24) tend to create low pressure, and negative terms tend to create high pressure (Rotunno and Klemp 1982). Because of the linear nature of the Laplacian operator, each RHS term can be considered to cause a contribution to π', and the sum of these contributions gives the total π'. All the terms except the last two reflect the effects of advection on the Exner function; these are referred to as the dynamic forcing on π'. The next two terms are the buoyant and diffusive forcings, respectively.

The dynamic terms in (2.24) are in a form such that the magnitude of the individual terms is dependent on the choice of orientation of the x and y axes. It is possible to rewrite them so that this is not the case. When this is done, the result is (see Appendix B):

$$\boldsymbol{\nabla} \cdot (\theta_{v0} \boldsymbol{\nabla} \pi') = \frac{\zeta_z^2 - 3\delta^2 - \mathcal{D}^2}{2} - 2\left[\boldsymbol{\nabla}_{\boldsymbol{H}} w \cdot \frac{\partial \mathbf{v_H}}{\partial z}\right] + \frac{\partial B}{\partial z} + \boldsymbol{\nabla} \cdot \mathbf{F}, \tag{2.25}$$

where incompressibility has been assumed, δ is $(\partial u/\partial x + \partial v/\partial y)$, and $\mathcal{D}$ is the magnitude of the horizontal deformation,

$$\mathcal{D}^2 = \left(\frac{\partial v}{\partial x} + \frac{\partial u}{\partial y}\right)^2 + \left(\frac{\partial u}{\partial x} - \frac{\partial v}{\partial y}\right)^2. \tag{2.26}$$

Therefore, regions of vertical vorticity of either sign tend to be associated with low pressure; regions of convergence/divergence and deformation are associated with high pressure. One-dimensional shear lines in a two-dimensional fluid motion have equal magnitude vorticity and deformation, and so they are not associated with dynamic pressure perturbations. On the other hand, an axisymmetric region of constant vertical vorticity and no radial velocity possesses zero horizontal deformation in its interior, and does tend to be associated with negative dynamic pressure perturbations.

2.5 Circulation

One disadvantage of only considering vorticity in connection with low-level mesocyclones and tornadoes is that it is defined at a point. Along a near-discontinuity in the wind field vorticity may reach large values. A better distinguishing mark of tornadoes might be an area-averaged vorticity. Such a measure is the circulation, which is defined for a particular closed curve C as

$$\mathcal{C} = \oint\limits_{C} \mathbf{v} \cdot \mathbf{dl}. \tag{2.27}$$

By Stokes' theorem, we have, equivalently,

$$\mathcal{C} = \iint\limits_{S} \boldsymbol{\zeta} \cdot \hat{\mathbf{n}} dA, \tag{2.28}$$

where S is the open surface enclosed by C. Thus the circulation measures an integration over S of the component of the vorticity vector normal to S at each point. It is convenient to work with because to compute the circulation around an area S all that is needed is the value of $\mathbf{v}$ along the boundary of S.

Suppose one wants to find the material derivative of the circulation. The time integration of the material derivative of the circulation is the circulation around the curve formed at all times by connecting the same fluid elements that composed the original curve (i.e, the material curve). It can be shown that (Dutton 1995):

$$\frac{d\mathcal{C}}{dt} = \oint\limits_{C} \frac{d\mathbf{v}}{dt} \cdot \mathbf{dl} + \oint\limits_{C} \mathbf{v} \cdot \frac{d}{dt}(\mathbf{dl}) = \oint\limits_{C} \frac{d\mathbf{v}}{dt} \cdot \mathbf{dl} + \oint\limits_{C} \mathbf{v} \cdot \mathbf{dv} = \oint\limits_{C} \frac{d\mathbf{v}}{dt} \cdot \mathbf{dl}, \tag{2.29}$$

since $\mathbf{v} \cdot \mathbf{dv} = d(v^2/2)$ which gives zero after integration around a closed contour. So the circulation tendency equation can be found by simply substituting (2.9) into (2.29):

$$\frac{d\mathcal{C}}{dt} = \oint\limits_{C} \left[-\theta_v(1 - r_c)\boldsymbol{\nabla}\pi - g\hat{\mathbf{k}} + \mathbf{F} \right] \cdot \mathbf{dl} = \iint\limits_{S} \left[\boldsymbol{\nabla}\pi \times \boldsymbol{\nabla}\theta_v(1 - r_c) + \boldsymbol{\nabla} \times \mathbf{F} \right] \cdot \hat{\mathbf{n}} dA. \tag{2.30}$$

The barotropic terms do not appear – only the baroclinic and diffusion terms can change the circulation. In the Boussinesq version of the circulation tendency equation,

$$\frac{d\mathcal{C}}{dt} = \oint_C \left[-\theta_{v0} \boldsymbol{\nabla} \pi' + B\hat{\mathbf{k}} + \mathbf{F} \right] \cdot \mathbf{dl}$$

$$= \iint_S \left[\boldsymbol{\nabla}_{\boldsymbol{H}} \pi' \times \frac{\partial \theta_{v0}}{\partial z} \hat{\mathbf{k}} + \boldsymbol{\nabla}_{\boldsymbol{H}} B \times \hat{\mathbf{k}} + \boldsymbol{\nabla} \times \mathbf{F} \right] \cdot \hat{\mathbf{n}} dA, \tag{2.31}$$

circulation cannot be generated over purely horizontal surfaces, except possibly through the diffusion term (Grasso 1996; Finley 1997). If we neglect $\boldsymbol{\nabla} \times \mathbf{F}$, and the θ_{v0} gradient term is neglected as in ....(2.19), circulation can only be generated when there are horizontal gradients of buoyancy along portions of S that extend in the vertical.

2.6 Eulerian Vorticity

The parcel-following or Lagrangian derivative of vertical vorticity is given by (2.18) for a Boussinesq atmosphere. The time derivative of vertical vorticity at a fixed point in space (Eulerian derivative) in this framework is thus:

$$\frac{\partial \zeta_z}{\partial t} = -(\mathbf{v} \cdot \boldsymbol{\nabla})\zeta_z - \zeta_z(\boldsymbol{\nabla} \cdot \mathbf{v_H}) + (\boldsymbol{\zeta_H} \cdot \boldsymbol{\nabla})w + \boldsymbol{\nabla} \times \mathbf{F}|_z. \tag{2.32}$$

This can be rewritten as:

$$\frac{\partial \zeta_z}{\partial t} = -(\mathbf{v_H} \cdot \boldsymbol{\nabla})\zeta_z - w\hat{\mathbf{k}} \cdot (\boldsymbol{\nabla} \times \frac{\partial \mathbf{v_H}}{\partial z}) - \zeta_z(\boldsymbol{\nabla} \cdot \mathbf{v_H}) + \left[\frac{\partial \mathbf{v_H}}{\partial z} \times \boldsymbol{\nabla}_{\boldsymbol{H}} w + \boldsymbol{\nabla} \times \mathbf{F} \right] \cdot \hat{\mathbf{k}}. \tag{2.33}$$

The advection term has been separated into a horizontal and a vertical contribution, and the tilting term $(\boldsymbol{\zeta_H} \cdot \boldsymbol{\nabla})w = (\partial w/\partial y - \partial v/\partial z)(\partial w/\partial x) + (\partial u/\partial z - \partial w/\partial x)(\partial w/\partial y) = -(\partial v/\partial z)(\partial w/\partial x) + (\partial u/\partial z)(\partial w/\partial y) = \hat{\mathbf{k}} \cdot [\partial \mathbf{v_H}/\partial z \times \boldsymbol{\nabla}_{\boldsymbol{H}} w]$.

It has been noted that the RHS of (2.33) can be expressed as the convergence of a two-dimensional vector (Haynes and McIntyre 1987; Weisman and Davis 1998). The first and third terms in (2.33) can be immediately combined into $-\boldsymbol{\nabla} \cdot (\zeta_z \boldsymbol{v_H})$ by a vector identity (Lewis and Ward 1989). Another vector identity involving the curl of the product of a scalar and a vector reveals that $\boldsymbol{\nabla} \times (w\partial \mathbf{v_H}/\partial z) = w(\boldsymbol{\nabla} \times \partial \mathbf{v_H}/\partial z) + \boldsymbol{\nabla} w \times \partial \mathbf{v_H}/\partial z$. Taking the dot product with $\hat{\mathbf{k}}$ gives $\hat{\mathbf{k}} \cdot \boldsymbol{\nabla} \times (w\partial \mathbf{v_H}/\partial z) = w\hat{\mathbf{k}} \cdot (\boldsymbol{\nabla} \times \partial \mathbf{v_H}/\partial z) + \hat{\mathbf{k}} \cdot (\boldsymbol{\nabla}_{\boldsymbol{H}} w \times \partial \mathbf{v_H}/\partial z)$. Using these results, we can write (2.33) as:

$$\frac{\partial \zeta_z}{\partial t} = -\boldsymbol{\nabla} \cdot (\zeta_z \boldsymbol{v_H}) - \hat{\mathbf{k}} \cdot \left[\boldsymbol{\nabla} \times w \frac{\partial \mathbf{v_H}}{\partial z} - \boldsymbol{\nabla} \times \mathbf{F} \right]. \tag{2.34}$$

Using the useful relation:

$$\boldsymbol{\nabla} \cdot (\mathbf{a} \times \hat{\mathbf{k}}) = \hat{\mathbf{k}} \cdot (\boldsymbol{\nabla} \times \mathbf{a}) \tag{2.35}$$

allows the conversion of the curl terms into divergences (in fact, horizontal divergences):

$$\frac{\partial \zeta_z}{\partial t} = -\boldsymbol{\nabla}_{\boldsymbol{H}} \cdot \left[\zeta_z \mathbf{v_H} + \left(w \frac{\partial \mathbf{v_H}}{\partial z} \times \hat{\mathbf{k}} \right) + \left(\hat{\mathbf{k}} \times \mathbf{F} \right) \right], \tag{2.36}$$

The first vector on the RHS is a flux of vertical vorticity by the horizontal wind; it combines the stretching and horizontal advection terms. The second vector is perpendicular to the vertical shear vector, and is also proportional to the vertical velocity; it combines the tilting and vertical advection terms. The third vector is perpendicular to the horizontal component of any remaining force.

There are advantages and disadvantages to using the Eulerian as opposed to the Lagrangian method of describing vorticity evolution. The Lagrangian vorticity equation definitively describes how an air parcel at a particular location acquired vorticity when the equation is integrated backwards in time (provided all the assumptions are appropriate). Using the Eulerian equation at a particular point might only provide the information that the vorticity was advected from somewhere else. However, obtaining the values of the terms in the Lagrangian equation requires knowledge of the position of the parcel versus time, which requires that one also perform a backward integration of the velocity versus time. In an Eulerian numerical model such as RAMS, information at each time is only stored for discrete points rather than for discrete parcels, so interpolation and approximation in determining the velocity and vorticity fields for a parcel are inevitable. The Eulerian equation is more consistent with how vorticity is actually generated by an Eulerian model.

2.7 Eulerian Circulation

The circulation tendency around a *horizontal* Eulerian contour enclosing an area S can simply be found by integrating (2.36):

$$\frac{\partial \mathcal{C}}{\partial t} = -\iint\limits_{S} \boldsymbol{\nabla} \cdot \left[\zeta_z \mathbf{v_H} + \left(w\frac{\partial \mathbf{v_H}}{\partial z} \times \hat{\mathbf{k}}\right) + \left(\hat{\mathbf{k}} \times \mathbf{F}\right)\right] dA. \tag{2.37}$$

One can use this equation to describe how circulation is increasing around a region of a storm, but if this is the case one should make sure that the horizontal velocities used are with respect to a reference frame moving with the storm region in question.

It is also possible to write (2.37) in terms of a line integral about the boundary of C. Relation (2.35) can be used to convert the cross product divergences in (2.37) back into the vertical component of a curl. For the term involving $\zeta_z \mathbf{v_H}$, we can use the similar relation:

$$\hat{\mathbf{k}} \cdot \left[\boldsymbol{\nabla} \times (\mathbf{a} \times \hat{\mathbf{k}})\right] = \hat{\mathbf{k}} \cdot \left[-\hat{\mathbf{k}}(\boldsymbol{\nabla} \cdot \mathbf{a}) + \frac{\partial \mathbf{a}}{\partial z}\right] = -\boldsymbol{\nabla} \cdot \mathbf{a}, \tag{2.38}$$

with the last equality valid if $\mathbf{a}$ is horizontal. Therefore, the integrand in (2.37) can be written as:

$$\frac{\partial \mathcal{C}}{\partial t} = \iint\limits_{S} \boldsymbol{\nabla} \times \left[\zeta_z \mathbf{v_H} \times \hat{\mathbf{k}} + -w\frac{\partial \mathbf{v_H}}{\partial z} + \mathbf{F}\right] \cdot \hat{\mathbf{k}} dA, \tag{2.39}$$

and after applying Stokes' theorem:

$$\frac{\partial \mathcal{C}}{\partial t} = \oint\limits_{C} \left[\zeta_z \mathbf{v_H} \times \hat{\mathbf{k}} - w\frac{\partial \mathbf{v_H}}{\partial z} + \mathbf{F}\right] \cdot \mathbf{dl}. \tag{2.40}$$

In a discrete numerical model vorticity cannot strictly be computed at a point; what one does in practice is compute the circulation around the appropriate planar grid cell, divide by the area of the grid cell to find the average vorticity perpendicular to the grid cell plane, and use this value as the vorticity component in that direction. So (2.40) has the advantage of being applicable to finding the change in circulation around a horizontal grid cell, although the component terms need to be interpolated to the horizontal grid cell circuit depending on the model grid staggering scheme.

2.8 Diffusion

To this point the diffusive force **F** has not been treated in detail, mainly because its treatment is not as mathematically clear as that of the other terms. In RAMS, this term can include surface drag, vertical diffusion, and horizontal diffusion – the latter two may be quite different because of the difference between the horizontal and vertical grid spacings.

If we assume an incompressible Newtonian gas, the fluid experiences a viscous force F_{vm} given by:

$$F_{vm} = \frac{1}{\rho}\frac{\partial}{\partial x_n}\left[\rho\nu\left(\frac{\partial u_m}{\partial x_n} + \frac{\partial u_n}{\partial x_m}\right)\right], \tag{2.41}$$

where ν is the coefficient of kinematic viscosity, and m, n are generalized indices in the Einstein summation notation, such that F_{vm} represents a viscous force vector with components $m = 1, 2, 3$, and the quantity within the brackets is the viscous stress tensor.

Generally the viscous stress is neglected for atmospheric motion because it is negligible on the scales of interest. But the Reynolds' stress due to turbulent motion is often not negligible. Numerical models such as RAMS often model subgrid-scale momentum fluxes by representing them as:

$$F_{sm} = \frac{1}{\rho}\frac{\partial}{\partial x_n}\left[\rho K_n\left(\frac{\partial u_m}{\partial x_n} + \frac{\partial u_n}{\partial x_m}\right)\right], \tag{2.42}$$

where K_n is the coefficient of 'eddy viscosity', and is a function of the atmospheric kinematics. It is subscripted by n to indicate that its treatment might be different for different coordinate axes.

In the limit of a constant-K, constant-density fluid, the second term in (2.42) becomes proportional to the gradient of the three-dimensional divergence, which would be zero in this case. This term is neglected in a commonly-used version of the RAMS diffusion scheme, based on that of Smagorinsky (1963); if we make this simplification, diffusion becomes:

$$F_{sm} = \frac{1}{\rho}\frac{\partial}{\partial x_n}\left[\rho K_n \left(\frac{\partial u_m}{\partial x_n}\right)\right]. \tag{2.43}$$

Let us also assume that the density is only a function of the vertical coordinate, and that for $n = 1, 2$, the coefficient of eddy viscosity has the constant value of K_H. We are left with:

$$F_{sm} = K_H \frac{\partial^2 u_m}{\partial x_l \partial x_l} + \frac{1}{\rho}\frac{\partial}{\partial z}\left[\rho K_V \left(\frac{\partial u_m}{\partial z}\right)\right], \tag{2.44}$$

where $l = 1, 2$, and K_V is the vertical coefficient of eddy viscosity.

In (2.44) the first term can be termed horizontal diffusion; for a signal in the u_m field where the horizontal Laplacian of u_m is roughly proportional to the negative of u_m, the signal will be exponentially decayed. The second term acts as vertical diffusion when the variation of ρ and K_V with height is neglected.

Taking the curl of (2.44) gives the diffusive tendency on vorticity. Considering the curl of the horizontal diffusion term using vector algebra reveals that:

$$\begin{aligned}\boldsymbol{\nabla} \times \nabla_H^2 \mathbf{v} = \boldsymbol{\nabla} \times \left[\nabla^2 \mathbf{v} - \frac{\partial^2 \mathbf{v}}{\partial z^2}\right] &= \boldsymbol{\nabla} \times \left[(\boldsymbol{\nabla}(\boldsymbol{\nabla} \cdot \mathbf{v}) - \boldsymbol{\nabla} \times \boldsymbol{\zeta})) - \frac{\partial^2 \mathbf{v}}{\partial z^2}\right] \\ &= \nabla^2 \boldsymbol{\zeta} - \frac{\partial^2 \boldsymbol{\zeta}}{\partial z^2} = \nabla_H^2 \boldsymbol{\zeta}. \end{aligned} \tag{2.45}$$

So the horizontal diffusion term simply diffuses vorticity of any orientation. Thus the terms viscosity and horizontal diffusion coefficient will be used interchangeably in this chapter.

2.9 Burgers Sheet and Vortex

Following Saffman (1992), assume that we have a zone of vertical vorticity in a region where there is no large-scale variation of any quantity in the y direction, and where the horizontal velocities do not vary in the z direction. We permit horizontal diffusion of the form (2.45), and air is converging in the x direction into the vortex sheet. There is no generation of vertical vorticity by either tilting or vertical advection because there is no vertical shear of the horizontal velocity. If a steady state is achieved, the vertical vorticity balance is between horizontal advection of vertical vorticity, convergent production, and diffusive destruction, according to:

$$u\frac{\partial \zeta_z}{\partial x} = -\frac{\partial u}{\partial x}\zeta_z + K_H\frac{\partial^2 \zeta_z}{\partial x^2}. \tag{2.46}$$

For constant K_H, this equation can be rewritten:

$$\frac{\partial}{\partial x}\left(-\frac{u\zeta_z}{K_H} + \frac{\partial \zeta_z}{\partial x}\right) = 0, \tag{2.47}$$

which suggests that

$$-\frac{u\zeta_z}{K_H} + \frac{\partial \zeta_z}{\partial x} = C(z), \tag{2.48}$$

where $C(z) = 0$ if the net vorticity flux is zero at infinity.

This is a first-order differential equation in x that can be solved for ζ_z if u is given as a function of x. Consider the case of uniform convergence into the vorticity sheet; then u can be expressed as $-\alpha x$ where α is a positive constant. The solution is then just

$$\zeta_z = \zeta_{z0}\exp\left(\frac{-\alpha x^2}{2K_H}\right). \tag{2.49}$$

This is Burgers vortex sheet (Burgers 1948). The vorticity has a maximum value along the y-axis and follows a Gaussian distribution away from the axis. The characteristic e-folding width of the vorticity band is given by $\delta_e = (2K_H/\gamma)^{1/2}$. As the diffusion constant goes to zero, the width of the band also goes to zero, becoming a tangential velocity discontinuity in the limit of zero diffusion.

Of course, in the real atmosphere turbulent transport cannot in general able to be represented by the eddy diffusion equation (2.42). However, when convergence is continually acting on a band of vorticity, some process must be invoked to explain why the vorticity does not collapse into an infinitesimally narrow sheet. At times, it will be assumed in this discussion that turbulent diffusion along vorticity bands in the real atmosphere can be adequately described by horizontal diffusion of the form in (2.45) provided that the implied characteristic Burgers vortex sheet width is of the same order of magnitude as the width of the vorticity band in the real atmosphere.

One can also speak of the axisymmetric Burgers vortex, which is found in the same way as the Burgers vortex sheet, with r, z replacing the dependent variables x, z. Here the radial velocity component for uniform axisymmetric convergence γ is given by $-\gamma r/2$, and the vorticity obeys:

$$\zeta_z = \zeta_{z0} \exp\left(\frac{-\gamma r^2}{4K_H}\right), \tag{2.50}$$

with characterisstic radius $(4K_H/\gamma)^{1/2}$.

Both of these idealized models presuppose a source for the vertical vorticity. The Burgers vortex possesses a finite but nonzero circulation Γ at large distances, which can be found by integrating the vorticity over all space to infinity: the result is:

$$\Gamma = \frac{4\pi\zeta_{z0}K_H}{\gamma}. \tag{2.51}$$

It is generally assumed that Γ, like γ, can be determined by the conditions in the large-scale environment. The maximum vorticity ζ_{z0} then becomes inversely proportional to the square of the characteristic Burgers vortex radius. For a given large-scale environment ζ_{z0} is only a function of the diffusion coefficient; in the inviscid limit, a point vortex with finite constant circulation is achieved.

Similarly, the Burgers vortex sheet can be integrated to infinity in the x direction to provide a finite circulation per unit y-direction length, σ, of (Neu 1984a):

$$\sigma = \left(\frac{2\pi K_H}{\alpha}\right)^{\frac{1}{2}} \zeta_{z0}, \tag{2.52}$$

where σ is specified by the environment.

2.10 Barotropic Instability

It was first demonstrated by Kelvin (1871) that if an infinitesimal wave-like perturbation is introduced to an infinitesimally-thin vortex sheet in a two-dimensional, inviscid, incompressible domain, the disturbance amplitude will grow exponentially. Hence a discontinuity in the tangential velocity is unstable. This phenomenon is generally known as Kelvin-Helmholtz instability (Helmholtz 1868; Kelvin 1871).[4] In fact, it can be shown the smaller the wavelength of the perturbation, the faster the growth rate (Saffman 1992).

Rayleigh (1880) considered the stability to wavelike perturbations of a long band of vorticity of finite width, and no variation of the mean state along its length. He found that a necessary condition for instability to infinitesimal disturbances was that an inflection point must exist in the mean state tangential velocity profile, or equivalently, the mean state vorticity gradient must change sign in the fluid. Because this process can occur with a constant-density fluid, it is often referred to in atmospheric science as barotropic instability,

---

[4] The theory can also be extended to cover a discontinuity in fluid density. In atmospheric science, the term Kelvin-Helmholtz instability is primarily used to describe the breakdown of a vertical shear layer in the presence of thermal stability, which inhibits the instability unless the vertical shear reaches a certain threshold.

to distinguish it from baroclinic instability, which requires the presence of density gradients (e.g., Hoskins et al. 1985).

The case of a thin band of constant vorticity surrounded by irrotational fluid can be considered to be the limit of a case that satisfies Rayleigh's criterion, such that there is a large negative gradient of vorticity at the right edge of the band (when the band extends lengthwise in the y direction), and a large positive gradient of vorticity at the left edge of the band. It was found by Rayleigh (1880) that short-wavelength infinitesimal disturbances were stable, but that exponential instability occurred under the influences of disturbances with wavelengths greater than approximately $5\Delta x$, where Δx is the width of the band of vorticity. There is also a wavelength of maximum instability, at approximately $8\Delta x$, with an e-folding growth time near $5/\zeta_z$, where ζ_z is the vorticity of the band.

It is possible to model this problem as the effect of two Rossby waves generated along the vorticity discontinuities at each edge of the vortex band (Guinn and Schubert 1993; Montgomery and Kallenbach 1997). When the wavelength is large enough compared to the width of the band, each Rossby wave is capable of inducing motion in the other wave such that each wave is in turn amplified. In the latter stages of this process linear perturbation theory no longer applies, but vorticity is seen to pool towards discrete centers, leaving thin spiraling vorticity streams to connect the centers (Guinn and Schubert 1993; Schecter et al. 2000). (See Figure 2.1).

It should be noted that in this barotropic instability model there is no vertical motion, and no way to generate vorticity. Thus vorticity can only change at a point by horizontal advection. Because the horizontal advection at a local maximum in the vorticity is zero, the value of the maximum vorticity does not change within this model (Schubert, personal communication).

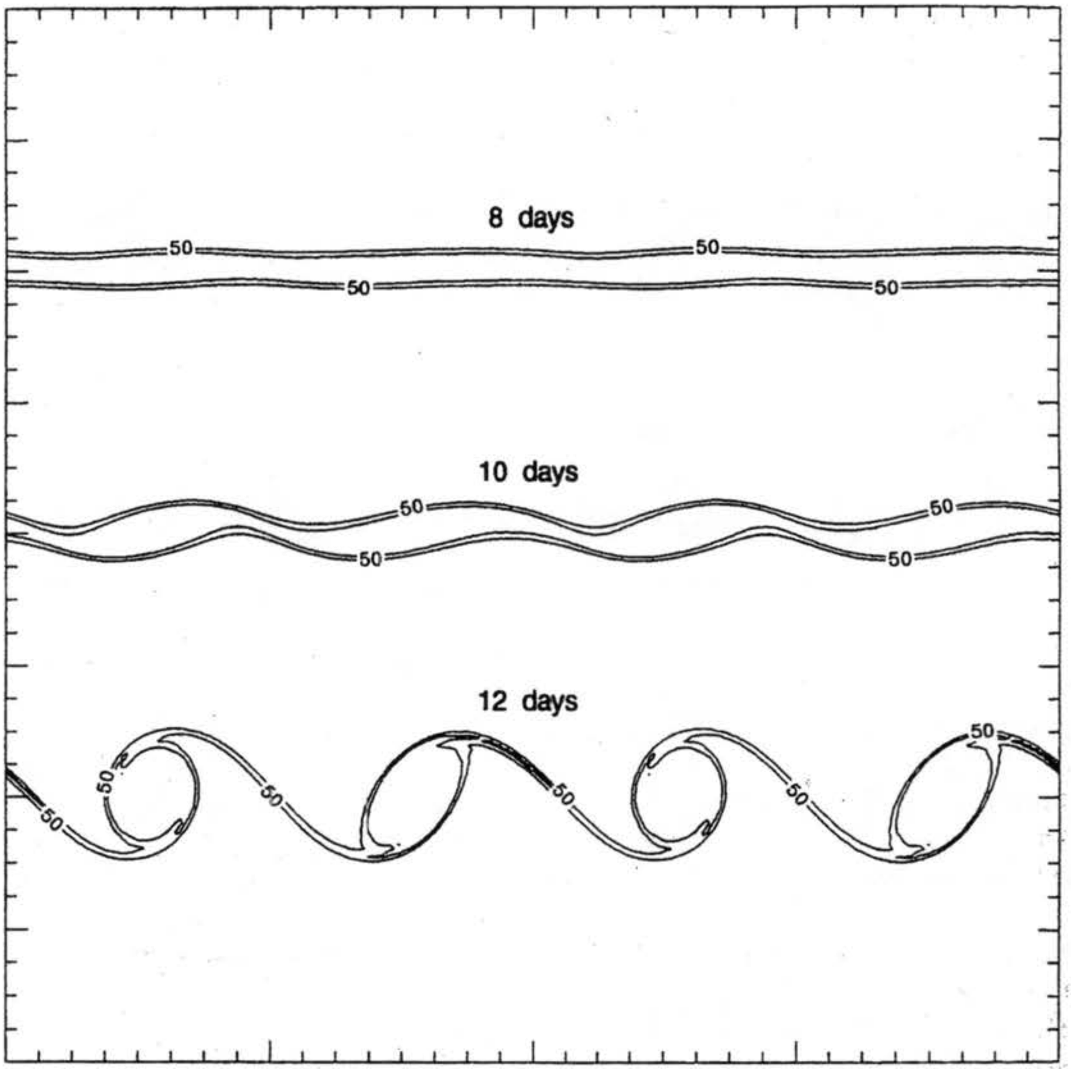

Figure 2.1: Vorticity bands in nondivergent simulation of intertropical convergence zone (ITCZ) breakdown. From Guinn and Schubert (1993).

2.11 Stretched Vortex Sheet Collapse

Corcos and Lin (1984) used numerical studies to examine the behavior of narrow vortex bands with low viscosity subject to unidirectional uniform convergence, as in the Burgers vortex sheet. They found that strong bands of vorticity showed a tendency to collapse into a point (Figure 2.2). Neu (1984a) developed an analytical model of the collapse process, and proved that the collapse occurs for a converged elliptical vortex region in the inviscid limit (i.e., infinitesimally thin), and more generally for vortex sheets when the lengthwise variation of σ is small compared to the convergence α. The collapse occurs because the vortex region tends to rotate under its self-induced velocity until the large-scale convergence advects all the vorticity of the sheet towards its axis of rotation (Figure 2.3).

When finite viscosity was taken into account, Neu found that the collapse of a converged narrow vortex band was not assured, but only occurred when

$$|\sigma| > 2(\nu\alpha)^{\frac{1}{2}}. \tag{2.53}$$

If it is assumed that to first order the narrow vortex band obeys the steady-state Burgers vortex sheet relation for ζ_{z0}, then we can express the instability criterion as:

$$|\zeta_{z0}| > \left(\frac{2}{\pi}\right)^{\frac{1}{2}} \alpha \tag{2.54}$$

Yet another representation of the instability condition comes from eliminating the viscosity in (2.53) using the Burgers vortex sheet e-folding width:

$$|\sigma| > \frac{\alpha\delta_{1/e}}{\sqrt{2}}. \tag{2.55}$$

Generally, the collapse occurs when the maximum vorticity within the vortex band exceeds the large-scale convergence (multiplied by a constant on the order of unity), or when the large-scale circulation density exceeds the product of the large-scale convergence and the

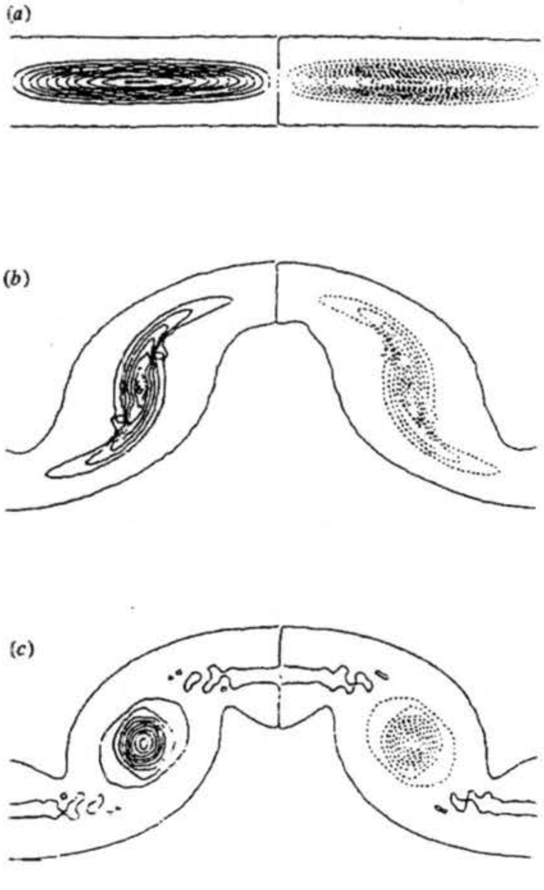

Figure 2.2: Collapse of a pair of counter-rotating vortices in a flow of uniform plane convergence. From Corcos and Lin (1984).

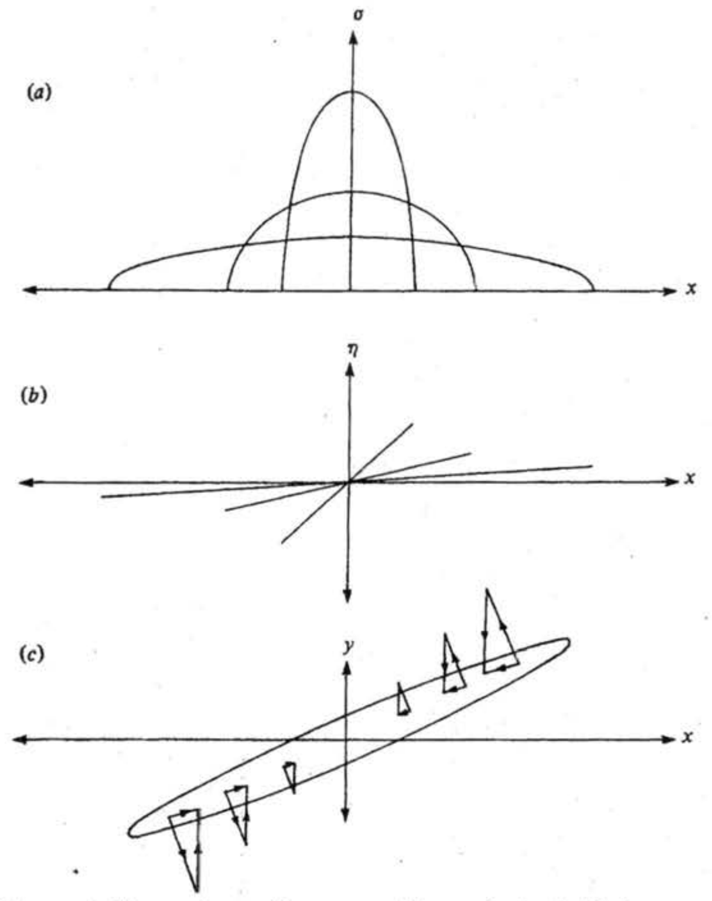

Figure 2.3: Depiction of vortex collapse process, according to Neu (1984a). The x-axis denotes the axis of the vortex sheet. The top schematic shows the focusing of circulation density, σ, at three successive times. The middle schematic shows the corresponding displacement of the vorticity strip from the x-axis, η. The bottom schematic shows the resultant velocity from the vector sum of the ambient convergence into the x-axis and the self-induced rotation for an elliptical vortex patch.

characteristic width of the vortex band. The end result of the collapse in the viscous case is a Burgers axisymmetric vortex with its radius specified by the values of α and ν, or equivalently α and $\delta_{1/e}$. The circulation of the final vortex according to Neu is the circulation excess of the vortex sheet, where the circulation excess is the difference between the actual circulation density and the threshold circulation density given in (2.53), integrated over the length of the vortex sheet that physically collapses.

Neu (1984b) showed that another factor that can hinder the collapse of an inviscid elliptical narrow vortex region in convergent flow is the presence of two-dimensional straining flow, i.e. a positive $\partial v/\partial y$ in the setup of (2.46). He found that collapse generally occurred when the semimajor axis length a was less than $[\Gamma/(\pi(\alpha\gamma')^{1/2})]^{1/2}$, where γ' is $\partial v/\partial y$ in our formulation, and Γ is the total circulation of the ellipse. Except for a few specific ellipse orientations, when a exceeded this threshold the ultimate result would be the extension of the ellipse into an infinitely-long vortex sheet.

For these ellipses the vorticity is constant, and the circulation of the ellipses is given by $\pi ab\zeta_z$, where b is the semiminor axis length. So the criterion for the collapse of the circulation can be written:

$$\frac{a}{b} < \frac{|\zeta_z|}{(\alpha\gamma')^{1/2}}, \tag{2.56}$$

which can be rearranged to give:

$$|\zeta_z| > \alpha\frac{a}{b}\left(\frac{\gamma'}{\alpha}\right)^{1/2}. \tag{2.57}$$

This resembles the viscous collapse condition in that the vorticity must be large compared to the convergence. Two aspect ratios appear, the ratio of the long axis of vorticity to the small axis, and the square root of the ratio of the divergence along the long axis to the convergence along the short axis. Roughly, collapse is facilitated when the convergence field is more uniaxial than the shape of the vorticity patch.

Multiplying both sides by b provides an equation in terms of σ:

$$|\sigma| > \alpha^{1/2} a \gamma'^{1/2} \tag{2.58}$$

Apparently, when the convergence is uniaxial such that γ' is zero, collapse is assured provided that a is finite, which reproduces the Neu (1984a) result. Conversely, any along-axis divergence is sufficient to prevent the collapse of an infinitely long vortex band. The quantity $a\gamma'^{1/2}$, like $\nu^{1/2}$ in (2.53), serves to hinder the collapse process. If $\gamma' < 0$ (both $\partial u/\partial x$ and $\partial v/\partial y$ are negative), then again collapse is assured.

Nolan (2001) showed in numerical simulations that an axisymmetric vortex in the presence of axial convergence is considerably more stable to perturbations than the same vortex in an environment without axial convergence. This result, though somewhat idealized, suggests that the concentrated stretched vortex is quite stable to dissipation once it forms.

2.12 Time-dependent Stretched Vortex Sheets

Consider a large scale, two-dimensional, viscous, irrotational flow with $\partial u/\partial x = -\alpha$ and $\partial w/\partial z = \gamma$, where α and γ are positive constants. By continuity, $\partial v/\partial y = \alpha - \gamma$. If $\alpha = \gamma$, as in the Burgers vortex sheet, the flow can be referred to as *plane strain*; for $\alpha < \gamma$, such as the Burgers axisymmetric vortex, we have *uniaxial strain*; for $\alpha > \gamma$, as in the non-collapsing ellipses of Neu (1984b), we have *biaxial strain* (Moffatt et al. 1994). Assume that the flow possesses a superimposed vertical vorticity and corresponding vorticity-induced velocity, but that neither is a function of either z or y. The governing vorticity equation is (Saffman 1992; Sec. 13.3):

$$\frac{\partial \zeta_z}{\partial t} - \alpha x \frac{\partial \zeta_z}{\partial x} = \gamma \zeta_z + \nu \frac{\partial^2 \zeta_z}{\partial x^2}. \tag{2.59}$$

If we substitute $\omega = \zeta_z \exp(-\gamma t)$, the equation reduces to

$$\frac{\partial \omega}{\partial t} - \alpha x \frac{\partial \omega}{\partial x} = +\nu \frac{\partial^2 \omega}{\partial x^2}. \tag{2.60}$$

Using a change of variables and the Green's function for the time-dependent diffusion equation, Kambe (1983) found the time-dependent solution to (2.60) given any sufficiently bounded initial condition $\omega(x, t = 0)$. Substituting for the original vorticity in his solution gives:

$$\zeta_z(\xi, \tau; t) = \frac{\exp(\gamma t)}{2\sqrt{\pi \nu \tau}} \int_{-\infty}^{\infty} \zeta_{z0}(\xi') \exp\left[-\frac{(\xi' - \xi)^2}{4\nu\tau}\right] d\xi', \tag{2.61}$$

where $\zeta_{z0}(x) = \zeta_z(x, t = 0)$, $\xi = xe^{\alpha t}$, and $\tau = (e^{2\alpha t} - 1)/2\alpha$.

In particular, if the initial vorticity has constant initial value of ζ_0 for $-R < x < R$, and zero otherwise, the integration can be performed to yield (in terms of x and t):

$$\zeta_z(x, t) = \frac{\zeta_0 e^{\gamma t}}{2} \left[\text{erf}\left(\frac{(R - xe^{\alpha t})\sqrt{\alpha}}{\sqrt{2\nu(e^{2\alpha t} - 1)}}\right) + \text{erf}\left(\frac{(R + xe^{\alpha t})\sqrt{\alpha}}{\sqrt{2\nu(e^{2\alpha t} - 1)}}\right)\right]. \tag{2.62}$$

Here erf(x) is the error function, defined by:

$$\text{erf}(x) = \frac{2}{\sqrt{\pi}} \int_0^x e^{-z^2} dz = \frac{2}{\sqrt{\pi}} \left[x - \frac{x^3}{3} + \frac{x^5}{10} - ...\right]. \tag{2.63}$$

If we consider the limit as t becomes large compared to $1/2\alpha$, so that the exponential terms dominate in the denominators, we get a solution for large times of:

$$\zeta_z(x, t_\infty) \approx \frac{\zeta_0 e^{\gamma t}}{2} \left[\text{erf}\left(\sqrt{\frac{\alpha}{2\nu}}(Re^{-\alpha t} - x)\right) + \text{erf}\left(\sqrt{\frac{\alpha}{2\nu}}(Re^{-\alpha t} + x)\right)\right] \tag{2.64}$$

If we also assume that t is large compared with $\ln(R/x)/\alpha$, a more stringent requirement near the y-axis, we can expand the error functions as Taylor series about $\pm x\sqrt{\alpha/2\nu}$. From the integral of (2.63), we have $\text{erf}(u+a) \approx \text{erf}(u) + a(2/\sqrt{\pi})e^{-u^2}$ when $a << u$. Therefore, we obtain:

$$\zeta_z(x, t_\infty) \approx \frac{\zeta_0 e^{\gamma t}}{2} \left[\text{erf}\left(-\sqrt{\frac{\alpha}{2\nu}}x\right) + Re^{-\alpha t}\sqrt{\frac{\alpha}{2\nu}}\frac{2}{\sqrt{\pi}} \exp\left(\frac{-\alpha x^2}{2\nu}\right)\right.$$

$$\left. + \text{erf}\left(\sqrt{\frac{\alpha}{2\nu}}x\right) + Re^{-\alpha t}\sqrt{\frac{\alpha}{2\nu}}\frac{2}{\sqrt{\pi}} \exp\left(\frac{-\alpha x^2}{2\nu}\right)\right]. \tag{2.65}$$

The two error function terms cancel because they are odd functions, leaving:

$$\zeta_z(x,t_\infty) = \zeta_0 e^{(\gamma-\alpha)t} R\sqrt{\frac{2\alpha}{\pi\nu}}\exp\left(\frac{-\alpha x^2}{2\nu}\right), \tag{2.66}$$

Note that even along the y-axis where $\ln(R/x)$ is infinite, this equation is still valid at all t provided that R in (2.64) is much larger than $\delta_{1/e} = (\alpha/2\nu)^{\frac{1}{2}}$, the characteristic Burgers vortex sheet width (this can be seen by applying the first term on the RHS of (2.63) to the small argument of the error functions).

For $\alpha = \gamma$ it is seen that at long times a steady state is approached, corresponding to the Burgers vortex sheet. The significance is that any initial unidirectional zone of vorticity, if subjected to plane strain, will tend to form a Burgers vortex sheet, if it is not one already. A finite segment of the Burgers vortex sheet may then break down into vortices by the Neu (1984a) mechanism. If $\alpha \neq \gamma$ the vorticity dependence on x is the same, but no steady-state is achieved; the amplitude grows exponentially for uniaxial strain ($\gamma > \alpha$), and decays exponentially for biaxial strain ($\gamma < \alpha$).

Now consider the case when t is small compared to $1/2\alpha$. In this case, the denominators of the error functions in (2.62) are near zero. Unless we are near $x = \pm R$, the vorticity is simply

$$\zeta_z(x,t) = \zeta_0 e^{\gamma t}\mathrm{erf}(\infty) = \zeta_0 e^{\gamma t}, \tag{2.67}$$

Until t is on the order of $1/2\alpha$, exponential growth in vorticity will occur when $\gamma > 0$; the actual value of α is not involved before this characteristic time.

The following scenario is thus suggested for the behavior of a unidirectional band of vorticity with width $2R$ in a constant straining field. If $\partial w/\partial z$ is positive, the band will contract towards the axis while the vorticity exponentially increases. This will continue at least until time on the order of $1/2\alpha$ From the large time equation (2.66), we have a maximum vorticity of $\zeta_0 R(2\alpha/\pi\nu)^{\frac{1}{2}}$ if we allow $t = 0$. It is suggested, then, that the vorticity will continue to increase in the vortex patch for $\gamma > 0$, until the maximum vorticity along the axis of convergence has increased by a factor of $R(2\alpha/\pi\nu)^{\frac{1}{2}}$, or $(2/\sqrt{\pi})(R/\delta_e)$. After that value has been reached, the vorticity will continue to exponentially increase in uniaxial strain, though at a reduced rate. In biaxial strain, however, the vorticity will begin to exponentially decrease from the maximum value – its maintenance would depend on vorticity being continuously supplied from the lateral boundaries.

Chapter 3

HISTORICAL BACKGROUND

3.1 Observations

The search for the source of the extreme values of velocity and vorticity (up to 2 s^{-1} according to Lemon and Doswell 1979) found in tornadoes has occupied atmospheric science researchers for decades. As early as the 1940s, Brooks (1949) noted that a number of tornadoes were accompanied by regions of significant reduced pressures on scales much larger than the actual tornado. He introduced the concept of the *tornado cyclone*, and surface observations have since confirmed the presence of rotating cloud features on a scale of several kilometers prior to tornadogenesis (Burgess and Donaldson 1979; Bluestein and Golden 1993). Brooks theorized that the contraction of a tornado cyclone could account for the vorticity found in a severe tornado even if frictional losses to the ground removed half of the angular momentum in the process. Fujita (1963) used the term *mesocyclone* to refer to circulatory features on a scale larger than that of the tornado but too small to be represented in synoptic analyses.

Browning (1964) noted that a significant fraction of severe storms in the northern hemisphere (including tornadic storms) differed from conventional convection in qualitative ways, particularly in that they essentially consisted of large single cells (now denoted as *supercells*) that continuously propagated to the right of the mean wind at all levels in the mid-troposphere, persisting for hours. Using radar reflectivity data, he was the first to develop a model of the supercell thunderstorm. His Severe Right (SR) storm develops in an environment with strong wind shear and a hodograph that veers with height, and moves to the right of the mean tropospheric wind. This behavior causes warm, moist, low-level air to exit and drop precipitation ahead of the storm, with cyclonically turning streamlines existing within the updraft. Dry mid-level air tends to have a component towards the right rear flank of the storm (see Figure 3.1). This air evaporatively cools and forms a downdraft that descends on the left rear flank of the storm. As this air diverges near the ground it lifts warm, moist air ahead of it, enhancing the inflow towards the storm. However, since the storm-relative component of the downdraft flow, as well as the location of the precipitation, is well away from the inflow sector, the inflow is generally not interrupted and the cell can become nearly steady-state. Features of this storm identifiable on radar include a weak echo region (WER) within the updraft at low and mid-levels, and a precipitation-caused hook-shaped echo at low levels. The WER is the result of the updraft being so intense that precipitation particles do not have time to grow to significant size until they have reached high levels in the storm. The hook echo is located near the edge of downdraft in a region of large hail, with rain becoming more prominent towards the forward flank of the storm. Tornadoes had been recognized as occurring in association with hook echoes (Garrett and Rockney 1962); the development of the supercell model explained the association as the result of the supercell structure being the origin of both.

Barnes (1970) was one of the first to propose an explanation for the origin of the supercell rotation. He invoked the concept of vortex lines, which are tangent to the vorticity within the fluid; their density is proportional to the magnitude of the vorticity. Under certain conditions (see Chapter 2), vortex lines merely advect with the fluid. In the supercell environment, the vertical wind shear implies the presence of horizontal vortex lines; when

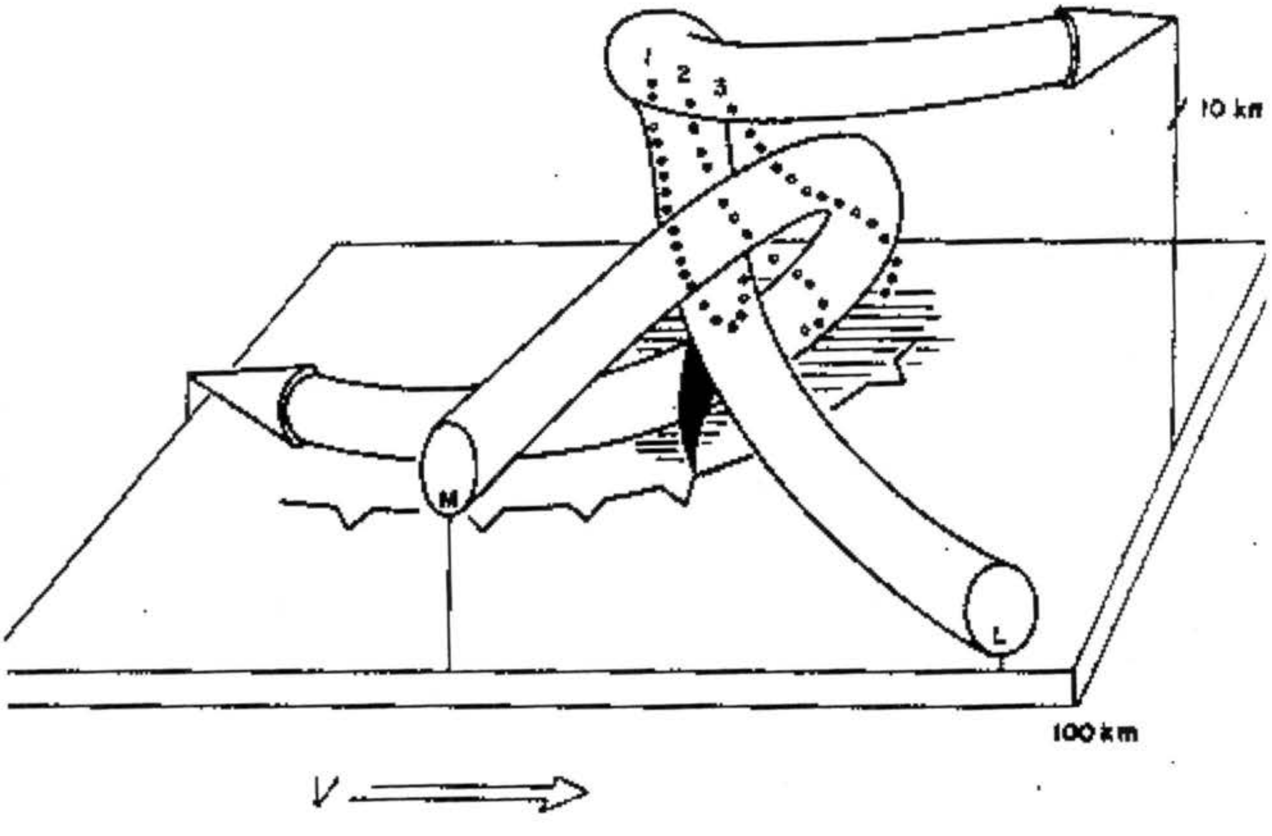

Figure 3.1: Depiction of airflow in a supercell. From Browning (1964)

these lines are advected into the supercell by the updraft, they are tilted upwards and create vertical vorticity.

The development of Doppler radar made possible the detection of mesocyclones from a distance and confirmed their existence within the thunderstorm well above cloud base (Donaldson 1970). Actual tornadoes were too small to be resolved by operational Doppler radar at any typical range. However, a distinctive Doppler signal known as the Tornado Vortex Signature (TVS) was found to nearly coincide with the 1973 Union City, OK tornado at ground level (Burgess et al. 1975). The TVS contains strong wind shear across successive azimuthal gates (20 m s^{-1}), no more than 1 km in range depth and several kilometers in height, persisting for around ten minutes. It was found that the TVS originated at midlevels (3-7 km) within the storm mesocyclone and then built both upwards and downwards. The descent of the TVS to the surface nearly coincided with the initiation of tornadic damage (Brown et al. 1978).

Using these and other observations, Lemon and Doswell (1979) further refined the picture of the supercell. They found that the model proposed by Browning (1964) is typical of the first stage of the supercell storm. In the next stage, the storm develops a bounded weak echo region (BWER), in which a region of low reflectivity is completely surrounded at a given height by regions of high reflectivity. The BWER represents the core of the updraft possessing the greatest updraft velocities of the storm at that level; the hydrometeors in this region have had less time within the storm to grow than those on the periphery of the updraft core, resulting in lower reflectivities. Meanwhile a mesocyclone becomes apparent in the region of the BWER, from 5-8 km above ground level. The mesocyclone appears to Doppler radar as a region of solid body rotation 5-10 km across with vorticity values near 0.01 s^{-1} (Burgess et al. 1982; Brandes 1984). At this time the storm often produces its largest output of hail to the surface. The final stage in supercell development, the collapse phase, is associated with strengthening downdrafts and weakening updrafts and BWER. But this is also the time that significant tornadoes are most likely to develop. During the collapse phase, the mesocyclone tends to migrate upwind from the updraft core to the boundary between the updraft and a region known as the rear-flank downdraft (RFD), in proximity to the hook echo. In their schematic of the supercell thunderstorm near the time of tornadogenesis (Figure 3.2), Lemon and Doswell clearly distinguish between the precipitation-cooled forward flank-downdraft (FFD) and the cooler, drier RFD. The RFD and 'divided mesocyclone' are seen to descend towards the surface together, and it is speculated that this process is closely associated with the formation of the hook echo and tornadogenesis. The descent of the TVS was also linked to that of the divided mesocyclone.

This picture suggested that, while the original midlevel updraft mesocyclone might intensify due to convergence, the formation of the tornado itself might be due to a completely different mechanism, probably involving tilting because it tends to occur along the updraft/downdraft gradient.

3.2 Supercell Modeling

In the mid-1970s, the growing sophistication of computer cloud models made it possible to attempt simulations of supercell thunderstorms. The model of Schlesinger (1975) was one of the first cloud models used for three-dimensional simulations, which is necessary to the proper simulation of supercells. His model was of coarse resolution (horizontal grid spacings of 3.2 km), did not include precipitation microphysics, and was anelastic. In an anelastic model $\nabla \cdot (\rho_0 \mathbf{v}) = 0$ where ρ_0 is generally a function of z only; sound waves cannot exist in such a model. A density-weighted divergence of the momentum equations leads to an elliptical equation for the pressure perturbation similar to (2.24). The elimination of sound waves was an advantage because it allowed the model to use relatively

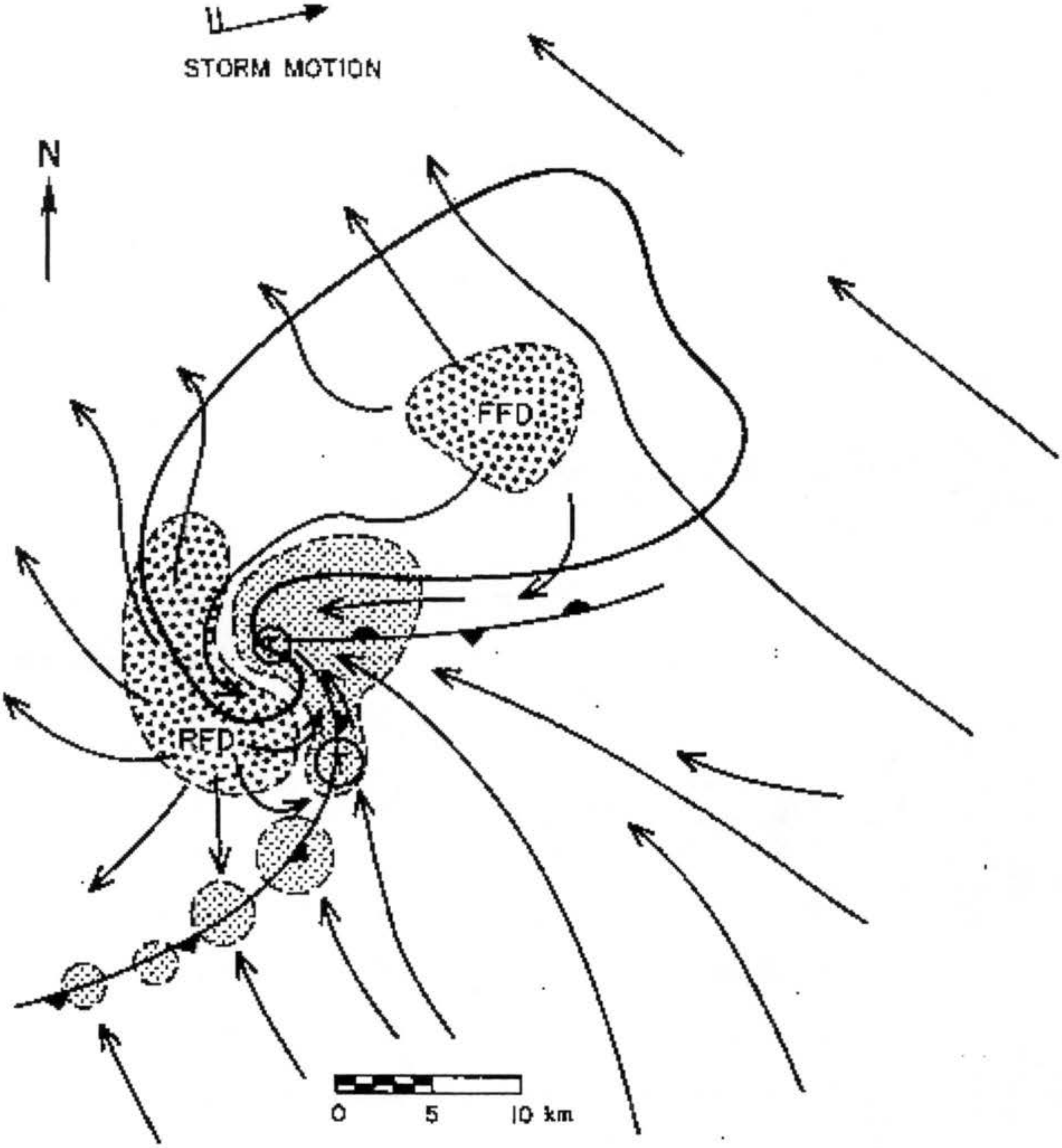

Figure 3.2: Plan view of tornadic supercell. Thin dots denote regions of updraft whereas thick dots denote regions of downdraft. Thick line is region of radar echo. The location of the tornado is marked by a T. From Lemon and Doswell (1979).

long time steps that normally would have produced sound wave instabilities, which would have crashed the model.

Schlesinger was able to create a vortex couplet a few kilometers above the surface by introducing a thermal plume in an environment with unidirectional wind shear. This showed that vertical vorticity could be produced by the presence of an updraft in an environment with vertical wind shear. However, it was not consistent with observations of supercells with an updraft dominated by the presence of vorticity of only one sign, usually positive.

Another of the early three-dimensional computer models developed to investigate the evolution of convection was that of Klemp and Wilhelmson (1978a). Their model was not anelastic, which required them to use a smaller time step with the pressure equation to prevent sound wave instability. However, the fact that the model was fully compressible made possible the explicit prediction of the pressure and the simplification of many of the numerical algorithms. They performed a number of simulations with Kessler rain microphysics at 1 km horizontal grid spacing and 500 m vertical grid spacing; these were the first simulations capable of producing storms with supercellular features. Klemp and Wilhelmson used horizontally-homogeneous simulations; an atmospheric sounding conducive to convection was assumed to represent the vertical profile of the atmosphere throughout the model domain. Actual model convection was initiated by introducing a 'warm bubble' (a region of elevated temperature) in the center of the domain at the simulation start.

In an initially unidirectional shear environment Klemp and Wilhelmson were able to simulate convection that subsequently split into two members. Storm-splitting was a phenomenon that had been observed and documented in the literature (Fujita and Grandoso 1968). In the numerical model, the weakening of the updraft that led to the splitting was caused by the presence of water loading in their Kessler microphysics scheme. The two updrafts were mirror images of each other when the Coriolis force was not included, and rotated in opposite senses. The cells separated from each other while demonstrating deviate motion; the right-mover displayed many of the characteristics of the severe right-mover model of Browning, including a cyclonic updraft, counterclockwise hooked-shaped downdraft, off-hodograph movement, and long lifetimes.

In an accompanying paper (Klemp and Wilhelmson 1978b), the authors were able to demonstrate that when the environmental hodograph turned clockwise with height, the development of the right member storm was favored, whereas a counterclockwise hodograph favored the left member's development; the Coriolis force was not a significant factor in producing asymmetries between the two storms. Thus the preference for cyclonic supercells in the Northern Hemisphere was shown to be due to the predominance of clockwise hodographs and not directly due to the rotation of the Earth.

Based on the Klemp and Wilhelmson simulations, Rotunno (1981) was able to explain how tilting could produce an updraft possessing vorticity predominantly of one sign. Considering for simplicity an environment with unidirectional westerly wind shear, the initial buoyant bubble bulges vortex lines upwards such that positive vorticity is found on the south side of the updraft whereas negative vorticity is found to the north. After a downdraft splits the convection, two storm result, each with positive vorticity to the south and negative vorticity to the north. But at low levels convergence occurs beneath the inflow in the updraft whereas divergence occurs in the central downdraft. Thus the positive vorticity of the southern storm is preferentially enhanced, while the northern storm's negative vorticity is enhanced.

Davies-Jones (1984) would give a more rigorous treatment of the rotation of supercells in the isentropic case. He defined a displacement parameter that represents the vertical distance the (horizontal) environmental isentropes are displaced upwards; the displacement is positive in a buoyant plume. The vertical velocity and vorticity are proportional to the dot products of the displacement gradient with the horizontal plume-relative velocity and horizontal vorticity, respectively. Thus supercells with strong correlations between vertical velocity and vertical vorticity occur in environments where the storm-relative wind and horizontal vorticity vectors are nearly parallel in the inflow. A disadvantage of using this method to forecast supercells is that the storm motion relative to the ground either must be known or estimated from the environmental conditions *a priori*.

Meanwhile Schlesinger (1980) investigated the splitting process in more detail using a version of his model with rain microphysics. He found evidence that downdrafts initiating the splitting developed on the flanks of the cloud condensate field, and trajectory analyses of parcels within these downdrafts showed that they possessed low equivalent potential vorticity, not typical of surface-based parcels. Thus, it was suggested that, in addition to condensate loading, an important component to the storm splitting process was the evaporative cooling of midlevel air[1]. But, most importantly, each nascent vorticity center of the unsplit storm was associated with a low pressure region. These low pressure regions produced a number of effects: the low pressure centers dynamically induced a downdraft between them, and kinematically the vorticity centers caused a flow field that brought low θ_e between them. Furthermore, the low pressure centers created upward pressure gradient forces beneath them. The net effect was a tendency to convert the initial storm updraft into two updrafts that propagated away from each other.

The elliptic pressure equation was then written as:

$$\nabla^2 P - \frac{g}{\gamma_0 R_d T_0}\frac{\partial P}{\partial z} = \frac{1}{R_d \rho_0 \theta_0}\left[\boldsymbol{\nabla}\cdot[-\rho_0(\mathbf{v}\cdot\boldsymbol{\nabla})\mathbf{v} + \rho_0\mathbf{F}] + g\frac{\partial}{\partial z}\rho_0\left(\frac{\theta'}{\theta_0} + aq'_v\right)\right.$$

$$\left. + g\frac{\partial}{\partial z}(-\rho_0 q_l)\right], \tag{3.1}$$

---

[1] Clark (1979) also found in his simulations that entrainment also could be a cause of storm splitting.

where $P = T_0 p'/\theta_0 p_0$, $\gamma_0 = c_p/c_v$, F is the frictional force, $a = 0.61$, q_v' is the water vapor mixing ratio, and q_l is the liquid water mixing ratio. The terms within the large brackets on the right-hand side are referred to as the dynamic, hydrostatic, and drag-induced forcings, respectively. Because it is linear in P, it is possible to invert the equation for P using each of the forcings separately and then to add the three solutions to obtain the total P. Thus one can define $P = P_{DYN} + P_H + P_{DRAG}$ and determine which term, if any, is making the dominant contribution to a given pressure feature. By following this procedure, Schlesinger found that the low pressure centers associated with the vortices were dynamic in origin (associated with the vorticity squared term (2.25)).

Rotunno and Klemp (1982) used a similar procedure to develop the theory for why the right-moving storm member possesses the stronger development in environments with clockwise-turning wind shear vectors, even at the earliest stages. They derived the following version of (3.1):

$$\nabla^2 \pi = -2\left(\frac{dU}{dz}\frac{\partial w}{\partial x} + \frac{dV}{dz}\frac{\partial w}{\partial y}\right) - \left(\frac{\partial u}{\partial x}\right)^2 - \left(\frac{\partial v}{\partial y}\right)^2 - \left(\frac{\partial w}{\partial z}\right)^2$$

$$-2\left(\frac{\partial u}{\partial z}\frac{\partial w}{\partial x} + \frac{\partial v}{\partial z}\frac{\partial w}{\partial y} + \frac{\partial u}{\partial y}\frac{\partial v}{\partial x}\right) + \frac{\partial B}{\partial z}, \qquad (3.2)$$

where it has been assumed that the model wind field can be decomposed into a base state environmental wind $(U(z), V(z), 0)$ and a perturbation wind (u, v, w) caused by the thermal bubble. Non-conservative forces have been neglected, so all the terms are dynamic terms except the last, which Rotunno and Klemp termed the buoyancy term. The dynamic terms have been decomposed into the non-linear terms that are second-order in the perturbation variables, and the linear term $-2((dU/dz)(\partial w/\partial x) + (dV/dz)(\partial w/\partial y))$ that involves the environmental shear vector. It is expected at least in the initial stages of convection that the linear term should be dominant in determining the pressure.

The nonlinear term suggests that a localized, axisymmetric region of vorticity is associated with low pressure, regardless of the sign of the vorticity. This is consistent with the results of Schlesinger (1980). The linear term suggests that the pressure is lower downshear of an updraft. Thus, if the environmental shear turns clockwise with height, the pressure will tend to decrease with height on the flank of the updraft to the right of the low-level shear vector. This normally corresponds to the right-mover in the case of storm splitting. The decrease in perturbation pressure with height adds an additional vertical acceleration that may be enough to sustain the storm along this flank. The left-mover, however, finds its growth inhibited by a downward perturbation pressure force. Rotunno and Klemp were able to invert the pressure equation in a numerical simulation and show that the linear term was indeed critical to the dynamics of their simulation.

3.3 Low-Level Vorticity

Davies-Jones (1982) noted that, whereas the origins of the mesocyclone coincident with the updraft core of supercells seemed well explained by the tilting of horizontal environmental vorticity by the updraft, this explanation was not sufficient to explain the origin of tornadic vertical vorticity near the ground because the vertical velocity gradients there are weak (prior to the existence of the tornado of course). Either vertical vorticity would have to be diffused towards the surface in an updraft, or low-level vertical vorticity would have to be transported to the surface somehow in a downdraft. Davies-Jones also showed in an idealized case that the magnitude of the vorticity vector would tend to increase exponentially in the direction of the primary axis of dilatation; in the case of a purely axisymmetric horizontally-convergent flow, the primary axis of dilatation is vertical.

The simulation of tornadic supercell case studies using a storm-resolving numerical model began with Klemp et al. (1981), who used the same model and setup as Klemp and

Wilhelmson (1978a) in order to investigate the Del City tornadic storm of 20 May 1977. A composite of two hodographs observed in the vicinity of the Del City storm was chosen to initialize the model. They succeeded in modeling the evolution of a supercell that reasonably resembled the Del City storm. Significant vorticity was generated near the 'triple point' of the storm close to the surface, at the boundary between updraft and downdraft. Klemp and Rotunno (1983) then decided to repeat the simulation with a 250 m fine grid introduced at 3600 seconds encompassing the surface vorticity maximum. The low-level vorticity (reaching values of $0.06\ \mathrm{s}^{-1}$) was found to develop separately from the mid-level mesocyclone, suggesting that its formation was due to a different process. Klemp and Rotunno proposed that the low-level vorticity was generated as air parcels approached the vortex along trajectories near and parallel to the forward flank gust front. Streamwise horizontal baroclinic vorticity thus was acquired by the air parcels, and was converted by tilting into vertical vorticity when the updraft was reached. Convergence beneath the storm's updraft would further enhance the vertical vorticity. One limitation of the simulation was that the vertical grid spacing remained at 500 m, so that a free slip lower boundary condition was required and a detailed analysis of near-surface dynamics was precluded. Another limitation was that the nested grid was one-way interactive, so the fine grid could only be integrated a limited amount of time before the fine grid conditions diverged significantly from those of the surrounding coarse grid. While the low-level vorticity was intensifying, a downdraft surged counterclockwise from the RFD around the low-level mesocyclone to its east side. This was termed the *occlusion downdraft*, and its origins were linked to dynamic forcings induced by the strong low-level rotation near the ground.

To test their hypothesized mechanism of low-level vorticity formation, Rotunno and Klemp (1985) performed an idealized horizontally-homogeneous simulation with a straight-line hodograph. By removing the effect of hydrometeor evaporation they were able to demonstrate that an evaporatively-cooled downdraft was necessary to form low-level vorticity. They also explicitly performed a backwards-trajectory analysis of a material contour enclosing the vorticity center, and showed how the change in circulation around the contour was consistent with the integrated baroclinity about the contour.

Davies-Jones and Brooks (1993) performed another investigation of the formation of low-level vorticity in a supercell simulation because, while the importance of storm-generated baroclinity to generating horizontal vorticity was acknowledged, the authors did not see how this process could result in significant vertical vorticity because of the argument of Davies-Jones (1982). They performed a material curve analysis of the supercell simulation of Brooks et al. (1993). This simulation involved a version of the Klemp-Wilhelmson model with 1 km horizontal grid spacing, 200 m vertical grid spacing, and an idealized hodograph formed by joining a low-level semicircular hodograph and an upper-level straight line hodograph. The authors confirmed that the largest values of horizontal vorticity, five times larger than the environmental values, were found in the vicinity of the storm gust front. The trajectory analyses showed that parcels acquired negative vorticity as they descended in the downdraft, but then the sign of the vorticity switched to positive at the lowest model level. This was explained by Figure 3.3. If parcels possessing streamwise environmental vorticity enter a downdraft, tilting induces negative vertical vorticity. In the absence of baroclinity, the vortex lines would simply follow the trajectories, but because of baroclinity the horizontal vorticity vectors make less of an angle towards the ground than the trajectories. Once the parcels approach the ground, a positive updraft gradient exists in the direction of the trajectory (because the vertical velocity increases from negative values towards zero). This tilts horizontal vorticity (which has been continually produced by baroclinity during descent) into positive vertical vorticity. The key difference between this scenario and that of Rotunno and Klemp (1985) is that parcels obtain positive vertical vorticity within the downdraft, rather than after they begin ascending the updraft.

Brooks et al. (1994) performed more idealized supercell simulations to examine the life cycle of the low-level mesocyclone. They found a link between the low level and midlevel mesocyclone, but only an indirect one. They argued that when the midlevel vertical wind shear was weak compared with the midlevel mesocyclone, precipitation would be wrapped around the mesocyclone and fall in the vicinity of the updraft. Low level vertical vorticity would at first rise rapidly due to tilting of baroclinically-generated horizontal vorticity. However, because of the volume of evaporated precipitation, the supercell would become outflow dominated: the gust fronts would rapidly surge ahead, cutting off the inflow to the storm and disrupting the steady-state nature of the Browning (1964) conceptual model. Thus, the low-level mesocyclone would not be persistent in this case. A persistent low-level mesocyclone required the more midlevel wind shear compared to midlevel mesocyclone strength. Under the proper conditions precipitation would be distributed farther from the storm updraft, leading to a delay in the development of low-level vorticity, but a more steady-state storm, and persistent low-level mesocyclone, would also result.

At the same time Walko (1993) performed idealized simulations of a vortex using the Regional Atmospheric Modeling System (RAMS). Instead of a supercell, a zone of heating was used to initiate dry convection. Three grids were used with horizontal grid spacings of 1600 m, 400 m, and 100 m; the vertical grid spacing was 20 m near the surface. A semi-slip lower boundary condition was utilized – the horizontal wind at the lowest model level is used to compute a surface stress, and this surface stress is in turn used in the computation of the vertical stress gradient that decelerates the wind. The environment was varied to incorporate cases with both ambient horizontal and vertical vorticity. Walko found that a strong axisymmetric vortex could form near the surface because of convergence, but only

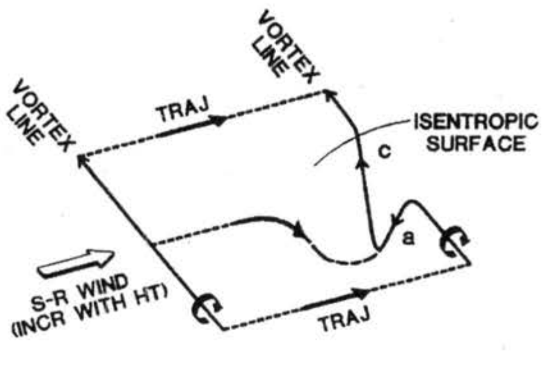

STREAMWISE BAROTROPIC VORTICITY

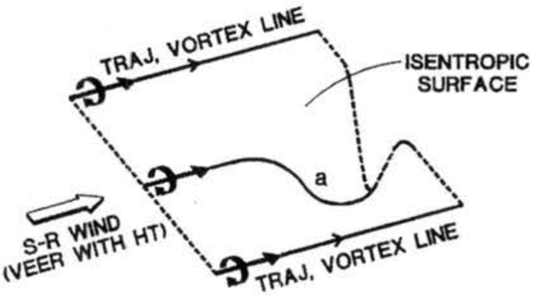

STREAMWISE VORTICITY WITH BAROCLINITY

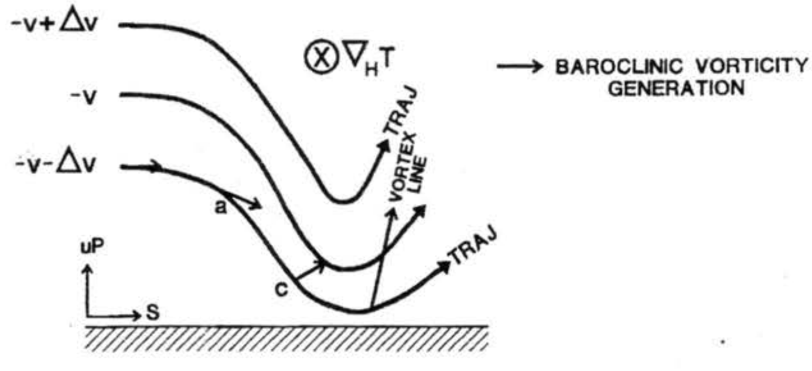

Figure 3.3: Depiction of the tilting of baroclinically-generated horizontal vorticity into positive vertical vorticity within a downdraft. From Davies-Jones and Brooks (1993).

in the cases where low-level vorticity was introduced in the initialization. Otherwise the generation of a significant vortex at the ground required the presence of downdrafts. This supported the arguments of Davies-Jones (1982) and Davies-Jones and Brooks (1993) that updraft tilting alone was not sufficient to generate significant low-level vorticity. However, baroclinity was not a positive contributor to the vorticity in these simulations; the role of the downdrafts was to tilt environmental horizontal vorticity into the vertical along the boundary between updraft and downdraft.

3.4 Tornadic Scales

Also using a descendant of the Klemp-Wilhelmson model, Wicker (1990) followed the procedure of Klemp and Rotunno (1983), and introduced a fine grid into the supercell simulation of Wilhelmson and Klemp (1981). The horizontal grid spacing was now 70 m, and the vertical grid spacing was stretched upwards from a minimum of 50 m near the ground. It was found that the near-ground vorticity could reach values of 0.35 s^{-1} if a semislip lower boundary condition was used, and a vortex persisted for a few minutes. Near-surface friction had prevented the tangential wind from achieving cyclostrophic wind balance, and the induced radial inflow concentrated and increased the strength of the vortex.

Wicker and Wilhelmson (1995) introduced a two-way interactive nesting scheme into their model, which allowed them to begin a fine grid nest tens of minutes before the low-level vorticity peaked in the corresponding one-grid simulation. This reduced the sensitivity of the vorticity evolution to the actual spawning of a nested grid. This and other refinements enable the authors to analyze in some detail the evolution of low level vorticity within a fine grid of 120 m horizontal grid spacing (the coarse grid possessed 600 m grid spacing). The minimum vertical grid spacing was 120 m, but still not fine enough to justify deviating from a free-slip boundary condition. The sounding used at initialization was a composite of three tornadic cases. The storm produced the characteristic rear flank downdraft and hook echo. The fine grid was spawned after 70 minutes of simulation; within the next 40 minutes two successive tornadic-strength vortices (ground-relative wind speed 60 m s^{-1}, pressure deficit 15 mb) developed. The tornadoes lasted approximately ten minutes each and formed as the low-level mesocyclone contracted. It was found that for at least the second vortex the contraction was associated with a dynamically-induced vertical pressure gradient force associated with an initial increase in circulation at a height of 1.5 - 3 km, which is slightly above cloud base. The near-surface circulation remained nearly constant during the contraction phase.

Wicker and Wilhelmson also performed backward trajectory analyses from the tornado. Similar to Rotunno and Klemp, they found that the baroclinic generation of vorticity along the forward-flank downdraft, and subsequent tilting into the vertical, was crucial. Unlike Davies-Jones and Brooks (1993), however, they found no evidence that vertical vorticity became positive before the parcels entered the updraft, to the limit of their model's vertical resolution.

At about the same time Grasso and Cotton (1995) used RAMS to perform a three-grid simulation using the Del City, Oklahoma sounding. The horizontal grid spacings for the grids were 1 km, 333 m, and 111 m. The vertical grid spacing was 25 m near the ground, and the lower boundary condition was semislip. At a semislip lower boundary the horizontal velocity is not constrained to zero, but is subject to retarding force due to parameterized turbulent momentum transfer. The model also possessed bulk mixed-phase microphysics. The resultant supercell developed similarly to previous modeling studies, and eventually a vortex was formed with $51\mathrm{m}\ \mathrm{s}^{-1}$ storm relative winds at the surface and a pressure deficit of 12.6 mb. The maximum pressure deficit occurred at a height of 365 m. Near the surface, the wind field was mostly convergent towards the vortex due to the presence of surface friction. The low pressure deficit seems to first become apparent near cloud base along the updraft/downdraft boundary in response to an increase in the total vorticity there. The decreased pressure aloft will cause an increased convergence beneath; this subsequently amplifies the low-level vorticity and decreases pressure at this new level. In this manner the pressure deficit region descends towards the surface.

For this process to occur there initially must be a source of low-level vorticity. Parcels possessing low-level vorticity were found to descend cyclonically in the precipitation downdraft, suggesting that the vorticity was generated baroclinically within the downdraft, but more detailed trajectory analyses were not performed.

Although there are some differences in the descriptions, tornadic vortices of similar strengths at similar resolutions are formed in the Wicker and Wilhelmson and Grasso and Cotton simulations. In both cases a source of low-level vorticity is required, presumably downdraft- produced baroclinity, but the precise location of vorticity generation either could not be determined or occurred too close to the surface to be adequately resolved. Once low-level vorticity was spawned, the actual generation of the tornadic vortex was initiated by dynamically-induced convergence beneath a mesocyclonic feature located near cloud base; thus it was required that this mesocyclonic feature and the near-surface baroclinically-generated vorticity be in close proximity to each other.

3.5 Horizontally-Heterogeneous Simulations

Grasso (1996) next applied RAMS to the simulation of a couple of tornadic case studies using the model's horizontally-heterogeneous mode. The coarse grid encompassed most of the continental United States, and was initialized with synoptic data at 75 km resolution. Four nested grids, including grids that were allowed to follow the movement of convection, permitted the simulation of supercell thunderstorms at 1 km grid spacing, and six nested grids permitted the simulation of tornadic vortices at 111 m grid spacing. In this manner it was hoped to examine the formation of the tornadic cases of 1991 May 15 in Luverne, Oklahoma and 1991 Apr 26 in Redrock, Oklahoma. No warm bubble was required to initiate the storms, as the synoptic forcings and surface characteristic gradients (soil moisture, land use type, etc.) accomplished this. In the Redrock case, the successive nestings did produce a tornadic vortex with wind speeds at the surface exceeding 100 m s^{-1}, which was comparable to what was observed in the actual tornado (Bluestein 1993). There were differences in evolution between the observed and modeled parent storms, however; the modeled storm stayed in the vicinity of the dryline whereas the observed storm became tornadic well away from the dryline.

For both vortices, the maximum vorticity values developed first at the surface, and then built upwards. A circulation analysis was attempted for the tornadoes but complicated by the movement of the modeled grids. It was found that the main source of low-level vertical vorticity was the tilting of horizontal vorticity in the downdrafts within a few hundred meters of the surface.

Finley (1997) also performed two horizontally-heterogeneous simulations using six nested grids with the same grid spacings as those of Grasso (1996). The cases simulated were the May case of the Grasso study and the 30 Jun 1993 HP supercell case of Kansas that was associated with weak tornadoes. The first case produced a tornado on the finest grid that developed secondary vortex circulations within the parent vortex, similar to a larger version of the secondary vortices often observed with observed tornadoes (Fujita 1970; Forbes 1978). The 30 Jun 1993 simulation produced two weak tornadoes that developed from near the surface upwards; the first was located along the gust front but away from the midlevel mesocyclone. A circulation analysis was performed on the 333 m fifth grid for a material curve that was advected backwards in time until it encountered the grid boundary at 18 minutes. During this period of time the baroclinic contribution to the circulation around the curve was negligible, and, if anything, slightly negative. Evidently the tornado formed by the convergence of circulation already present in the environment at the earliest time attainable in the circulation analysis. The second model tornado in the June case formed near the mesocyclone in a bow-echo-like structure, and was also subjected to a circulation analysis for 18 minutes. It was revealed that, because of surface stresses, the circulation around the material curve actually decreased as it converged towards the tornado. Again, this demonstrated that the low-level circulation already existed at the beginning time of the analysis. Trajectory analyses of individual parcels showed that both tilting and convergence were important to increasing the vertical vorticity of parcels reaching the tornado. The vorticity increases occurred for parcels entering the tornado from both the updraft and downdraft sectors; as in Wicker and Wilhelmson (1995), the source of vertical vorticity immediately above the surface remained unexplained.

3.6 Recent Observations

The Verification of the Origins of Rotation in Tornadoes EXperiment (VORTEX) was a field project that took place in the southern Great Plains over the 1994 and 1995 severe storm seasons (Rasmussen et al. 1994). For the project observational platforms were poised to converge on potentially tornadic supercells to follow their evolution in unprecedented detail. These included a mobile mesonet (Straka et al. 1996), the airborne ELectra DOppler RAdar (ELDORA) (Wakimoto et al. 1998), and mobile 3-cm (Wurman et al. 1996) and 3-mm (Bluestein et al. 1995) Doppler radar. The goals of the experiment were cast in terms of scientifically verifiable hypotheses concerning tornadogenesis and related processes; therefore, the documentation of otherwise promising supercells that failed to produce tornadoes was also important. Though the 1994 season was notable in its lack of tornadic storms over the field project region, a number of tornadic supercells were captured by the VORTEX platforms in 1995.

Rasmussen and Straka (1996) were able to use the mobile mesonet to achieve kilometer-scale resolution of the surface conditions during the formation of the powerful Dimmitt tornado of 2 June 1995. Immediately prior to the formation of the tornado, they noted the presence of an intense low-level mesocyclone that had already been 'occluded' by an extension of the RFD. Most of the downdraft had near-surface θ_e values, suggesting that it was evaporatively-cooled low-level air, except for a core of low-θ_e air with origins near 700 mb. An inflow low (caused by the interaction of the updraft and environmental wind shear) was present in advance of the storm; the low-level mesocyclone was nearly encircled by a ring of high pressure. During the tornado, the RFD surged eastward, and high temperatures were found in the RFD to the south-southeast of the tornado, suggesting that air parcels been dynamically forced to descend dry-adiabatically. The dissipation stage was associated with the arrival of the low-θ_e air at the tornado vortex. In a proposed synthesis, the authors suggest that the occlusion of the tornado cyclone by downdraft preceded tornadogenesis, but it was suggested that the origins of the occluding downdraft was dynamically-driven by the already extent low-level mesocyclone, similar to the Klemp and Rotunno (1983) hypothesis. Because of the occlusion, inflow air could not reach the region of tornadogenesis, so the vorticity had to be generated elsewhere. It was first proposed that the occluding downdrafts carried the vorticity needed for tornadogenesis. During the entire lifetime of the storm there were almost no gradients of temperature at the surface (except for those in the dynamically-driven occlusion downdraft), in contrast to the scenario of Rotunno and Klemp (1985). However, temperatures were 10°C warmer at Lubbock to the south. It was later found that a surface thermal boundary was present 15-25 km south of the storm, and that the storm had in fact crossed the boundary about thirty minutes prior to the first analysis time (Rasmussen et al. 2000). So, it was then suggested that the baroclinity of the boundary could have generated horizontal vorticity that could after tilting serve as the source of vorticity needed for tornadogenesis.

Wakimoto et al. (1998) used ELDORA to capture in dual-Doppler analysis the hour-long evolution of a low-level mesocyclone into a tornado near Garden City, KS on 16 May 1995. They clearly showed that the low-level mesocyclone and midlevel mesocyclone developed separately 8-10 km apart, but then merged into the main updraft. A dynamically-forced occlusion downdraft began to form within and just to the east of the mesocyclone twenty minutes later. After another twenty minutes, the occlusion downdraft had reached 30 m s^{-1}, and tornadogenesis occurred. Wakimoto and Liu (1998) observed the tornado form in a ring of vorticity surrounding the occlusion downdraft, and propose that the tornadogenesis process was analogous to 'vortex breakdown' occurring in the low-level mesocyclone (Rotunno 1984), caused by sufficient 'swirl' in the outer flow.[2]

Also notable were the null cases: significant supercell thunderstorms that showed evidence of strong low-level mesocyclones, but failed to produce tornadoes. Three such cases were documented by Trapp (1999); they all possessed strong mesocyclones within a few hundred meters of the ground that persisted at least fifteen minutes, but none produced a tornado. He speculated that some reasons for tornadogenesis failure include the development of an outflow-dominated storm, too great a stability in the boundary layer, and the absence of a lifting force such as a favorable dynamic pressure gradient or sufficient buoyancy.

Blanchard and Straka (1998) had used ELDORA, DOW (Doppler On Wheels), and mobile mesonet data to examine a supercell that formed in Beaver County, OK on 8 June

---

[2] It has since been noted that true vortex breakdown is not necessary to explain the descent of a dynamically-induced downdraft within the mesocyclone (Trapp 2000).

1995. This was the first storm that formed (1845 UTC) on a day that would later see powerful tornadoes develop in the Texas Panhandle. This particular storm produced large hail? and an intense low-level mesocyclone, but only a brief funnel cloud developed during its lifetime. Blanchard and Straka postulated that the low level buoyancy in the environment may have been too weak to generate the vertical accelerations needed for tornadogenesis.

Wakimoto and Cai (2000) examined a powerful supercell that developed on 12 May 1995 near Hays, KS that never underwent tornadogenesis despite the presence of a low-level mesocyclone with vorticity values exceeding $0.04\mathrm{s}^{-1}$. There was even an occlusion downdraft, and a comparison between this storm and the Garden City storm revealed few differences (Cai and Wakimoto 1998). Greater precipitation amounts in the Hays storm may have led to the deeper cold pool reported for that storm (2.3 km vs. 1.4 km for the Garden City storm), but a strong inflow kept the storm steady state, instead of outflow-dominated (Brooks et al. 1994). The Hays low-level mesocyclone was slightly larger and possessed a tangential wind speed that decayed less rapidly with radius than the Garden City mesocyclone, which more closely followed the $1/r$ profile of a potential flow far field. They also noted that both storms exhibited a pressure minimum near 2 km, but only in the tornadic Garden City storm did the pressure minimum descend to the surface. However, it was not clear how either of these differences were related to the presence or absence of tornadogenesis.

These results suggested that the kinematical differences between the tornadic low-level mesocyclone and the non-tornadic one might be extremely subtle, possibly not resolvable by either existing observational platforms or cloud-scale numerical models. Thus efforts were intensified to try to find some observable environmental parameters that could distinguish between tornadic and non-tornadic storms and make the forecasting problem tractable.

forward-flank downdraft itself. Both baroclinity and pre-existing vertical vorticity along the boundary were important to the subsequent generation of strong vertical vorticity in these simulations. Interestingly, though, it was found that neither varying the boundary temperature gradient nor the cross-boundary horizontal wind shear had much of an effect on the vorticity evolution as long as they exceeded certain minimum thresholds.

Adlerman et al. (1999) performed a simulation with 500 m horizontal grid spacing and as small as 100 m vertical grid spacing near the ground. The model used was the Advanced Regional Prediction System (ARPS), with warm Kessler-scheme microphysics. Free slip boundary conditions were applied at the surface. The initialization was from the Del City sounding used by the Klemp and Rotunno and Grasso and Cotton studies. They found that their low-level mesocyclone dynamically initiated an occlusion downdraft; once this downdraft reached the surface, it enhanced convergence and led to a rapid intensification of the mesocyclone. The modeled storm was seen to produce a peak in low-level vorticity after 6600 seconds, which subsequently decayed, but re-intensified by 11400 seconds. The more rapid intensification of the second vorticity maximum was explained by noting that initially the cold pool θ contours were oriented so that little of the horizontal vorticity generation was streamwise, until cyclonic trajectories and low-level acceleration developed; after the first occlusion, however, the θ contours remained in a position well suited to the creation of streamwise vorticity.

3.8 Models of Tornadogenesis – DPE and NST

Trapp and Davies-Jones (1997) used an idealized axisymmetric model to investigate how a vortex would form in the presence of ambient convergence and vorticity fields. They found that when convergence of vorticity was strongest aloft, a vortex descended to the surface via the 'dynamic pipe effect' (DPE) mechanism (Leslie, 1971). In this process, radial convergence into the vortex continues to increase the vorticity until the winds are in cyclostrophic balance with the pressure deficit associated with the vortex. At this point radial convergence stops, and air is drawn up into the pressure deficit from below. This causes horizontal convergence of vorticity to begin below the vortex, and the process continues at progressively lower levels. The significance of the Trapp and Davies-Jones study is that they found that when the vorticity convergence is greater near the ground, or nearly constant throughout the depth of the column, the vortex spins up nearly simultaneously across its depth, without the slow descent associated with the dynamic pipe effect.

Trapp et al. (1999) have since classified observed tornadic events into those with a descending tornado vortex signature (TVS), and those without descending TVSs. Trapp and Mitchell found that about half of the tornadoes studied were not accompanied by descending TVSs. If these are associated with the two modes of tornadogenesis described in Trapp and Davies- Jones, then the implication is that a large fraction of tornadoes form rapidly and little or no radar warning may be possible.

Lee and Wilhelmson (1997a) had investigated non-supercell tornadogenesis (henceforth referred to as NST) using a dry semislip numerical model. They simulated a north-south cold pool boundary with 100 m grid spacing in both the horizontal and the vertical directions. Winds were southerly on the warm side of the boundary, with speeds increasing with height; the cool side was motionless initially. A transition zone in θ and winds existed between the two. As time progressed, the cool air propagated towards the warm air as a density current. A vortex sheet with $\zeta_{max} = 0.025$ s^{-1} developed. Random thermal perturbations were introduced into the transition zone. 'Lobe-and-cleft' instabilities were seen to form underneath the head of the density current due to unstable stratification; these served as triggers for barotropic horizontal shearing instability to begin. Vortices were apparent by 1000 s approximately every 2-3 km, although some would later merge. By around 2000 s, the vortices were highly occluded, and began to dissipate. The differential velocity across the vortices reached 25 m s^{-1}, and circulation reached 55000 m^2 s^{-1}. Near the ground stretching also was significant towards intensifying the vortices, and even nearer the ground surface friction caused significant horizontal vorticity that was tilted into the vertical by the convergence into the vortex. Without surface friction, the vortices were more elongated and occluded.

3.9 Tornado Climatologies

Rasmussen and Blanchard (1998) used over six thousand 0000 UTC soundings from 1992 to determine which sounding forecast parameters such as mean shear, storm relative helicity, CAPE, etc., could best distinguish between three categories: ordinary thunderstorms, non-tornadic supercells, and tornadic supercells.[3] As expected, parameters such as storm-relative helicity served well to distinguish supercell soundings from ordinary thunderstorm soundings, but were less effective at distinguishing tornadic from non-tornadic supercell soundings. The most effective parameters at distinguishing between tornadic and non-tornadic supercells were various combinations of CAPE and vertical shear (especially the energy-helicity index (EHI)), and measures of low-level buoyancy such as the lifting condensational level (LCL) and convective inhibition (CIN). Tornadoes were associated with large values of both CAPE and SRH; furthermore, the mean LCL height was considerably less for tornadic supercells (800 m) than for non-tornadic supercells (1200 m). Tornadic supercells had average CIN values of 12, compared with 35 for non-tornadic supercells. However, CAPE immediately above the LFC was not a good discriminant between the two. The implication is that the thermodynamics below cloud base (e.g, the potential negative

---

[3] Actually, the criteria for distinguishing the categrories were the presences of significant cloud-to-ground lightning but no severe weather, large hail but no significant tornadoes, and significant tornadoes.

buoyancy of the downdrafts) are more important to tornadogenesis than the thermodynamics above cloud base, where dynamic forcing might be more important.

Markowski et al. (2000) performed a climatology of 30 storms possessing hook echoes from 1994-1999. Eighteen of these were associated with tornadoes; of the other twelve, eleven had mesocyclones at the surface. The mobile mesonet was used to sample the thermodynamic field of the RFDs accompanying these hook echoes. It was found that non-tornadic RFDs generally had large deficits in both θ_v and θ_e when compared to the low-level environmental air (about 8 K and 12 K, respectively). Tornadic cases had average θ_v and θ_e deficits of 3 K and 7 K, and tended to have positive CAPE values for the lifting of the RFD air. Otherwise, little difference was noticeable between tornadic and non-tornadic low-level mesocyclones. As in Rasmussen and Straka (1996), it was found that occlusion occurred prior to tornadogenesis. Tornadogenesis failure in cold-RFD cases seemed less associated with the surging of the occluding downdrafts ahead of the storm, and more associated with the resistance of the downdraft air to being lifted by the storm.

3.10 Current Research Goals

As can be seen much has been learned and accomplished already in terms of understanding the formation of tornadoes. But there are still some difficult questions. As might be expected, the final transition from low-level mesocyclone is still poorly understood. This stage occurs on a scale to small to have been resolved by essentially any numerical storm simulation, and by any observational study until very recently. It is not clear if the fairly-well answered question of the origin of the low-level mesocyclone is also the answer to the question of the origin of the tornado. The close similarity of the low-level mesocyclones between certain tornadic and non-tornadic supercells, however, would lead one to conclude that something more is involved. The Markowski et al. and Rasmussen and Blanchard studies would suggest a thermodynamic influence. The Trapp and Davies-Jones study emphasizes the role of dynamical vertical pressure gradients, which are also implicated in the Wicker and Wilhelmson and Grasso and Cotton modeling studies. However, the Grasso and Finley studies produced powerful vortices with little apparent forcing from above.

The goal of this study is to increase understanding of how a powerful vortex might be generated using the RAMS model, or at least how a powerful model vortex might be generated. It is hoped that the factors that favor the development of a strong vortex are identified. In order to accomplish this, the modeling studies of Grasso (1996) and Finley (1997) will be simplified considerably, so that only a supercell in idealized environments will be discussed. Of course, the problem cannot be simplified to the extent that a powerful vortex does not develop. We also do not have the resources to perform simulations with grid spacings adequate to resolve a typical tornado, although we have come close (55 m horizontal grid spacing, 40 m vertical grid spacing). Therefore, like all previous studies we will have to use arguments of plausibility to relate modeled vortices to atmospheric tornadoes. Fortunately, in our simulations we have found a qualitative difference between a low-level mesocyclone and a distinctly more axisymmetric, concentrated vortex.

A second question is inherently contained in this procedure: can the intensity of the Grasso and Finley vortices be reproduced by an idealized model, or are the specific mesoscale features in their horizontally-variable simulations required to explain the strength, or even the existence, of the vortices? Finally, there is the question of whether any of the means that a numerical model may develop a 'tornado-like vortex' (there may be several) are related to real tornadoes, or if they are artifacts of the numerical algorithm (such as grid nesting). We will address these issues in later chapters.

Chapter 4

BASELINE SIMULATION

In this section one particular simulation that produced a fairly-strong low-level vorticity center will be analyzed in some detail. This simulation generated a right-moving supercell thunderstorm that resembled those in the literature, and under the influence of baroclinity exhibited a persistent low-level mesocyclone along the gust front. However, the low-level mesocyclone exhibited a stage in which the vorticity rapidly increased in magnitude and became concentrated into a closed circulation with a sharply decreased central pressure and vertical continuity. The analysis of this process will also serve as a basis of comparison for other experiments to be presented.

4.1 RAMS Model

RAMS is a non-hydrostatic, compressible model of the primitive equations which combined the modeling efforts of a non-hydrostatic cloud model (Tripoli and Cotton 1982) and a hydrostatic mesoscale model (Mahrer and Pielke 1982). The model contains predictive equations for u, v, w, the Exner function π, ice-liquid potential temperature θ_{il}, and various species of water substance (see for example Pielke et al. 1992). The ice-liquid potential temperature is a potential temperature that includes the presence of hydrometeors and is conserved in the absence of radiation, diffusion, or hydrometeor sedimentation (Tripoli and Cotton 1981). The horizontal coordinates are either Cartesian or polar-stereographic, and in the vertical a terrain-following σ_z coordinate is utilized (Gal-Chen and Sommerville 1975). An Arakawa-C grid (Arakawa and Lamb 1981) defines the variables; the u, v, and w wind components are staggered one-half positive grid length from the scalar variables. Two-way interactive nested grids (Clark and Farley 1984) may be spawned within any other grid.

These simulations use a subgrid parameterization based on that of Smagorinsky (1963), using modifications to the vertical diffusion introduced by Lilly (1962) and Hill (1974). In the Smagorinsky scheme the diffusive flux of a quantity is proportional to its gradient, so that the diffusive forcing involves a second derivative. The characteristic of the Smagorinsky scheme is that the constant of proportionality, the eddy diffusion coefficient, is proportional to the magnitude of the velocity deformation. There is also a factor that is a function of the grid spacing.

In the horizontal direction a certain minimum value of the eddy diffusion coefficient regardless of deformation is specified by the user, in order to minimize numerical noise. For this simulation, the horizontal diffusion coefficient was simply made a constant in order to simplify the analysis. There was no significant difference found when compared with simulations performed using the standard RAMS diffusion.

The microphysics scheme used is that of Walko (1995). The scheme uses seven categories of condensed water species: cloud water, rain, pristine ice, snow, aggregates, graupel and hail. These species are assumed to follow size distributions which obey gamma function with a user-specified width parameter ν. For $\nu = 1$, the distribution is exponential with size, whereas higher values of ν create increasingly narrower modes in the size distribution. Mixing ratios for all species except cloud water are predicted by microphysical equations. The mixing ratio of total water is also predicted. The mixing ratio of cloud water is diagnosed by assuming that condensation occurs until 100% water saturation is reached. The number concentration for pristine ice is predicted by nucleation equations (Meyers et al. 1992). The number concentrations for other species are determined in this study either by specification (cloud water) or by diagnosis from the mixing ratio and the specification of the mean hydrometeor diameter (rain, snow, aggregates, graupel, hail).

These simulations are highly idealized. The effects of radiation and surface fluxes were switched off. The experiment to be presented is also free slip. As discussed in the background section, previous simulations of low-level mesocyclones in the literature have been predominantly free slip. It has been found difficult to use model surface drag to produce a noticeable effect on a supercell's cold pool and not adversely affect the model environmental winds (Wicker and Wilhelmson 1995). Furthermore, it has been argued that in the presence of a strong pressure gradient the logarithmic surface wind profile used to compute the stress in a semislip model is only applicable very near the surface (Lewellen 1993). Nonetheless it is freely acknowledged that the absence of surface effects is a shortcoming of the simulation.

4.2 Initial Convection

The simulation described here was horizontally-homogeneous within a domain consisting of 150×150 grid points at 333 m horizontal grid spacing. In order to eliminate the spawning of fine grids as a possible trigger for the concentration of vorticity, only one grid was used in the initial simulation. However, at a later point in the analysis a simulation containing a $111m$ fine grid was performed. There were 35 vertical grid levels whose spacing increased away from the ground, increasing from 40 m to a maximum of 2 km. Because the lowest level model quantities (except for w) are defined below the 'surface', for most variables the

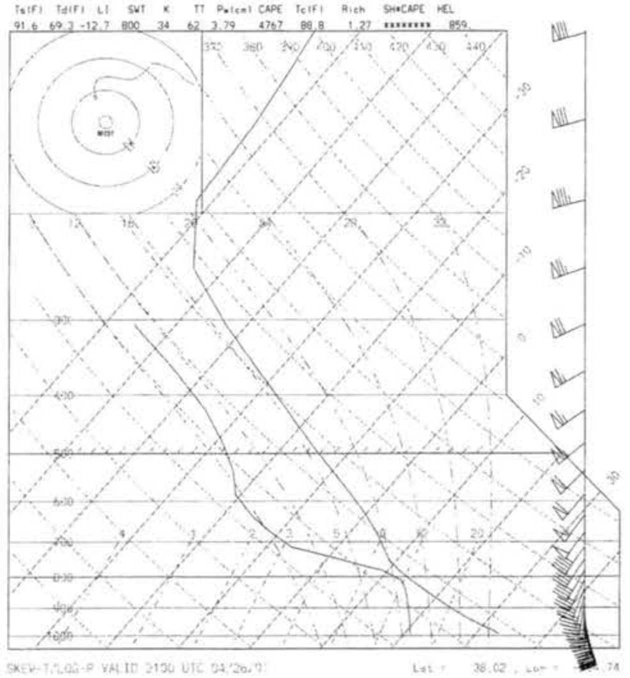

Figure 4.1: Skew-T log-p diagram showing vertical sounding used in model initialization, based on Grasso (2000).

lowest level is at a height of 19 m. A timestep of 2 seconds was used for the coarse grid and 0.5 seconds for the subsequent fine grid.

The vertical atmospheric structure was derived from a sounding used by Grasso (2000) in his idealized supercell simulations (Figure 4.1). The sounding is highly unstable and possesses great amounts (over 4000 J) of Convective Available Potential Energy (CAPE). There is a moist layer near 800 mb; above this the atmosphere rapidly becomes much drier. The hodograph neither possesses pure speed shear or directional shear, but some characteristics of both; above approximately three kilometers the shear increases in magnitude and becomes largely westerly. The surface pressure is given as 990 mb.

Convection was initialized through the introduction of a warm bubble in with a temperature perturbation of 2 K and additionally a 20% increase in water vapor content. The extent of the bubble was 10 km × 10 km in the horizontal and 1500 m in the vertical. In order to keep the convective activity from translating out of the domain, a constant storm velocity of $u = 6$ m s^{-1}, $v = 13$ m s^{-1} was subtracted from the hodograph at the time of initialization.

Full bulk microphysics was used, but because the simulation was idealized and on short time scales, neither radiation schemes nor surface fluxes were incorporated in the simulation. Furthermore, for simplicity and to facilitate comparisons with previous idealized modeling studies, surface drag was not used in these simulations.

The convection that formed split into two member storms, a right-mover and a left-mover. Consistent with previous simulations in the literature (e.g., Klemp and Wilhelmson 1978a), the right-moving member displayed a strong correlation between positive vertical vorticity and vertical velocity, whereas in the left-moving storm they are anti-correlated (Figure 4.2). The correlation between vertical vorticity and vertical velocity has now been proposed as the best defining characteristic of the supercell (Doswell and Burgess 1993).

Attention was focused on the right-moving storm for the remainder of the simulation, and the left-moving storm gradually propagated out of the model domain.

4.3 Low-Level Vorticity Intensification

By 2700 s the low-level vorticity has reached mesocyclonic strength along the gust front (Figure 4.3), usually defined to be 0.01 s^{-1} (Brandes 1984). Figure 4.4 shows that this region possesses a strong gradient in θ and noticeable deformation in the wind field. The low θ_e values indicate that the air behind the gust front has origins near 3 km. Horizontally, the midlevel air is centered about two regions associated with the two member storm downdrafts. To the north of the right-mover storm the zone of deformation continues along the boundary of the low-level and midlevel θ_e air. However, to the east of this zone there is a

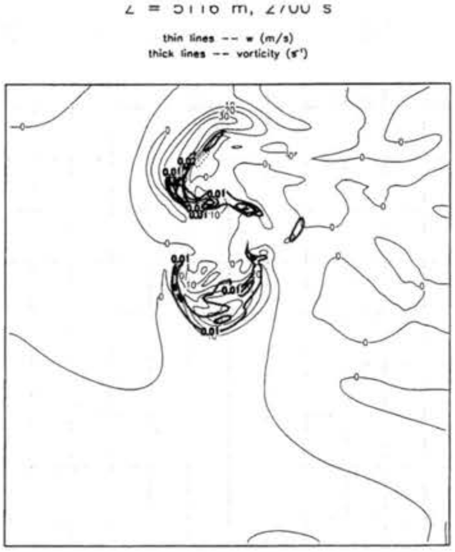

Figure 4.2: Vertical velocity (thin contours) and vertical vorticity (thick contours) at 2700 s and 5116 m above surface within Grid 1. Domain is 50 km × 50 km. Contour increments are 10 m s^{-1} for vertical velocity and 0.01 s^{-1} for vertical vorticity.

region of near-surface θ_e values but with depressed θ, suggesting that the air here originates near the surface, but is evaporatively-cooled by precipitation.

The horizontal vorticity field (Figure 4.5) indicates that in the region of maximum low-level vertical vorticity the horizontal vorticity is mainly directed towards the northwest due to the wind shear in the environment. The horizontal vorticity that is induced baroclinically by the cold pool is easy to identify because it is significantly larger in magnitude and rotates clockwise around the cold pool. The location of vertical velocity also suggests where convergence along the gust front is most intense (figures showing gust front convergence will be shown later).

Model code was written to output the location of the maximum vertical vorticity at each timestep after 2700 s for four different heights, as well as the value of that vorticity maximum. The four levels used were $k = 2$, 6, 10, and 14, with model heights of 19 m, 234

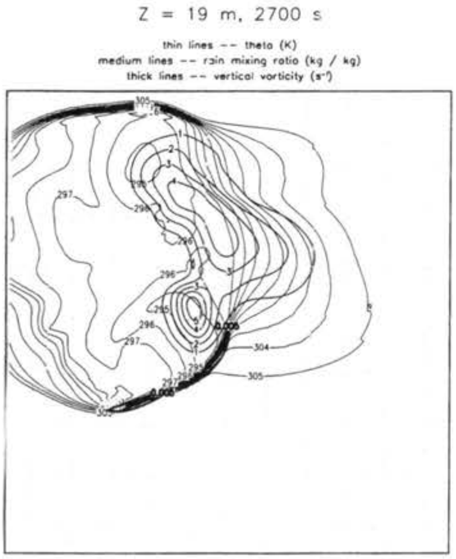

Figure 4.3: Potential temperature (thin contours), rain mixing ratio (medium contours) and vertical vorticity (thick contours) at 2700 s and 19 m above surface within Grid 1. Contour increments are 1 K for potential temperature, 1 g kg^{-1} for rain mixing ratio, and 5×10^{-3} s^{-1} for vertical vorticity.

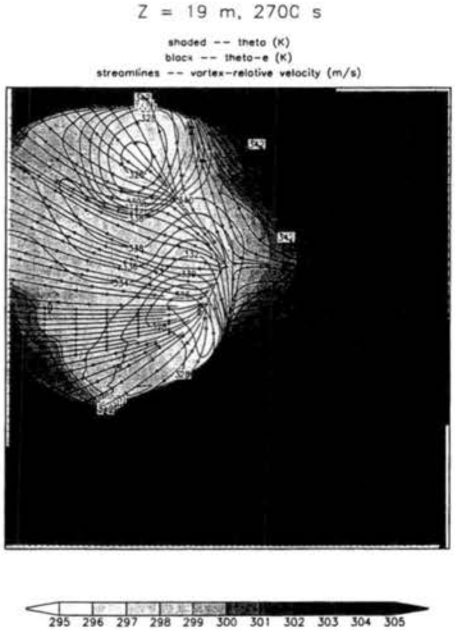

Figure 4.4: Equivalent potential temperature (shaded), potential temperature (contoured in 1 K increments), and vortex-relative streamlines at 2700 s and 19 m above the surface. The meaning of vortex-relative is given in the text.

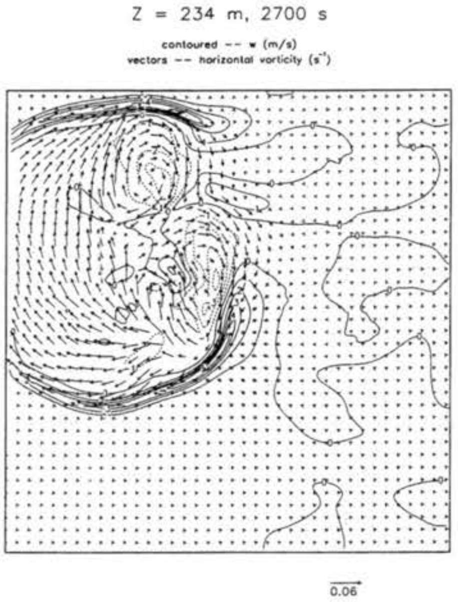

Figure 4.5: Vertical velocity (contoured in 1 m s^{-1} increments) and horizontal vorticity vectors at 2700 s and 234 m above the surface. The unit of the reference horizontal vorticity is s^{-1}.

m, 608 m, and 1263 m, respectively. As an example, a plot of the j coordinate of the 234 m vorticity maximum is shown in Figure 4.6. During some periods the vorticity maximum simply translates with a relatively constant velocity, suggesting that it is a single entity. At other times, the location experiences a discrete 'jump' to a new location, indicating that a new location of vorticity has amplified and exceeded the vorticity value of the old location. Such a jump occurs at 3202 s.

Figure 4.7 is a plan view where the vorticity maximum location is plotted for each 30 s increment at the four heights, beginning with 2700 s. All the maxima generally move eastward with time; this can be used to determine the temporal sequence of the marked locations. Initially the maxima at the different heights are scattered across the grid, and the largest 1263 m value is even located in the downdraft of the left-mover for a while. However, eventually the maximum vorticity at all heights jumps to a single location that

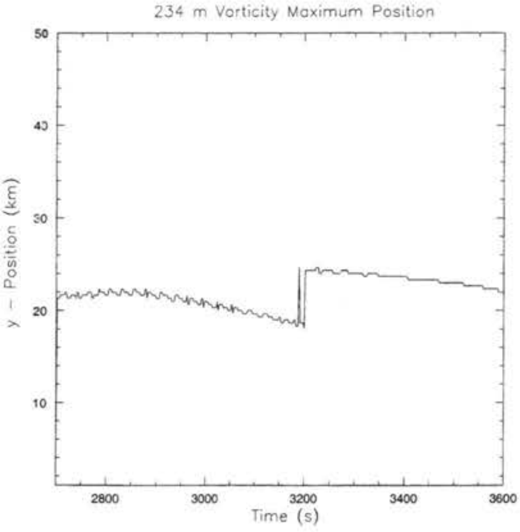

Figure 4.6: North-south location of 234 m vorticity maximum in single grid simulation versus time.

height	time of jump
1263 m	3062 s
608 m	3154 s
234 m	3202 s
19 m	3222 s

Table 4.1: Simulation time when maximum domain vorticity becomes located at the vertically co-located vorticity center shown in the later stages of Figure 4.7, for 19 m, 234 m, 608 m, and 1263 m above the surface.

translates steadily to the southeast relative to the grid. This location is near the northern tip of the inflow sector, which is typically the region that supercell tornadoes develop (Lemon and Doswell 1979). The time that this final jump occurs for each level is shown in Table 4.1; it is seen that the jump first occurs at the highest levels, and by 3225 s has reached the surface.

The value of the maximum vorticity experiences drastic changes during this period, as is apparent from Figure 4.3. The vorticity, already well above the standard mesocyclonic threshold, increases fivefold in 300 s. The vorticity 'surge' occurs at all levels but is strongest near the surface, reaching values of $0.14 \ \mathrm{s}^{-1}$.

4.4 Vorticity Jump

What is the reason for the jumps in vorticity? Figure 4.9 shows the $t = 3100$ s vertical vorticity at 608 m, near the time of the vorticity jump at this level. At this time there are two discrete vorticity centers of approximately equal magnitude, the northernmost of which will eventually dominate. From the plot of convergence (Figure 4.10) it can be seen that the convergence (and hence the stretching tendency on vertical vorticity) is no greater at the northernmost center than at the southern, so some other mechanism must account for this center's later predominance. A clue is provided by Figure 4.11, which shows the vertical motion field and the horizontal vorticity vectors. The southern vorticity center is

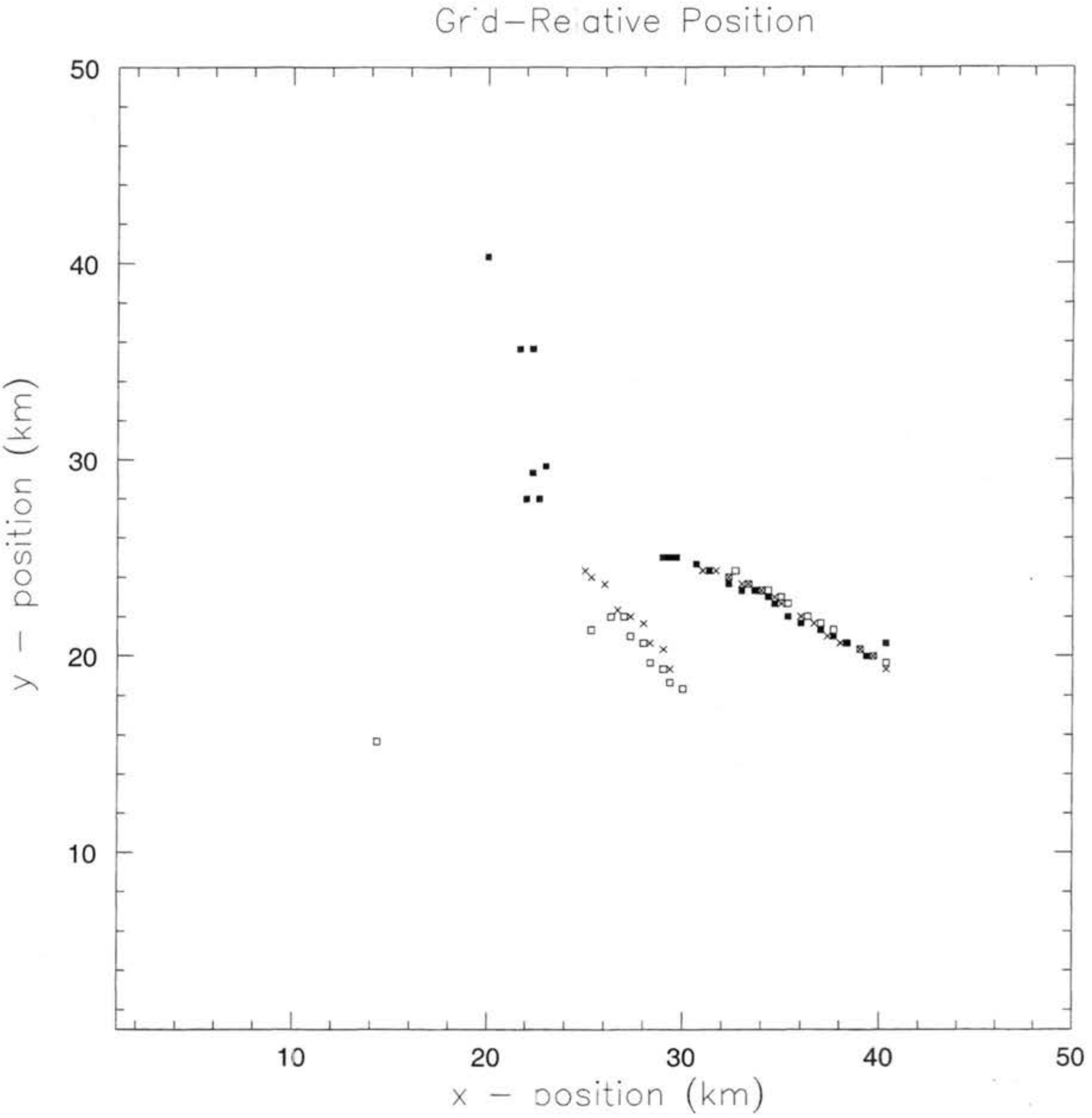

Figure 4.7: Grid position of maximum domain vertical vorticity, in 50 s increments after 2700 s. open squares – 19 m; crosses – 234 m; closed squares – 1263 m. Motion is to the east with time.

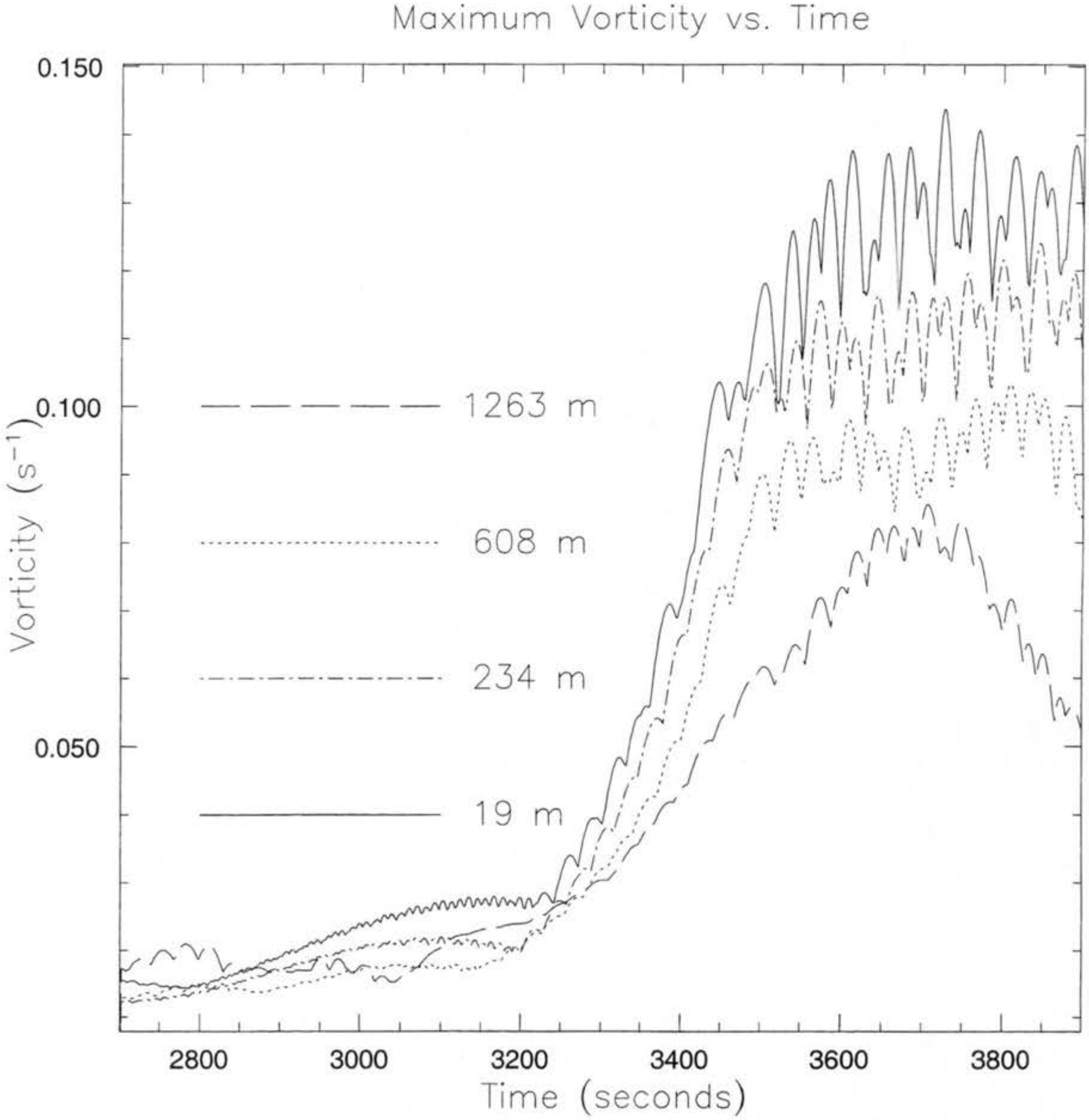

Figure 4.8: Maximum vorticity within model domain versus simulation time for 19 m, 234 m, 608 m, and 1263 m above the surface.

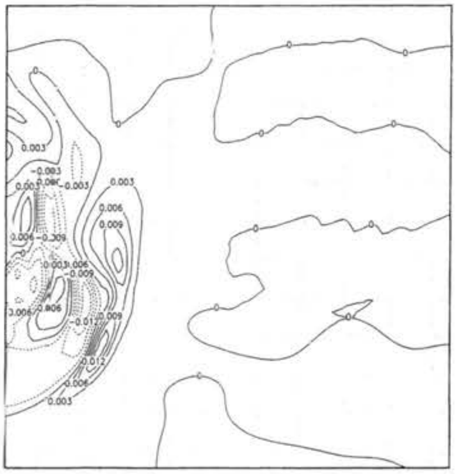

Figure 4.9: Vertical vorticity at 3100 s and 608 m above surface. Contour increment is $3 \times 10^{-3}\ \mathrm{s}^{-1}$.

located in the most favorable position for positive tilting of the environmental vorticity vectors directed towards the northwest, assuming that the center obtains its vorticity from easterly inflow. However, much larger is the magnitude of the vorticity vectors associated with baroclinic generation along the gust front. These vectors are positioned for positive generation of vorticity to the northeast of the northern center, and negative generation to the southwest. However, the vortex-relative inflow[1] is from the northeast, so presumably tilting is a positive source of vorticity for this location. A plot of the vortex- relative streamlines and tilting term (Figure 4.12) confirms that there is positive tilting in the inflow of the northern vortex but not in the southern, assuming that streamlines can serve as a surrogate for trajectories. By 3300 s, the northern vorticity center has clearly become dominant (Figure 4.13).

Thus, we have a scenario where the appearance of significant baroclinically- produced

---

[1] The vortex-relative velocity is found by subtracting the grid-relative northern vortex velocity from the grid-relative velocity at a point. The vortex velocity is assumed to be $u = 13\ \mathrm{m\,s}^{-1}, v = -8\ \mathrm{m\,s}^{-1}$

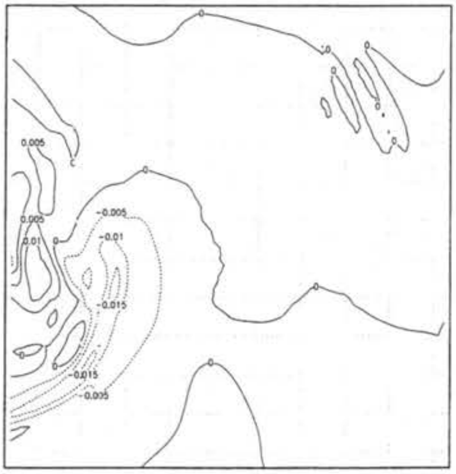

Figure 4.10: Same as Figure 4.9, but for two-dimensional velocity divergence. Contour increment is 5×10^{-3} s^{-1}.

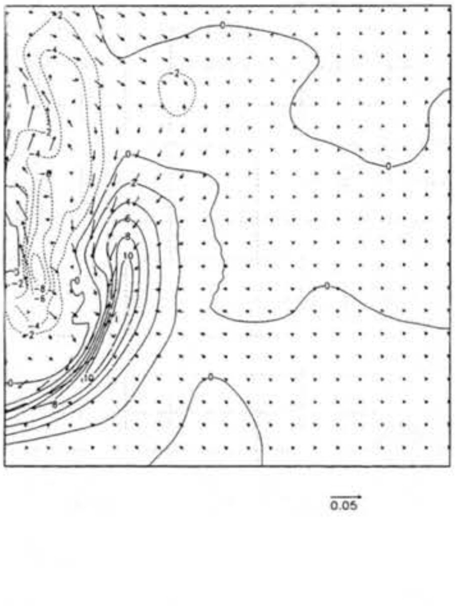

Figure 4.11: Same as Figure 4.9, but with vertical velocity contoured and horizontal vorticity vectors (s^{-1}) superimposed. Contour increment is 2 m s^{-1} for vertical velocity.

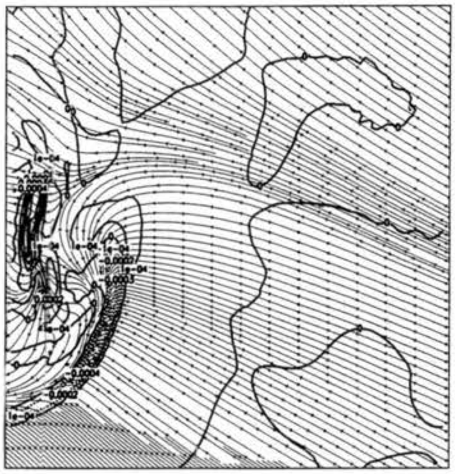

Figure 4.12: Same as Figure 4.9, but with the tilting contribution to the vertical vorticity tendency contoured and vortex-relative streamlines superimposed. Contour increment is $1 \times 10^{-4}\ \mathrm{s}^{-2}$.

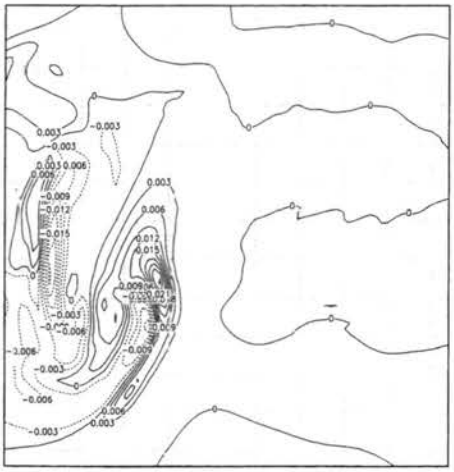

Figure 4.13: Vertical vorticity at 3300 s and 608 m above the surface. Contour increment is $3 \times 10^{-3}\ \mathrm{s}^{-1}$.

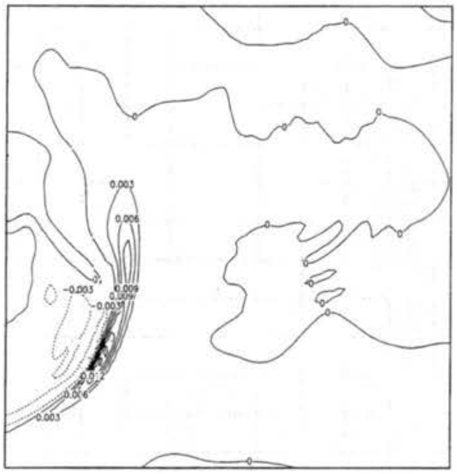

Figure 4.14: Same as Figure 4.9, but at 62 m above the surface. Contour increment is $3 \times 10^{-3}\,\mathrm{s}^{-1}$.

horizontal vorticity leads to the production of a new vertical vorticity center. Why does the vorticity jump begin aloft and then progress to the surface? Figure 4.14 shows the vertical vorticity for 3100 s but at the 62 m level, where the vorticity jump has not yet occurred. Two distinct vorticity centers are still apparent, but the northern one is considerably weaker than the southern one. Figure 4.15 shows the inflow streamlines and tilting term at the 62 m level. As at the higher level, there is positive tilting in the inflow region to the northern vorticity center, but the magnitudes are lower by about a factor of five (the contouring interval has been reduced by a factor of ten). The reason for this is neither the direction nor the magnitude of the horizontal vorticity vectors, which is actually larger at the 62 m level than the 608 m level (Figure 4.16), but rather the magnitude of the w-gradient, smaller at the 62 m level simply because w itself is smaller. Thus the vertical vorticity jumps to the northern location at higher levels first because the w-gradient and the tilting terms are greater there.

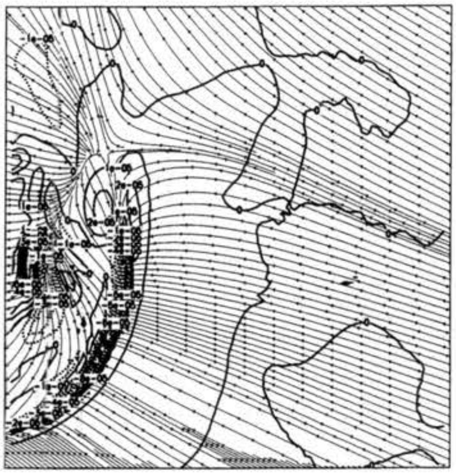

Figure 4.15: Same as Figure 4.12, but at 62 m above the surface. Contour increment is 1×10^{-5} s^{-2}.

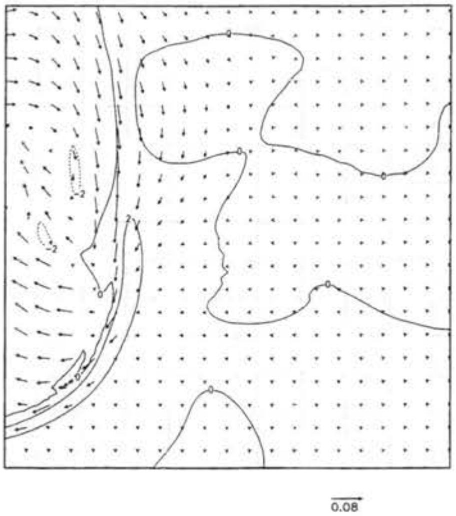

Figure 4.16: Same as Figure 4.11, but at 62 m above the surface. Contour increment for vertical velocity is 2 m s^{-1}.

4.5 Fine Grid Vorticity Initialization

With it being established that the rapid vorticity intensification at the surface is not an artifact of grid nesting, a nested grid with 111 m grid spacing was introduced at 3300 s around the northern vorticity center, after the vorticity centers become co-located but prior to the most rapid intensification. The fine-grid domain contains 119×119 grid points, a region approximately 13 km square.

At the initial time of the fine grid (Figure 4.17) the band of vorticity is concentrated in a strip within the gust front convergence zone, extending approximately 1 km across. The maximum value of the vorticity is 0.04 s^{-1}. The perturbation pressure field and vortex-relative velocity vectors are shown in Figure 4.18. No pressure deficit is apparent at the vorticity maximum; in fact, there is a relative pressure maximum associated with the gust front. The center of the high pressure associated with the downdraft is located just to the northwest of the fine grid. There are a couple of low pressure features visible on the grid. In the surface air just east of the gust front there is a broad region of lower pressure that resembles the inflow low sometimes reported with supercell thunderstorms (Barnes 1978; Rasmussen and Straka 1998), and will be referred to as such in this section for simplicity.

To the northwest of the vorticity maximum is another low-pressure feature. A west-east cross-section through the center of the low pressure (Figure 4.19) reveals that this feature is most intense at a height of 1500 m near the height of the undisturbed cloud base. In the vicinity is a tilted band of vorticity located on the boundary between the updraft and downdraft in the lowest three kilometers (Figure 4.20). This is similar to the divided mesocyclone of Lemon and Doswell (1979), and will henceforth be referred to as the 'divided 'mesocyclone'. The lowest pressure is located where the divided mesocyclone penetrates into the main cloud; beneath this level the divided mesocyclone is on the interface between

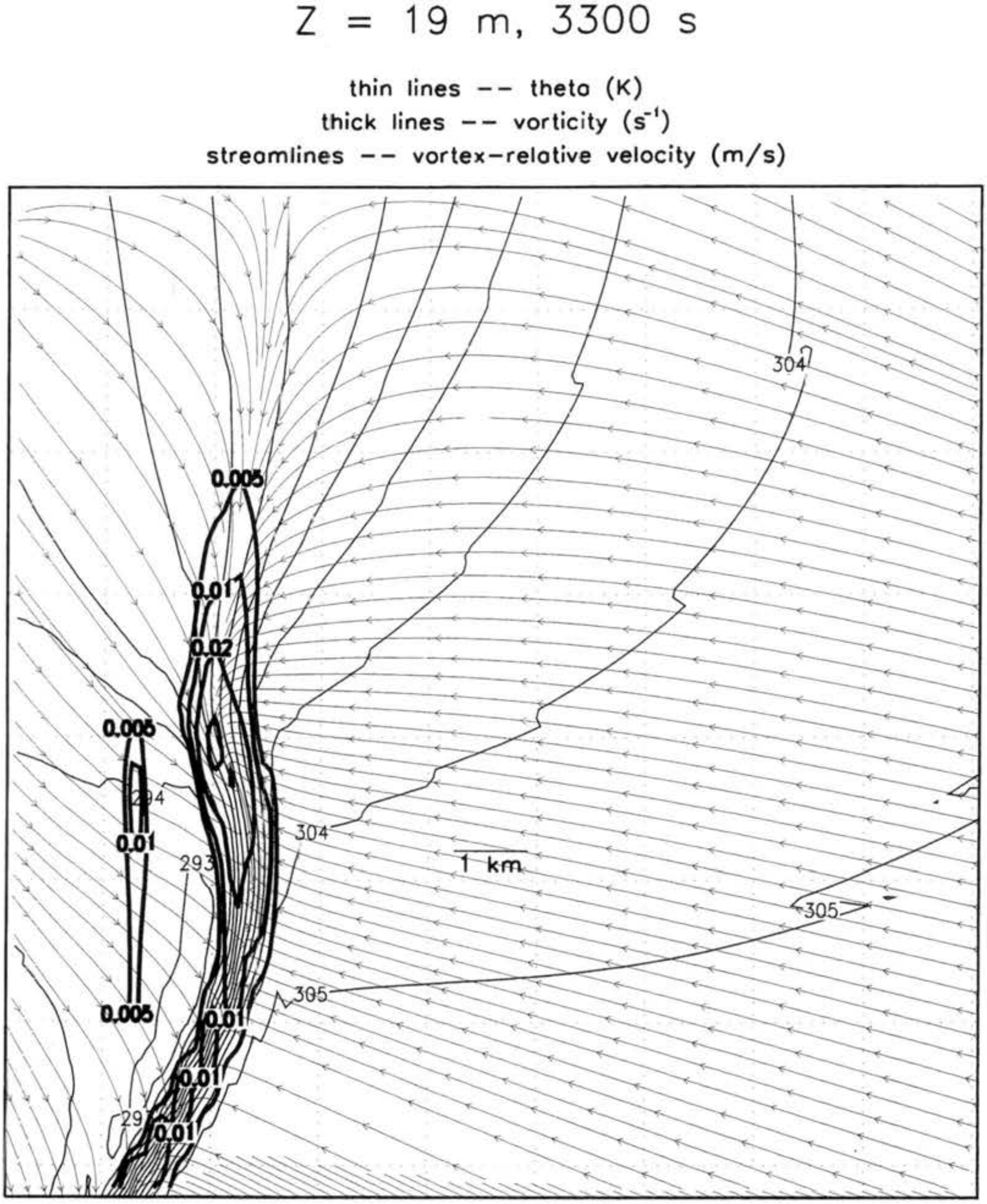

Figure 4.17: Potential temperature, vertical vorticity, and vortex-relative streamlines for Grid 2 at 3300 s and 19 m above the surface. Potential temperature is represented by thin contours in 1 K increments; vertical vorticity is represented by thick contours whose values double every increment beginning with 5×10^{-3} s^{-1}. For reference, a line segment indicating a distance of 1 km is provided.

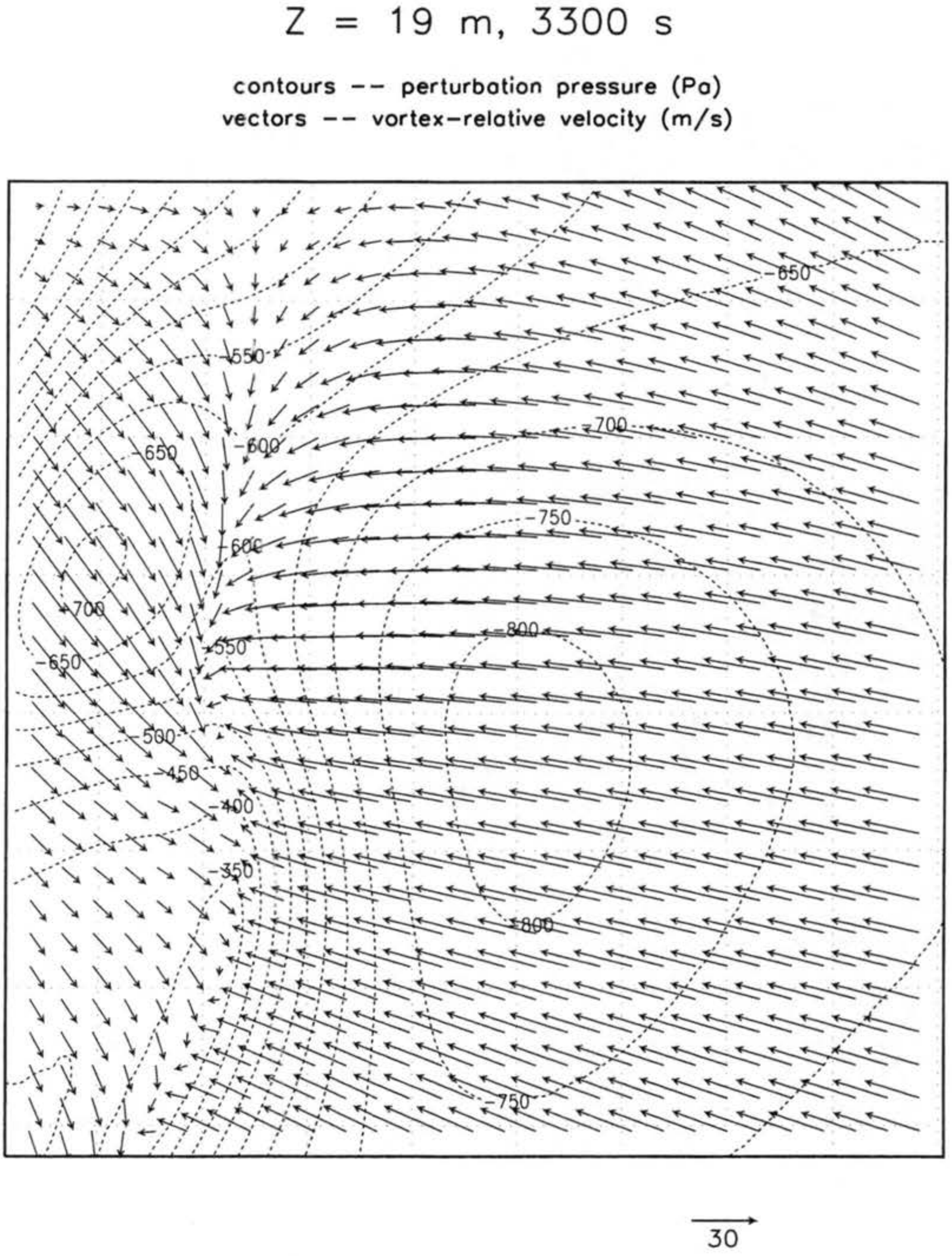

Figure 4.18: Perturbation pressure and vortex-relative velocity vectors for Grid 2 at 3300 and 19 m above the surface. Contours of perturbation pressure have an increment of 50 Pa (0.5 mb). Magnitude of reference vector has units of s^{-1}.

the lowered cloud base and clear air. The pressure is lowered at the ground directly beneath the divided mesocyclone at cloud base even though the strongest vorticity itself is located a couple kilometers to the east.

Figure (4.21) shows the perturbation pressure at 1493 m and the combined magnitude of the vorticity, deformation, and divergence terms to the Exner-function equation (2.25) for regions where the combination is positive (i.e., heuristically producing low pressure). A very good correlation is found, indicating that the vertical vorticity forcing (the only positive contribution to the Laplacian here) is mainly responsible for the location of the mesolow. However, the vertical shear contribution is also not negligible here (compare Figure 4.22). A notch of lowered pressure within the cold pool to the rear of the storm is also due to the vertical shear term. The vertical vorticity is significant along the gust front in the south of the domain, but here the deformation and divergence terms are enough to eliminate any lowering of the pressure. In fact, generally pressures are high along the gust front (see Figure 4.18).

The inflow low is fairly constant with height but gradually disappears above cloud base, as is apparent in Figure 4.19. There is no strong Laplacian function at the location of the inflow low, but Figure 4.23 shows a good correlation between a weak signal in the shear term and the lowest pressure (the contributions from the other terms are even smaller). What the figure is showing is the interaction between the environmental vertical wind shear and the updraft gradient to the east of the storm; essentially the 'inflow low' is simply the linear term associated with the lowered pressure downshear of a storm.

The center of the strongest downdraft is near the highest pressure of the cold pool; this is not located in the region of lowest θ, which is to the south (Figure 4.24). A simple derivation of a pressure relation follows. The vertical Boussinesq momentum equation can

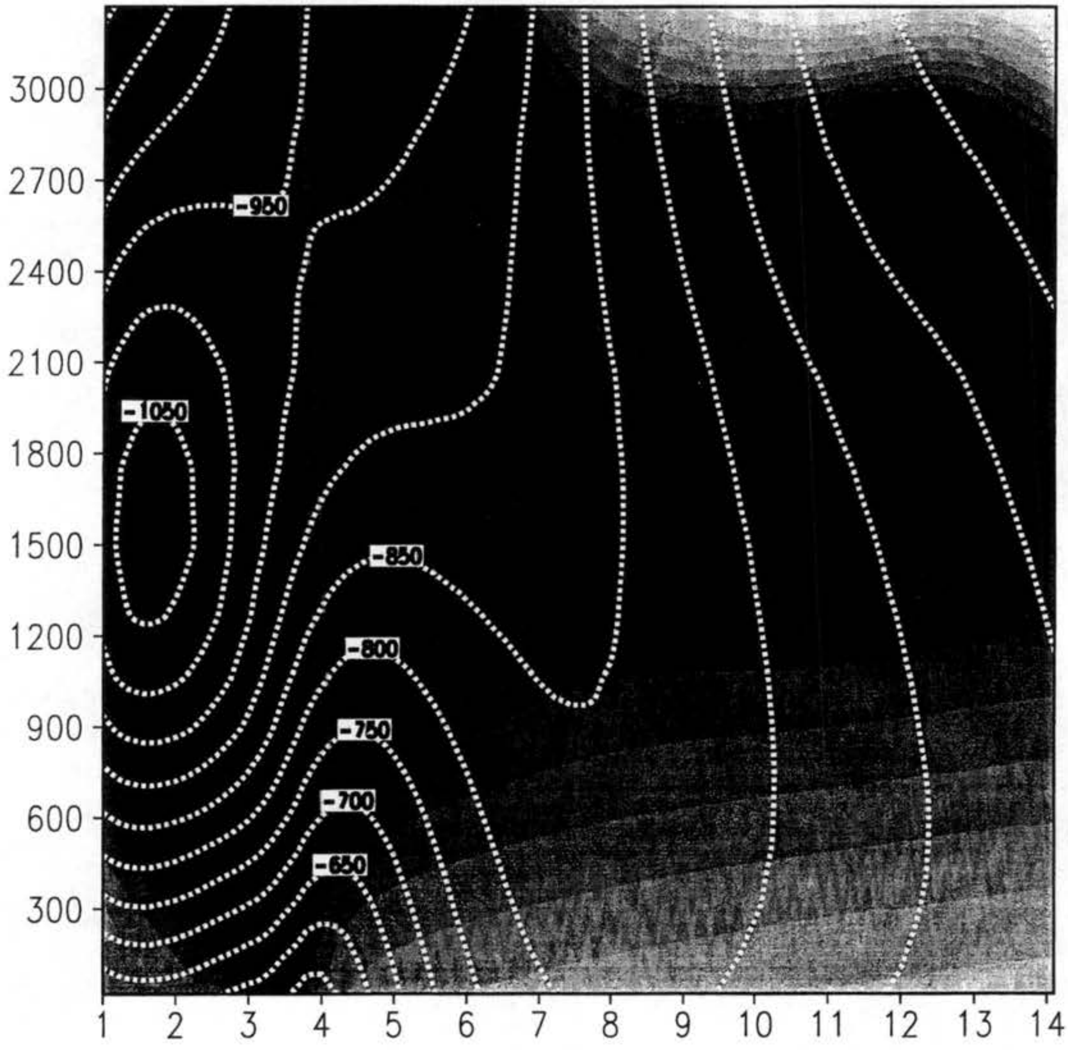

Figure 4.19: West-to-east cross section through 'divided mesocyclone' at 3300 s. White dashed contours are perturbation pressure in 50 Pa (0.5 mb) increments. Increasingly darker shading represents increasing relative humidity, with darkest shade representing over 90% relative humidity. Labels on y-axis represent height above surface in meters. Labels on x-axis represent horizontal distance in kilometers.

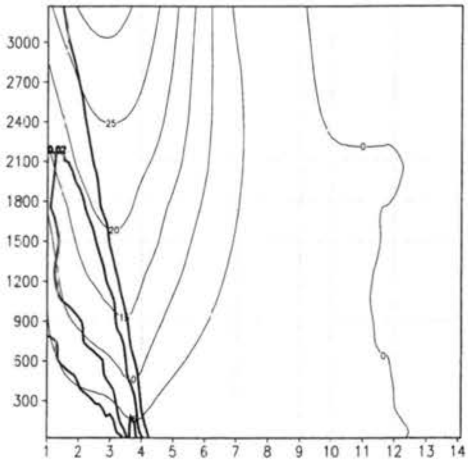

Figure 4.20: West-to-east cross section through 'divided mesocyclone' at 3300 s. Light contours are vertical velocity (5 m s^{-1}) and dark contours are vertical vorticity (0.01 s^{-1}). Labels on y-axis represent height above surface in meters. Labels on x-axis represent horizontal distance in kilometers.

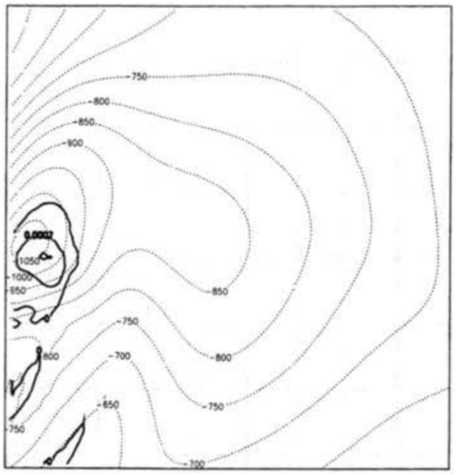

Figure 4.21: Combined two-dimensional vorticity, deformation, and divergence contributions to the Laplacian equation (2.25) in regions where positive, at 3300 s and 1493 m above the surface. Light contours are perturbation pressure in 50 Pa increments; dark contours are Laplacian contributions in 2×10^{-4} s^{-2} increments.

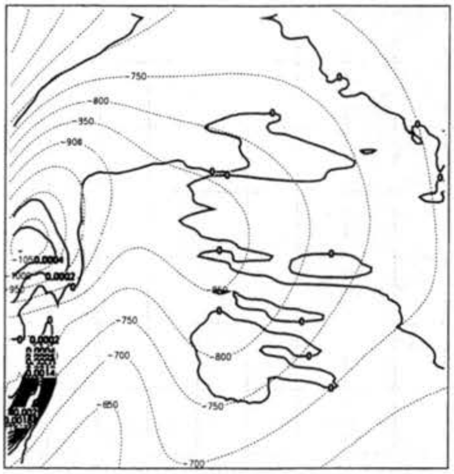

Figure 4.22: Same as Figure 4.21, but including the vertical shear contributions to the Laplacian.

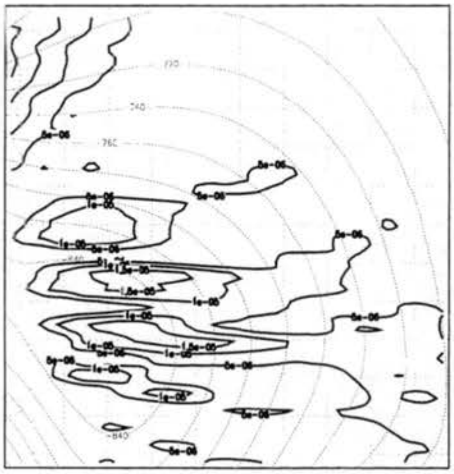

Figure 4.23: Close-up of 'inflow low' in fine grid at 3300 s and 1263 m above surface. Thin contours show perturbation pressure in 20 Pa increments while thick contours show the vertical shear Laplacian contribution in 1×10^{-5} s^{-2} increments.

be written:

$$-\theta_{v0}\frac{\partial \pi'}{\partial z} + B = \frac{dw}{dt} = \frac{dw}{dz}\frac{dz}{dt} = \frac{d}{dz}(w^2), \tag{4.1}$$

with z the height of a parcel following the parcels' motion. If we integrate from the ground ($z = 0, w = 0$) to the height H where the parcel began its descent ($w = 0$), then:

$$\int_0^H B dz - \theta_{v0}\int_0^H \frac{\partial \pi'}{\partial z} dz = 0, \tag{4.2}$$

where the variation of the basic-state virtual potential temperature has been neglected. The pressure integral strictly cannot be integrated directly because the partial derivative keeps x and y fixed while the integration is over a trajectory. But if we neglect horizontal variations then

$$\pi'(z = 0) = \frac{1}{\theta_{v0}}\int_0^H B dz, \tag{4.3}$$

when $\pi' = 0$ at the start of descent.

Even though θ is not noticeably different at the pressure maximum from its value to the south, the downdraft originates far higher at the pressure maximum, which is located to the north of the main cloud base, underneath the lower surface of the anvil. If the buoyancy is integrated over the region of the pressure maximum to a height of 4000 m, a value approximately 400 J kg^{-1} less than that of the inflow is obtained, which translates to an Exner function of approximately 1.3 J kg^{-1} K^{-1} greater using (4.3); using $dp' \approx c_p p d\pi'/R\pi$ this corresponds to 4.4 mb at the surface pressure. This closely corresponds to the difference in pressure between the peak downdraft at the surface and the ambient air away from the influence of the inflow low in Figure 4.18.

This downdraft consists of very dry, low θ_e air (Figure 4.25) that has been evaporatively cooled by hydrometeors falling into it, predominantly hail. In contrast, the region to the

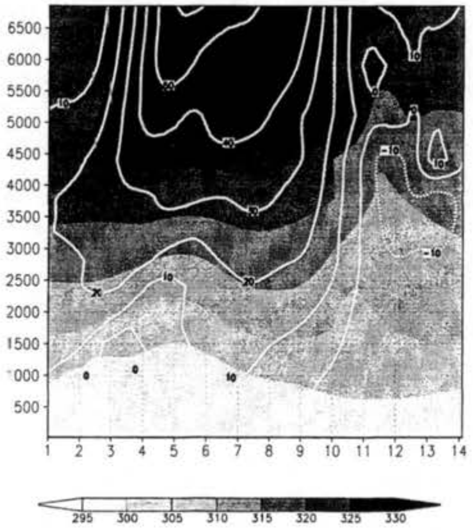

Figure 4.24: South-north cross section at i = 5 through fine grid at 3300 s. Shading is potential temperature in Kelvin while contours show vertical velocity every 10 m s^{-1}.

south is located beneath the main updraft. Significant quantities of hail are generated above this location as well, but within the cloud most of the hydrometeors beneath 4000 m are in the rain category.

As apparent in Figures 4.17 and 4.18, the pressure maximum is a region of divergent streamlines. The velocity magnitude increases away from the cold pool towards the divided mesocyclonic low. Consider the Bernoulli function:

$$BN = \frac{p'}{\rho_0} + \frac{|\mathbf{v_H}|^2}{2}. \tag{4.4}$$

This function is conserved for two-dimensional steady-state motion provided there is no vertical vorticity or friction. The Bernoulli function does incorporate the effect of pressure work on accelerating or decelerating the flow. As Figure 4.26 shows, the variations in vortex-relative wind speed are well explained by invoking the pressure work performed by the high and low pressure centers. So divergence tends to occur between the high pressure and the divided mesocyclonic low, and convergence occurs when the velocity vectors

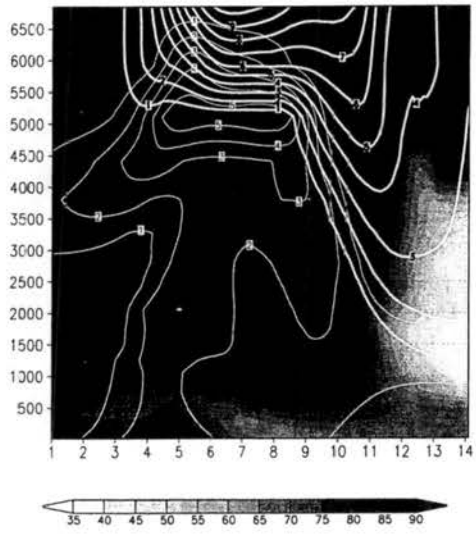

Figure 4.25: Same as Figure 4.24, but with shading representing relative humidity, thin contours representing rain mixing ratio every 1 g kg^{-1}, and thick contours representing hail mixing ratio every 1 g kg^{-1}.

'overshoot' the low pressure and are directed towards higher pressure. Near the ground, convergence is associated with positive vertical motion while divergence is associated with negative vertical motion; thus there is a band of low-level uplift between the two low pressure centers.

Because the center of the main downdraft and the location of the most negatively buoyant air are not co-located, the horizontal vorticity vectors show a significant streamwise component (Figure 4.27) in the vicinity of the divided mesocyclone. (If the downdraft and theta contours were parallel, one would expect divergent flow from the downdraft but baroclinic generation of vorticity in the cross-flow direction, and the vortex-relative velocity and horizontal vorticity vectors should be nearly perpendicular. This can in fact be seen to occur near the gust front near the north and south boundaries of the domain in Figure 4.27). Because of the streamwise horizontal vorticity component, there is upward tilting of this

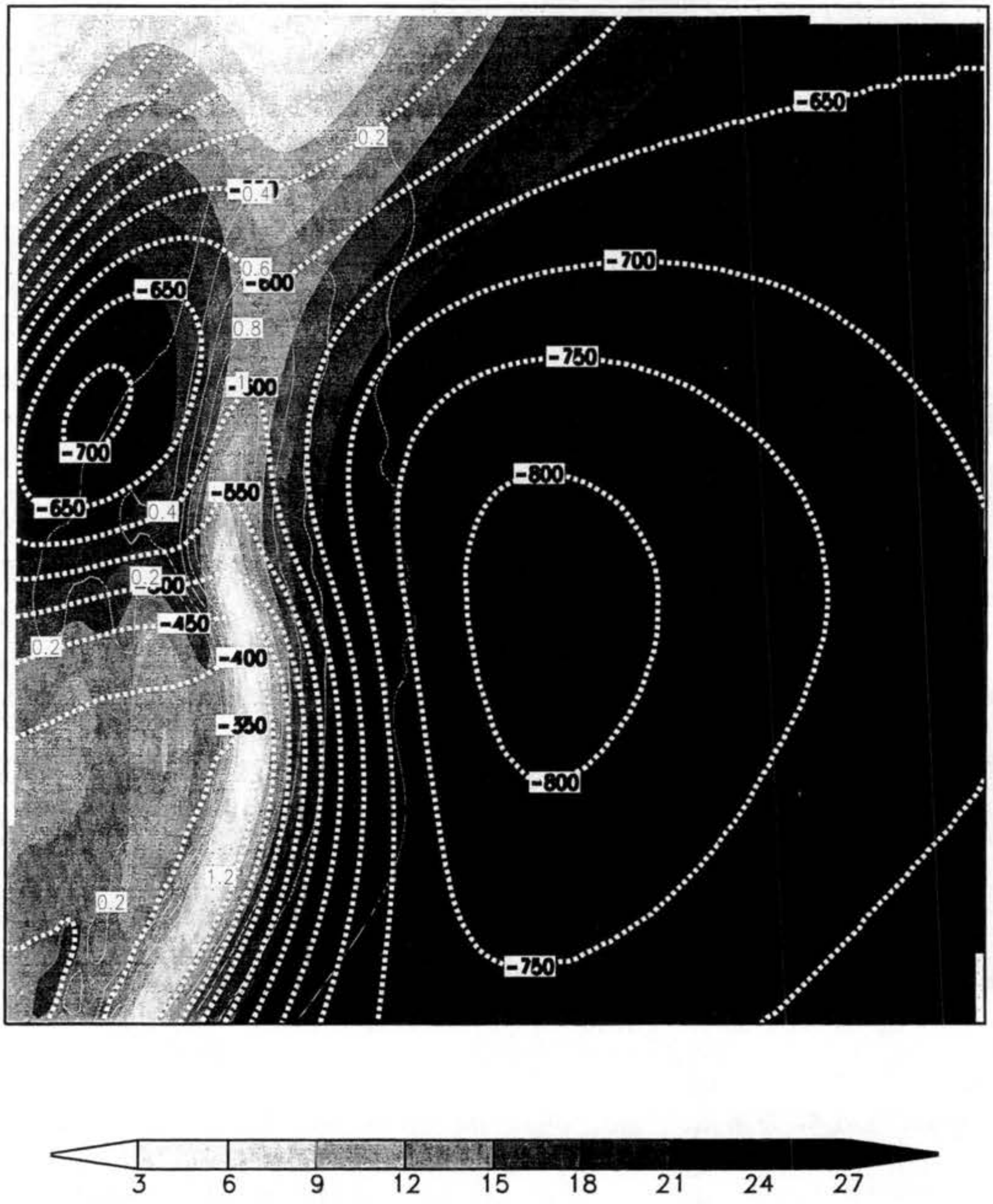

Figure 4.26: Vortex-relative horizontal wind speed (shaded), vertical velocity (thin sold contours), and perturbation pressure (thick dashed contours) at 3300 s and 19 m above surface. Contour increments are 3 m s^{-1} for horizontal wind speed, 0.2 m s^{-1} for vertical velocity, and 50 Pa for pressure.

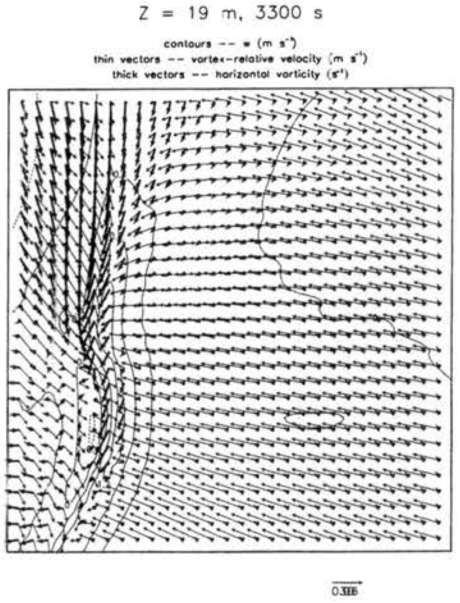

Figure 4.27: Vertical velocity (contours with increment 0.4 m s^{-1}), vortex-relative velocity (thin vectors), and horizontal vorticity (thick vectors) at 3300 s and 19 m above surface.

vorticity and positive vertical vorticity production as parcels diverge from the downdraft. (Actually, upward tilting occurs whenever w increases in the direction of the horizontal vorticity vector, so positive vertical vorticity production occurs even before the updraft is reached, i.e. when w is still negative.) This is consistent with the findings of Grasso (1996) and Grasso and Cotton (1995) that baroclinic vorticity is generated in the downdraft and henceforth tilted into vertical vorticity even before the parcel has ceased descending.

Looking at the coarse grid at 3300 s gives a larger scale view of the vorticity band. Most of the vorticity is located in a north-south region approximately 6 km long (Figure 4.28). Also shown in the figure is $\partial v/\partial y$, which represents the stretching deformation along the axis of the vorticity band. It is seen that significant vorticity largely resides in the region where $\partial v/\partial y$ is negative. The magnitude of $\partial u/\partial x$, the stretching deformation in the cross-band direction, is uniformly negative along the gust front, as expected (Figure 4.29), though it is larger in the region of the strongest vorticity. So intense vorticity forms

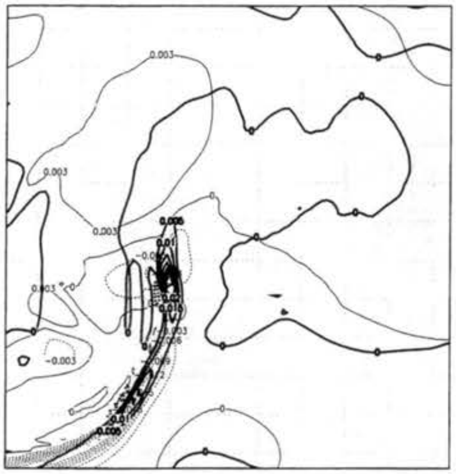

Figure 4.28: Vertical vorticity for Grid 1 at 3300 s and 19 m above surface. Thick contours represent vertical vorticity in increments of 5×10^{-3} s^{-1}. Thin contours represent the value of $\partial v / \partial y$ with increments of 3×10^{-3} s^{-1}.

in a band whose length seems determined by the presence of uniaxial stretching. This is consistent with the theoretical result found in the previous chapter that vorticity in a linear band should eventually decay when there is biaxial stretching, but continue increasing in uniaxial stretching.

4.6 Fine Grid Vorticity Evolution

By 3360 s (one minute later), the rapid vorticity intensification has begun (Figure 4.30). The maximum vorticity in the vortex band has now reached near 0.1 s^{-1}; this leads the development in the single-grid simulation by 40 seconds. The band itself has approximately the same north-south extent as before but has narrowed, to approximately 600 m. There is a noticeable bowing of the line of vorticity, with a wavelength on the order of 2-3 km. The maximum vorticity occurs in the segment of the band that has tilted into a northwest-southeast configuration, pointing towards the outflow from the downdraft.

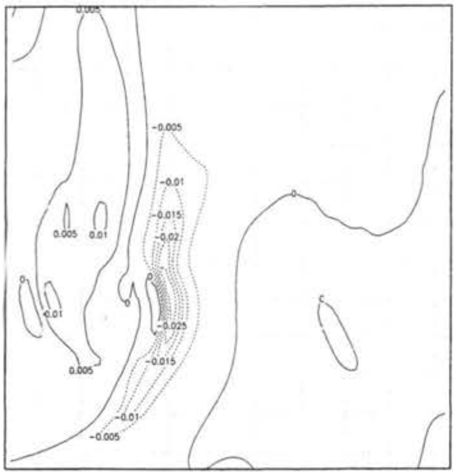

Figure 4.29: Same as Figure 4.28, except shows contours of $\partial u/\partial x$ in increments of $5 \times 10^{-3}\ \mathrm{s}^{-1}$.

However, despite the vorticity increase at low levels, the pressure still has only barely dropped at the vorticity maximum (Figure 4.31). The other pressure features have shown little change.

At 3420 s (Figure 4.32) the low level vorticity has reached 0.18 s^{-1} and has become more concentrated. Vorticity trails off from the maximum in two north-south bands with an elliptical WNW-ENE core; the whole structure resembles a barred-spiral galaxy. At this time a large surface pressure drop has occurred at the location of the vortex (Figure 4.33), with a 5 mb pressure difference between the vortex core and the nearby gust front. Notably, at the 1263 m level (Figure 4.35) the pressure deficit apparent at low levels is absent (Figure 4.34); the vorticity maximum at this level is only one-third of the surface value at this time. This is strong indication that the vortex concentration does not form in response to a drop of pressure aloft, but rather begins near the surface. The dynamic contributions to the Laplacian equation at the surface at this time (Figure 4.36) show that the only significant

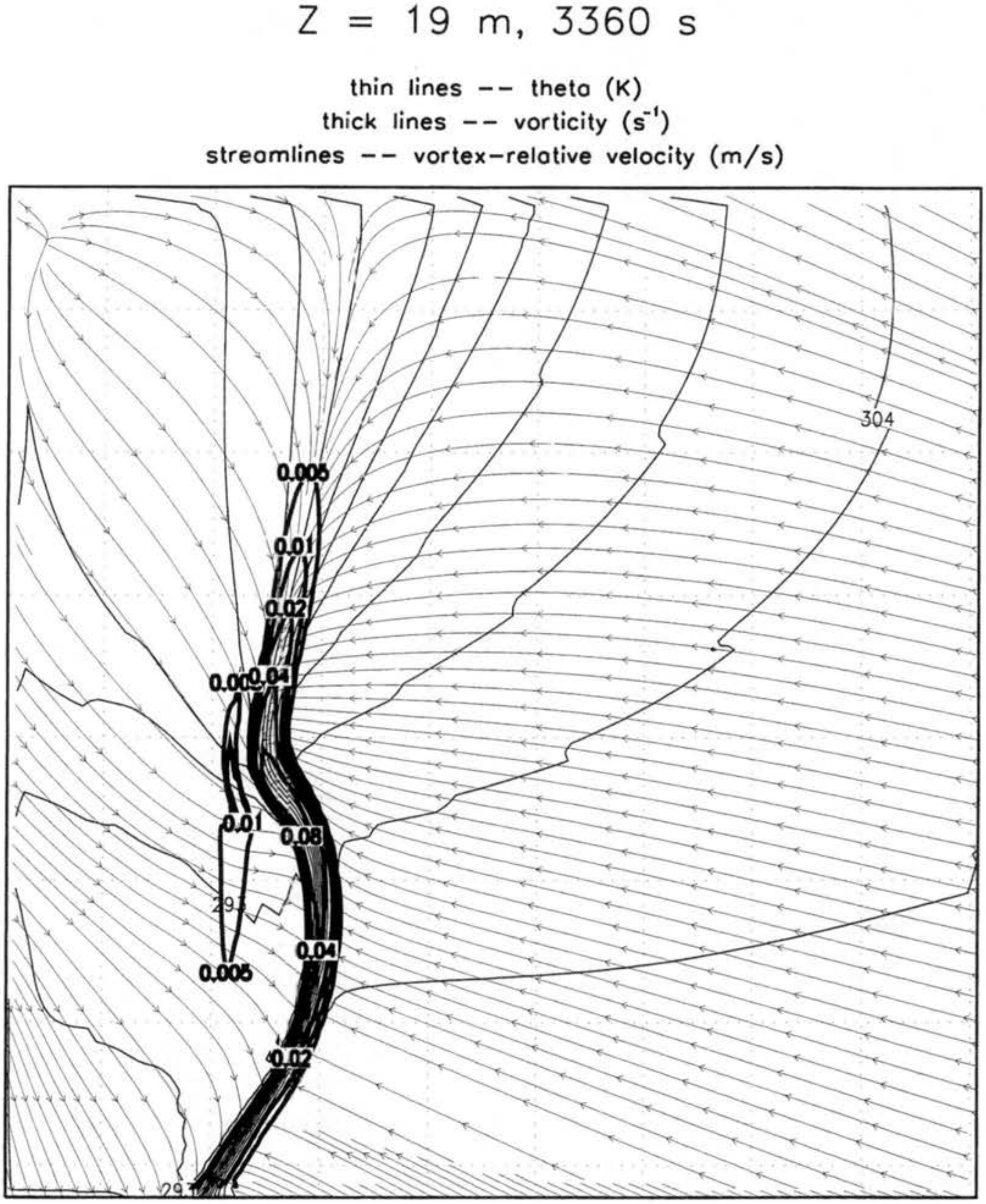

Figure 4.30: Same as Figure 4.17, but at 3360 s. Contour levels for vertical vorticity double every increment beginning with 5×10^{-3} s^{-1}.

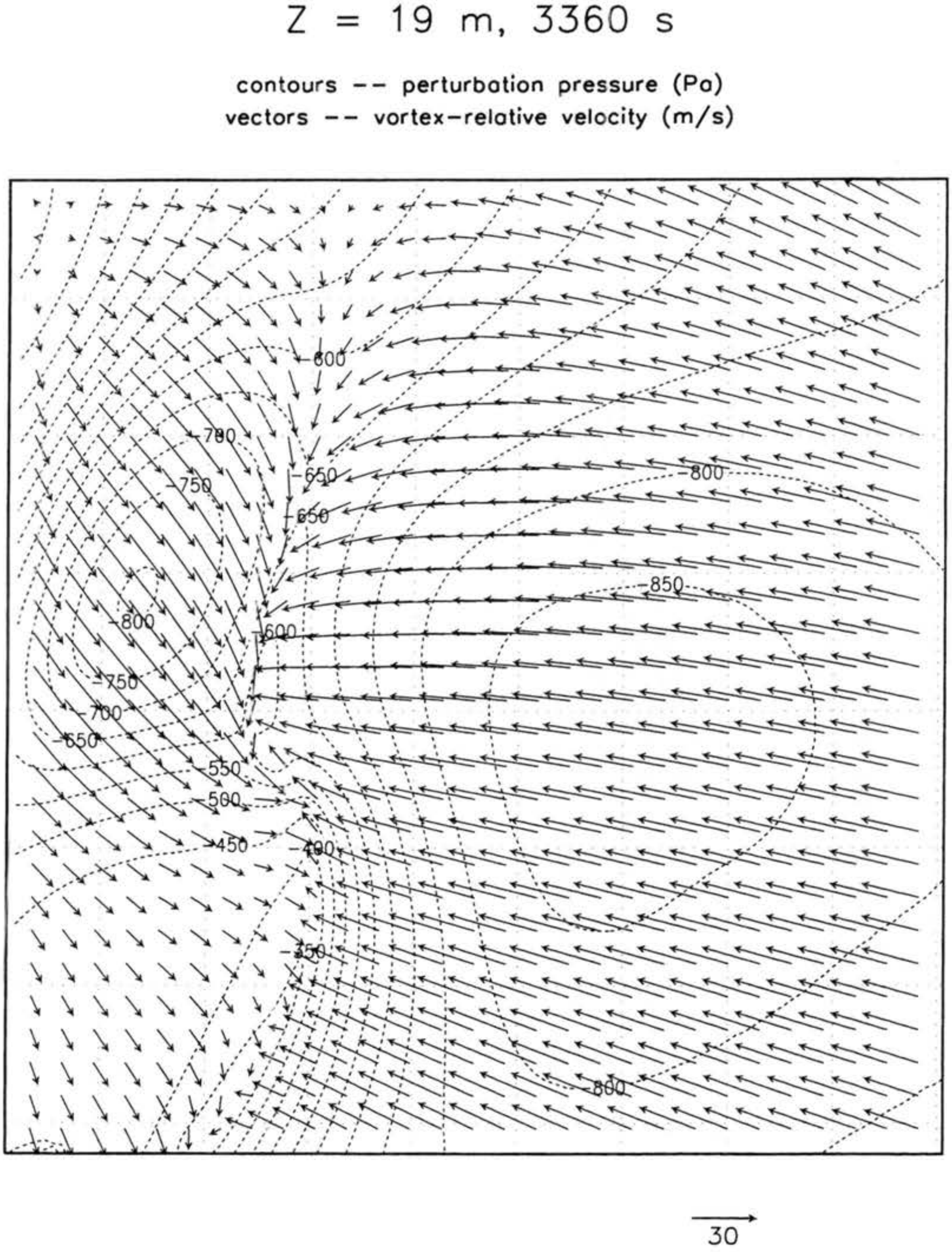

Figure 4.31: Same as Figure 4.18, but at 3360 s.

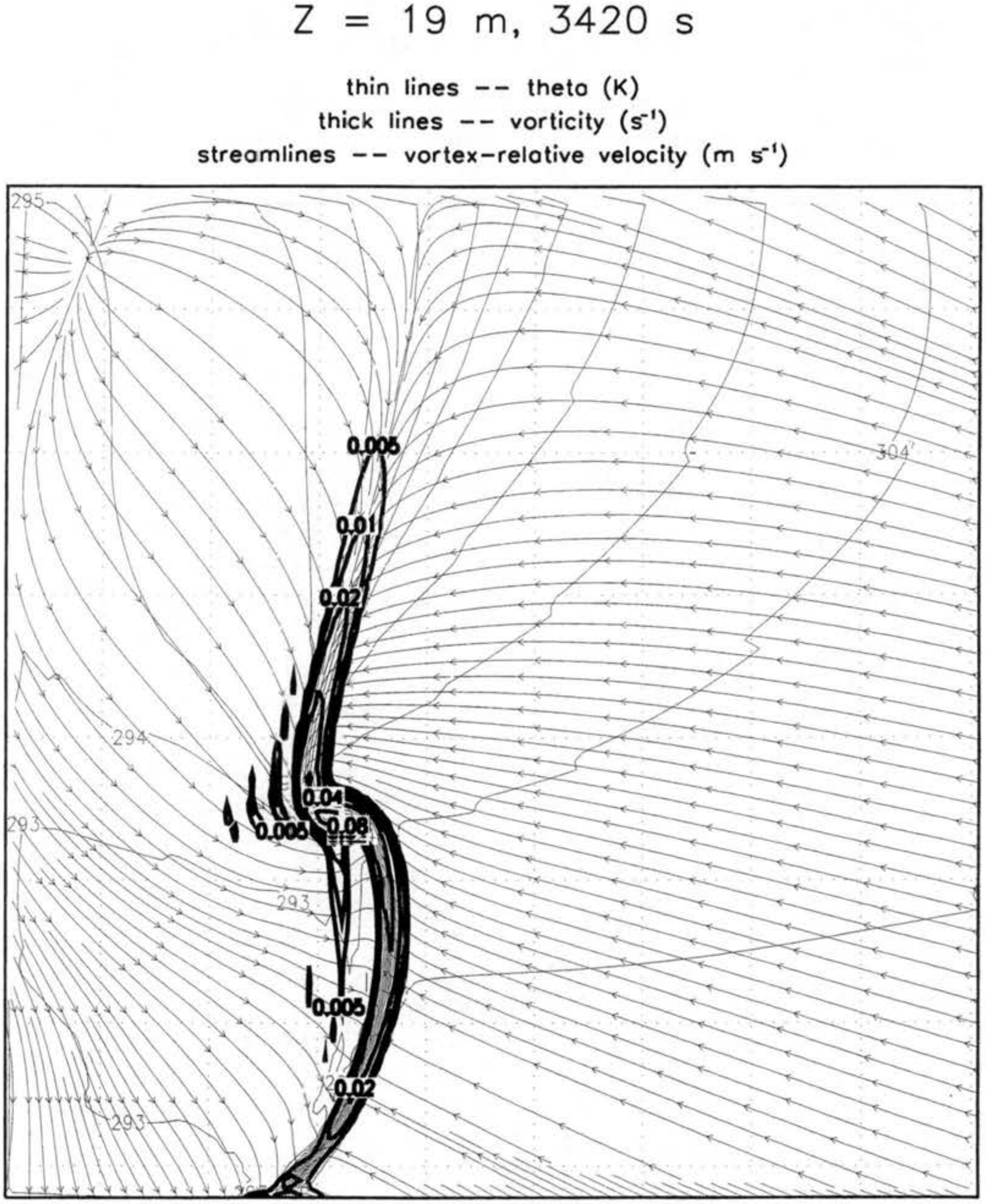

Figure 4.32: Same as Figure 4.17, but at 3420 s. Contour levels for vertical vorticity double every increment beginning with 5×10^{-3} s^{-1}.

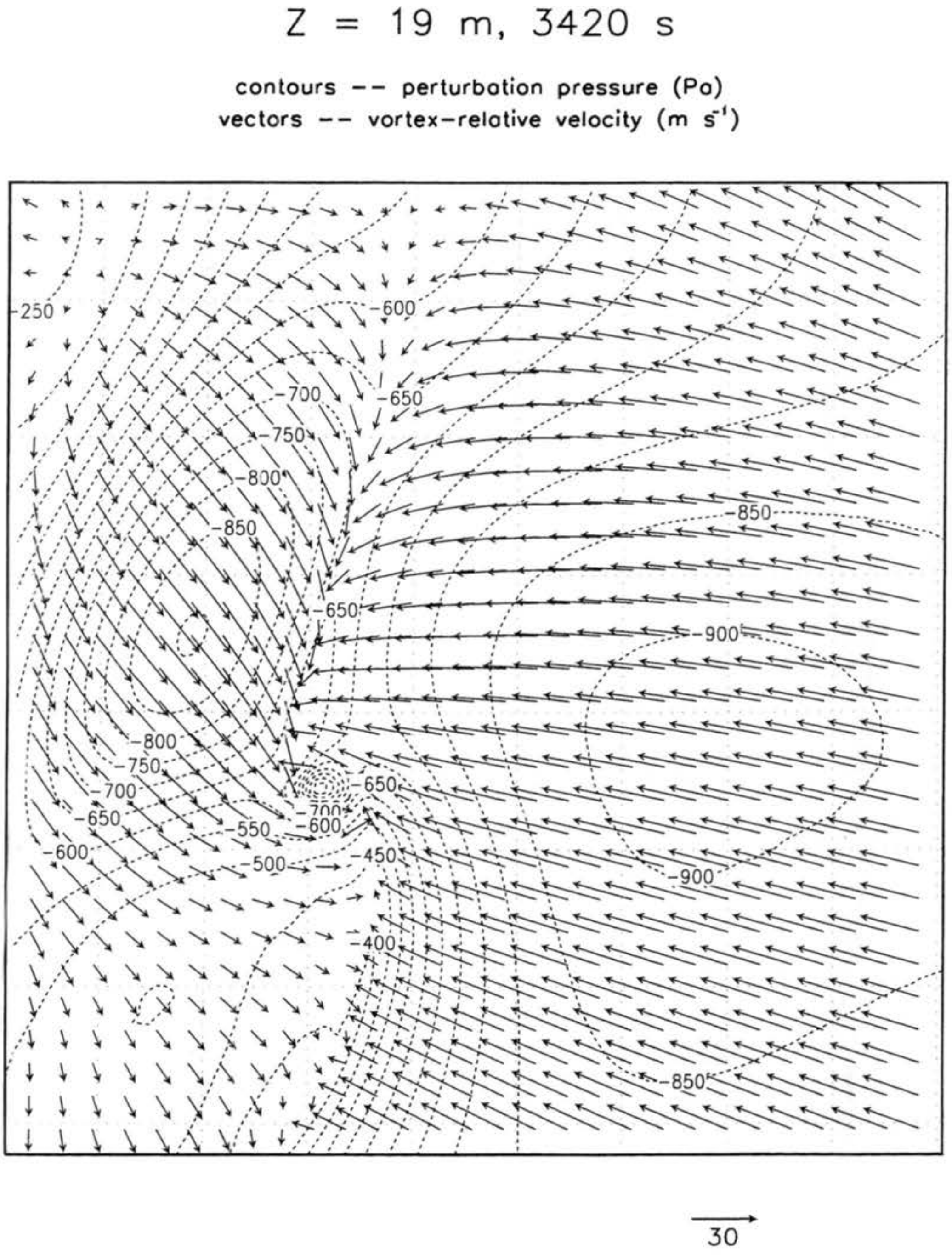

Figure 4.33: Same as Figure 4.18, but at 3420 s.

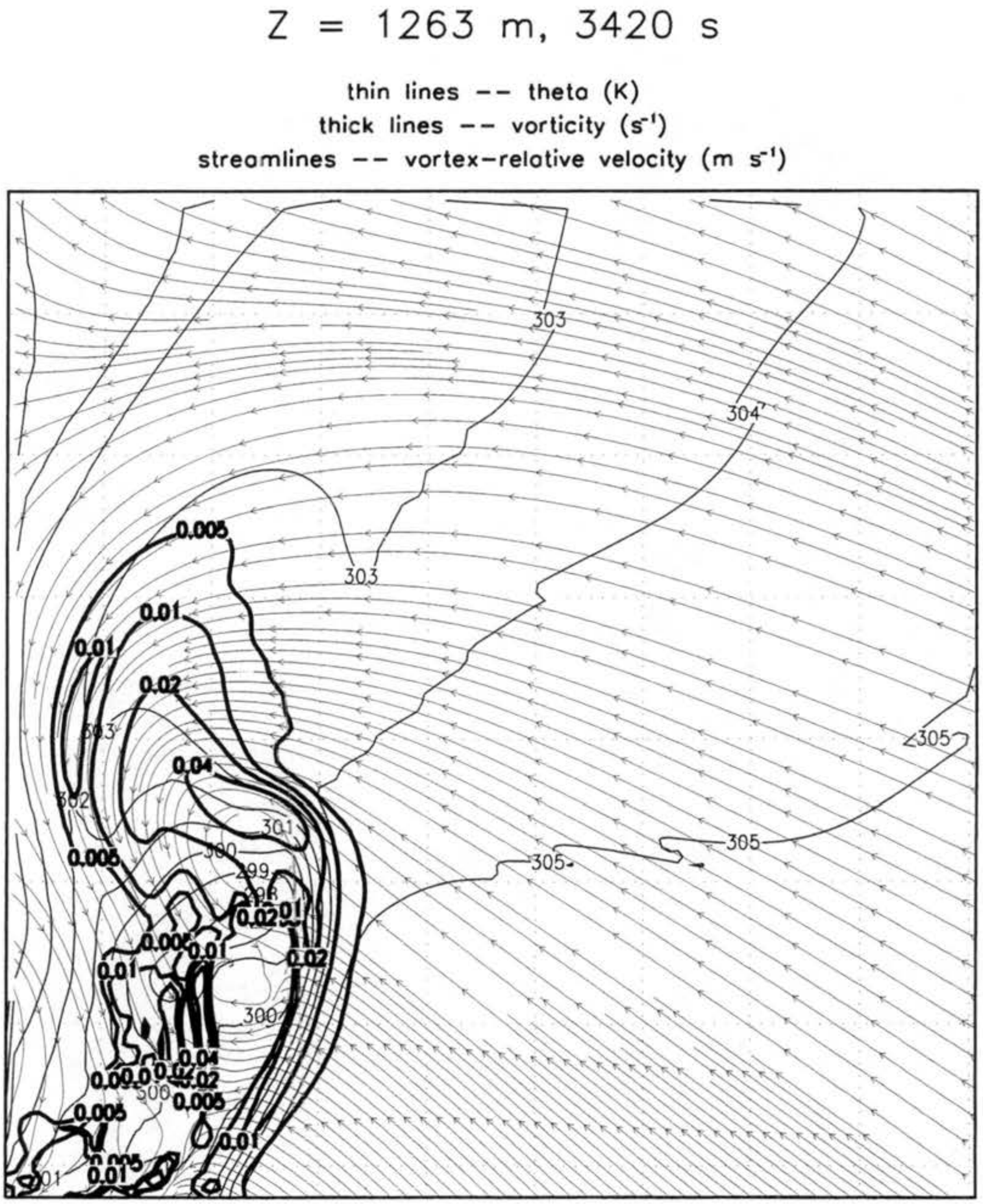

Figure 4.34: Same as Figure 4.32, but for 1263 m above the surface.

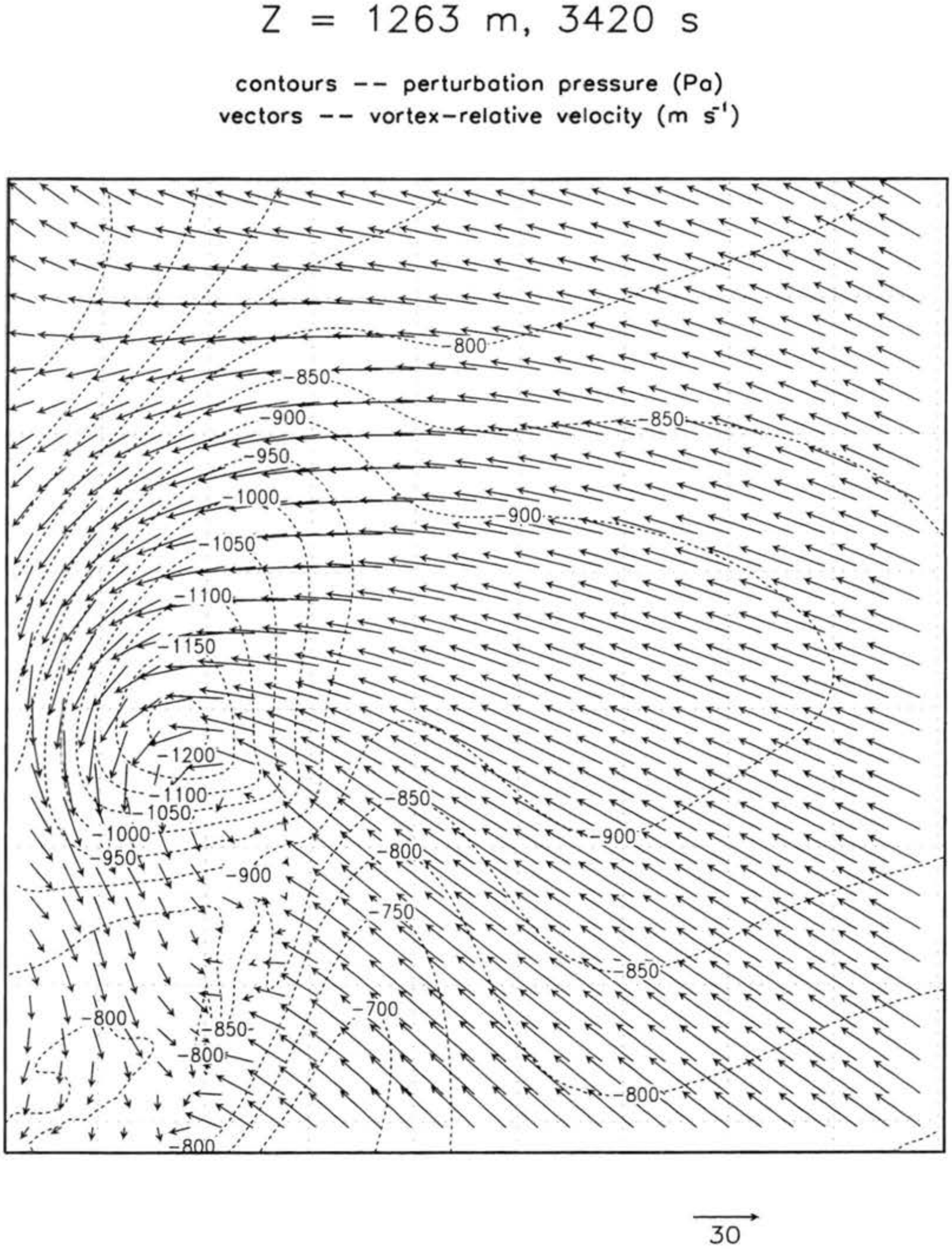

Figure 4.35: Same as Figure 4.33, but for 1263 m above the surface.

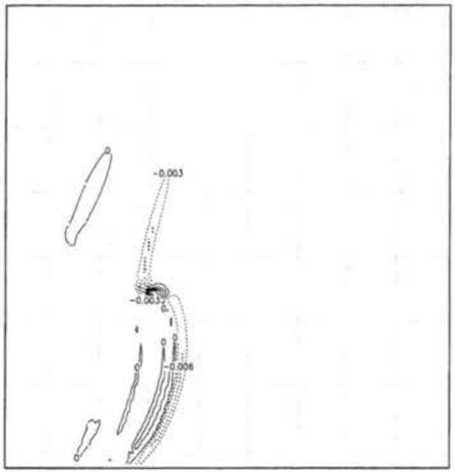

Figure 4.36: Contributions to the Laplacian equation (2.25) from all dynamic terms at 3420 s and 19 m above the surface. Contour interval is 3×10^{-3} s^{-2}.

positive terms at the surface are in fact located in a compact region at the vorticity maximum, whereas surrounding regions along the gust front have a negative contribution to the Laplacian. The same plot at 3300 s (Figure 4.37) shows that the Laplacian contributions are much weaker (the contour interval is ten times less), and furthermore that they are nowhere significantly positive.

By 3600 s, the surface vortex is near its peak (Figure 4.38). The maximum vorticity has concentrated into a circular region that has migrated to the southwest away from the gust front into the cold pool. The vorticity structure shows some resemblance with that of the non-linear pooling of vorticity in a two-dimensional barotropic framework (Guinn and Schubert 1993), where vorticity is seen to concentrate into discrete centers that are connected by spiraling filaments. The maximum surface vorticity is 0.27 s^{-1}, which is comparable to values found in past idealized tornadic simulations with grid spacings near 100 m (Wicker and Wilhelmson 1995; Grasso and Cotton 1995). However, 100 m grid spacing is

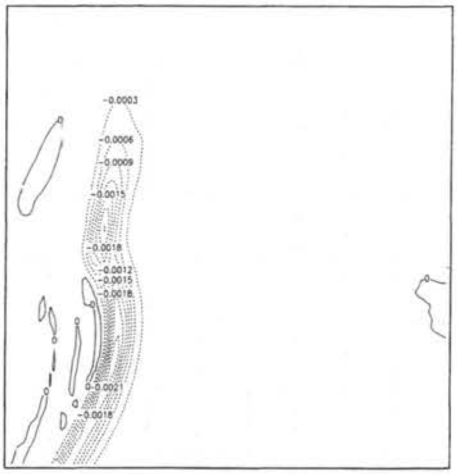

Figure 4.37: Same as Figure 4.36, but at 3300 s. Contour interval is 3×10^{-4} s^{-2}.

still coarse to represent all but the largest tornadoes, and the vortex-relative tangential wind velocities are still only around 30 m s^{-1} (Figure 4.39), although the grid-relative velocities approach 50 m s^{-1} on the southwest side of the vortex. There is now a 12-mb pressure difference between the center of the vortex and the neighboring flow, and a 7 mb difference between the vortex center and the 200-m radius of the 0.1 s^{-1} vorticity region. Kossin and Schubert (2001) also noted the sudden pressure drop that can accompany the sudden concentration of vorticity into an axisymmetric region.

At the 1263 m level (Figure 4.40), there is also a concentrated vorticity center at this time, although it is located due west of the 19 m vorticity maximum, and has less than half the magnitude (0.12 s^{-1}). Nonetheless, there is a strong pressure drop at this level as well (Figure 4.41). Now we clearly have two distinct pressure centers at this level, in contrast to earlier times when only one center was present near this level (compare Figures 4.19 and 4.21). The positive Laplacian contributions from the vertical shear and vorticity terms are shown in Figures 4.42 and 4.43 respectively. (Note that the increment is five times larger

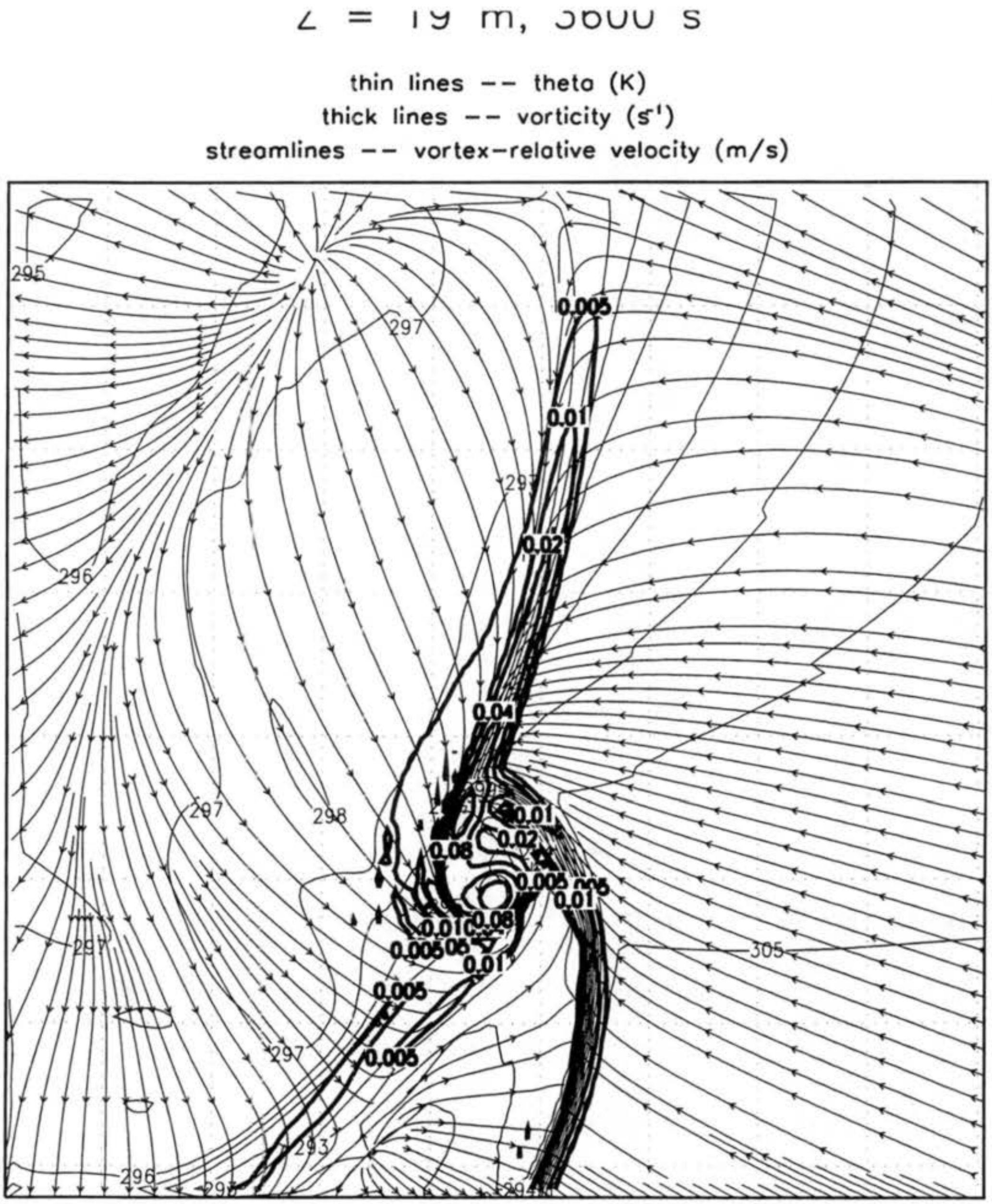

Figure 4.38: Same as Figure 4.17, but at 3600 s. Contour levels for vertical vorticity double every increment beginning with 5×10^{-3} s^{-1}.

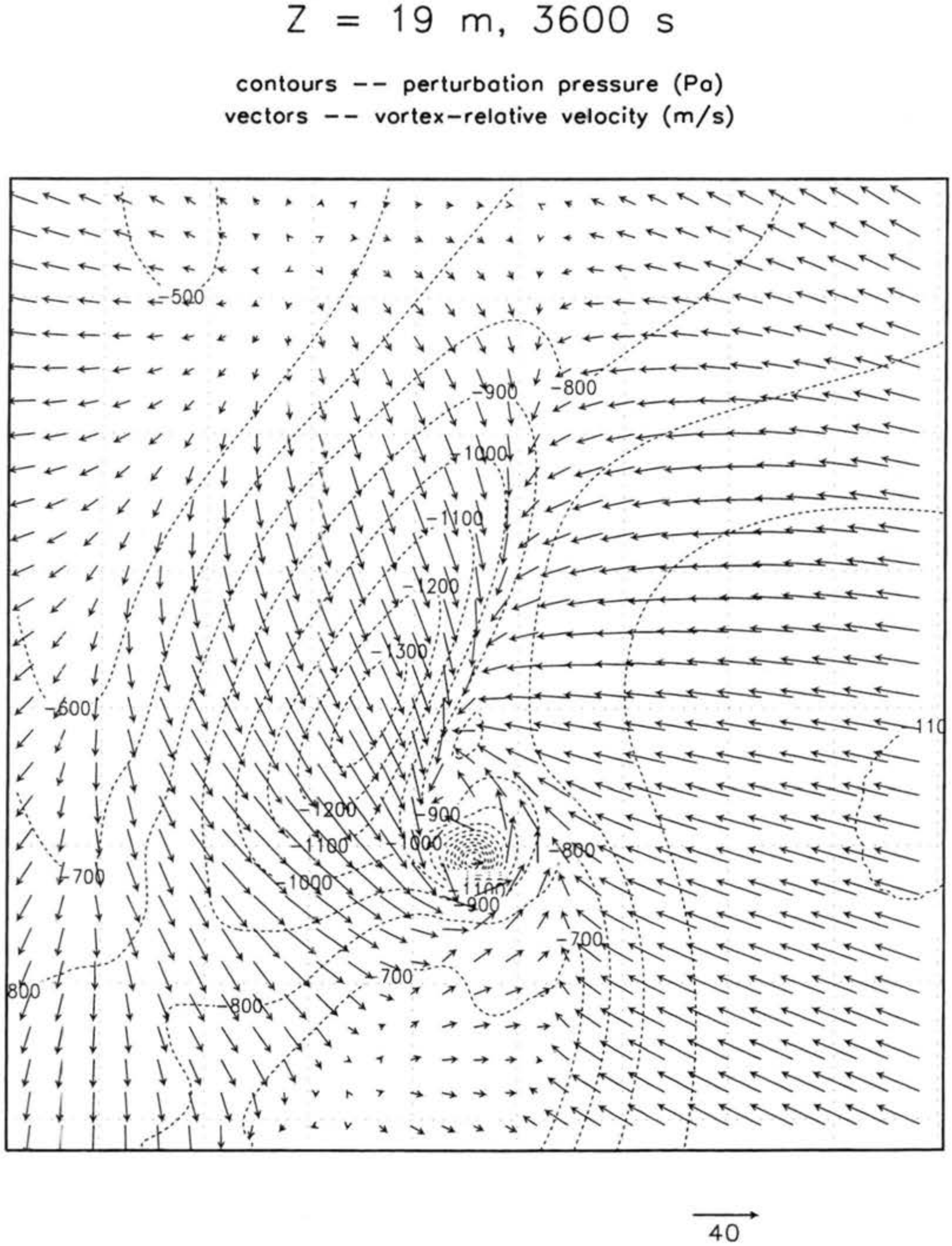

Figure 4.39: Same as Figure 4.18, but at 3600 s. Minimum perturbation pressure in vortex is -1900 Pa (-19 mb).

than in the 3300 s plots.) The divided mesocyclone low to the northwest is still apparent as a region of enhanced vorticity, although at this time the vertical shear contribution to lowering the pressure at the divided mesocyclone seems more important. Clearly though the new vortex has the dominant influence on the pressure, with nearly equal vertical shear and vorticity contributions; the divided mesocyclone remains a distinct feature. Figure 4.44 confirms that the divided mesocyclone resides on the boundary between the main updraft and the downdraft to the northwest. However, a very intense downdraft is apparent just to the north of the main vortex, nearly encircled by strong updraft. This feature resembles the occlusion downdraft referred to in both observational (Barnes 1978; Lemon and Doswell 1979; Wakimoto et al. 1998) and modeling studies (Klemp and Rotunno 1983; Wicker and Wilhelmson 1995) as a localized but intense extension of the RFD within or in the close proximity of a low-level vortex. In the observational studies the occlusion of the mesocyclone is often seen as a component of tornadogenesis (Lemon and Doswell 1979), and in detailed observational studies the occlusion downdraft has been observed prior to tornadogenesis (Wakimoto et al. 1998; Markowski et al. 2000). In modeling studies the development of occlusion downdrafts and the intensification of a low-level vortex are nearly simultaneous processes, and a modeled occlusion downdraft has been shown to be dynamically forced by intense vorticity at low levels (Klemp and Rotunno 1983). Of course, these two views may not be inconsistent if a distinction is made between an intense low-level mesocyclone capable of dynamically forcing a downdraft, and the subsequent tornado. Here, it is also found that what may be termed the 'occlusion downdraft' forms almost simultaneously with the intense vortex, and so like the vortex is first apparent at low levels (compare to Figure 4.34, which is while the concentrated vortex exists near the surface).

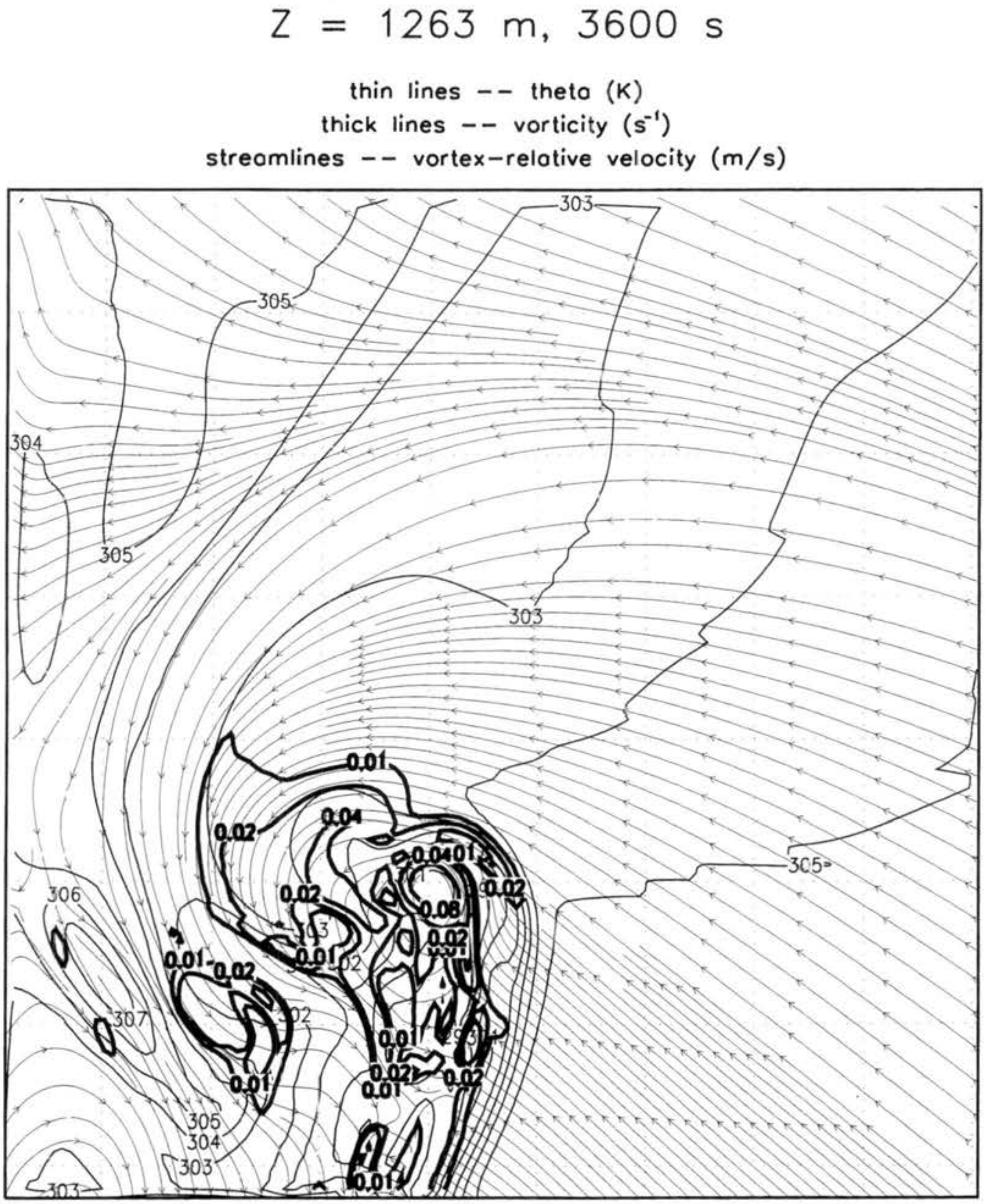

Figure 4.40: Same as Figure 4.34, but at 3600 s. Contour levels for vertical vorticity double every increment beginning with 1×10^{-2} s^{-1}.

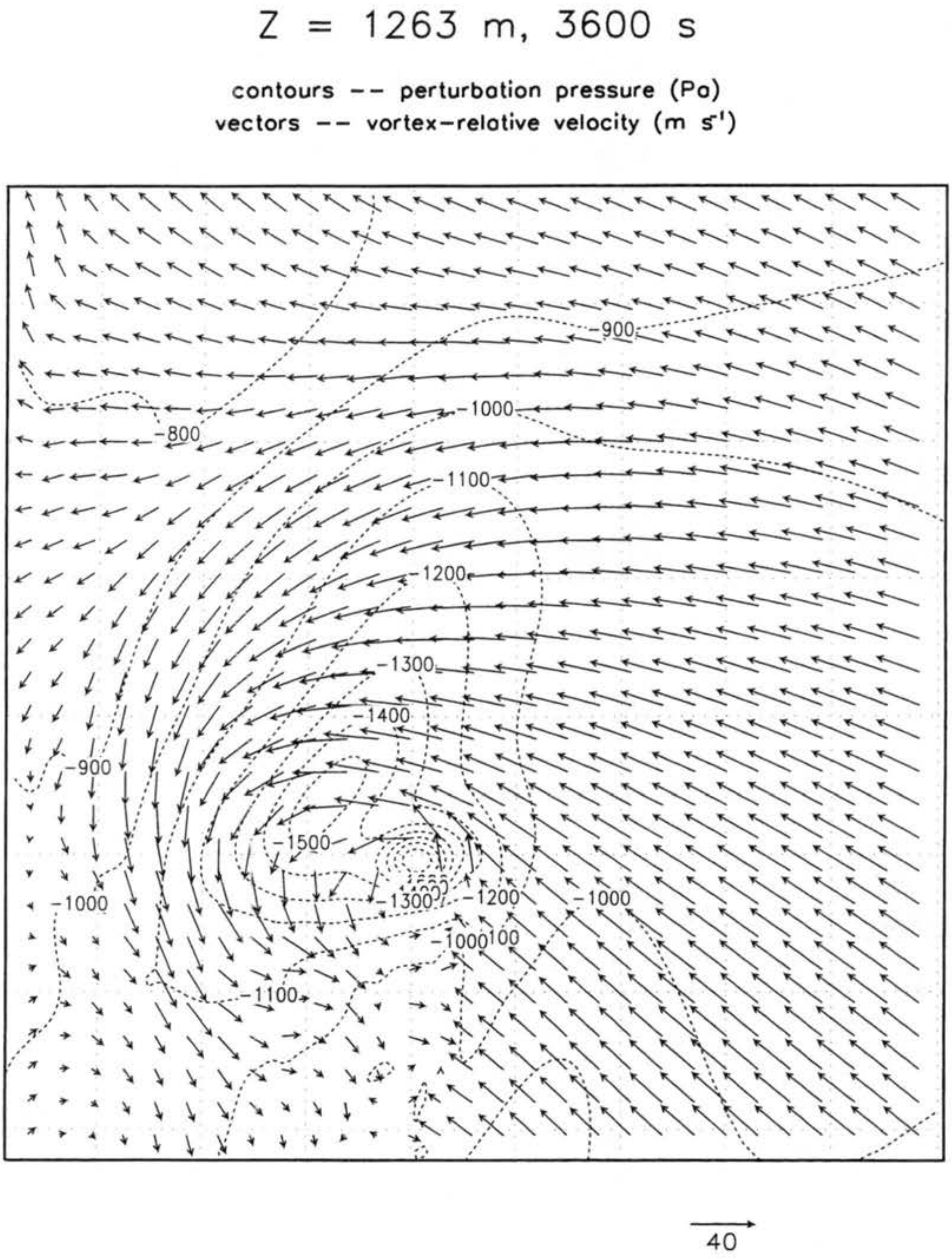

Figure 4.41: Same as Figure 4.34, but at 3600 s. Contour increment is 100 Pa (1 mb). Minimum perturbation pressure in vortex is -19 mb.

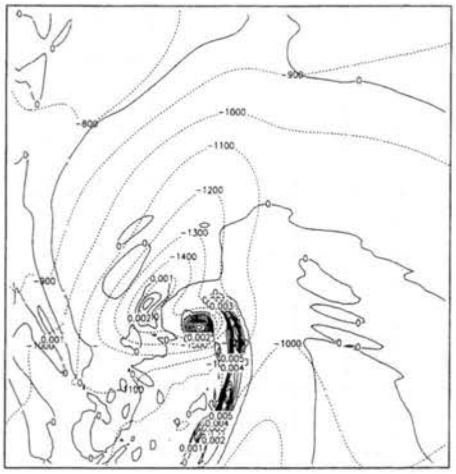

Figure 4.42: Contributions to the Laplacian equation (2.25) due to vertical shear terms, in regions where they are positive, at 3600 s and 1263 m above surface. Contour increment is 1×10^{-3} s^{-2}. Dashed contours show perturbation pressure with an increment of 100 Pa (1 mb).

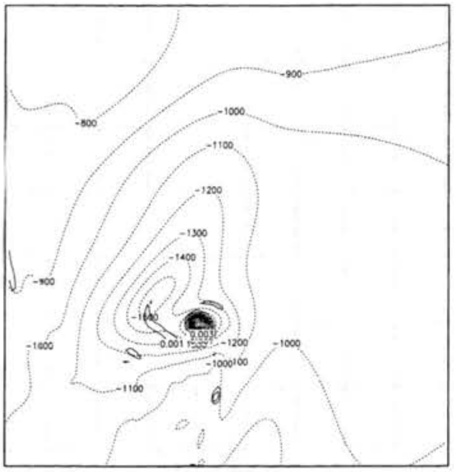

Figure 4.43: Same as Figure 4.42, but showing the vorticity contribution to the Laplacian.

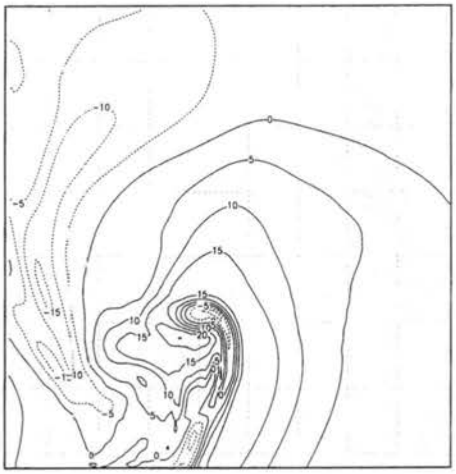

Figure 4.44: Same as Figure 4.42, but showing vertical velocity, with increment of 5 m s^{-1}.

Figure 4.45: Same as Figure 4.44, but at 3420 s.

By 3900 s, the vorticity has peaked, although it still remains large. Large fluctuations occur in the vorticity values near the surface, while at 1263 m the vorticity has begun a noticeable decay (see Figure 4.3). At the surface, the vorticity now has a ring structure pendant on a strip of vorticity that is an extension of the forward-flank gust front (Figure 4.46). Possibly with higher resolution this process would reveal the intensification of secondary vortices on the tornadic scale around the ring of vorticity, as has been observed in nature (Wakimoto and Liu 1998) and in modeling studies (Finley 1997).

4.7 Summary

In this chapter the evolution of a low-level mesocyclone, at both 333 m and 111 m grid spacing, is described. Near 3200 s the vertical vorticity beneath the cloud becomes nearly vertically co-located at a point along the FFD near its junction with the RFD. This feature forms in response to baroclinic processes along the FFD. Soon afterwards, the vorticity rapidly intensifies and forms a closed circulation with a depressed central pressure, beginning near the surface. An occlusion downdraft becomes apparent at approximately the same time. This intensification is not an artifact of grid nesting (although on grids with finer resolution the maximum vorticity is greater), and also appears to be distinct from the formation of the baroclinic low-level mesocyclone. The latter is first apparent near cloud base whereas the former occurs first near the surface, and results in the formation of a pressure minimum distinct from the pressure minimum associated with a 'divided mesocyclone'. The cause of the rapid vorticity surge appears to be convergence from the pressure maximum associated with the cold pool; possibly the rotation of the vortex sheet along the gust front facilitates its convergence by the ambient wind field. These ideas will be assessed in a more quantitative fashion in the next chapter.

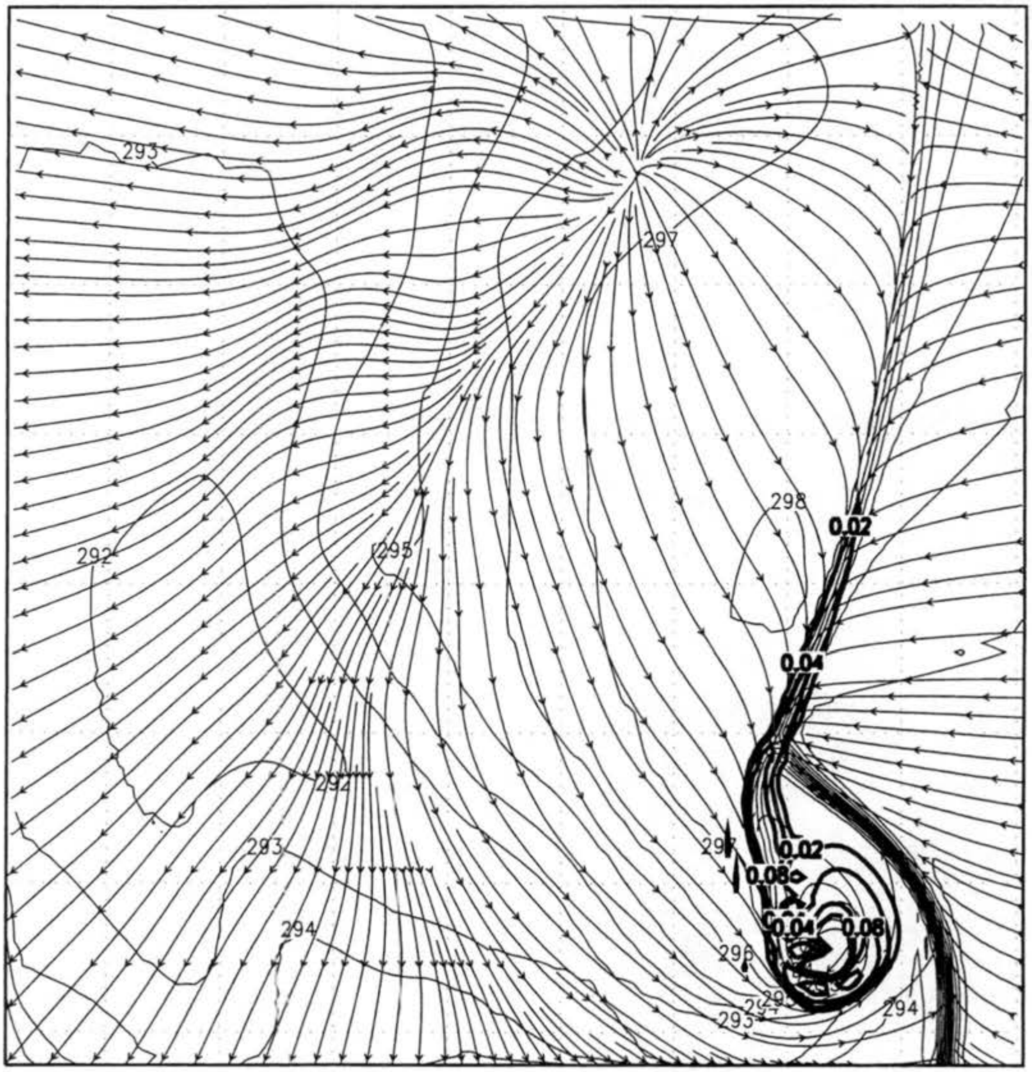

Figure 4.46: Same as Figure 4.17, but at 3900 s. Contour levels for vertical vorticity double every increment beginning with 2×10^{-2} s^{-1}.

Chapter 5

ANALYSIS – FOURIER MODES

In this section a Fourier mode analysis will be performed on the circulation of the intensifying vortex. The purpose of the analysis will be to determine the geometry of the intensification process, with an ultimate goal of quantifying the similarities between the current model simulation and other simulations of vortex dynamics in the literature.

5.1 Circular Eulerian curves

Suppose we compute the circulation around a circular horizontal Eulerian curve. It is then convenient to use cylindrical coordinates, (r, Θ, z), to express the circulation as:

$$\mathcal{C} = \oint\limits_{C} \mathbf{v} \cdot \mathbf{dl} = r \int_0^{2\pi} v_\Theta d\Theta, \tag{5.1}$$

and the circulation tendency equation as:

$$\frac{\partial \mathcal{C}}{\partial t} = \oint\limits_{C} \left[\zeta_z \mathbf{v_H} \times \hat{\mathbf{k}} - w \frac{\partial \mathbf{v_H}}{\partial z} + \mathbf{F} \right] \cdot \mathbf{dl} = r \int_0^{2\pi} \left[\overbrace{-v_r \zeta_z}^{(1)} - \overbrace{w \frac{\partial v_\Theta}{\partial z}}^{(2)} + \overbrace{F_\Theta}^{(3)} \right] d\Theta, \tag{5.2}$$

where r is the radius of the contour.

Consider the horizontal advection/convergence term (1) for now. It can be thought of as $2\pi r$ times the azimuthal average of the product of $-v_r$ and ζ_z around a circle. The value of both of these quantities around a circle when sufficiently well-behaved can be decomposed into a Fourier series of modes such as:

$$v_r = v_{r0} + v_{r1s}\sin\Theta + v_{r1c}\cos\Theta + v_{r2s}\sin 2\Theta + v_{r2c}\cos 2\Theta + ...$$

$$\zeta_z = \zeta_{z0} + \zeta_{zr1s}\sin\Theta + \zeta_{zr1c}\cos\Theta + \zeta_{zr2s}\sin 2\Theta + \zeta_{zr2c}\cos 2\Theta + ... \qquad (5.3)$$

Because the sine and cosine functions of the series are orthogonal over the interval $[0, 2\pi]$, the $v_{r...}$ and $\zeta_{z...}$ constants can be found using:

$$v_{r0} = \frac{\int_0^{2\pi} v_r d\Theta}{\int_0^{2\pi} d\Theta}, \qquad v_{r1s} = \frac{\int_0^{2\pi} v_r \sin\Theta d\Theta}{\int_0^{2\pi} \sin^2\Theta d\Theta}, \qquad v_{r2s} = \frac{\int_0^{2\pi} v_r \sin 2\Theta d\Theta}{\int_0^{2\pi} \sin^2 2\Theta d\Theta}, ...$$

$$\zeta_{z0} = \frac{\int_0^{2\pi} \zeta_z d\Theta}{\int_0^{2\pi} d\Theta}, \qquad \zeta_{z1s} = \frac{\int_0^{2\pi} \zeta_z \sin\Theta d\Theta}{\int_0^{2\pi} \sin^2\Theta d\Theta}, \qquad \zeta_{z2s} = \frac{\int_0^{2\pi} \zeta_z \sin 2\Theta d\Theta}{\int_0^{2\pi} \sin^2 2\Theta d\Theta}, ... \qquad (5.4)$$

The integrals of the squares of all the trigonometric functions above are π over the given interval.

When one substitutes the Fourier representations of (5.3) into (5.2), only the products of the same trigonometric functions survive the integral. Thus one has:

$$-r\int_0^{2\pi} v_r\zeta_z d\Theta = -r\left[2\pi v_{r0}\zeta_{z0} + \pi v_{r1s}\zeta_{z1s} + \pi v_{r1c}\zeta_{z1c} + \pi v_{r2s}\zeta_{z2s} + \pi v_{r2c}\zeta_{z2c} + ...\right]. \qquad (5.5)$$

What do the terms in (5.5) represent? Suppose that there is constant convergence and vertical vorticity within the circular contour, and that the convergence term is the only contribution to changing the vertical vorticity within the contour. The change in circulation about the contour would be:

$$\frac{\partial\mathcal{C}}{\partial t} = -r\zeta_z\int_0^{2\pi} v_r d\Theta = -r\zeta_{z0}(2\pi)v_{r0}, \qquad (5.6)$$

since $\zeta_z = \zeta_{z0}$ when it is constant. Thus the first term in (5.5) can be considered to be large-scale convergence over the curve.

Now consider the case of pure horizontal advection of vorticity, where there is a constant horizontal wind velocity and vorticity gradient. This will be the case if the wind vector is (u_0, v_0) and the vertical vorticity is given by $c_{x0}x + c_{y0}y$, which produces a constant gradient vector of (c_{x0}, c_{y0}). The radial component of any constant vector (a, b) at an angle Θ around a circle is given by $a\cos\Theta + b\sin\Theta$; thus, the radial component of the velocity is $u_0\cos\Theta + v_0\sin\Theta$. The vertical vorticity is $c_{x0}(r\cos\Theta) + c_{y0}(r\sin\Theta)$. Since the trigonometric functions are the only parameters that are a function of position around the circle, we can immediately write the Fourier decompositions $v_r = v_{r1c}\cos\Theta + v_{r1s}\sin\Theta$ and $\zeta_z = \zeta_{z1c}\cos\Theta + \zeta_{z1s}\sin\Theta$. The circulation tendency is then:

$$\frac{\partial \mathcal{C}}{\partial t} = -r\int_0^{2\pi} v_r\zeta_z d\Theta = -r\int_0^{2\pi} \left(v_{r1c}\cos\Theta + v_{r1s}\sin\Theta\right)\left(\zeta_{z1c}\cos\Theta + \zeta_{z1s}\sin\Theta\right)d\Theta. \tag{5.7}$$

Again, the products of sine and cosine terms vanishes upon integration, leaving

$$\frac{\partial \mathcal{C}}{\partial t} = -r\left(v_{r1c}\zeta_{z1c}\pi + v_{r1s}\zeta_{z1s}\pi\right). \tag{5.8}$$

The first-order cosine and sine terms in (5.5) are revealed to be the large-scale x-direction and y-direction advection of vertical vorticity, respectively.

The higher-order terms have no such simple interpretation as large-scale versions of terms in the vorticity equation. They can be considered to be 'eddy' contributions to the circulation tendency, and are positive when there is a positive correlation between $-v_r$ and ζ_z of a particular mode. An example of the second cosine mode consists of positive vorticity with radial inflow along the y-axis, and negative vorticity with radial outflow along the x-axis.

A similar decomposition can be performed on the vertical advection/ tilting term (2) in (5.2), with w replacing ζ_z and $\partial v_\Theta / \partial z$ replacing v_r. We then have:

$$-r \int_0^{2\pi} w \frac{\partial v_\Theta}{\partial z} d\Theta = -r \left[2\pi w_0 {\frac{\partial v_\Theta}{\partial z}}_0 + \pi w_{1s} {\frac{\partial v_\Theta}{\partial z}}_{1s} + \pi w_{1c} {\frac{\partial v_\Theta}{\partial z}}_{1c} + \pi w_{2s} {\frac{\partial v_\Theta}{\partial z}}_{2s} \right.$$

$$\left. + \pi w_{2c} {\frac{\partial v_\Theta}{\partial z}}_{2c} + \ldots \right]. \tag{5.9}$$

In this instance the zeroth-order term represents large-scale vertical advection, and the first-order cosine and sine terms represent the tilting of x-vorticity and y-vorticity into the vertical, respectively. The higher-order terms are eddy correlations of w and $\partial v_\Theta / \partial z$ around the circle. The second order terms are invoked by Rothfusz and Lilly (1989) to explain the formation of a laboratory vortex by convergence superimposed onto an environment with horizontal streamwise vorticity.

Other interpretations can be given to the zeroth-order terms. The zeroth-order term for (1) is:

$$-2\pi r v_{r0} \left(\frac{\int_0^{2\pi} \zeta_z d\Theta}{2\pi} \right) = -r v_{r0} \int_0^{2\pi} \left[\frac{1}{r} \frac{\partial}{\partial r}(r v_\Theta) - \frac{\partial v_r}{r \partial \Theta} \right] d\Theta = -v_{r0} \frac{\partial}{\partial r} \int_0^{2\pi} r v_\Theta d\Theta$$

$$= -v_{r0} \frac{\partial \mathcal{C}}{\partial r} \tag{5.10}$$

if the velocity field is continuous. In a region of net radial inflow, a positive large-scale convergence term implies that the circulation increases with radius. Meanwhile the zeroth-order term for (2) is simply:

$$-2\pi w_0 r {\frac{\partial v_\Theta}{\partial z}}_0 = -2\pi w_0 r \left(\frac{\int_0^{2\pi} \frac{\partial v_\Theta}{\partial z} d\Theta}{2\pi} \right) = -w_0 \frac{\partial \mathcal{C}}{\partial z}, \tag{5.11}$$

and so is simply the advection of circulation by the azimuthally- averaged vertical velocity.

Furthermore, from Galilean invariance we know that we can subtract an arbitrary constant vector (a, b) from the velocity field without changing the physics of the problem[1]. Thus, we may choose to subtract any $a \cos\Theta + b \sin\Theta$ from the radial velocity around the circular contour where a and b are independent of position along the contour. The result will then correctly describe the change in circulation around a contour of the given shape translating at a velocity (a, b) in the original reference frame. So if in particular we choose $a = v_{r1c}$ and $b = v_{r1s}$, then the v_r equation in (5.3) is unaltered except for the loss of the first-order terms, which causes the large-scale horizontal advection in (5.5) to vanish.

In summary, then, it is fair to consider the first order terms in (1) as representing an advection of circulation; they vanish in a reference frame moving at velocity (v_{r1c}, v_{r1s}), and one of the other terms in the circulation equation must be invoked to explain the creation of circulation where none existed before. Nevertheless, because the contour is not a material contour, there is no assurance that the velocity (v_{r1c}, v_{r1c}) will have a simple relationship to the velocity of any particular air parcel or storm feature (in particular any vortex). So it is still important to consider this term in the circulation budget.

5.2 Fourier Components – Uniform Two-Dimensional Strain

Consider now the uniform two-dimensional straining flow problem in section 1.12...., where there is maximum convergence into the y-axis, and either divergence or convergence into the x-axis. Vorticity is neglected in the large-scale flow. The velocity is given by $\mathbf{v} = -\alpha x \hat{\mathbf{x}} - \beta y \hat{\mathbf{y}}$. The radial velocity in this case is

$$v_r = u\cos\Theta + v\sin\Theta = -\alpha r\cos^2\Theta - \beta r\sin^2\Theta = -\left[\frac{\alpha r}{2} + \frac{\beta r}{2}\right] - \left[\frac{\alpha r}{2} - \frac{\beta r}{2}\right]\cos 2\Theta. \tag{5.12}$$

---

[1] An exception is surface drag, which as is normally treated is a function of the magnitude of the velocity specifically with respect to the ground.

For the case of uniform plane convergence, $\beta = 0$, and the radial velocity field consists of two equal, negative components, the zeroth-order and second order cosine. When the convergence is uniaxial, $\beta > 0$, and the zeroth-order component will be greater than the second-order cosine. For biaxial convergence, $\beta < 0$, and the second-order cosine term will be the greater.

A graphical depiction of the superposition of the zeroth-order and second-order cosine azimuthal modes of equal negative magnitude is shown in Figure 5.1. If this is taken as a representation of the radial velocity, it can be seen that the maximum radial velocity is inward and along the x-axis. The radial velocity then decays to zero along the y-axis but is nowhere positive.

The superposition of a positive unit zeroth-order mode and a negative unit second-order cosine mode is shown in Figure 5.2. In this case there is a positive concentration along the y-axis and values near zero in the vicinity of the x-axis. This can be a crude representation of the vortex band of section 2.12, which shows no variation in the y-direction and resides near the axis. It can be shown that the limit of an infinitesimally narrow band along the y-axis is achieved using the Fourier series:

$$f(\Theta) = C(1 - \cos 2\Theta + \cos 4\Theta - \cos 6\Theta + \cos 8\Theta - \cos 10\Theta ...) \tag{5.13}$$

after proper normalization.

What happens to the circulation tendency when the radial velocity field of (5.12) is combined with the vorticity field of (5.13)? From (5.5), we see that only the zeroth-order and second-order cosine terms are non-zero. In fact, when $\beta = 0$, the products $-v_{r0}\zeta_{z0}$ and $-v_{r2c}\zeta_{z2c}$ are equal in magnitude but opposite in sign. The large-scale convergence term is positive because both the average radial inflow and average positive vorticity around a circular contour. But the second-order term is negative because the radial inflow and

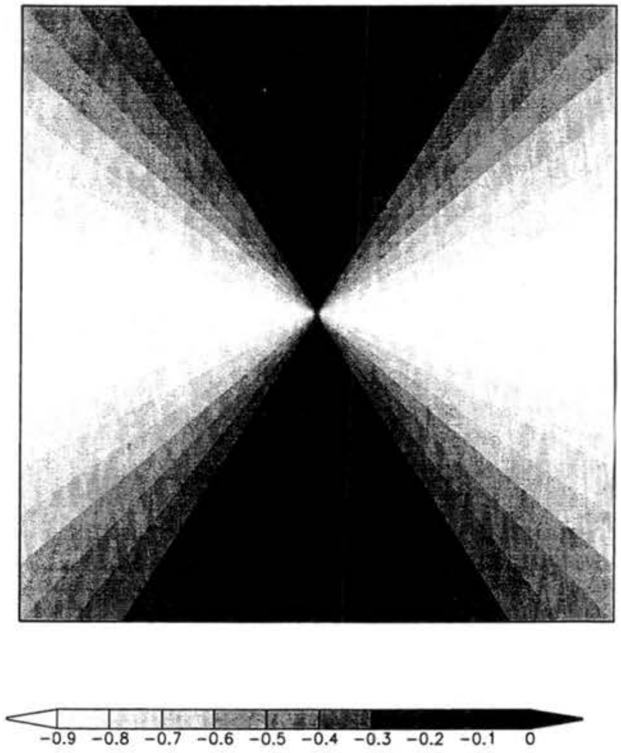

Figure 5.1: Depiction of the superposition of the zeroth-order and second-order cosine azimuthal modes of equal negative magnitude. Total magnitude is normalized to negative unity.

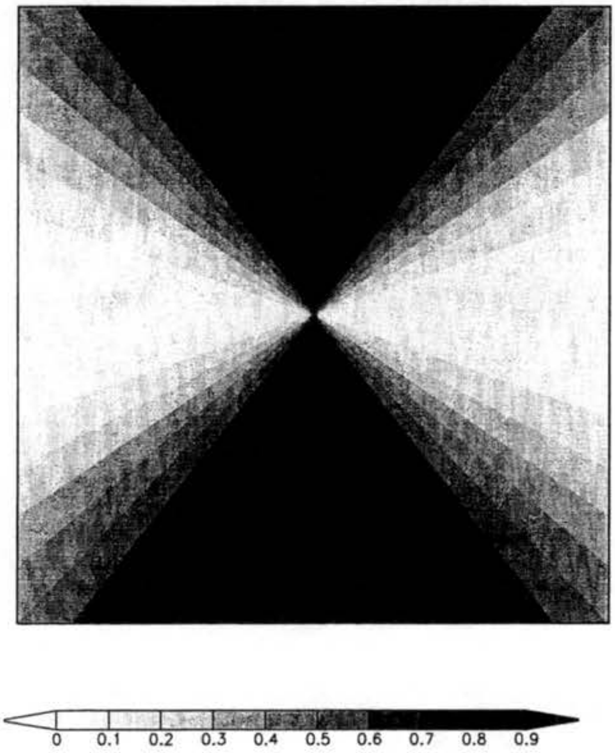

Figure 5.2: Depiction of the superposition of the zeroth-order and second-order cosine azimuthal modes of equal magnitude but opposite signs. Total magnitude is normalized to unity.

positive vorticity peak in opposite quadrants. The large-scale convergence term in (5.5) has an extra factor of two: thus in our idealized framework the net circulation tendency is positive. Physically, this is due to the fact that away from the axes the quantity $-v_r\zeta_z$ is positive definite. The circulation will continue to increase unless other factors such as vertical motion or (in the Burgers vortex sheet) diffusion contribute negative circulation tendencies.

Now, consider the uniform strain case where the axis of maximum radial convergence is not along the x-axis, but is rotated an angle Θ_0 from it. If α and β are defined as the derivatives of the velocity components parallel to and perpendicular to the $\Theta = \Theta_0$ line, respectively, then the expression for v_r becomes:

$$v_r = -\left[\frac{\alpha r}{2} + \frac{\beta r}{2}\right] - \left[\frac{\alpha r}{2} - \frac{\beta r}{2}\right] \cos 2(\Theta - \Theta_0)$$

$$= -\left[\frac{\alpha r}{2} + \frac{\beta r}{2}\right] - \left[\frac{\alpha r}{2} - \frac{\beta r}{2}\right] (\cos 2\Theta \cos 2\Theta_0 - \sin 2\Theta \sin 2\Theta_0). \tag{5.14}$$

So the presence of the second-order sine term simply represents a rotation of the Figure 5.1 pattern; under this rotation the value of $v_{r2s}^2 + v_{r2c}^2$ remains constant at $r^2(\alpha - \beta)^2/4$. However, the specific decrease in v_{r2c} caused by rotation of the wind field would decrease the magnitude of the negative second-order term in (5.5) for our idealized framework; thus the circulation tendency would be enhanced. Similarly, the vorticity band can be rotated while the wind field is held fixed and would increase the vorticity tendency. This latter scenario is a mathematical argument consistent with the scenario described in Neu (1984a); when a Burgers vortex sheet segment is rotated from the y- axis, there is a better correlation between the radial inflow and the vorticity, which then acts to concentrate the vorticity into intense vortices.

5.3 Fourier Components – Baseline Simulation

The various contributions to the horizontal convergence tendency to the circulation were found for the control simulation. A circular contour of radius 666 m was used for the calculations. Velocity values were interpolated to $4n$ points equally spaced on the circular contour, where $n\Delta x$ is the radius of the contour.

Results are shown in Table 5.1 for the two-grid simulation at 3300 s, 3360 s, and 3420 s at the lowest model level. These times represent, respectively, the fine-grid initialization, the peak of the intensification process, and the establishment of a low-level concentrated pseudo-circular vortex. The contours are centered about the location of the maximum circulation found within the domain.

As mentioned previously, the first-order terms can be thought of as representing the net advection of the circulation with respect to the model grid, and vanish when a velocity of (v_{r1c}, v_{r1s}) is subtracted out. The values of v_{r1c} and v_{r1s} in the table document the general southeastward movement of the circulation with respect to the grid. They compare well to the average speed of the vortex in Figure 4.7 of $u = 11.4\text{m s}^{-1}$ and $v = -6.9\text{m s}^{-1}$. If (v_{r1c}, v_{r1s}) were to coincide with the instantaneous velocity of the vortex, then the circulation of the material curve could be said to translate with the vortex.

Examining the other terms reveals that the dominant ones are the zeroth-order term, which is positive, and the second-order cosine term, which is negative. Next in importance is the second-order sine term. It is seen that, at the initialization time, the zeroth-order and second-order cosine modes of the radial velocity are nearly equal; the zeroth-order and second-order cosine modes of the vorticity are nearly equal but opposite in magnitude. From the discussion in the previous section, it appears that we are looking at a close representation of a vortex sheet in uniform two-dimensional strain. The value of the v_{r2s}

3300s	3360s	3420s	
-8.40	-8.22	-8.43	v_{r0}
0.0112	0.0115	0.0055	ζ_{z0}
394	396	194	$-2\pi r v_{r0}\zeta_{z0}$
11.7	14.7	10.7	v_{r1c}
-0.0017	0.0060	0.0055	ζ_{z1c}
42	-185	-123	$-\pi r v_{r1c}\zeta_{z1c}$
-10.4	-12.9	-6.88	v_{r1s}
-0.0006	0.0007	0.0050	ζ_{z1s}
-13	19	72	$-\pi r v_{r1s}\zeta_{z1s}$
-7.26	-7.58	-7.52	v_{r2c}
-0.0161	-0.0069	-0.0100	ζ_{z2c}
-244	-110	-157	$-\pi r v_{r2c}\zeta_{z2c}$
3.49	2.03	-0.0357	v_{r2s}
-0.0082	-0.0140	-0.0219	ζ_{z2s}
60	60	-2	$-\pi r v_{r2s}\zeta_{z2s}$
0.162	-3.39	-0.919	v_{r3c}
0.0070	-0.0006	0.0109	ζ_{z3c}
-2	-4	21	$-\pi r v_{r3c}\zeta_{z3c}$
-0.774	-0.250	-1.76	v_{r3s}
0.0049	-0.0088	0.0033	ζ_{z3s}
8	-5	12	$-\pi r v_{r3s}\zeta_{z3s}$
0.945	-2.50	0.325	v_{r4c}
0.0008	-0.0088	-0.0159	ζ_{z4c}
-2	-46	11	$-\pi r v_{r4c}\zeta_{z4c}$
-0.232	0.727	1.98	v_{r4s}
0.0017	-0.0156	0.0006	ζ_{z4s}
1	24	-2	$-\pi r v_{r4s}\zeta_{z4s}$

Table 5.1: Fourier components of radial velocity, vertical vorticity, and contributions to the circulation tendency for an Eulerian circle of radius 666 m on Grid 2. Only components to fourth order are shown. Values are shown at 60 minute increments.

term suggests that the axis of maximum radial convergence is rotated from the x-axis by $0.5\arctan(-v_{r2s}/-v_{r2c}) = -12.8°$. The value of $(v_{r2c}^2 + v_{r2s}^2)^{0.5}$ of 8.05 is slightly less than the magnitude of v_{r0}; from (5.12) we see that this implies that we nearly have plane convergence, but the flow is slightly uniaxial, as had been noted in the previous chapter. The vorticity modes reflect a concentration along the y-axis. For the vorticity the negative second-order cosine mode is actually larger in magnitude than the zeroth-order mode; this suggests that there is actually some negative vorticity along the circulation contour (not counting the contributions from the higher order terms). The vorticity band is rotated from the x-axis by an angle of $0.5\arctan(\zeta_{z2s}/\zeta_{z2c}) = -76.5°$, which is a rotation of $13.5°$ from the y-axis. But higher order vorticity modes are non-negligible, suggesting that the vorticity structure is significantly more complicated than our idealized model.

At 3360 s, the total circulation tendency from the modes listed in the table has increased by 50%. In large part this is due to the change in the second-order cosine contribution from -240 m^2 s^{-2} to -110 m^2 s^{-2}. The zeroth-order terms have hardly changed. The most important difference is in the second-order vorticity terms, which have shifted from $\zeta_{z2c} = -0.0161\ \mathrm{s}^{-1}, \zeta_{z2s} = -0.0082\ \mathrm{s}^{-1}$ to $\zeta_{z2c} = -0.0069\ \mathrm{s}^{-1}, \zeta_{z2s} = -0.0140\ \mathrm{s}^{-1}$. The vorticity band now lies at an angle of $0.5\arctan(\zeta_{z2s}/\zeta_{z2c}) = -58.1°$ with respect to the x-axis, or $31.9°$ with respect to the y-axis. The magnitude of the second-order vorticity mode has also decreased from $0.0181\ \mathrm{s}^{-1}$ to $0.0156\ \mathrm{s}^{-1}$; nonetheless even if the magnitude of this mode had not changed, the rotation of the mode would still change ζ_{z2c} to $-0.0080\ \mathrm{s}^{-1}$ by 3360 s, a factor of two decrease. Thus the increase in circulation tendency is chiefly attributable to the rotation of the band of vorticity away from the y-axis to a position more favorable for radial convergence. The increase in circulation tendency could be even larger, but the radial inflow band also has rotated slightly counterclockwise, so that it is now inclined $0.5\arctan(-v_{r2s}/-v_{r2c}) = -7.7°$ from the x-axis.

Figure 5.3 presents a more continuous picture of the evolution of the angular separation between the vorticity band and the axis of maximum radial inflow. Whereas the two are largely perpendicular at the start, the angle decreases throughout the period of vortex strengthening, largely due to changes in the vorticity orientation. The vorticity band appears to rotate counterclockwise at an increasing rate, which bears little relation to the axis radial inflow after the time of greatest vortex intensification, near 3430 s. From Figure 5.4, it can be seen that at the end of the intensification period the magnitude of the second-order modes for both radial velocity and vertical vorticity decrease sharply. We can conclude that near the end of the vortex spinup process, the region loses its band-like geometry, and becomes more axisymmetric.

Table 5.2 shows data for the vertical contribution to the circulation tendency. Most significantly, it shows that these terms are much smaller in magnitude than the dominant terms in the horizontal contribution at the location of the maximum circulation. Thus we can concentrate on the radial flux of vertical vorticity in explaining the development of large values of circulation. However, the ultimate source of the vertical vorticity must be due to the vertical contribution terms acting elsewhere in the domain. Near the vortex, the largest terms in this table are actually negative contributions to the circulation: the large-scale vertical advection and tilting of y-direction vorticity. The largest single negative contribution is from the vertical advection of vertical vorticity after the vortex has already intensified. This is a strong indication that the vortex is not being transported to the surface in a downdraft but forms at the surface and is advected upwards. The higher order terms are not significant.

Figure 5.5 shows the magnitude of the large scale tilting terms on Grid 2 at 3300 s. Significant values are found to the north of the circulation center along the θ_e gradient, and in a narrow strip to the east of the vorticity center. The first order sine terms (large

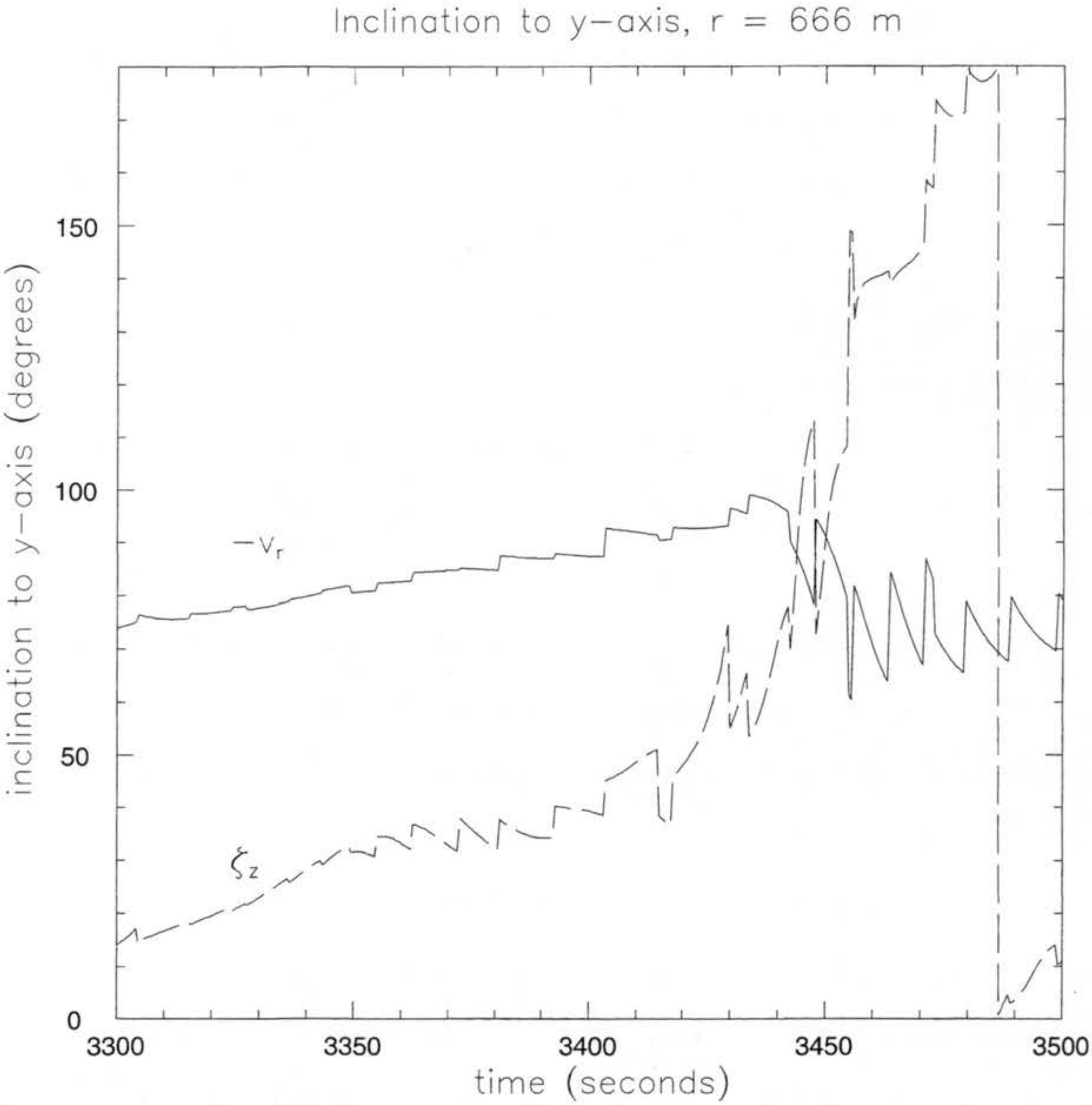

Figure 5.3: Orientation angle of second-order for inward radial velocity, $-v_r$, and vertical vorticity, ζ_z, with respect to the positive y-axis. Results are for a circular contour with 666 m radius centered at the location of maximum vertical vorticity on Grid 2.

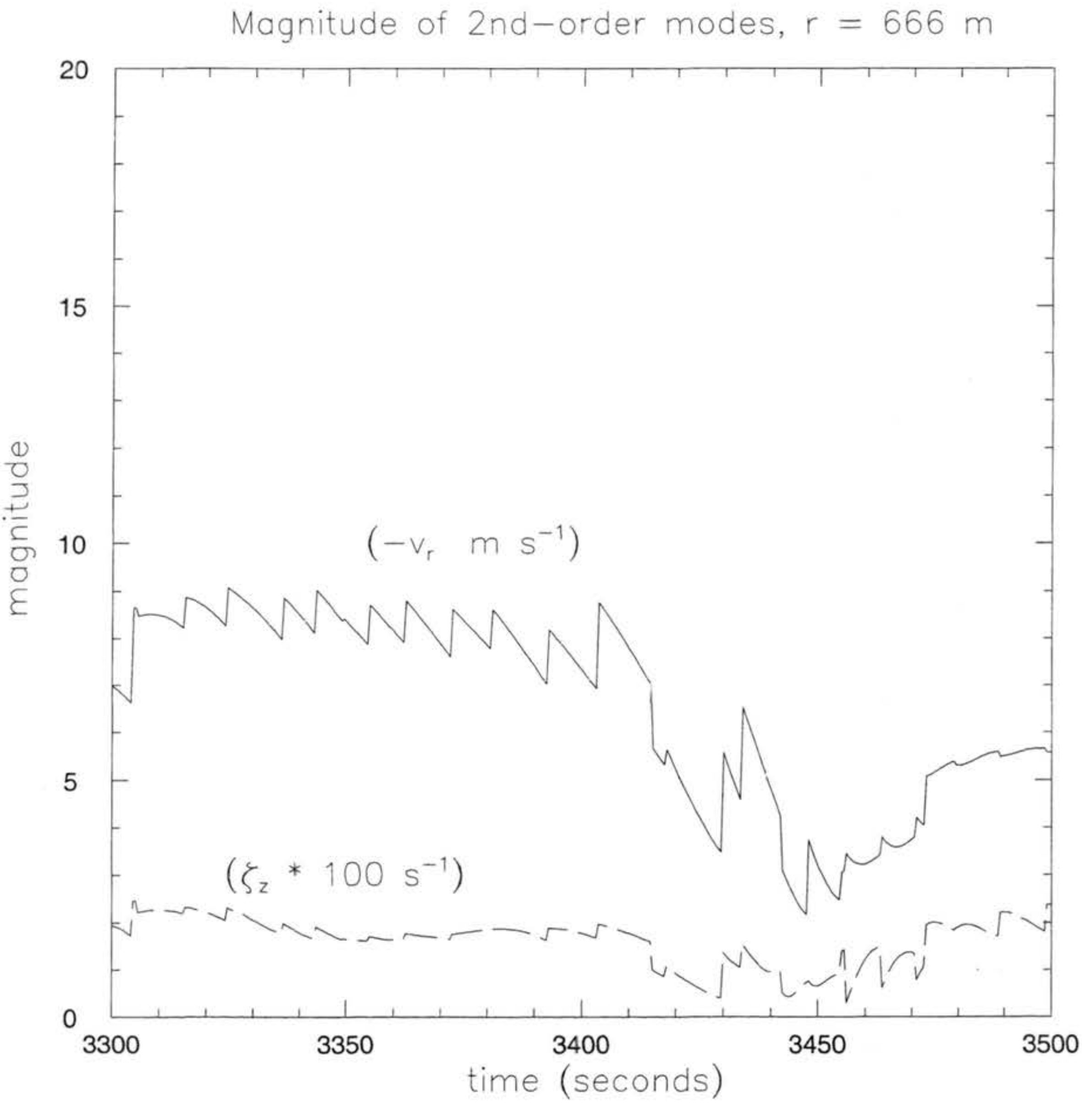

Figure 5.4: Same as Figure 5.3, but depicting the magnitudes of the total second-order modes.

3300s	3360s	3420s	
0.79	0.73	0.81	w_0
0.0002	0.0109	0.0089	$\partial v_\Theta/\partial z_0$
-0.7	-33	-30	$-2\pi r w_0 \partial v_\Theta/\partial z_0$
0.14	0.21	-0.12	w_{1c}
-0.0054	-0.0173	-0.0244	$\partial v_\Theta/\partial z_{1c}$
2	8	-6	$-\pi r w_{1c} \partial v_\Theta/\partial z_{1c}$
0.17	0.45	0.42	w_{1s}
0.0370	0.0251	0.0119	$\partial v_\Theta/\partial z_{1s}$
-13	-24	-10	$-\pi r w_{1s} \partial v_\Theta/\partial z_{1s}$
-0.30	-0.04	0.03	w_{2c}
0.0095	-0.0044	0.0176	$\partial v_\Theta/\partial z_{2c}$
6	-0.4	-1	$-\pi r v_{2c} \partial v_\Theta/\partial z_{2c}$
-0.31	-0.33	-0.48	w_{2s}
-0.0123	-0.0063	0.0061	$\partial v_\Theta/\partial z_{2s}$
-8	-4	6	$-\pi r v_{2s} \partial v_\Theta/\partial z_{2s}$

Table 5.2: Same as Table 5.1, but for the Fourier components of vertical velocity and tangential wind vertical shear. Only components to second order are shown.

scale tilting of y-directed vorticity) are responsible to the positive circulation tendency to the north (Figure 5.6). This term, in turn, is large because $\partial v_\Theta/\partial z|_{1s}$ is large (Figure 5.7), which is an indicator of strong vertical wind shear directed from east to west. This is consistent with the baroclinic generation of horizontal vorticity along the gust front. This vertical wind shear extends to the circulation center, and the tilting is positive as long as the vertical velocity derivative is southward (Figure 5.8).

5.4 Nondivergent Vortex Patch Rotation

Given that the rotation of the vorticity band with respect to the radial convergence is significant towards increasing the circulation, we next should investigate the causes of the rotation. Two possibilities present themselves:

- the rotation is due to the self-induced rotation of the vorticity patch and can be explained by the local vorticity field

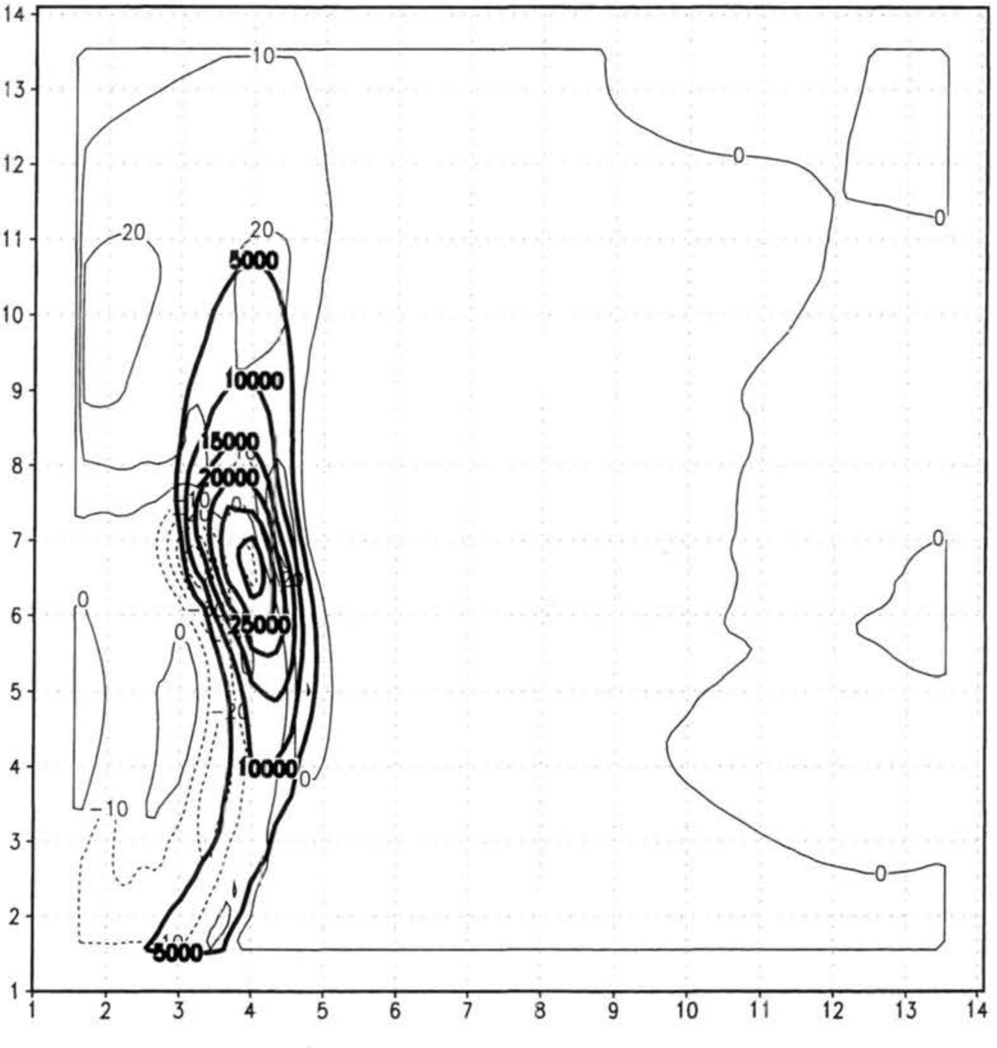

Figure 5.5: Magnitude of first-order vertical contributions to the circulation tendency (thin contours) for a 666 m radius contour, at 3300 s on Grid 2. Contours are in increments of 10 m^2 s^{-2}. Thick contours represent circulation and are in increments of 5000 m^2 s^{-1}. Axes give distance in kilometers for reference.

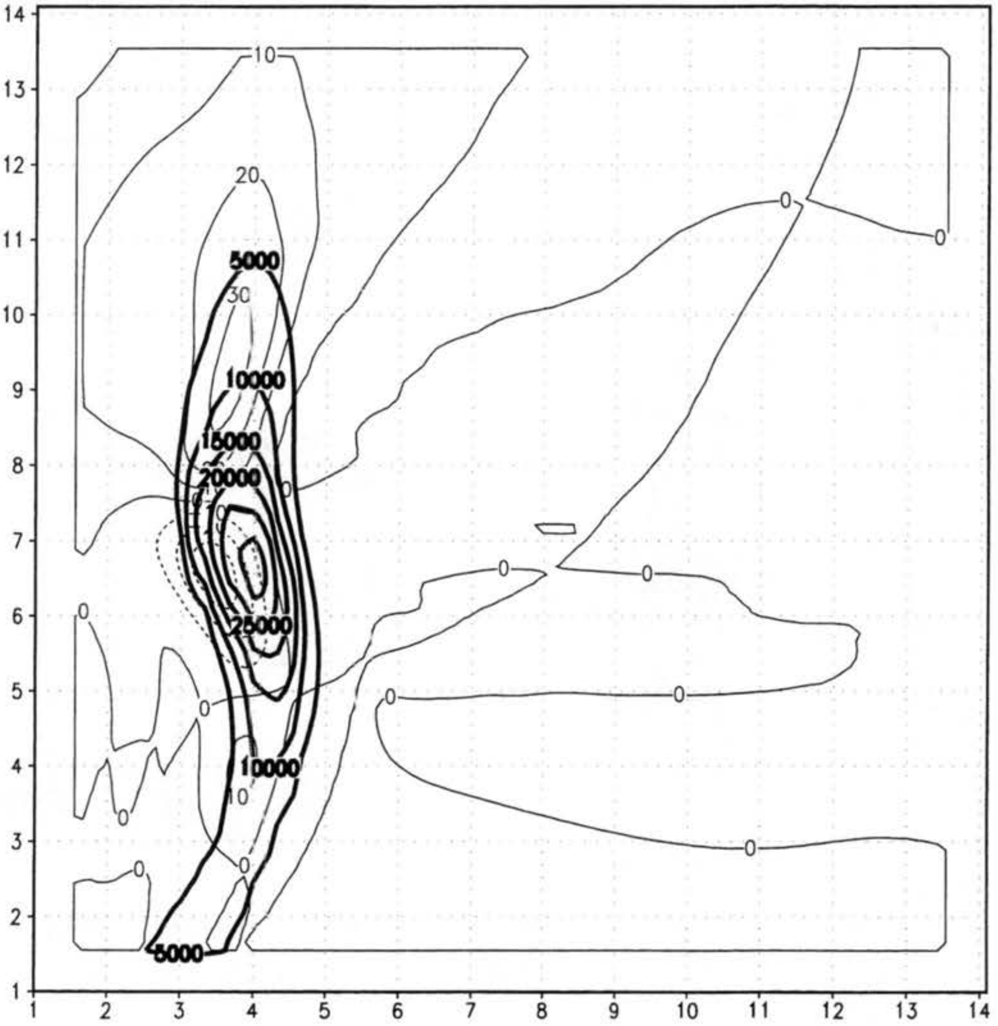

Figure 5.6: Same as Figure 5.5, but showing only the first-order sine contributions.

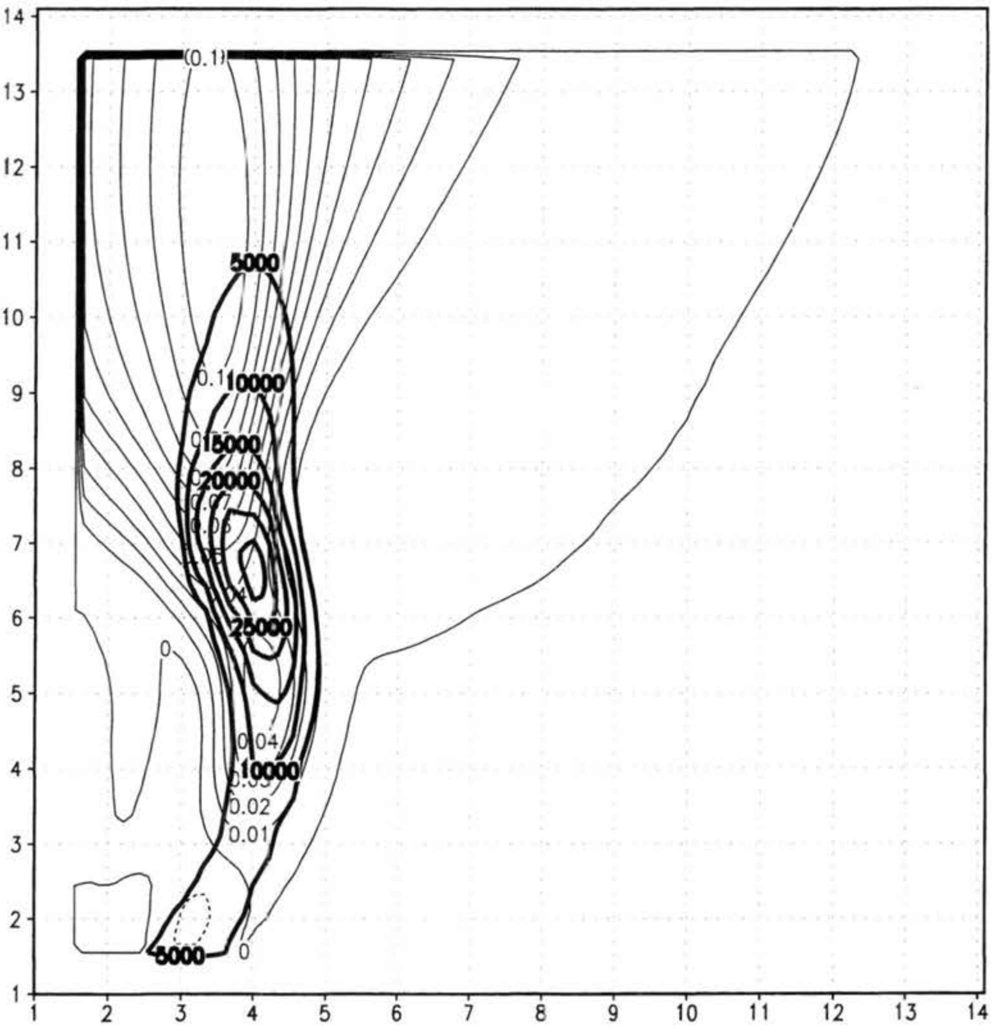

Figure 5.7: Same as Figure 5.5, but showing magnitude of first-order sine component of $\partial v_\Theta/\partial z$ (thin contours). Contours are in increments of 0.01 s^{-1}.

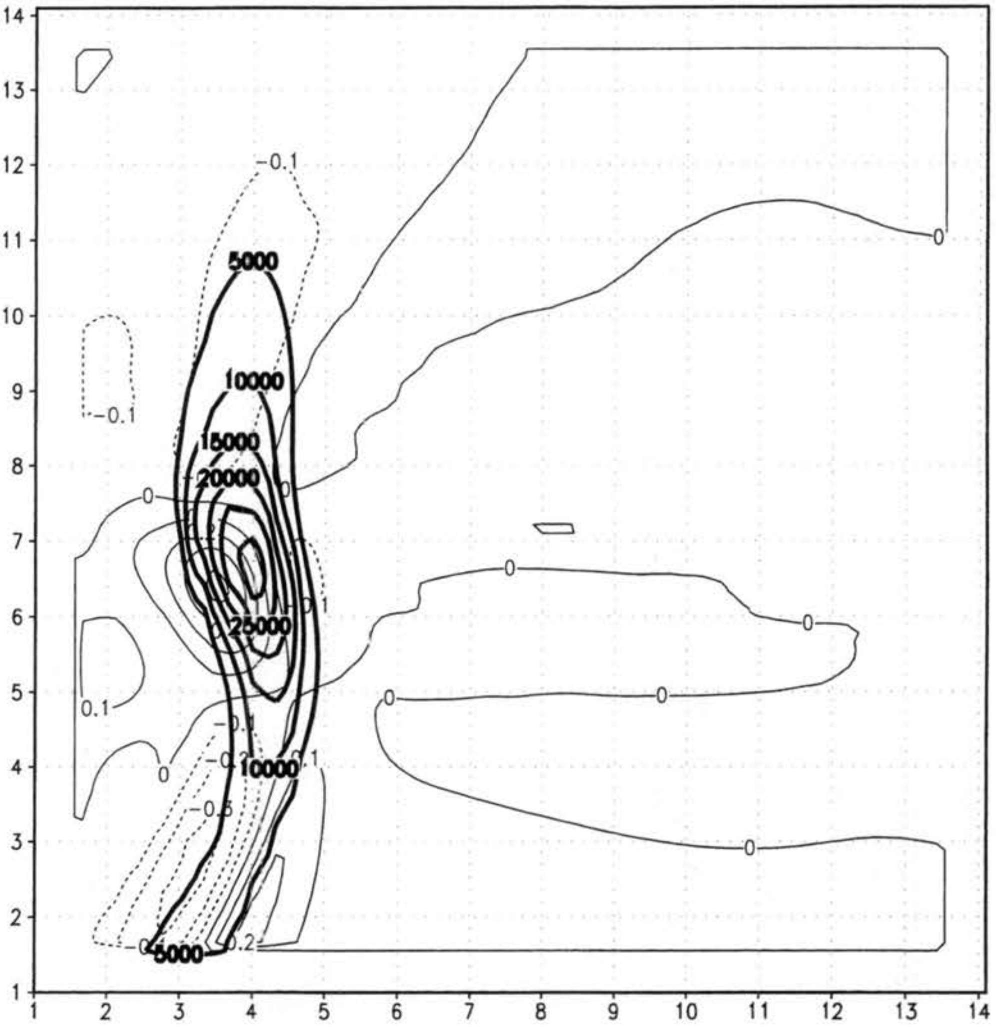

Figure 5.8: Same as Figure 5.5, but showing magnitude of first-order sine component of w (thin contours). Contours are in increments of 0.1 m s^{-1}.

- the rotation is not explainable locally, but is due to storm-scale processes.

The self-induced rotation of a patch of vorticity is due to the fact that parcels near the tip of the patch are induced to move about the axis of the patch by the vorticity of other parcels that are closer to the axis. Rotation does not occur for an infinitely long strip of vorticity because parcels extend along the strip in each direction and their induced rotation cancel at a particular point. For the finite patch however there is insufficient vorticity away from the axis to counteract the rotation, and the patch rotates as a whole.

It is well known that an ellipse possessing constant vorticity in its interior residing in a nondivergent, nonstraining fluid rotates with an angular velocity:

$$\frac{d\Theta}{dt} = \zeta \frac{\eta}{(1+\eta)^2}, \tag{5.15}$$

where η is the aspect ratio a/b of the ellipse, a and b being the semimajor and semiminor axes, respectively. This is the Kirchhoff vortex patch (Saffman 1992).

Thus one option is to approximate the low-level mesocyclone as an elliptical vorticity patch, compute the rotation rate, and compare it to the rotation rate in the simulation. One problem with this approach is that the mesocyclone is not simply a patch of constant vorticity with zero vorticity outside; the vorticity gradually decreases towards zero, particularly along the axis of the vorticity band, which is oriented nearly north-south. (This direction will henceforth be referred to as the along-band direction, as opposed to the across-band direction.)

This concern was addressed through the use of a two-dimensional barotropic pseudo-spectral vorticity model, described in Kossin and Schubert (2001). Because the model is incompressible and two-dimensional, vorticity is materially conserved in the model (neglecting diffusion). The processes of stretching and tilting cannot be represented in such a model, but the self-rotation of vorticity patches can be. The spectral model can thus be

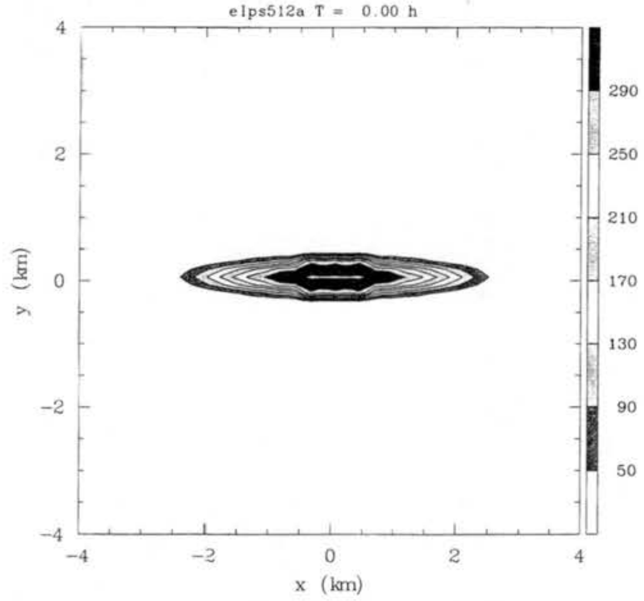

Figure 5.9: Vorticity at initialization of pseudo-spectral barotropic two-dimensional model. Shading is incremented every 4×10^{-3} s^{-1}.

initialized with an arbitrary vorticity patch, and the vorticity-induced movement in the absence of stretching can be compared to the movement in the fully three-dimensional RAMS model.

The pseudo-spectral model was initialized with conditions designed to represent the main vorticity distribution of the Grid 2 initialization in the baseline simulation. The vorticity distribution is shown in Figure 5.9; the central part consists of an ellipse with constant vorticity of 0.03 s^{-1} and dimensions 2100 m $\times$ 600 m. Beyond each semimajor axis, the vorticity decreases towards zero over a distance of 2000 m; similarly, the vorticity decreases towards zero in 100 m beyond each semiminor axis. A cubic spline is used to set the vorticity in these regions, which will be referred to as the vorticity tails.

The pseudo-spectral model possesses 512 degrees of freedom for each grid point. The boundary conditions are cyclic, but the domain was made large enough so that interactions

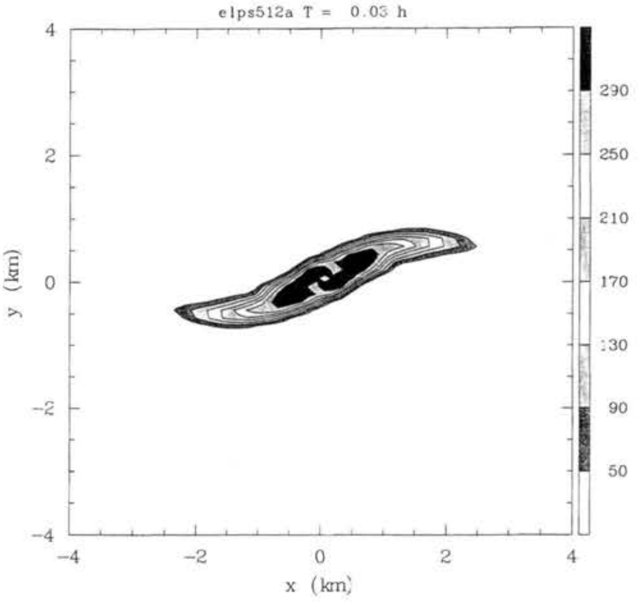

Figure 5.10: Same as Figure 5.9, but at 120 s.

with the boundary would be minimized. A slight negative vorticity exists in the far field region in order to keep the total domain circulation zero. For numerical stability purposes, numerical diffusion is used in the model, with a constant diffusion coefficient. For further details on the model the reader is referred to Kossin and Schubert (2001)

After 120 seconds of simulation time, the vorticity distribution can be seen in Figure 5.10. It is apparent that the central vorticity ellipse has rotated counterclockwise. The vorticity tails however are lagging the rotation of the ellipse. The ultimate fate of the tails is to become increasingly extended and thinned due to the rotation of the ellipse (Figure 5.11); eventually the tails break off while the central ellipse undergoes axisymmetrization (Melander et al. 1987).

Table 5.3 shows the orientation of the major axis of the central ellipse at various times in terms of the angular displacement from the x-axis. For the first 210 s of the model run,

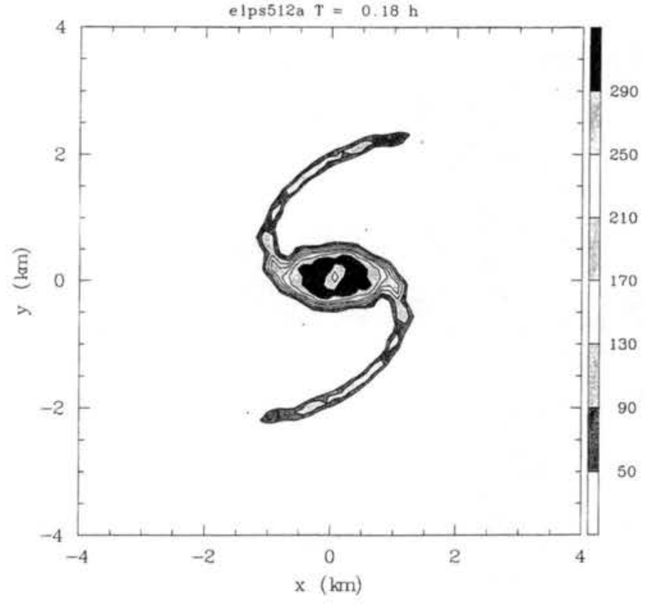

Figure 5.11: Same as Figure 5.9, but at 660 s.

the rotation rate is a relatively constant 12.9° per minute. We can compare this rate to that of a Kirchhoff's vortex patch with the dimensions of the central ellipse. Using (5.15), we obtain 17.8° per minute. Note from (5.15) that the greater the aspect ratio, the smaller the rotation rate. Furthermore, reducing the average vorticity decreases the rotation rate. So we might expect that an ellipse with 'tails' would rotate slower than one without tails. We also might expect that as the ellipse rotates ahead of its tails, this effect would be reduced, and the ellipse would increase its rotation rate. The table substantiates this expectation.

How do these values compare to the RAMS simulation? Recall that at 3300 s on Grid 2 we determined that the second-order mode of the vorticity distribution about a loop of radius 666 m was oriented at an angle of $-76.5°$ to the model x-axis. The same method gave the maximal radial convergence (i.e., the axis of contraction) at an angle of $-12.8°$. At 3360 s, the vorticity orientation is $-58.1°$, but the axis of contraction is now $-7.7°$. The

time (s)	angle to x-axis (degrees)
0	0
30	6
60	12
90	19
120	24
210	45
390	90

Table 5.3: Orientation of major axis of central vorticity ellipse in pseudo-spectral simulation over time.

vorticity band has rotated $18.4°$ degrees in an absolute sense, but $13.3°$ with respect to the axis of contraction. In this conceptual framework the rotation of the axis of contraction must be ascribed to storm-scale processes. However, the rotation of the vorticity band with respect to this axis seems well explained by its self-induced velocity.

5.5 Divergent Vortex Patch Rotation

Neu (1984b) considered the more general case of elliptical vorticity patches residing in any incompressible straining field of form $\mathbf{v} = \alpha x\hat{\mathbf{x}} + \beta y\hat{\mathbf{y}} - (\alpha + \beta)z\hat{\mathbf{z}}$. The equations for the time rate of change of the two axis dimensions and the angle between the major axis of the ellipse and the x-axis are:

$$\frac{da}{dt} = a(\alpha\cos^2\Theta + \beta\sin^2\Theta) \tag{5.16}$$

$$\frac{db}{dt} = b(\alpha\sin^2\Theta + \beta\cos^2\Theta) \tag{5.17}$$

$$\frac{d\Theta}{dt} = \zeta\frac{\eta}{(1+\eta)^2} - \frac{\alpha-\beta}{2}\frac{\eta^2+1}{\eta^2-1}\sin 2\Theta, \tag{5.18}$$

where a is the major axis length while b is the minor axis length.

If β is much smaller than α, we can simplify (5.16) - (5.18) by neglecting the β terms, obtaining:

$$\frac{da}{dt} = a\alpha\cos^2\Theta \tag{5.19}$$

$$\frac{db}{dt} = b\alpha \sin^2 \Theta \tag{5.20}$$

$$\frac{d\Theta}{dt} = \zeta \frac{\eta}{(1+\eta)^2} - \frac{\alpha}{2}\frac{\eta^2+1}{\eta^2-1}\sin 2\Theta. \tag{5.21}$$

To close this set of equations we can find the rate of change of the aspect ratio $\eta = a/b$ to be:

$$\frac{d\eta}{dt} = \frac{1}{b}\frac{da}{dt} - \frac{a}{b^2}\frac{db}{dt} = \alpha\eta(\cos^2\Theta - \sin^2\Theta) = \alpha\eta\cos 2\Theta. \tag{5.22}$$

We see from this set of equations that the presence of plane convergence reduces the rate of rotation of the vorticity band once $\Theta \neq 0$. This is due to the fact that the plane convergence is forcing the vorticity band to align with the axis of dilatation. The angle at which the rotation rate becomes zero is given by:

$$\sin 2\Theta_{max} = \frac{\eta}{(1+\eta)^2}\frac{\eta^2-1}{\eta^2+1}\frac{2\zeta}{\alpha}. \tag{5.23}$$

How do we apply these equations to the RAMS simulation? Here, instead of deriving the Fourier modes from the strain as before, we will derive the strain from the Fourier modes. First define the x-axis as the planar axis of contraction; if the large-scale flow is given by $-\alpha x\hat{\mathbf{x}} - \beta y\hat{\mathbf{y}}$, we should have $|\alpha| > |\beta|$. Using (5.14), we obtain:

$$\alpha = \frac{-v_{r0} + \sqrt{v_{r2s}^2 + v_{r2c}^2}}{r} \tag{5.24}$$

and

$$\beta = \frac{-v_{r0} - \sqrt{v_{r2s}^2 + v_{r2c}^2}}{r} \tag{5.25}$$

if $v_{r0} < 0$; the axes used to determine v_{r2s} and v_{r2c} are arbitrary. Applying these equations to the RAMS baseline simulation at 3300 s gives $\alpha = 2.47 \times 10^{-2}\mathrm{s}^{-1}$ and $\beta = 5.18 \times 10^{-4}\mathrm{s}^{-1}$. Clearly the environment is neither strongly uniaxial nor biaxial, and we are justified in neglecting β in a qualitative picture.

$-v_{r0}$	v_{r2c}	v_{r2s}	$-v_{r0}+\sqrt{v_{r2s}^2+v_{r2c}}^{2}$	radius (m)
6.30	-5.14	3.20	12.35	444
8.24	-5.95	3.74	15.27	666
9.54	-6.14	3.91	16.82	888
10.52	-6.20	4.24	18.03	1110
11.39	-6.42	4.72	19.36	1332
12.12	-6.60	5.18	20.51	1554
12.74	-6.71	5.59	21.47	1776
13.26	-6.81	5.95	22.30	1998
13.70	-6.90	6.31	23.05	2220

Table 5.4: Values of zeroth and second-order Fourier components of the radial velocity for circular contour of various radii, centered on the location of the maximum vorticity on Grid 2 at 3300s. Velocity units are m s^{-1}.

However, there is one more requirement that should be satisfied by a field of uniform plane convergence: the quantity $-v_{r0}+\sqrt{v_{r2s}^2+v_{r2c}}^{2}$ should be proportional to the radius of the circular contour. Table 5.4 shows the validity of this assessment. The radial velocity modes increase with radius, but much more slowly than one would expect from a linear function of radius. This is an indication that the convergence is largely confined to a narrow region. So it is not fully justified to speak of the plane convergence as being uniform, but to first order we will use the value of α computed above to determine the effect of the large-scale strain on the vorticity patch.

The aspect ratio of the central ellipse in the spectral model simulation was $2100/600 = 3.5$. Using this value along with $\zeta = 0.03$ s^{-1} and $\alpha = 0.0247$ s^{-1} gives $\Theta_{max} = 10.4°$. For angles greater than this, the rotation rate becomes negative. During the rotation of the vortex patch η is changing as well, which must be considered. But $d\eta/dt$ is positive for angles between $0°$ and $45°$. The quantity $(\eta^2-1)/(\eta^2+1)$ is very nearly unity for $\eta^2 >> 1$, and $\eta/(1+\eta)^2$ decreases as η increases. Thus the rotation of the vorticity band in the RAMS model to angles significantly greater than $10°$ from the axis of dilatation cannot be explained given the presence of the strong plane convergence field, though the rotation rate is well explained if one does not take the convergence field into account. We are thus led to consider whether barotropic instability can be invoked to explain the deviation of the vorticity band from the axis of dilatation. This scenario will also be considered in a two-dimensional inviscid framework; but now it is crucial that the geometry is predominately one-dimensional in the base state, with only small initial perturbations from this state.

5.6 Barotropic Instability

The instability of a vortex sheet of finite width to infinitesimal wave-like disturbances was first treated by Rayleigh (1880). The instability can be seen to be the result of the phase locking between counter-propagating Rossby waves on each interface (Guinn and Schubert 1993). The conceptual framework for the problem consists of a north-south mean state flow of magnitude V for $x > x_0$ and $-V$ for $x < -x_0$, with a zone of constant vorticity V/x_0 in between; there is no other large-scale flow. The extreme vorticity gradient at x_0 generates a Rossby wave of speed $-V/2kx_0$ where k is the wavenumber of the infinitesimal disturbance. Similarly a wave of speed $V/2kx_0$ is generated on the western interface. In addition, the influence of each Rossby waves extends to the opposite influence, so that at x_0 the Rossby wave at $-x_0$ induces motion with speed $(V/2k_{x0})e^{-2kx_0}$. It is this mutual interaction that can lead to phase-locking and an exponentially growing disturbance if kx_0 is small enough (i.e., if the wavelength is long enough compared to the width of the vorticity strip). It can be shown that disturbances with a wavelength greater than approximately $10x_0$ will be unstable, and that the most unstable mode is one with a wavelength near $16x_0$ (Guinn and Schubert 1993). The e-folding time of the most unstable disturbance is given by $10x_0/V$

The presence of plane strain complicates the situation, however. Neu (1984a) states that the presence of uniform shear alters the growth rate of barotropic instability for an infinitesimal vortex sheet, although it doesn't eliminate the instability. Second, for a vortex

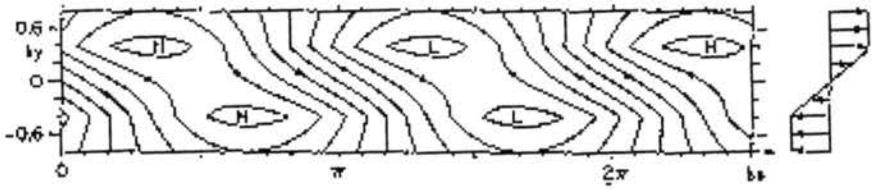

Figure 5.12: Isolines of perturbation pressure for most unstable mode of finite-width vorticity layer. Base state mean wind profile is shown at the right. From Gill (1982)

strip of finite width, the presence of plane strain will decrease the width of the strip unless some other force such as viscous diffusion is significant. As a vortex strip is converged in a process for which diffusion in insignificant, however, two things in particular will happen. The decreased width of the strip will increase the average vorticity of the strip, and hence decrease the timescale of the instability. Also, in plane convergence the speed towards the axis decreases towards the axis. Therefore, at some point during the contraction process we can expect that barotropic instability will eventually occur despite the presence of the uniform convergence.

A heuristic way of determining the relative importance of the instability compared to the convergence is to take the ratio $(V/2\alpha k x_0^2)e^{-2kx_0}$, which is the ratio of the speed induced by the Rossby wave at the opposite interface to the large-scale convergent motion. If we use $V/x_0 = \bar{\zeta}_z$ and assume that kx_0 is that of the most unstable disturbance, we obtain:

$$\frac{\text{barotropic instability}}{\text{convergence}} \approx 0.57\frac{\bar{\zeta}_z}{\alpha}. \tag{5.26}$$

Note that this ratio is less than one if we use the parameters from 3300 s that initialized the ellipse ($\zeta_z = 3 \times 10^{-2}$ s^{-1}; $\alpha = 2.47 \times 10^{-2}$ s^{-1}). Thus we might expect the future evolution of the vorticity patch at this point to consist mainly of convergence towards the axis of contraction. However, because the ratio is not much different from unity, the actual evolution should show features of both processes.

A scaled view of the vorticity band at 3360 s is shown in Figure 5.13. It can be seen that the width of the vorticity band at this time has narrowed from 600 m to approximately 400 m. The maximum instability half-wavelength is now 1600 m. This corresponds very well to the distance between the westward notch near the region of maximum vorticity and the maximum eastward surge of the gust front to the south. There is no evidence of a continuation of this wave pattern to the south. However, this could be a function of the reduced vorticity in this region, which is closer to 0.02 s^{-1} relative to the values of at least 0.04 s^{-1} in the heart of the wave. For the two regions we can calculate e-folding times of 250 and 125 seconds respectively. Recall that the northern vorticity center becomes dominant near the surface at 3222 s. Thus the wave pattern seems consistent with barotropic instability occurring around the region of maximum vorticity. Using $0.03 \times (600\ \mathrm{m}/400\ \mathrm{m}) = 0.045$ s^{-1} for a vorticity value gives the ratio in (5.26) a value of 0.94, suggesting that for the area in general the barotropic instability mechanism is becoming significant.

The barotropic instability itself cannot increase the values of the vorticity, but it can reorient a segment of the vorticity band so that there is a greater net horizontal vorticity flux by the plane convergent flow, as described in previous sections. Vorticity rapidly concentrates into discrete centers as described in Neu (1984a), and the subsequent evolution differs considerably from classic two-dimensional barotropic instability.

5.7 Comparison to NST Tornadogenesis

Because of the similarities of this process to the NST mechanism modeled by Lee and Wilhelmson (1997a-c), a comparison is appropriate here. Their simulation is semislip with a drag coefficient ($C_D = 0.06$ in dry simulations to 0.002 in moist ones.). The domain is cyclic in the along-front direction. Because of the surface drag the cold pool is retarded

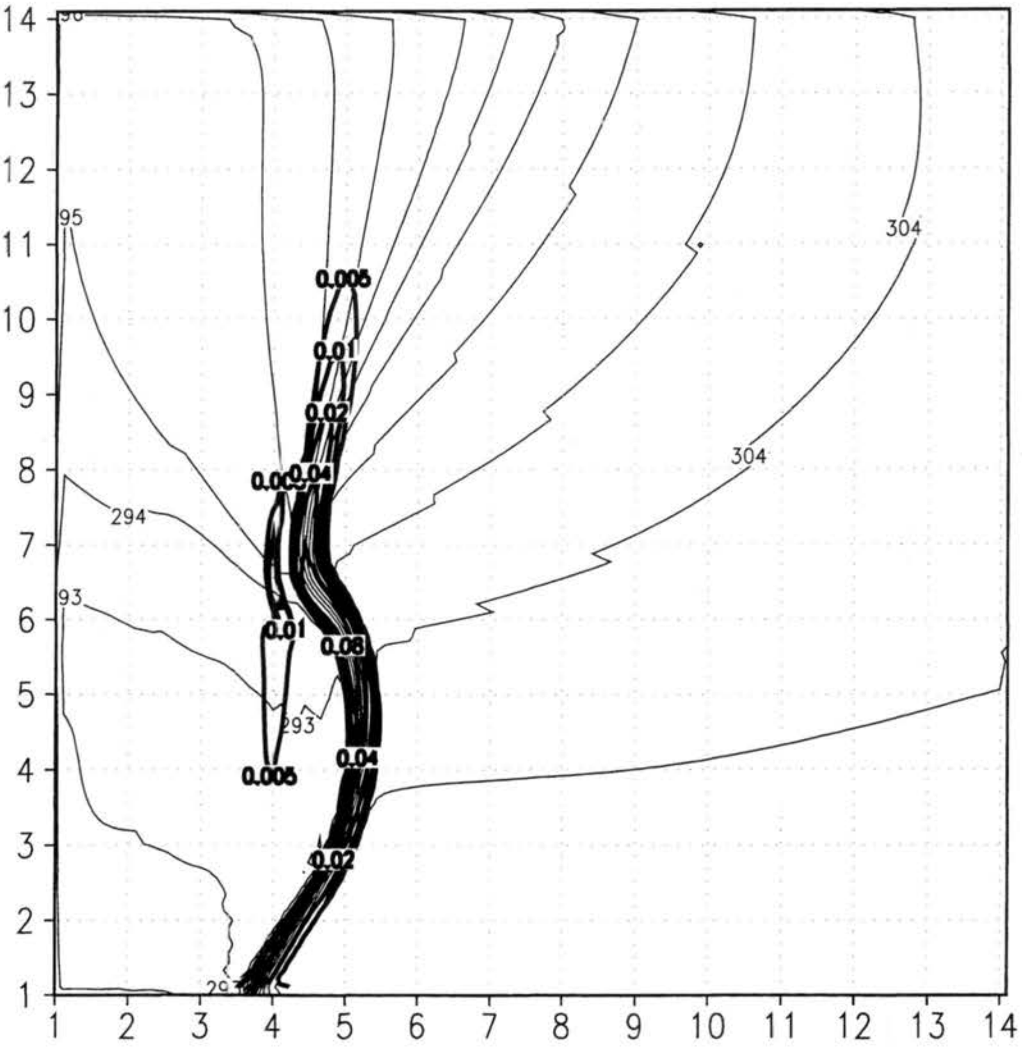

Figure 5.13: Potential temperature (thin contours) and vertical vorticity (thick contours) for Grid 2 at 3360 s. Potential temperature contours are every 1 K. Vorticity contour increments double every level beginning at 0.005 s^{-1}. Scale on vertical and horizontal axes is distance in kilometers.

near the surface, creating thermal instability just ahead of the surface front. It is this instability that serves as the focus point for vortex evolution, which then proceeds according to barotropic dynamics, eventually becoming nonlinear as vorticity pools into discrete regions (see Figure 5.14). Their vorticity on a grid with 100 m horizontal grid spacing is of the same order of magnitude as ours with comparable grid spacing (≈ 0.1 s^{-1}). However, the ambient horizontal convergence is weak (≈ 0.004 s^{-1}) compared to ours, and frictional convergence into the developing vortices is essential to amplifying the vorticity in reasonable amounts of time. Still, it takes about 1000 s for their vortices to achieve vertical vorticity of 0.1 s^{-1} by the frictionally-induced convergence (Lee and Wilhelmson 1997a). Of course, for a pre-existing thermal boundary, there is, so to speak, ample time to generate this vorticity before the formation of convection, and it is hypothesized that these misocyclonic vortices become the seeds of future NST after convection enhances the convergence beneath them. In our simulation, however, the relatively limited extent of the front in the along-front direction would limit the possibility of vortex-merger processes, and interaction with the ambient convergent field would probably be required to produce a concentrated vortex.

5.8 Strength of Vortex

If the proposed mechanism properly describes the formation of the vortex, it is possible to draw some conclusions about its ultimate strength. Consider the Burgers vortex. It can be shown that the maximum tangential speed of the Burgers vortex is approximately $0.72\Gamma/2\pi r_{max}$ (Davies-Jones 1986), where Γ is the total circulation and r_{max} is the radius of maximum tangential speed. For the Burgers vortex r_{max} is approximately $2.24(\nu/\gamma)^{\frac{1}{2}}$, where ν is the viscosity and γ is the vertical divergence.

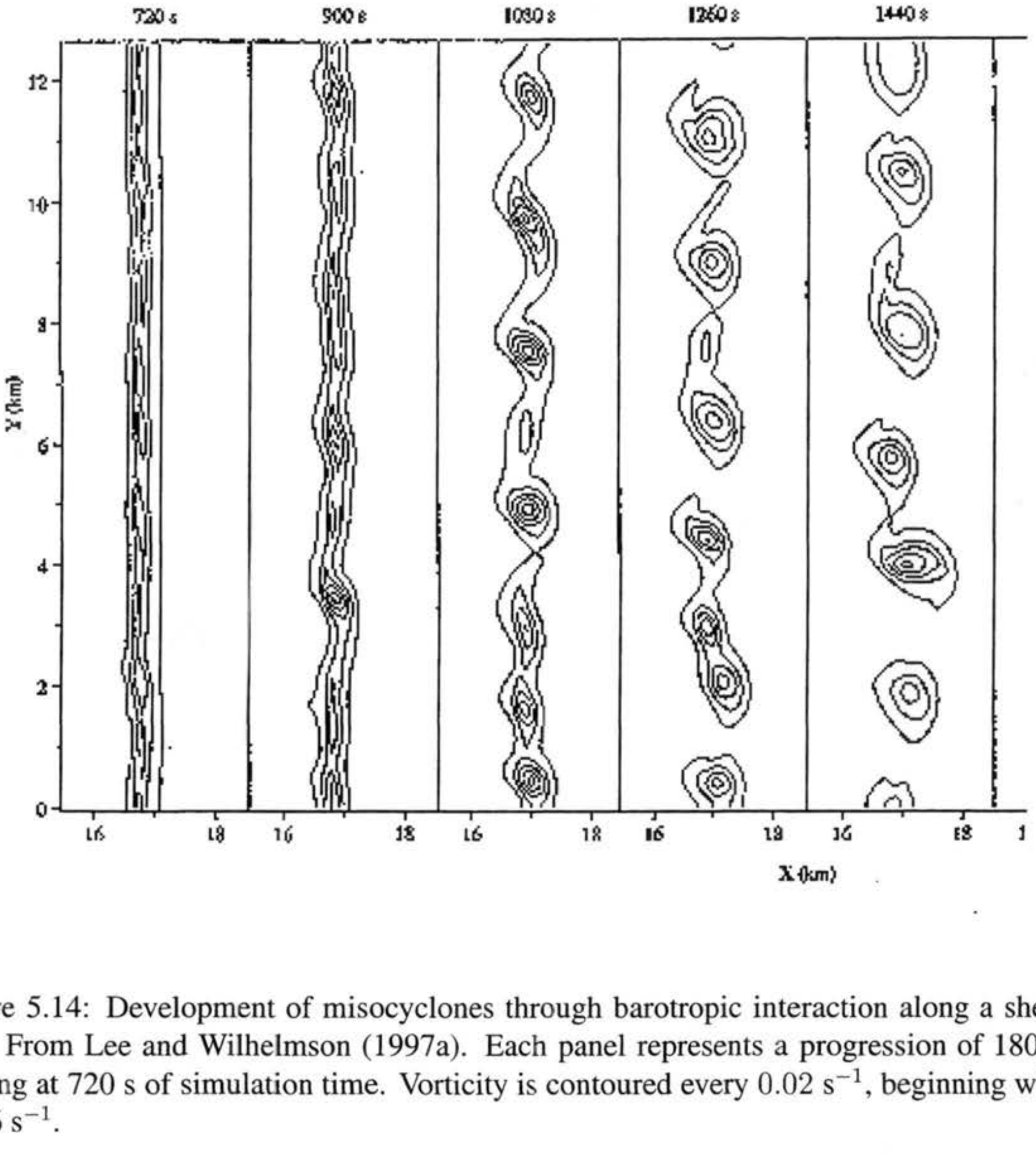

Figure 5.14: Development of misocyclones through barotropic interaction along a shear line. From Lee and Wilhelmson (1997a). Each panel represents a progression of 180 s, starting at 720 s of simulation time. Vorticity is contoured every $0.02\ \mathrm{s}^{-1}$, beginning with $0.005\ \mathrm{s}^{-1}$.

According to Neu (1984a), during the collapse process the circulation excess, given by

$$\Gamma_c = \int [\sigma - 2(\nu\gamma)^{\frac{1}{2}}]dy, \tag{5.27}$$

remains constant for the segment of the vortex band that is collapsing, and thus represents the circulation of the final Burgers vortex. Let r_{draw} represent the initial radial distance of the vortex band segment that is drawn into the final vortex, such that if the final vortex position is at the origin, the limits of integration at the start of the collapse process are $y = -r_{draw}$ and $y = r_{draw}$. We can express σ as the constant value $2v_{env}$ if we idealize the vortex band as the region between parcels with $v = v_{env}$ in the positive x direction and parcels with $v = -v_{env}$ in the negative x direction. Substituting all of these relations into (5.27) gives

$$\Gamma_c = 4r_{draw}[v_{env} - (\nu\gamma)^{\frac{1}{2}}]. \tag{5.28}$$

In the current simulation the horizontal eddy diffusion coefficient, which we will use in place of ν, has a value of 108 m s^{-2}. Using $\gamma = 2.47 \times 10^{-2}$ s^{-1}, we get a value for $(\nu\gamma)^{\frac{1}{2}})$ of 1.57 m s^{-1}. Meanwhile, the region of the band with vorticity 0.03 s^{-1} and width 600 m would correspond to a value of σ of $0.03 \times 600 = 18$ m s^{-1}, which implies that $v_{env} = 9$ m s^{-1}. Using these values in (5.28) shows that we are relatively close to the inviscid limit, where the vortex band segment becomes a vortex sheet segment, the final vortex circulation is simply the vortex sheet segment circulation, and the final vortex is simply a point vortex.

Substituting Γ_c for Γ in the expression for the maximum Burgers vortex tangential velocity, v_{max}, gives:

$$v_{max} = \frac{1.44}{\pi}\frac{r_{draw}}{r_{max}}[v_{env} - (\nu\gamma)^{\frac{1}{2}}]. \tag{5.29}$$

When the flow is nearly inviscid, the two determinants of the maximum vortex tangential velocity are the environmental vertical vorticity present along the vortex band, as represented by v_{env}, and the distance along the vortex band from which vertical vorticity can be pulled into the final vortex. Note, however, that even if the flow is nearly inviscid, some viscosity must be assumed in order to determine the scale of r_{max}, unless an independent means of determining the final size of the vortex is used.

For the mechanism described in this chapter, we can assume that the maximum length of the vortex band that can be drawn into the final vortex is one-half of the wavelength of maximum barotropic instability, i.e., the distance from a wave crest to a wave trough. The actual distance may prove to be less, resulting in a lower circulation and lower tangential wind. The half-wavelength of the most unstable barotropic mode is approximately $4\Delta x$ for a band with width Δx, and thus r_{draw} should be $2\Delta x$.

The e-folding length of a Burgers vortex sheet is $(2\nu/\gamma)^{\frac{1}{2}}$. If we approximate the width of the band is approximately two of these lengths, then we obtain 187 m. This however is considerably less than the estimated width of the band at the time that waves become apparent (400 m at 3360 s). This confirms that during the vortex concentration process we do not begin with a Burgers vortex sheet, but rather with a band of vorticity that is in the process of converging into a Burgers sheet, as analyzed by Kambe (1983). We had estimated that waves should first become apparent when $\bar{\zeta_z} \approx \gamma/0.57$, or equivalently when the width $\Delta x \approx 0.57\sigma/\gamma$. Using $\sigma = 18$ m s^{-1} and $\gamma = 2.47 \times 10^{-2}$ s^{-1}, we get 415 m, which is very close to the observed value at 3360 s. If we use this general expression for the width of the vortex band, use $r_{draw} = 2\Delta x$, and use $r_{max} \approx 2.24(\nu/\gamma)^{\frac{1}{2}}$ for the circular Burgers vortex (Davies-Jones 1986), we obtain:

$$\frac{r_{draw}}{r_{max}} \approx 1.02\frac{v_{env}}{(\nu\gamma)^{\frac{1}{2}}}. \tag{5.30}$$

Substituting (5.30) into the v_{max} relation (5.29) gives a final result of:

$$v_{max} \approx \frac{(1.44)(1.02)}{\pi} \frac{v_{env}}{(\nu\gamma)^{\frac{1}{2}}}[v_{env} - (\nu\gamma)^{\frac{1}{2}}] \approx 0.47 \frac{v_{env}}{(\nu\gamma)^{\frac{1}{2}}}[v_{env} - (\nu\gamma)^{\frac{1}{2}}], \quad (5.31)$$

which yields $v_{max} \approx 20$ ms^{-1} using model values.

The actual maximum tangential velocity of the final vortex is around 25 m s^{-1}, which can be seen in the wind speed field in Figure 5.15 after the translational velocity has been subtracted out. The circular Burgers vortex has a pressure deficit of $1.68\rho v_{max}^2$ in its core (Davies-Jones 1986); using $\rho = 1.1$ kg m^{-3} and $v_{max} = 25$ m s^{-1} produces $\Delta p = 11.6$ mb, which also compares favorably to the local pressure deficit in the simulation.

Our predicted value for the tangential wind speed is a bit low. It should be noted, however, that r_{max} using model values is $2.24(\nu/\gamma)^{\frac{1}{2}} = 148$ m, which is not much larger than the grid spacing of 111 m. We could imagine that the final concentrated Burgers vortex is 'aliased' onto a vortex with radius 111 m because of the limitations of grid spacing. Since v_{max} is proportional to the inverse of r_{max} for the same circulation, the enforced contraction of the vortex would increase v_{max} by $148/111 = 1.33$ times, which would more than account for the value of v_{max} observed in the model. The aliased vortex would be overly concentrated for the values of diffusion and convergence, though, and eventually would be expected to diffuse circulation into the environment. In any event, a number of broad assumptions went into the derivation of (5.31), and it is best regarded as an order-of-magnitude estimate for vortices and sheets with these characteristic length and velocity scales.

We can attempt to estimate the maximum tangential winds that can be produced by this mechanism. The strongest tornadoes possess horizontal wind speeds well in excess of 100 m s^{-1}. The strongest values of v_{env} along environmental shear lines are on the order of 15 m s^{-1} (Lee and Wilhelmson 1997a). From (5.29), we would need r_{draw}/r_{max} to be

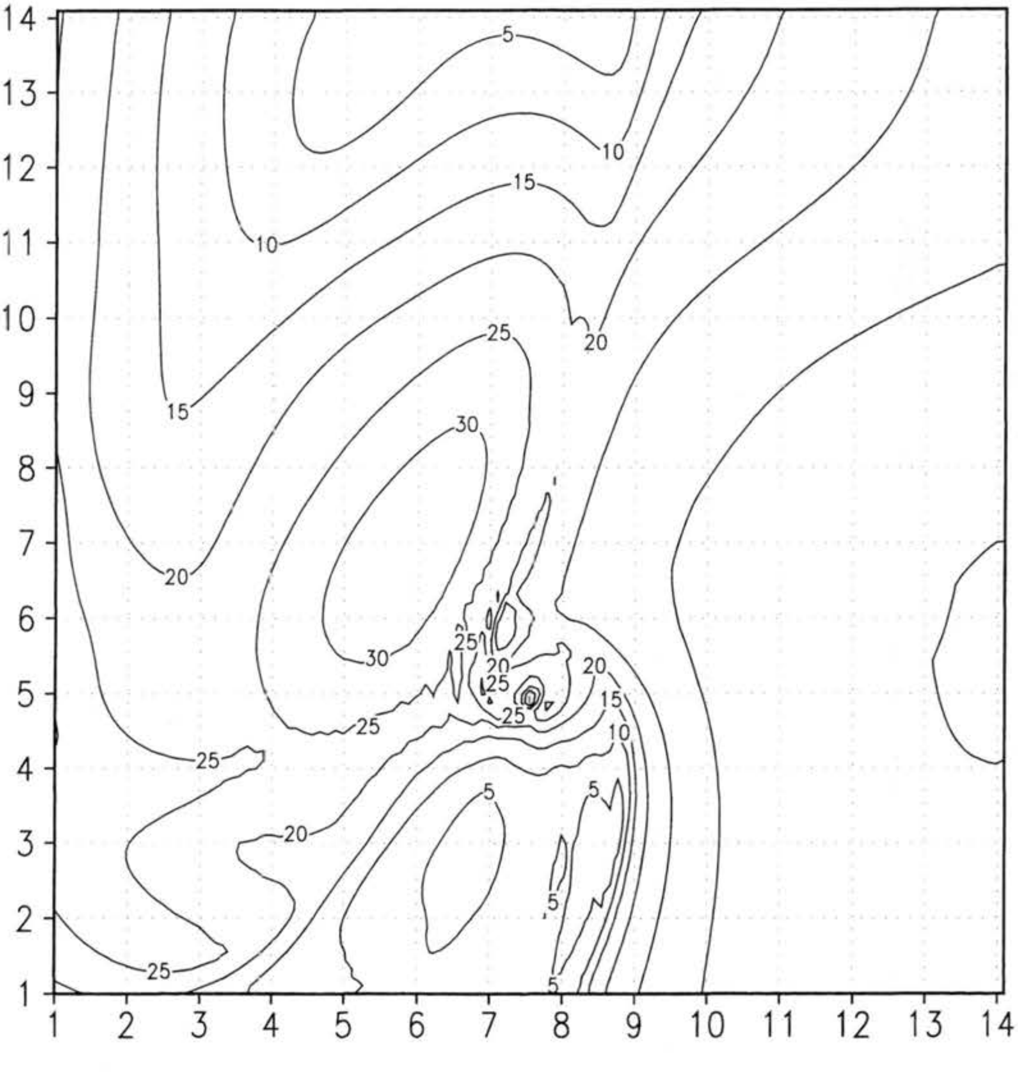

Figure 5.15: Vortex-relative speed at 3600 s on Grid 2. Vortex translational velocity is $u = 19$ m s^{-1}, $v = -6$ m s^{-1}, and was found by removing the first-order modes from the velocity pattern of the vortex.

at least 14.5 in order to have a chance of generating a 100 m s^{-1} vortex. Using the model data we found r_{draw}/r_{max} to be approximately $(2 \times 400)/148 = 5.4$. There is reason to believe that this ratio should not much exceed 5.4. In our framework r_{draw}/r_{max} is equal to $2\Delta x/r_{max}$, where Δx is the width of the vortex band at the start of the process. The model of Neu (1984a) applies to Burgers vortex sheets and circular vortices that have the same characteristic length scales. In our study, Δx is not quite twice as large as the diameter of the final vortex, $2r_{max}$. Although we would expect the width of the vortex band to continue to narrow at during the early stages, at later stages the central region has rotated such that its width is no longer being contracted by the plane convergence. We may surmise that a vortex band will not collapse into a concentrated vortex with a diameter much smaller than the width of the band via this mechanism. Therefore, for simplicity, we will make the assumption that $r_{draw}/r_{max} \approx 5.4$ is close to the maximum value that we can expect. Using this assumption in (5.29) provides a maximum expected tangential wind speed of approximately 37 m s^{-1}, well short of the wind speeds of the most powerful tornadoes.

Some mention will be made here of the thermodynamic speed limit method of estimating the maximum tornadic wind speeds (Lilly 1969; Kessler 1970; Snow and Pauley 1984). In this method it is assumed that the negative pressure perturbation of a tornado is determined by the CAPE of the environment with respect to an air parcel that represents the parent thunderstorm. The pressure deficit is basically determined by vertically integrating the parcel buoyancy and assuming hydrostaticity. Normally, the buoyancy of the convection would induce a vertical motion field, which would temporarily evacuate air from beneath the convection. Horizontal convergence would rapidly be induced to prevent the evacuation of air, and the full hydrostatic negative perturbation pressure would not be apparent. However, if the air underneath the storm possesses sufficient circulation, conservation of angular momentum will eventually prevent horizontal convergence from occurring. If horizontal convergence is inhibited, the pressure will continue to drop due to the evacuation of mass until the vertical motion is inhibited by the adverse pressure gradient. At a level where vertical motion is inhibited, the pressure deficit must be the integrated buoyancy to the top of the atmosphere (assuming that the vertical motion and pressure deficit are both zero at the top of the atmosphere). The tangential wind speed is then calculated from the pressure deficit by assuming cyclostrophic balance, as well as a reasonable vorticity distribution.

Using the thermodynamic method, Lilly (1969) found that the maximum expected CAPE of 3800 J kg^{-1} implied a maximum pressure deficit of 45 mb and a maximum tangential wind speed of 62 m s^{-1} for an assumed one-celled vortex. Note that this method alone also cannot account for the wind speeds of the most powerful tornadoes. Attempts have been made to explain the highest tornadic wind speeds by a variety of methods, including assuming that the tornadic vortex contains a subsiding, adiabatically-warmed core (Walko 1988), and explaining the enhanced wind speeds as the result of a strong axial jet dynamically induced by a no-slip boundary condition (Fiedler and Rotunno 1986; Lewellen 1993; Nolan et al. 2000). Conceivably, these influences could also enhance a natural version of the vortex modeled in this study. Or, it is possible that the combination of storm buoyancy with the converged vortex mechanism can produce a tangential wind of the necessary strength; larger storm buoyancy could induce convergence that would concentrate the circulation into a region even smaller than the circular Burgers vortex, with correspondingly higher velocities. Of course, finer horizontal grid resolution would be required to model such a process. Or, larger storm buoyancy could draw in vorticity from a larger distance than $r_{draw} = 2\Delta x$, and hence increase the circulation for a final vortex of a given size.

The other way to generate a more intense vortex from a line of vorticity would be to have a mesoscale (or synoptic scale) source of convergence and vorticity, which could also draw in circulation from a distance greater than is possible with the barotropic method. This explanation may apply to the strong 26 Apr 1991 tornado-like vortex of Grasso (1996). That study was horizontally- heterogeneous, and developed the tornadic supercell near a dryline that exhibited mesoscale vorticity.

More on the relationship between pressure and vortex formation will be discussed in Chapter 7.

5.9 Summary

The Eulerian inviscid circulation tendency equation for a horizontal circular contour was separated into components using a Fourier decomposition. This decomposition provides large-scale versions of the convergence, tilting, and advection terms found in the Eulerian vertical vorticity equation, as well as higher-order terms that represent eddy correlations. The horizontal terms involve the radial velocity and vertical vorticity and involve the processes of horizontal advection and convergence. The vertical terms involve vertical velocity and the vertical shear of the tangential wind, and involve the processes of vertical advection and tilting.

This analysis was performed on Grid 2 of the RAMS baseline simulation during the time that the vortex was intensifying most rapidly. It was found that the horizontal terms are dominant during this process. The fact that both the zeroth-order and second-order terms were significant allowed some inferences about the geometry of the process. In particular, the spinup of the vortex is not axisymmetric, and the axes of the vorticity and large-scale radial convergence are largely perpendicular until the vortex has already fully developed. During the stage of rapid vorticity intensification, the axis of vorticity rotates so that there is a greater component of the large-scale radial convergence along it. The vorticity then rapidly concentrates towards the axis of the band.

The most likely scenario for the intensification is the following. Initially there is a thin band of vorticity situated in uniform plane convergence. The band becomes more and more concentrated at first because dissipation is insufficient to balance the convergence, but, in a manner consistent with the Kambe (1983) framework, is evolving towards the Burgers vortex sheet. However, before this state is reached, barotropic instability begins. This instability causes the rotation of the vorticity axis in a localized region. There is now a better correlation between vorticity and the large-scale radial convergence, and the vorticity begins to concentrate into a discrete center. Soon the presence of this center dominates the dynamics of the region. Time and length scales of this process correspond well to theoretical predictions. However, this process alone does not seem capable of generating wind speeds comparable to those of the strongest tornadoes.

Chapter 6

TRAJECTORY ANALYSIS

6.1 Average Vertical Vorticity

Let us *define* the average vertical vorticity, $\bar{\zeta_z}$, for a closed horizontal contour, C, through the use of the circulation:

$$\bar{\zeta_z} = \frac{\oint\limits_C \mathbf{v} \cdot \mathbf{dl}}{\iint\limits_C dx\, dy}. \tag{6.1}$$

The average vertical vorticity is a function of the velocities and positions of all the fluid elements on C. We can use Stokes' theorem to find:

$$\bar{\zeta_z} = \frac{\oint\limits_C \mathbf{v} \cdot \mathbf{dl}}{\iint\limits_C dx\, dy} = \frac{\iint\limits_C [\boldsymbol{\nabla} \times \mathbf{v}]_{\mathbf{k}} dx\, dy}{\iint\limits_C dx\, dy}, \tag{6.2}$$

which is simply an average value of the vertical component of the velocity curl within the contour, assuming that the velocity is smooth enough in the region for its curl to be computed. If we take the limit as the area goes to zero, we simply get:

$$\bar{\zeta_z} = [\boldsymbol{\nabla} \times \mathbf{v}]_{\mathbf{k}}, \tag{6.3}$$

which of course is the actual vertical vorticity component at the limit point of C. With the use of arbitrary planar contours, this procedure can in fact be used to define the normal component of the curl in a manner not dependent on the coordinate system (Lewis and

Ward 1989). In a continuous differentiable fluid we can take this limit as the contour size shrinks to zero, and the resultant average vertical vorticity can be considered a property of a single point in the fluid, dependent only on the velocity derivatives at that point, which are evaluated over arbitrarily small volumes. In particular, we can assign such an average vertical vorticity to each point on the forward (or backward) trajectory of any starting point in the fluid. Thus the average vertical vorticity in the limit of infinitesimal area can be considered a material property of fluid elements that evolves according to the local conditions at the fluid element (for example, as shown in (2.15)).

6.2 Discrete Case

We can apply the average vertical velocity to the case of a discrete Eulerian grid to approximate true vertical vorticity at a location. We can choose a horizontal contour that consists of the perimeter of a grid cell.

For the Arakawa-C grid of RAMS, the grid cells formed by connecting the T-points on the grid possess U-points at the midpoints of the horizontal sides and V-points at the vertical side midpoints (Figure 6.1). Thus each side can be said to possess a velocity component parallel its direction, facilitating the computation of the $\oint\limits_C \mathbf{v} \cdot \mathbf{dl}$ term in the average vertical vorticity.

In order to compute the line integral we need some way to relate $\mathbf{v}$, which are defined at grid points, to finite-length sides around the integration contour. The most straightforward choice for the grid cell perimeter is to assume that $\int \mathbf{v} \cdot \mathbf{dl}$ for each side is simply the tangential velocity defined at the midpoint of each side times the length of the side. This method gives for the average vertical vorticity of the grid cell with T point (i, j) at the lower left corner:

$$\zeta_{zD}|_{i,j} = \frac{(v_{i+1,j} - v_{i,j})\Delta x + (u_{i,j+1} - u_{i,j})\Delta y}{\Delta x \Delta y}, \tag{6.4}$$

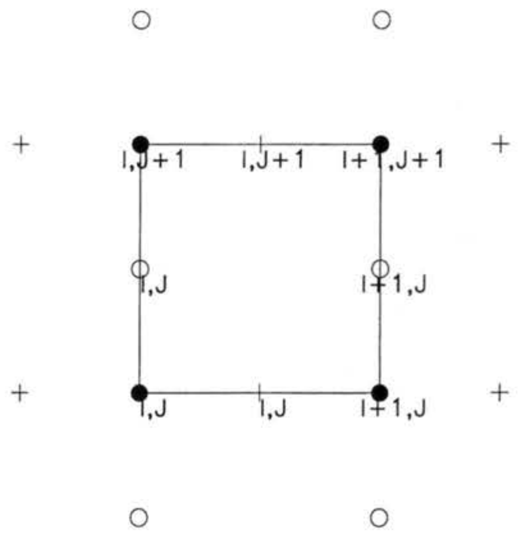

Figure 6.1: Contour used to define grid cell discrete vertical vorticity for point at horizontal coordinates (I,J). Solid circles denote model T points; open circles denote model V points; crosses denote model U points. Direction of contour integration is counterclockwise.

where the quantity ζ_{zD} will be referred to as the discrete vertical vorticity, which is dependent on the grid staggering scheme and the chosen contour. Obviously, this equation gives the same result as that obtained by approximating the derivatives in the vertical component of the velocity curl by a finite differences across the grid cell.

One disadvantage of this scheme is that the non-tangential velocity components on a side (e.g., the value of v on the south perimeter) are undefined. These components are needed, however, if one is to perform a trajectory analysis of the contour. Either both u and v must be defined as being valid at the same locations, or some interpolation procedure must be used on the radial wind component. One possible scheme is to interpolate both u and v at all sides of the grid cell perimeter, using the four neighboring U and V points for the appropriate velocity component. For example, along the southern side the u velocity to the east of the midpoint would be a weighted average between $u_{i,j}$ and $u_{i+1,j}$; to the west of the midpoint the weighted average would be between $u_{i-1,j}$ and $u_{i,j}$. The resultant discrete vertical vorticity using this method will not be identical to the finite-difference vorticity of the grid cell because it will be dependent on the velocities of neighboring grid cells. But now both u and v for closed curves are continuous functions of position on the curve. We may thus decide that we want more than four points with which to compute trajectories. We then can divide each side of the grid cell initially into a number of collinear line segments. The discrete vertical vorticity is now given by

$$\zeta_{zD} = \frac{\sum_{1}^{N} \mathbf{v}_{mid} \cdot \Delta \mathbf{l}}{\Delta x \Delta y}, \tag{6.5}$$

where $\mathbf{v}_{mid}$ is the interpolated velocity at each segment midpoint, and $\mathbf{v}\cdot\Delta\mathbf{l} = u\Delta x,\ v\Delta y,\ -u\Delta x,\ -v\Delta y$ for the south, east, north, and west sides, respectively. In the trajectory analysis we advect the N endpoints of the line segments, and then reconnect the endpoints in order to compute the new circulation. Note that in this approximation the line segments are not material lines, and the accuracy of the method is dependent upon the spacing between the adjacent material points along the contour.

A key difference of all the average vorticities from the pointwise vorticity in a continuous fluid is that we are not justified in taking the limit as the contour size decreases to zero, because we have no information on scales smaller than the grid cell. Even if we were to interpolate to find model velocities and hence vorticities within a grid cell, these would still remain a function of at minimum the four grid point velocities along the perimeter. (If we use interpolation with neighboring grid points, all the velocities within the grid cell can be a function of up to twelve grid points.) The discrete vertical vorticity for the material contour corresponding to a grid cell perimeter will thus be a function of the forward (or backward) trajectories from a set of points, which will not in general stay localized to a single grid cell. Thus ζ_{zD} *cannot* be said to be locally deterministic in an Eulerian model at all times along a trajectory [1], even if 'local' is allowed to include the whole grid cell perimeter surrounding an interpolated trajectory, or even any region of *fixed* size surrounding the trajectory. Analyses of the sources (or destinations) of the discrete vertical vorticity along a trajectory in an Eulerian grid most resemble a discrete version of the circulation equation for the material contour corresponding to the initial horizontal contour. However, over a *single* timestep, it still remains true that the discrete average vorticity is a deterministic function of the velocity field over a fixed-size region, as given in (2.37). So it is still useful to talk about the vorticity tendency for a single grid cell over a timestep.

6.3 Average Vertical Vorticity Tendency along Trajectories

We now consider how the average vertical vorticity can be said to change following trajectories. Vertical vorticity in an inviscid Boussinesq system can only change along a trajectory by tilting or stretching, but neither of these processes appear in the circulation tendency equation. How can the average vertical vorticity be used to represent these processes? In general the trajectories of a horizontal material contour will not remain horizontal, so the definition of the average vertical vorticity for the material curve will have to be made more general than in the previous sections.

First we need a general definition of the area of a three dimensional curve in a plane whose normal unit vector is given by $\hat{\mathbf{k}}$. Define a position vector $\mathbf{l}$ extending from an origin to a point on the curve. The sector from the origin to an increment $\mathbf{dl}$ defines a planar triangle with area of magnitude $(\mathbf{l} \times \mathbf{dl})/2$. The magnitude of the projection of this area onto the plane with normal $\hat{\mathbf{k}}$ is found by taking the dot product with $\hat{\mathbf{k}}$. If we integrate

---

[1] Of course, in time the material contour may encompass the whole model domain; at this point, the model is locally deterministic in the sense that the behavior of the set of all model grid points is trivially only a function of those grid points themselves.

around the curve, we find that:

$$A_k = \hat{\mathbf{k}} \cdot \oint_C (\frac{\mathbf{l}}{2} \times \mathbf{dl}). \tag{6.6}$$

The areas A_i and A_j, which are projections onto planes normal to the other coordinate axes, can be defined by substituting the appropriate unit vector into (6.6), so in general

$$A_m = \hat{\mathbf{m}} \cdot \oint_C (\frac{\mathbf{l}}{2} \times \mathbf{dl}). \tag{6.7}$$

For a closed curve, there will be two directions of integration, one of which will produce a negative area, the other a positive area. So, by convention, we can define the direction of integration as that which makes A_k positive. If we use this convention, A_i and A_j may or may not be positive.

A more convenient form with which to work is found by applying a vector identity to the triple product in the integrand:

$$A_k = \oint_C (\hat{\mathbf{k}} \times \frac{\mathbf{l}}{2}) \cdot \mathbf{dl}. \tag{6.8}$$

Now define the unit vector $\hat{\mathbf{r}}$ as that which satisfies $\mathbf{l} = r\hat{\mathbf{r}} + z\hat{\mathbf{k}}$, with r positive. Then $\hat{\mathbf{k}} \times \mathbf{l} = r\hat{\mathbf{\Theta}}$ where $\hat{\boldsymbol{\theta}}$ is defined as $\hat{\mathbf{k}} \times \hat{\mathbf{r}}$. Thus the area can also be expressed as

$$A_k = \oint_C \frac{r\hat{\mathbf{\Theta}}}{2} \cdot \mathbf{dl}. \tag{6.9}$$

Since $\mathbf{dl} = (\frac{dr}{ds}\hat{\mathbf{r}} + r\frac{d\Theta}{ds}\hat{\mathbf{\Theta}})ds$ with s being the arc length, in the special case where $\mathbf{l}$ can be expressed as $\mathbf{l}(\Theta)$ the projected area can be rewritten as:

$$A_k = \int_0^{2\pi} \frac{r^2}{2} d\Theta = \int_0^{2\pi} \int_0^{r} r' dr' d\Theta. \tag{6.10}$$

This is the standard form of the two-dimensional area integral in polar coordinates, and we also see that proper direction of integration is that for which θ is an increasing function.

So now we are ready to define the general area average vorticity. To convert the total circulation into a total vorticity we can divide the circulation by $(A_i^2+A_j^2+A_k^2)^{0.5}$. Next, we can take the vertical 'component' of this quantity by multiplying by $A_k/(A_i^2+A_j^2+A_k^2)^{0.5}$. So, finally, the area average vorticity for a general curve is given by:

$$\bar{\zeta_z} = \frac{A_k \oint\limits_C \mathbf{v}\cdot\mathbf{dl}}{A_T^2}. \tag{6.11}$$

where $A_T^2 = A_i^2 + A_j^2 + A_k^2$ with each A_m given by (6.7). For a horizontal contour, (6.11) reduces to (6.1).

It is straightforward to take the material derivative of (6.11). The result is:

$$\frac{d\bar{\zeta_z}}{dt} = \bar{\zeta_z}\frac{d}{dt}(\ln\frac{A_k}{A_T}) + \bar{\zeta_z}\frac{d}{dt}(\ln\frac{1}{A_T}) + \frac{A_k}{A_T^2}\oint\limits_C \frac{d\mathbf{v}}{dt}\cdot\mathbf{dl}. \tag{6.12}$$

The first term increases $\bar{\zeta_z}$ when the total curve area remains constant but the projection onto a horizontal plane increases. The second term increases $\bar{\zeta_z}$ when the orientation to the vertical remains constant but the total curve area decreases. Thus the first two terms are the average vorticity analogs to the tilting and stretching vorticity terms, respectively. Because of the factor of $\bar{\zeta_z}$, both terms can lead to exponential growth, though the tilting term is self-limiting when the curve becomes completely oriented in the xy plane.

The third term represents the $\bar{\zeta_z}$ tendency due the changes in circulation around a material curve. So, for instance, if we neglect diffusion and let $d\mathbf{v}/dt = -\nabla(\theta_{v0}\pi') + B\hat{\mathbf{k}}$, the third term becomes:

$$\frac{A_k}{A_T^2}\oint\limits_C \frac{d\mathbf{v}}{dt}\cdot\mathbf{dl} = \frac{A_k}{A_T^2}\int\limits_0^{s_f} B\frac{dz}{ds}ds, \tag{6.13}$$

where s is the arc length parameter from some reference point on the curve. We see that baroclinity can change the average vertical vorticity, but only when the curve is neither completely horizontal (when dz/ds is zero) nor vertical (when A_k is zero).

For a curve with zero projection into the xy plane, A_k and $\bar{\zeta_z}$ are zero, and both the circulation and stretching terms in (6.12) are zero. However, the tilting term is not necessarily zero because the natural logarithm approaches negative infinity when A_k approaches zero. For $A_k = 0$ the tilting term can be written as:

$$\frac{d\bar{\zeta_z}}{dt} = \frac{\oint \mathbf{v} \cdot \mathbf{dl}}{A_T^2} \frac{dA_k}{dt}. \tag{6.14}$$

6.4 Discrete Vorticity Tendency Along Trajectories

In analogy to (6.11), we can define the general discrete vertical vorticity:

$$\zeta_{zD} = \frac{A_k \sum \mathbf{v} \cdot \Delta \mathbf{l}}{A_T^2}, \tag{6.15}$$

where the area projections A_m are given by

$$A_m = \hat{\mathbf{m}} \cdot \sum (\frac{\mathbf{l}}{2} \times \Delta \mathbf{l}). \tag{6.16}$$

The summations are performed over all the segments in the material curve and defining $\mathbf{l}$ as the position vector of the midpoint of each segment. The value of $\mathbf{v}$ is found by interpolating the vector field to the position of each segment midpoint.

Similarly, we can use (6.12) to obtain the discrete vorticity tendency equation:

$$\frac{d\zeta_{zD}}{dt} = \zeta_{zD} \frac{d}{dt} (\ln \frac{A_k}{A_T}) + \zeta_{zD} \frac{d}{dt} (\ln \frac{1}{A_T}) + \frac{A_k}{A_T^2} \sum \frac{d\mathbf{v}}{dt} \cdot \Delta \mathbf{l}. \tag{6.17}$$

6.5 Material Contour Evolution in RAMS

Here we perform a backwards trajectory analysis of a material contour on Grid 1 (333 m grid spacing) starting from 3600 s, which is close to the time when the vorticity reaches its maximum. The quantity ζ_{zD} as found in (6.15) is used to represent the average vorticity of this contour during the backwards trajectory. The contour at the initial time of the analysis, 3600 s (henceforth referred to as the reference time to minimize confusion), is simply the square perimeter of the grid cell of greatest vorticity at the reference time. The height of the initial contour is at the second model level above the ground (62 m) in order to allow freedom of movement both upwards and downwards. It is assumed that the vertical velocity is zero at the ground, and, consistent with the free-slip condition, there is no vertical shear of the horizontal wind at the surface.

The grid perimeter is divided into 200 line segments of equal length, and their endpoints are subjected to backwards trajectory analysis. A Runge-Kutta method (accurate to fourth order) is used in the time integration of the trajectory. This method requires model output at each half-step. Thus model output every 6 s was used in the analysis, but the method produces trajectory information every 12 s.

Linear interpolation is used for both u and v at all of the trajectory points. Let (x_0, y_0) be the horizontal position of the T point $T_{i,j}$. The interpolated velocity at any point (x, y) on or within the grid cell to the northeast of $T_{i,j}$ is given by:

$$u = [1 - |0.5 - x_{fac}|]\,[1 - y_{fac}]\,u_{i,j} \;+\; [1 - |0.5 - x_{fac}|]\,[y_{fac}]\,u_{i,j+1}$$

$$+\; [|0.5 - x_{fac}|]\,[1 - y_{fac}]\,u_{i\pm1,j} \;+\; [|0.5 - x_{fac}|]\,[y_{fac}]\,u_{i\pm1,j+1}$$

$$v = [1 - |0.5 - y_{fac}|]\,[1 - x_{fac}]\,v_{i,j} \;+\; [1 - |0.5 - y_{fac}|]\,[x_{fac}]\,v_{i+1,j}$$

$$+\; [|0.5 - y_{fac}|]\,[1 - x_{fac}]\,u_{i,j\pm1} \;+\; [|0.5 - y_{fac}|]\,[x_{fac}]\,u_{i+1,j\pm1}, \qquad (6.18)$$

where $x_{fac} = (x - x_0)/\Delta x$ and $y_{fac} = (y - y_0)/\Delta y$. The positive choice in the ± sign of the u equation is used when $x_{fac} > 0.5$, and of the v equation when $y_{fac} > 0.5$.

Figures 6.2a-d and 6.3 show the horizontal position of the material contour at t = -60 s, -120 s, -180 s, -240 s, and -300 s relative to the reference time. It is seen that after only five minutes the backward trajectory of the grid cell boundary acquires a greatly filamented structure, reminiscent of the forward trajectory of a grid cell shown in Figures 2 and 3 of Welander (1955). At 3300 s the curve consists of a central hooked appendage with a long tendril that loops counterclockwise and nearly encircles it. The tip of the tendril is ill-defined in the xy plane, but Figure 6.5, which is a yz projection of the curve, reveals that the curve in this region extends to a height of over 150 m. Interestingly, the rest of the contour has descended to virtually ground level by this time.

As the curve collapses in forward time from the 3300 s position, the inner hooked loop contracts as it rotates counterclockwise, following a path coinciding with the tendril. By 3480 s the hooked loop has reached and absorbed the crescent-shaped region at the easternmost portion of the curve in Figure 6.3. In the final two minutes the tendril is drawn inwards toward the rest of the contour. From Figure 6.3 it can be seen that both the hooked loop and crescent-shaped regions consist of points that make up the north and east sides of the contour at 3600 s. All of the points on the south and west sides of the contour are found, at 3300 s, in the tip of the tendril, well above the surface. The orientation of the curve in this area makes baroclinic generation of circulation possible. However, both sides of the vertical tip are in close horizontal proximity to one other; unless there is an extremely large horizontal temperature gradient here, it is not clear how baroclinic generation of circulation can be important at this time.

Figures 6.4 and 6.6 show the θ_e values of the parcels of the material curve at 3300 s. The parcels of the crescent-shaped region all consist of air with very large equivalent potential temperatures, indicative of low-level origins. This is consistent with the vertical elevation of these parcels at this time. The parcels in the tendril tip, on the other hand, have θ_e values less than 331 K, again consistent with their location, elevated in a downdraft. The parcels

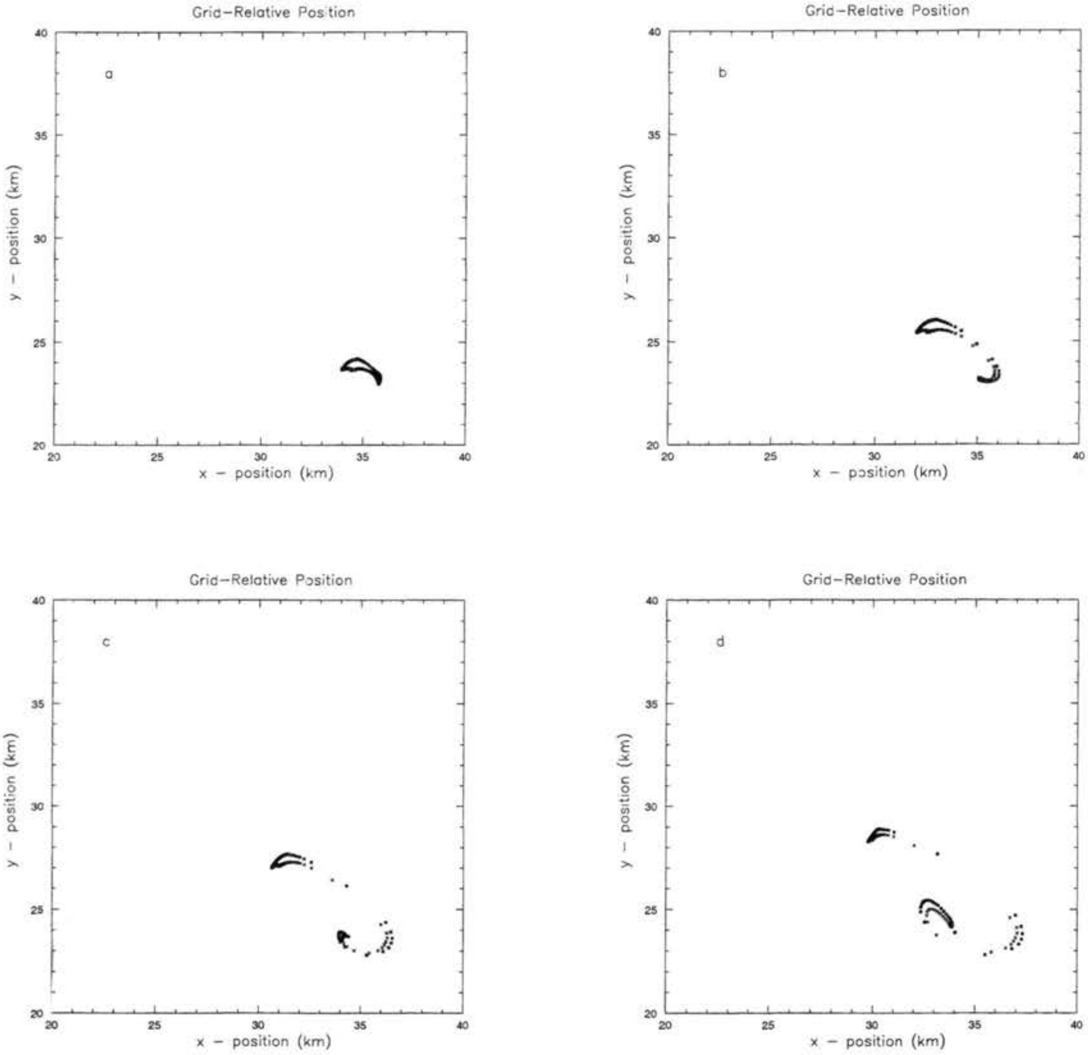

Figure 6.2: Material contour at: a) 3540 s, b) 3480 s, c) 3420 s, and d) 3360 s during Grid 1 simulation. Contour consists of 200 points spaced 6 m apart in a square around grid cell of highest average vorticity at 3600 s, subjected to a backwards trajectory analysis. Open triangles denote points along the west side of the contour at initialization; open squares, the south side; crosses, the east side; and solid squares, the north side.

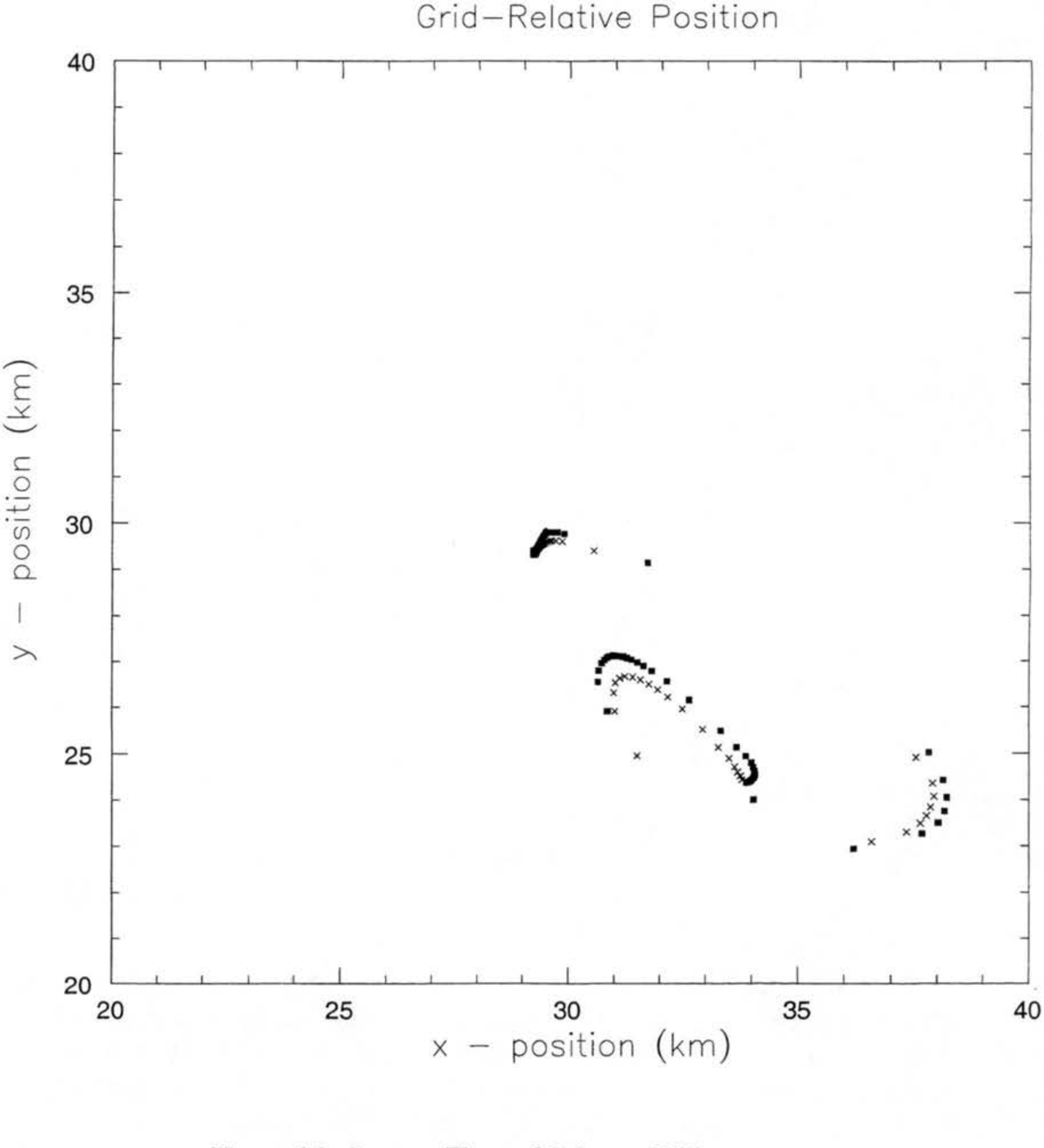

Figure 6.3: Same as Figure 6.2, but at 3300 s.

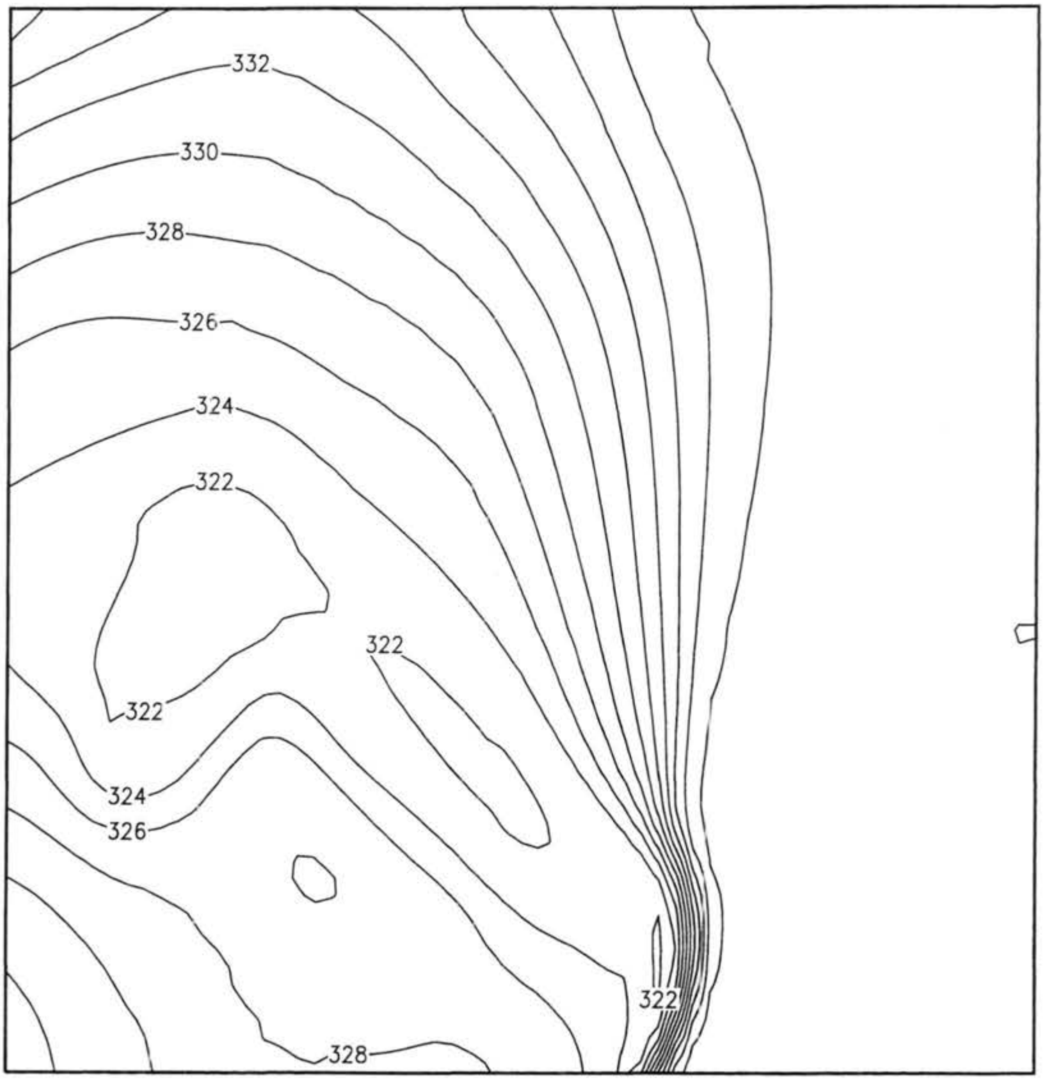

Figure 6.4: Same as Figure 6.3, but showing θ_e values at 3300 s. Domain size is same as that of Figure 6.3.

of this time period, but then rises again. We can also see that the circulation is negative at times prior to 3444 s; at these times, the curve is highly filamented, and the resolution of the curve in these areas is poor, which lends a degree of uncertainty to the results. It is true, though, that there is some negative vorticity in the region between the hooked loop and the crescent-shaped region (Figure 6.7).

Table 6.2 is a kinematic calculation of the ζ_{zD} tendency terms using the information in Table 6.1. Temporal differences are computed over 12 s intervals while other quantities are averaged over that interval; the value of the average stretching, tilting, and circulation tendency terms are then applied at the time midway through the interval. We see that the average stretching term for the curve completely dominates the average tilting term (the scale is 10^2 times smaller for the tilting term), and is the same sign as the circulation, which means that the stretching term is always acting to increase the magnitude of the circulation. The circulation tendency term does not show as systematic a pattern, but is roughly as significant as the stretching term at most times. The tilting term, when it is at its largest near the reference time, is actually negative, except for the last timestep, where it achieves its greatest absolute magnitude.

We can use (6.12) to obtain a condition where the average stretching term must be greater than the average tilting term. Assume that A_k has any nonzero value. We can then directly write the expression for the stretching term minus the tilting term as:

$$\bar{\zeta_z}\frac{d}{dt}\ln(\frac{1}{A_T}) - \bar{\zeta_z}\frac{d}{dt}\ln(\frac{A_k}{A_T}) = \bar{\zeta_z}\frac{d}{dt}\ln(\frac{1}{A_k}). \tag{6.19}$$

For the case of positive circulation ($\bar{\zeta_z} > 0$), whenever the projection of the curve into the xy plane is decreasing in area, the average stretching is greater (i.e., more positive) than the average tilting for the curve. If furthermore $A_i^2 + A_j^2$ is not increasing fast enough to cause A_T to increase, the average stretching will be positive. We can see from the tables

time (s)	circulation ($\mathrm{m}^2\ \mathrm{s}^{-1}$)	A_i (m^2)	A_j (m^2)	A_k (m^2)	ζ_{zD} (s^{-1})
3600	11688.17	0.00	0.00	110890.88	0.1054024
3588	13624.75	-2682.97	-167.80	174485.78	0.0780666
3576	12428.79	-3946.36	-669.05	279168.47	0.0445116
3564	6811.73	-3911.92	-1577.55	392949.97	0.0173329
3552	4953.02	-3308.49	-628.75	505078.59	0.0098060
3540	8295.51	-1786.62	1339.04	629109.81	0.0131859
3528	10051.45	502.91	2957.33	768414.94	0.0130806
3516	10592.15	3003.44	3267.51	918155.31	0.0115361
3504	10191.87	5085.72	2262.89	1076757.25	0.0094651
3492	9860.94	6341.89	148.88	1242545.12	0.0079359
3480	9168.77	6760.25	-2450.58	1404990.50	0.0065257
3468	6516.68	6423.04	-4834.52	1548935.12	0.0042071
3456	3333.42	5666.80	-6241.89	1706481.62	0.0019533
3444	1966.85	5239.59	-6710.18	1852592.00	0.0010617
3432	-295.57	5583.17	-7045.19	2006061.75	-0.0001473
3420	-744.13	6477.04	-7524.28	2181301.50	-0.0003411
3408	-2433.02	8043.41	-8270.93	2365245.50	-0.0010286
3396	-5650.34	10129.39	-9506.75	2572230.50	-0.0021966
3384	-9245.24	12691.22	-11034.21	2784603.25	-0.0033200
3372	-9142.06	15746.09	-12703.88	3027187.75	-0.0030199
3360	-6632.53	18951.67	-14318.52	3298011.75	-0.0020110
3348	-4521.33	22200.63	-16009.49	3558586.50	-0.0012705
3336	-6737.20	25688.51	-17925.20	3770205.00	-0.0017868
3324	-7102.73	29405.42	-19887.10	3933750.50	-0.0018054
3312	-6889.41	33706.70	-21793.92	4084518.25	-0.0016866
3300	-6779.78	38465.03	-23745.94	4226613.00	-0.0016039

Table 6.1: Circulation, contour projection areas, and discrete vertical vorticity for material curve during backward trajectory analysis, beginning at 3600 s. Projection areas A_i, A_j, and A_k are areas of the projection of the curve onto planes normal to the x axis, y axis, and z axis, respectively. At 3600 s contour consisted of 200 equally spaced points about a grid cell with length 333 m centered about region of maximum vertical vorticity as found by finite-difference method.

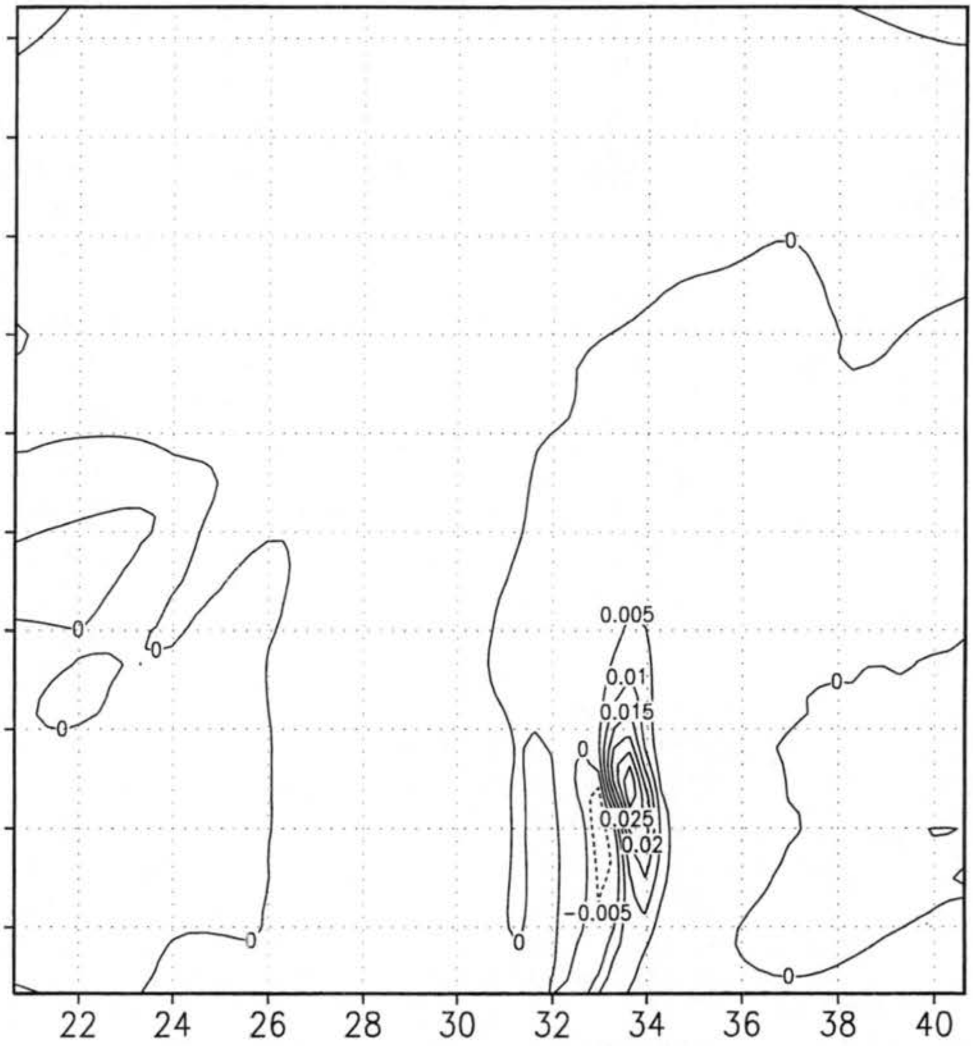

Figure 6.7: Vertical vorticity at 3300 s on Grid 1 contoured every $0.005\ \mathrm{s}^{-1}$. Axis labels are distance in kilometers.

time (s)	tilting ($1 \times 10^{-6}\mathrm{s}^{-2}$)	stretching ($1 \times 10^{-4}\mathrm{s}^{-2}$)	circulation term ($1 \times 10^{-4}\mathrm{s}^{-2}$)
3594	0.91	34.66	-11.90
3582	-0.08	24.00	4.64
3570	-0.12	8.81	14.34
3558	-0.04	2.84	3.50
3546	-0.02	2.10	-4.97
3534	0.00	2.19	-2.12
3522	0.00	1.83	-0.54
3510	0.00	1.39	0.34
3498	0.00	1.04	0.24
3486	0.00	0.74	0.44
3474	0.00	0.44	1.50
3462	0.00	0.25	1.63
3450	0.00	0.10	0.64
3438	0.00	0.03	0.98
3426	0.00	-0.02	0.18
3414	0.00	-0.05	0.62
3402	0.00	-0.11	1.09
3390	0.00	-0.18	1.12
3378	0.00	-0.22	-0.03
3366	0.00	-0.18	-0.66
3354	0.00	-0.10	-0.51
3342	0.00	-0.07	0.50
3330	0.00	-0.06	0.08
3318	0.00	-0.05	-0.04
3306	0.00	-0.05	-0.02

Table 6.2: Magnitude of average tilting, average stretching, and circulation tendency contributions to the discrete vertical vorticity tendency during the backward trajectory analysis of the material contour described in Table 6.1. Terms correspond to those found in (6.17). Note different scale for tilting terms.

that these conditions do in fact apply at the times when the curve's circulation is positive. The same conditions but with a negative circulation will cause the average stretching term to possess a greater negative value than the average tilting term.

The clustering of points in Figure 6.3 suggests that there may be a way to continue to trace the source of vorticity backwards in time even when the circulation of the entire material curve is (or appears to be) negative. It is apparent that along both of the north and east sides of the contour at the reference time there are at least two points from which parcels on opposite sides become arbitrarily distant over the backwards integration. For each of the inner hook-shaped region, the crescent-shaped region, and the tendril tip region, the distance to other regions is growing much more rapidly than the size of the region itself. The difference in θ_e values between the crescent-shaped region and the other regions further indicates these parcels of air have greatly different source regions, and there is no reason not to expect the distance between the regions to continue to grow in (backwards) time. This implies the existence of at least two unstable trajectories in reverse time on both the north and east sides of the reference contour, from which all points no matter how close will ultimately diverge some finite distance (Lorenz 1963). The presence of a mixture of θ_e values in the inner hook-shaped region suggests that in time an unstable trajectory may appear here as well. In fact, this region may be the remains of an earlier combination of high and low θ_e air that is simply rotating in place while the internal θ_e gradients are weakened by diffusion. But for now we will treat it as one region.

We can imagine partitioning the original contour into three distinct subcontours as in Figure 6.8, where the subcontour lines within the grid cell are in close proximity to all the unstable backward trajectory points. Adjacent subcontours can be made arbitrarily close, but are located on opposite sides of the set of unstable points. The result of the backward trajectory analysis of the subcontours will then be three spatially- distinct material contours, but whose circulation at the reference time should sum to the circulation of the original contour. When our linear interpolation scheme is used, we find that if we map the original RAMS material curve onto the unit square, the unstable trajectory points on the curve are found near $(0.20, 1.00)$, $(0.35, 1.00)$, $(1.00, 0.45)$, and $(1.00, 0.61)$. We can assign the 200 material points on the perimeter of the grid cell either to Region I (corresponding to the tip of the tendril), Region II (the crescent-shaped region), or Region III (the inner hooked loop). Three points near the unstable trajectories and one in the northeast corner

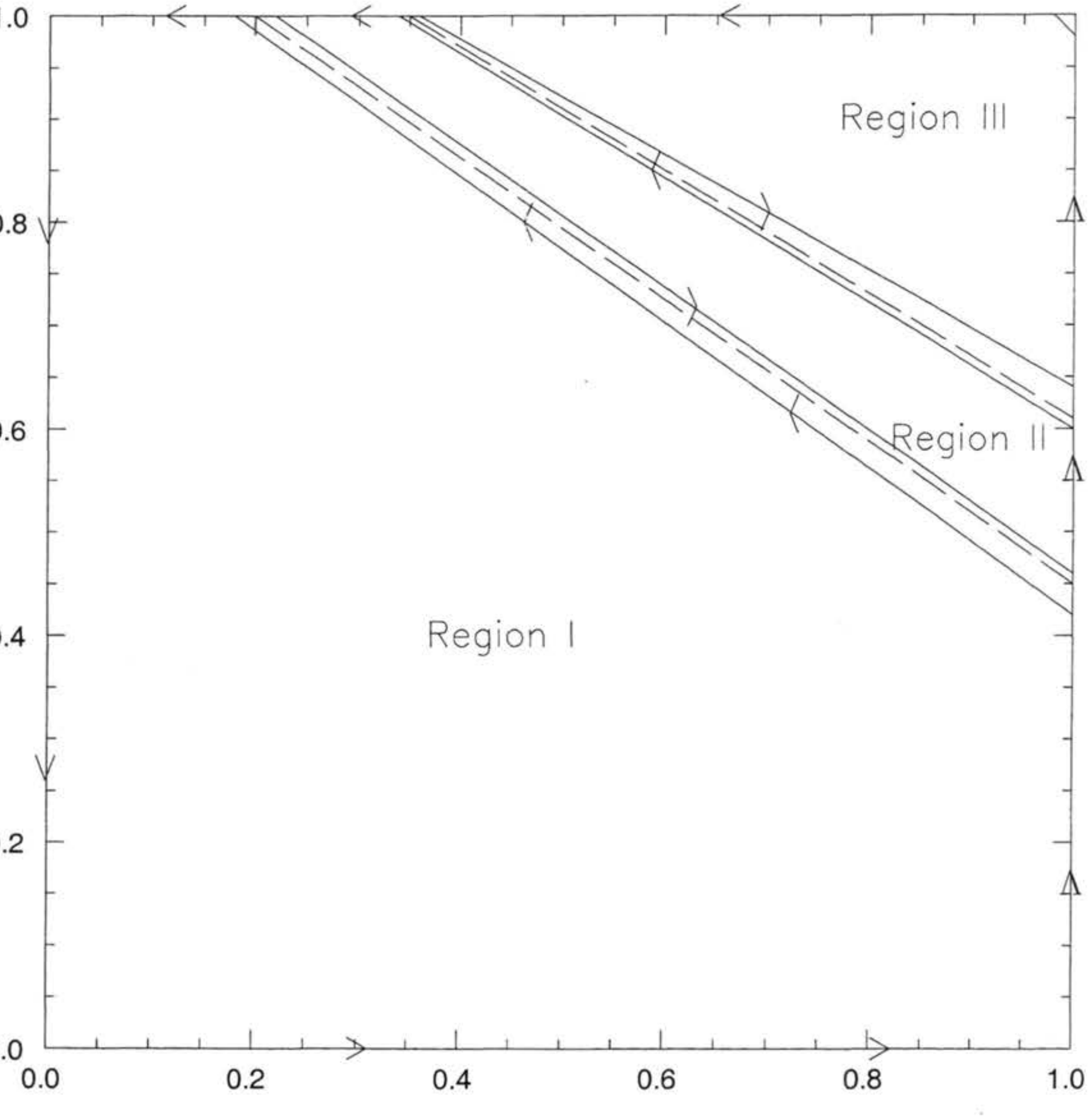

Figure 6.8: Division of a circulation contour enclosing the unit square into three subcontours. Dashed line indicates the set of unstable backwards trajectory points, which is assumed to be a line segment within the unit square. Positions of unstable points on the perimeter correspond to those of the original RAMS material contour.

of the reference material contour were excluded in order to keep the remaining contours reasonably compact at 3300 s. The 3300 s distribution of points from all three regions (Figure 6.9) confirms that three well-segregated subcontours have been generated. No other unstable trajectories are obvious for this period, although the mixture of θ_e in Region III suggests that in (backwards) time it too may develop an unstable trajectory.

Note that we have eliminated the need to calculate circulation over the longest and narrowest portions of the tendril. Furthermore, because the tendrils are narrowest near the unstable trajectories, the subcontour extensions within the original grid cell in Figure 6.8 are precisely those portions of the subcontours that become pinched together and shrink to almost zero length. The implication is that we need not be concerned about determining the material points of the 'subcontour extensions' within the original grid cell; to compute the trajectories of the subcontours we may simply consider the points on the perimeter of the original grid cell, and then connect the endpoints with single line segments to close the loop. If these connecting segments are of a length on the order of the model grid spacing, then the precise location of the connecting segments is a function of the interpolation procedure anyway; and if the connecting segments are of lengths on the order of those of the other subcontour segments, then the accuracy of the circulation calculation over the connecting segments should be as accurate as that over the rest of the contour.

However, it should be kept in mind that the total circulation contribution of the tendril regions is not necessarily negligible; if we find this in fact to be the case, we will be forced to examine these long, narrow regions.

Also, while convenient, converting the material contour backwards trajectory problem into three subcontour backwards trajectory problems raises some questions of determinism. If we were to take the limit as the grid size approaches zero, we would expect the analysis to reduce to finding the circulation history in the neighborhood of a point's backwards

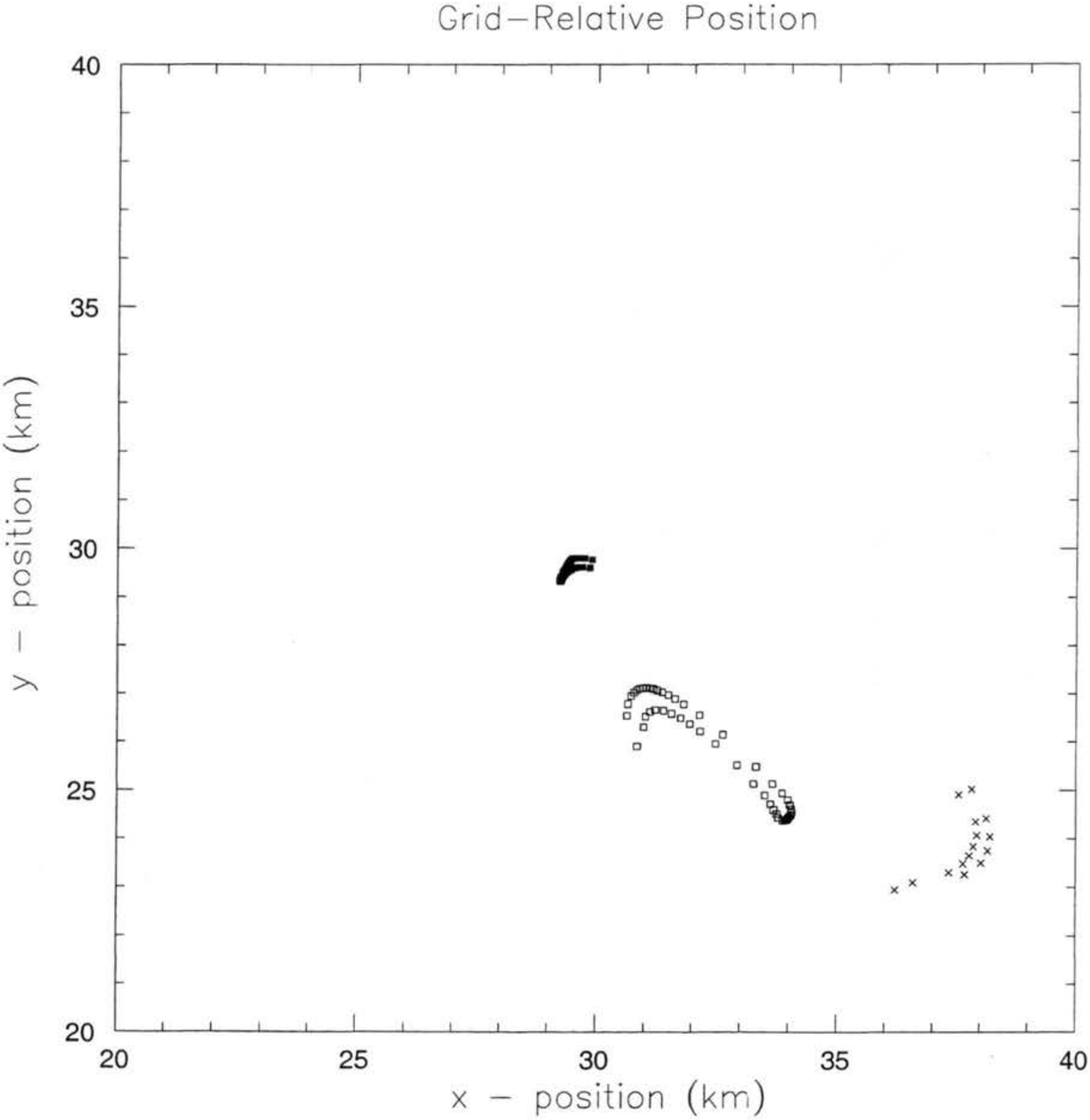

Figure 6.9: Same as Figure 6.3, but where solid squares denote points in Region I, crosses denote points in Region II, and open squares denote points in Region III.

trajectory, which is unique. What are we to conclude, then, about sources of circulation when in the discrete case we three separate source regions?

In order to address this question, first consider the original square contour at the reference time, where all velocity on and within the grid cell can be considered to be linearly extrapolated. Because of the linear interpolation, we have essentially assumed constant velocity gradients and hence vertical vorticity within the grid cell. (In the current procedure this is strictly true only for a quadrant of the grid cell because of the influence of neighboring grid cells in the average; we will assume this effect is small in the discussion that follows, although this is not necessary for the conclusion.) Thus, each subcontour should contain the same average vorticity, and the circulation of each subcontour should be proportional to its enclosed area. During the backwards trajectory analysis the average vorticity of each contour will begin to differ from each other. Now consider analyzing the results of the backwards trajectory analysis in forward time, back towards the reference state. The fact that at the reference time the velocity fields must be linear within the grid cell imposes a constraint on the flow (including, in particular, that the final average vorticity for all subcontours must become identical). This constraint will, in forward time, be perceived as a 'forcing'. The forcing in fact will resemble diffusion, in that it removes any non-linear velocity gradients and tends to equilibrate neighboring vorticity values. However, this forcing is entirely an artifact of the interpolation procedure. Furthermore, the numerical model during the actual simulation possesses 'real' diffusion, which will tend to remove non-linear velocity gradients on scales larger than the grid cell, with much the same effect.

Thus, if when examining the subcontours, it is apparent that one subcontour is losing circulation diffusively to the other subcontours, we may safely attribute the source of the circulation to the trajectory of that subcontour. If however all subcontours seem to be gaining most of their circulation diffusively in ways that cannot be explicitly resolved, then it can be concluded that the extended tendril regions are the main source of circulation.

6.6 Subcontour Evolution in RAMS

Now we will attempt to divide the material contour into subcontours. The points on the perimeter of the grid cell at the reference time are assigned to Region I, Region II, and Region III as in Figure 6.9. We then close all the subcontours by connecting the points of each region across the grid cell using line segments, as described in the previous section.

Tables 6.3-6.5 show the average vorticity and related quantities for the Region I, II, and III subcontours, respectively. We do in fact see that the average vorticity of each of subcontours are all nearly equal to each other and to the average vorticity of the whole contour.

Consistent with the linear interpolation, the average vertical vorticity of all subcontours is the same at 3600 s, to within roundoff error. It is clear, though, that the average vorticity of Region I is of a very transient nature. This subcontour possesses no positive circulation at 3552 s; its circulation increases fivefold in the final 36 seconds, which of course is independent of either large scale tilting or stretching. Recall that this subcontour corresponds to parcels within the vertical tip of the tendril at 3300 s, and contains fully 131 of the 200 points on the perimeter of the original grid cell.

Region III, in contrast, actually peaks in average vorticity at 3588 seconds, and loses a considerable portion of its circulation in the final time period. Otherwise, its circulation remains remarkably constant over the final hundred seconds, and the circulation is generally decreasing in forward time for the hundred seconds before that. Region III, corresponding to the inner hook area, contains average vorticity in excess of $0.05\ \mathrm{s}^{-1}$ over the final three minutes.

Region II, corresponding to the crescent-shaped region at 3300 s, contains negative circulation while it is crescent-shaped. The circulation becomes positive near 3444 seconds. Recall that near this time the crescent-shaped region is merging with the hook-shaped region. By 3492 the circulation has reached a value of 2000 $\mathrm{m}^2\ \mathrm{s}^{-1}$ that it will maintain until just before the reference time, when the circulation decreases in a manner similar to Region III. The average vorticity stays near $0.02\ \mathrm{s}^{-1}$, but then sharply increases in the final minute due to a great contraction in horizontal area (nearly a tenfold decrease from 3528 s to 3600 s.

This analysis is quantified in Table 6.6. The circulation tendency term is generally negative at the final times for Regions II and III, but positive for Region I. Near 3474 seconds, the circulation tendency term is positive for Region II, but still negative for Region III. Prior to 3570, the most significant positive average stretching occurs in Region III, from 3402-3462 seconds.

It thus appears clear that, if one is to attribute a specific trajectory to the average vorticity, it would lie within Region III. However, it is instructive to compare the circulation of the entire contour with the sum of the circulation of the three subcontours (Figure 6.10). For the final minute there is close agreement between the two, but from 3460-3540 s the circulation for the whole contour is considerably larger than that of the subcontours. Prior to 3460 seconds, the whole contour circulation becomes negative whereas the circulation of the subcontours stays nearly constant. Since the connection between Region II and Region III, which contains negative vorticity, disappears near 3444 s, a reasonable explanation is that the negative circulation for the whole contour reflects that of the Region II – Region III connection, but that the Region I – Region II connection contains positive circulation. When Region II becomes absorbed into Region III the total circulation sharply increases and achieves a large positive value due in large part to the Region I – Region II tendril. The

time (s)	circulation ($\mathrm{m^2\ s^{-1}}$)	A_i ($\mathrm{m^2}$)	A_j ($\mathrm{m^2}$)	A_k ($\mathrm{m^2}$)	ζ_{zD} ($\mathrm{s^{-1}}$)
3600	8889.07	0.00	0.00	84520.94	0.1051700
3588	8514.27	-1595.80	80.90	132349.03	0.0643225
3576	6755.55	-997.63	-207.06	213949.47	0.0315747
3564	1654.59	943.28	-1301.04	295856.28	0.0055924
3552	-282.91	1659.34	-2091.51	381951.59	-0.0007406
3540	2419.61	2483.49	-2355.98	473786.66	0.0051067
3528	2738.61	3095.34	-2672.91	564616.75	0.0048501
3516	774.82	3452.71	-3086.06	645416.81	0.0012004
3504	480.85	3735.01	-3435.11	707187.75	0.0006799
3492	349.04	4021.92	-3715.71	750873.06	0.0004648
3480	432.09	4390.30	-3991.66	774731.69	0.0005577
3468	300.24	4847.20	-4295.36	777004.69	0.0003864
3456	167.77	5431.47	-4598.91	757309.69	0.0002215
3444	84.86	6227.50	-4969.87	718377.44	0.0001181
3432	62.24	7404.99	-5602.50	664625.56	0.0000936
3420	80.80	8860.04	-6400.84	601188.50	0.0001344
3408	134.39	10569.33	-7386.05	533233.94	0.0002519
3396	214.70	12547.75	-8491.25	465161.16	0.0004611
3384	325.92	14753.33	-9713.40	400229.44	0.0008128
3372	462.62	17372.03	-11154.19	340352.66	0.0013542
3360	599.79	20240.60	-12669.52	286403.16	0.0020798
3348	704.63	23293.38	-14183.24	238824.66	0.0029124
3336	788.61	26640.13	-15834.95	197113.12	0.0039043
3324	869.61	30158.92	-17632.29	160704.02	0.0051671
3312	947.16	34126.45	-19590.67	128836.93	0.0067244
3300	1000.03	38427.78	-21771.69	100820.78	0.0083218

Table 6.3: Same as Figure 6.1, but for the Region I subcontour.

time (s)	circulation ($\mathrm{m}^2\ \mathrm{s}^{-1}$)	A_i (m^2)	A_j (m^2)	A_k (m^2)	ζ_{zD} (s^{-1})
3600	897.21	0.00	0.00	8716.28	0.1029355
3588	1616.07	-361.64	-105.97	14649.29	0.1102445
3576	2140.45	-975.20	-158.26	24042.82	0.0888763
3564	1578.73	-1616.61	-44.98	40161.33	0.0392461
3552	2123.16	-1174.54	473.19	54621.46	0.0388495
3540	1719.27	-949.32	799.49	69019.00	0.0249020
3528	2360.02	-711.85	1186.73	85559.55	0.0275761
3516	2108.22	-458.74	1393.36	105447.47	0.0199892
3504	2265.48	-234.65	1384.68	131106.27	0.0172778
3492	2229.96	-154.55	1167.45	163527.39	0.0136359
3480	1728.91	-257.39	864.17	200766.28	0.0086114
3468	1084.21	-500.34	608.65	242149.73	0.0044774
3456	724.39	-744.23	450.06	285621.56	0.0025362
3444	385.89	-932.99	389.43	327439.75	0.0011785
3432	-78.47	-1069.55	360.16	366166.25	-0.0002143
3420	-408.25	-1158.22	324.41	403329.69	-0.0010122
3408	-510.73	-1216.66	294.73	437695.94	-0.0011668
3396	-488.68	-1261.56	270.97	469720.12	-0.0010404
3384	-353.50	-1300.65	262.59	499327.78	-0.0007079
3372	-304.95	-1337.30	263.53	525536.56	-0.0005803
3360	-311.95	-1371.96	267.76	548316.31	-0.0005689
3348	-263.79	-1404.97	272.09	567351.50	-0.0004649
3336	-227.31	-1435.85	274.99	583193.88	-0.0003898
3324	-197.89	-1465.15	276.74	595777.75	-0.0003322
3312	-163.74	-1492.87	277.18	605458.19	-0.0002704
3300	-138.58	-1519.29	274.19	612300.25	-0.0002263

Table 6.4: Same as Table 6.1, but for the Region II subcontour.

time (s)	circulation ($\mathrm{m}^2\ \mathrm{s}^{-1}$)	A_i (m^2)	A_j (m^2)	A_k (m^2)	ζ_{zD} (s^{-1})
3600	1314.82	0.00	0.00	12042.82	0.1091785
3588	2450.04	-480.56	-67.67	18177.14	0.1346909
3576	2170.66	-1356.95	-202.33	25890.34	0.0836058
3564	2729.25	-2429.42	-134.13	31485.29	0.0861689
3552	2048.56	-3021.67	845.70	33052.83	0.0614248
3540	2247.75	-2665.27	2487.35	34200.13	0.0649849
3528	2366.46	-1464.16	3926.58	34545.43	0.0675092
3516	2571.98	136.11	4557.84	35107.14	0.0720455
3504	2842.13	1601.19	4175.78	36425.38	0.0768674
3492	3144.08	2478.48	2919.41	38176.18	0.0815366
3480	3430.76	2636.25	1143.64	41306.62	0.0826559
3468	3640.49	2138.23	-430.90	45991.96	0.0789773
3456	3802.38	1077.22	-1214.03	53082.08	0.0715652
3444	4653.75	21.28	-1294.95	64065.39	0.0726109
3432	5377.98	-674.62	-1023.33	84699.02	0.0634819
3420	7228.63	-1092.04	-683.71	118779.09	0.0608506
3408	8255.46	-1022.76	-262.74	179354.36	0.0460272
3396	6937.19	-661.19	-15.82	268504.31	0.0258363
3384	4899.03	-156.75	18.59	374711.94	0.0130741
3372	5127.11	267.88	-32.01	488944.53	0.0104861
3360	6206.77	520.24	-74.89	617420.62	0.0100527
3348	6478.52	662.87	-121.80	764259.62	0.0084769
3336	6204.94	751.06	-181.43	927019.31	0.0066934
3324	5911.96	801.36	-255.55	1101290.88	0.0053682
3312	5488.35	840.48	-342.07	1283117.50	0.0042774
3300	5223.26	873.11	-457.40	1462515.62	0.0035714

Table 6.5: Same as Table 6.1, but for the Region III subcontour.

time	Region I			Region II			Region III		
	tlt.	str.	circ. tnd.	tlt.	str.	circ. tnd.	tlt.	str.	circ. tnd.
3594	0.01	31.68	3.03	0.03	46.15	-54.80	0.04	41.87	-65.28
3582	0.00	19.19	8.96	0.04	41.15	-23.98	0.10	32.27	10.88
3570	0.00	5.02	17.12	0.00	27.39	15.54	0.11	13.95	-16.31
3558	0.00	0.52	4.84	-0.02	9.99	-9.79	0.09	3.08	17.46
3546	0.00	0.39	-5.32	0.00	6.21	5.52	0.06	1.86	-4.89
3534	0.00	0.73	-0.52	0.00	4.70	-6.99	0.09	0.65	-2.84
3522	0.00	0.34	2.72	0.00	4.14	2.22	0.06	1.00	-4.84
3510	0.00	0.07	0.36	0.00	3.38	-1.12	-0.05	2.23	-6.20
3498	0.00	0.03	0.15	0.00	2.85	0.20	-0.16	2.94	-6.67
3486	0.00	0.01	-0.09	0.00	1.90	2.32	-0.18	5.21	-5.98
3474	0.00	0.00	0.14	0.00	1.02	2.45	-0.09	7.15	-4.00
3462	0.00	-0.01	0.14	0.00	0.48	1.14	-0.04	8.95	-2.73
3450	0.00	-0.01	0.09	0.00	0.21	0.92	-0.02	11.28	-12.21
3438	0.00	-0.01	0.03	0.00	0.04	1.12	-0.01	15.83	-8.27
3426	0.00	-0.01	-0.02	0.00	-0.05	0.72	0.00	17.52	-15.59
3414	0.00	-0.02	-0.08	0.00	-0.07	0.20	0.00	18.35	-5.99
3402	0.00	-0.04	-0.13	0.00	-0.06	-0.04	0.00	12.08	5.11
3390	0.00	-0.08	-0.22	0.00	-0.04	-0.23	0.00	5.40	5.43
3378	0.00	-0.15	-0.31	0.00	-0.03	-0.08	0.00	2.61	-0.45
3366	0.00	-0.24	-0.37	0.00	-0.02	0.01	0.00	2.00	-1.65
3354	0.01	-0.37	-0.33	0.00	-0.01	-0.07	0.00	1.65	-0.33
3342	0.02	-0.53	-0.32	0.00	-0.01	-0.05	0.00	1.22	0.27
3330	0.04	-0.73	-0.37	0.00	-0.01	-0.04	0.00	0.87	0.24
3318	0.11	-0.99	-0.42	0.00	0.00	-0.05	0.00	0.61	0.30
3306	0.27	-1.27	-0.34	0.00	0.00	-0.03	0.00	0.43	0.16

Table 6.6: Same as Table 6.1, but for each of the three subcontours.

circulation of this tendril in turn decreases through diffusion into the other subcontours as well as its environment.

So we are faced with the challenging situation that a large portion of the circulation of the original material contour at the reference time resides on a scale less than six meters wide in at least one dimension, and only remains manifest on a resolvable scale via the effects of diffusion, either physical or numerical.

6.7 Vorticity Kneading

It is still of value to continue the backward trajectory analysis for the parcels in the Region III contour. The circulation of Region III from 3300 - 3600 s shows no sign of being acquired diffusively. The contribution of Region III to the total circulation in Figure 6.10 is small simply because the total area of Region III is small. Region III therefore is an opportunity to further trace the origins of the vertical vorticity that is much easier to work with than the extended tendril.

The Region III subcontour was integrated backwards in time for a further 300 s using the same procedure as in the previous section. It should be noted that the final time of 3000 s is prior to the 'vorticity jumps' at any level, which appear to be caused by baroclinic effects along the gust front.

Figures 6.11 a-d and Figure 6.12 show the configuration of the Region III subcontour at successively earlier 60 s increments. As speculated earlier, the Region III subcontour does possess a couple of unstable trajectory points, and seems to break down into two even smaller subcontours. The image resembles that of a medicine capsule being separated into two portions. The Region III subcontour seems to form from the combination of high θ_e air from the southeast and low θ_e air from the downdraft to the northwest (Figure 6.13);

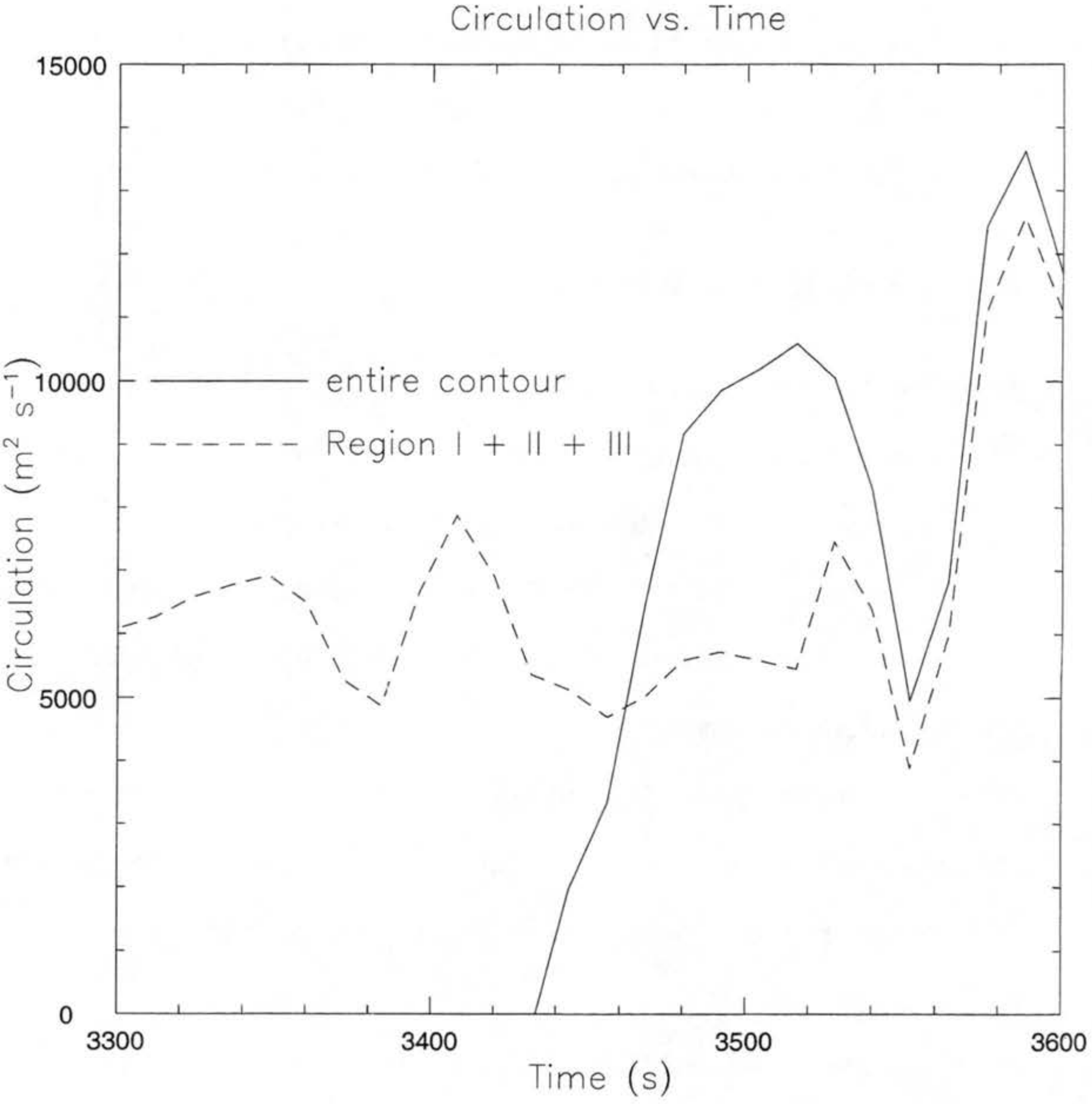

Figure 6.10: Circulation of the whole material contour in Table 6.1, and of the three sub-contour regions.

the subcontour then rotates 360° before combining again with air parcels from these source regions, namely Regions II and I.

One difference between the backward-time evolution of the original contour and that of the Region III subcontour, however, is that the width of long region connecting the two source clusters of air parcels for Region III is not much narrower than the width of the cluster regions themselves. The ends of the two source clusters of material points do not conveniently 'pinch' together. On the other hand, the shape of Region III itself, even when subject to extreme extension, is well-behaved and straightforward to calculate.

Therefore we will divide Region III into further subcontours, Regions IIIa, IIIb, and IIIc, where IIIa contains the low θ_e source parcels, IIIc contains the high θ_e source parcels, and IIIb is the transition region in between, wholly contained between four points of the Region III set (Figure 6.14). This time, however, the subcontour boundaries within Region III will be explicitly translated as material curves, by creating 200 additional material points to surround Region IIIb. Region IIIb at 3300 s is a quadrilateral connecting the four points of Region III closest to the unstable trajectory; each side of this quadrilateral is decomposed into 50 equally-spaced points for the backwards trajectory analysis. The material points used for the remainder of Regions IIIa and IIIc are simply those of the original Region III.

Tables 6.7 - 6.9 show the circulation and average vorticity information for Regions IIIa-c from 3000 - 3300 s. It can be seen that only in Region IIIb is there mesocyclonic vertical vorticity by 3300 s. Both Regions IIIa and IIIb make significant contributions to the circulation of Region III while the high θ_e parcels of Region IIIa are not significant. The circulation in the other two regions remain relatively constant from 3120 - 3300 s, but the 3000 - 3120 s time period is when most of the circulation is generated. Circulation generation appears to occur slightly earlier for Region IIIb than for Region IIIa. Because these areas are near a baroclinic zone, and because the circulation is generated when the

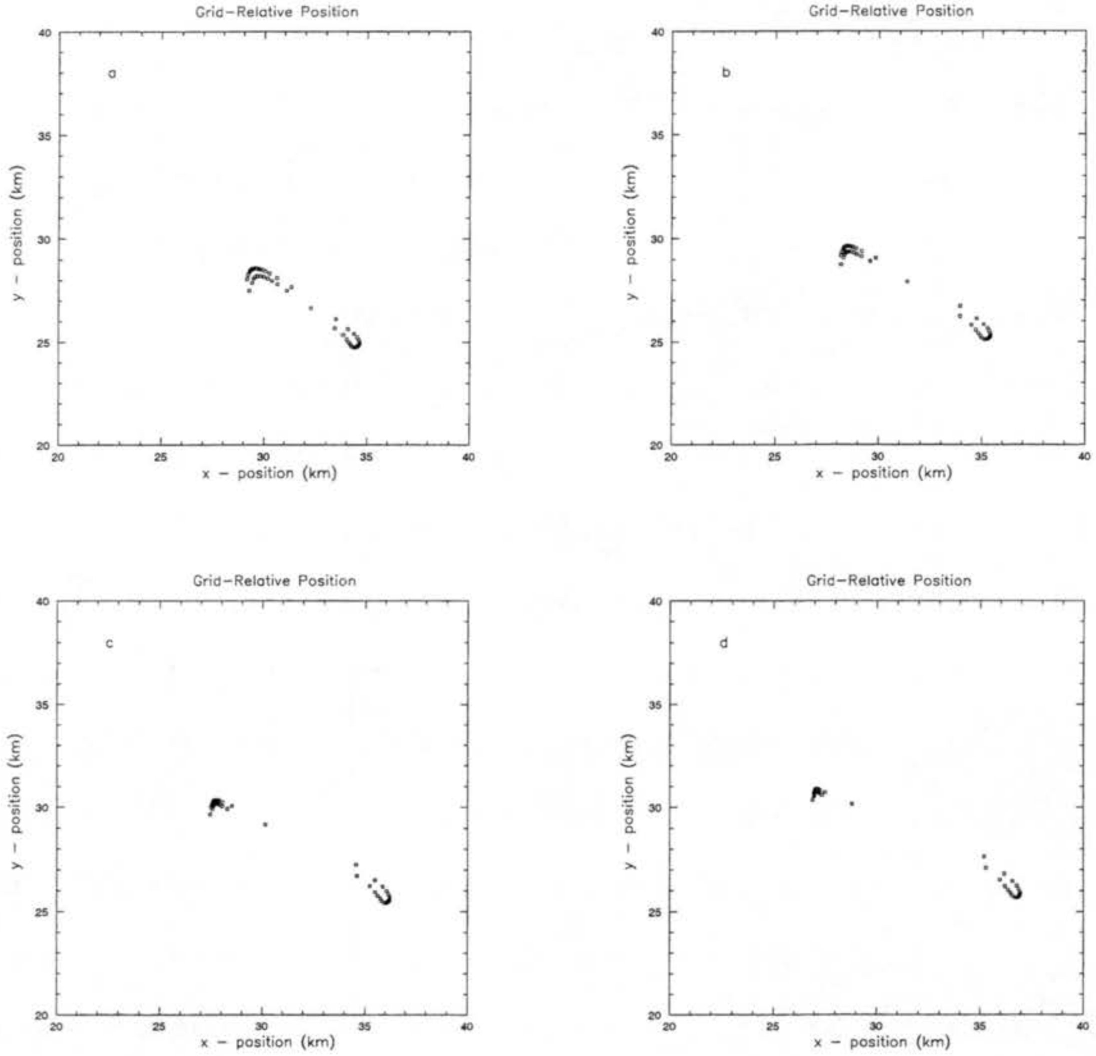

Figure 6.11: Region III subcontour at: a) 3240 s, b) 3180 s, c) 3120 s, and d) 3060 s during Grid 1 simulation.

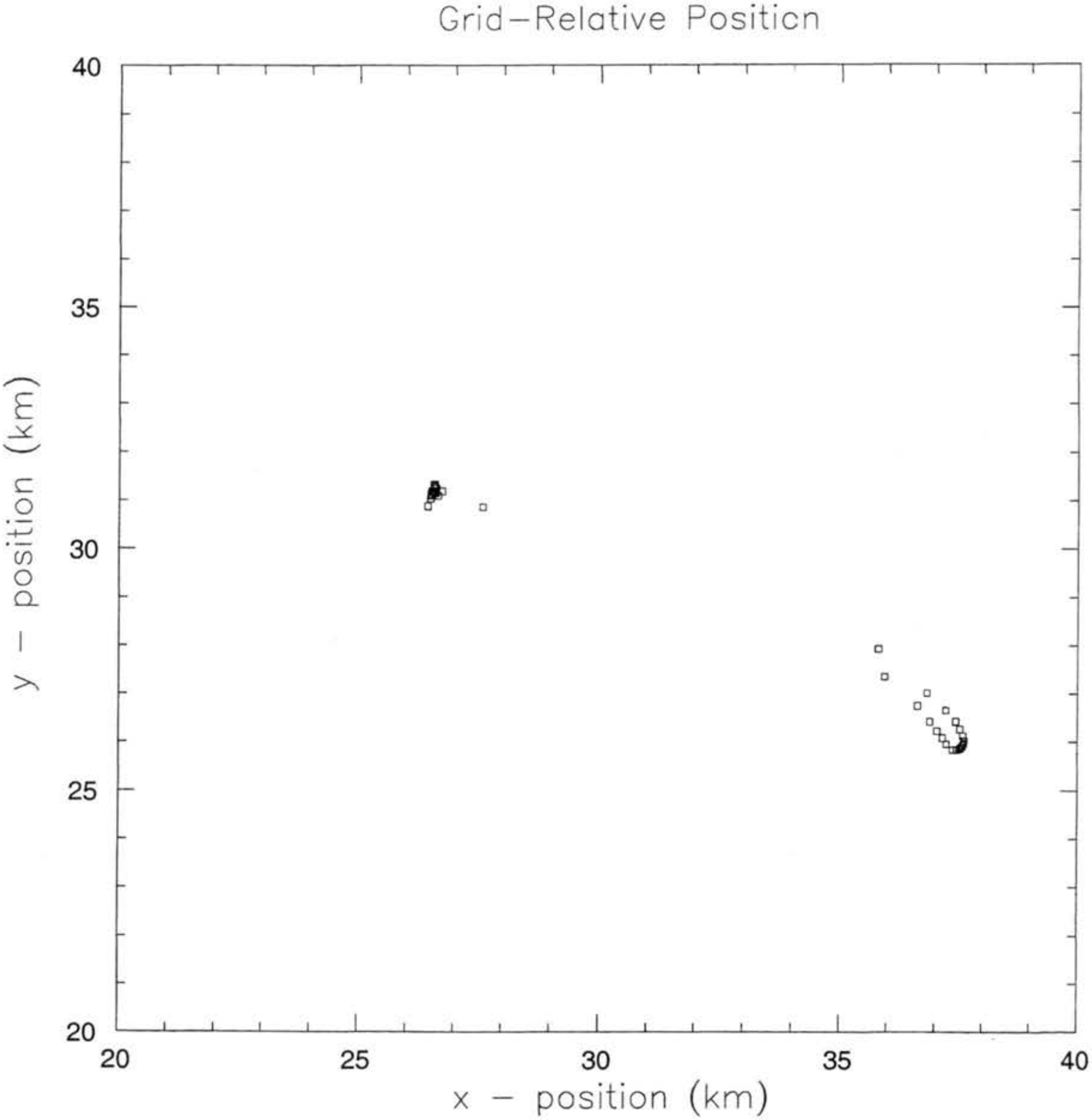

Figure 6.12: Same as Figure 6.11, but at 3000 s.

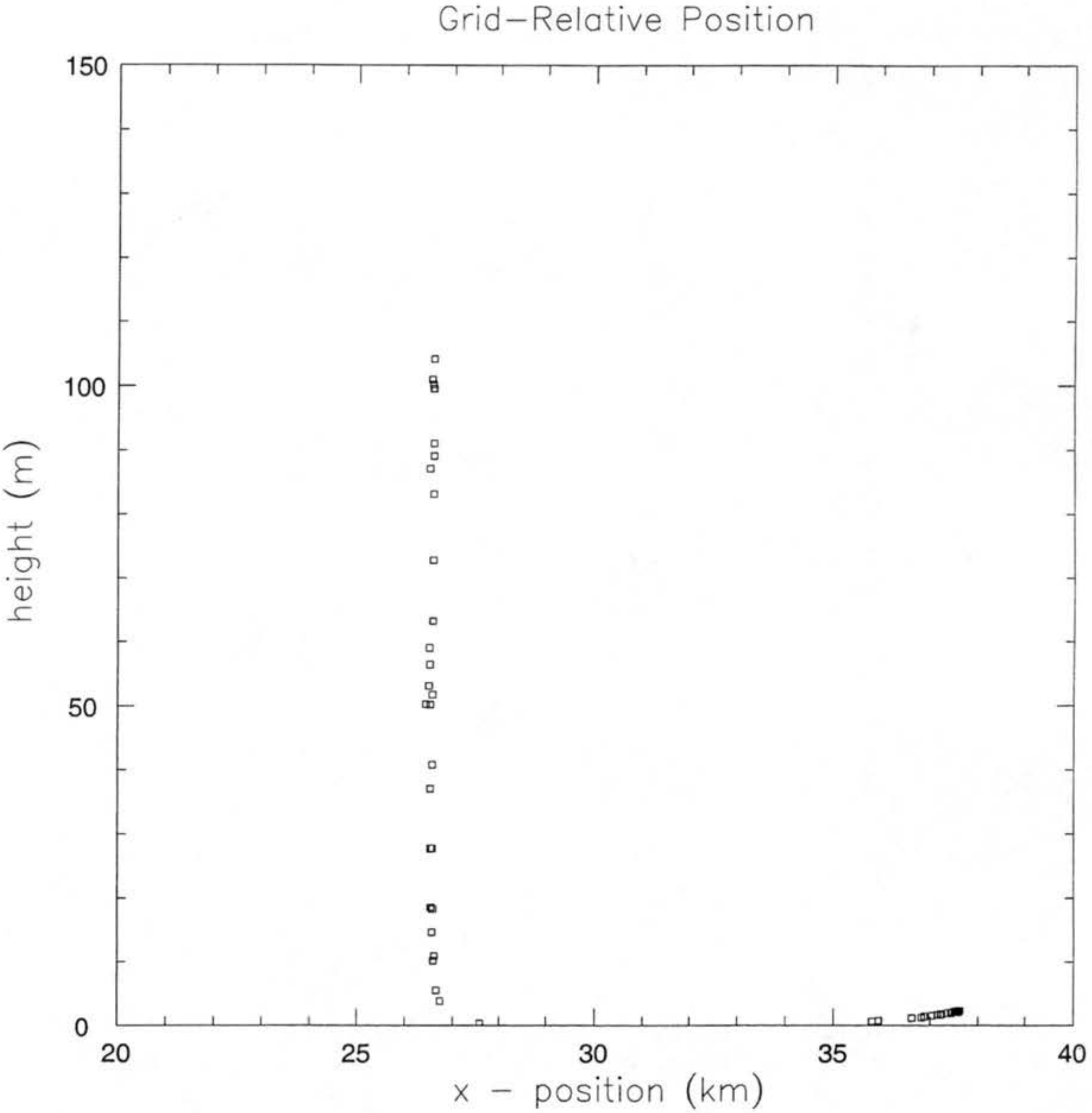

Figure 6.13: Same as Figure 6.12, but showing a side view of the subcontour from the xz plane.

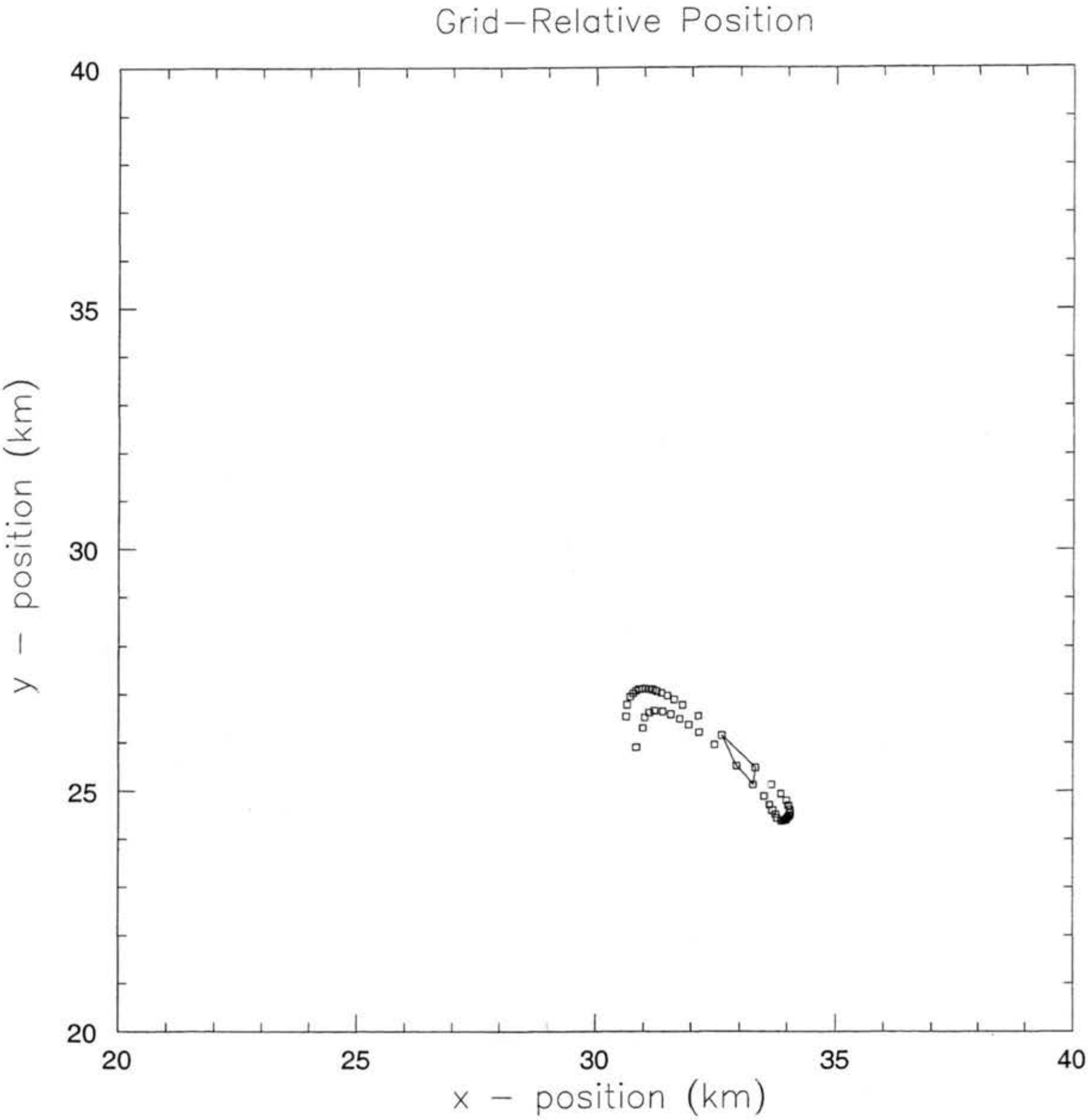

Figure 6.14: Same as Figure 6.11, but at 3300 s. Solid line denotes Region IIIb subcontour

time (s)	circulation ($\mathrm{m^2\ s^{-1}}$)	A_i ($\mathrm{m^2}$)	A_j ($\mathrm{m^2}$)	A_k ($\mathrm{m^2}$)	ζ_{zD} ($\mathrm{s^{-1}}$)
3300	2190.06	1278.35	-777.97	938192.69	0.0023343
3288	2160.00	1446.21	-863.09	984954.19	0.0021930
3276	2347.48	1625.18	-950.34	1008565.25	0.0023275
3264	2395.82	1811.24	-1037.38	1009797.19	0.0023726
3252	2339.82	2006.80	-1118.04	990178.44	0.0023630
3240	2262.14	2206.50	-1198.18	952659.19	0.0023745
3228	2276.88	2412.29	-1271.41	903265.88	0.0025207
3216	2150.83	2621.19	-1332.82	842862.00	0.0025518
3204	2148.87	2838.26	-1379.24	777442.50	0.0027640
3192	2216.37	3059.23	-1410.23	707024.62	0.0031347
3180	2315.61	3288.02	-1423.22	636565.31	0.0036375
3168	2416.12	3521.86	-1420.32	565680.75	0.0042710
3156	2441.09	3763.07	-1399.76	496402.72	0.0049172
3144	2387.49	4008.23	-1367.02	430782.88	0.0055417
3132	2376.79	4263.82	-1322.13	368685.84	0.0064457
3120	2217.05	4523.36	-1268.16	311389.66	0.0071182
3108	1904.24	4801.26	-1217.28	259759.45	0.0073281
3096	1746.24	5538.96	-1358.65	213330.80	0.0081797
3084	1620.06	6811.78	-1675.66	172696.69	0.0093655
3072	1330.22	8382.02	-2088.52	137132.36	0.0096620
3060	1212.73	9967.59	-2514.83	106728.60	0.0112583
3048	1094.60	11222.95	-2778.05	81109.48	0.0132265
3036	888.06	12753.28	-3136.00	60185.09	0.0140848
3024	904.28	14699.39	-3586.84	42935.01	0.0187348
3012	700.67	17132.15	-4173.63	28735.60	0.0177133
3000	681.45	19454.51	-4758.25	17008.55	0.0167879

Table 6.7: Same as Table 6.1, but for the Region IIIa subcontour over the time period 3000 - 3300 s.

subcontours have significant orientations perpendicular to the y-axis (i.e., they have tilt in the north/south direction), it is tempting to ascribe the origin of the circulation to the baroclinity term in the circulation equation. Yet it was found that the resolution of the material contour was insufficient to provide an adequate analysis of the circulation source terms.

In Table 6.10 we display the large-scale stretching, tilting, and circulation tendency terms for subcontours IIIa and IIIb. It can be seen how near 3000 s tilting is actually the greatest contribution to the average vertical vorticity of Region IIIa; later, the circulation

time (s)	circulation (m^2 s^{-1})	A_i (m^2)	A_j (m^2)	A_k (m^2)	ζ_{zD} (s^{-1})
3300	2721.33	-16.76	27.13	188560.41	0.0144321
3288	2885.60	-32.83	21.82	261581.58	0.0110313
3276	2986.21	-52.31	13.66	352148.88	0.0084800
3264	2999.04	-71.87	3.27	459454.91	0.0065274
3252	2963.58	-88.84	-9.01	582159.88	0.0050907
3240	2908.01	-102.61	-23.41	718635.00	0.0040466
3228	2855.08	-113.87	-40.07	866611.38	0.0032945
3216	2783.64	-122.95	-58.50	1023454.81	0.0027199
3204	2704.58	-130.45	-78.90	1186154.38	0.0022801
3192	2686.19	-136.03	-100.37	1352294.50	0.0019864
3180	2487.30	-140.12	-123.15	1518727.25	0.0016378
3168	2451.93	-142.89	-147.01	1682118.25	0.0014576
3156	2399.86	-144.13	-171.81	1840840.75	0.0013037
3144	2258.19	-144.16	-197.65	1991640.62	0.0011338
3132	2081.94	-142.74	-223.87	2133173.00	0.0009760
3120	1916.48	-140.19	-251.16	2264995.50	0.0008461
3108	1787.36	-136.27	-278.17	2384879.75	0.0007495
3096	1618.73	-131.21	-305.51	2492819.75	0.0006494
3084	1567.84	-124.83	-332.65	2589156.00	0.0006055
3072	1367.62	-117.23	-359.68	2672649.75	0.0005117
3060	1195.30	-108.45	-386.56	2744219.50	0.0004356
3048	1133.68	-98.53	-413.25	2803574.25	0.0004044
3036	660.51	-87.28	-439.71	2851191.50	0.0002317
3024	621.35	-74.75	-466.05	2887841.75	0.0002152
3012	181.36	-61.02	-492.59	2913782.75	0.0000622
3000	61.24	-46.19	-519.58	2929976.00	0.0000209

Table 6.8: Same as Table 6.7, but for the Region IIIb subcontour.

time (s)	circulation ($\mathrm{m}^2\ \mathrm{s}^{-1}$)	A_i (m^2)	A_j (m^2)	A_k (m^2)	ζ_{zD} (s^{-1})
3300	612.24	-388.50	293.41	335784.97	0.0018233
3288	358.04	-447.15	295.47	393558.09	0.0009097
3276	187.45	-487.07	297.40	450610.44	0.0004160
3264	122.17	-514.16	298.04	506315.84	0.0002413
3252	129.70	-534.29	296.79	559926.69	0.0002316
3240	164.86	-551.42	293.05	610665.94	0.0002700
3228	150.46	-566.95	287.38	657937.56	0.0002287
3216	102.87	-580.68	280.79	701364.75	0.0001467
3204	121.81	-593.40	272.90	740332.75	0.0001645
3192	121.94	-605.36	264.18	774840.56	0.0001574
3180	91.63	-616.91	253.61	804380.50	0.0001139
3168	94.95	-627.37	242.60	829220.06	0.0001145
3156	85.10	-637.04	231.30	849458.62	0.0001002
3144	85.08	-645.86	220.32	865709.06	0.0000983
3132	81.09	-654.22	209.41	878180.12	0.0000923
3120	75.31	-662.29	198.58	887284.81	0.0000849
3108	82.07	-669.90	187.86	893496.44	0.0000919
3096	66.18	-676.87	177.33	896936.00	0.0000738
3084	60.29	-683.26	167.13	898295.75	0.0000671
3072	54.00	-689.25	156.86	897735.62	0.0000602
3060	59.22	-694.83	146.77	895686.19	0.0000661
3048	61.15	-699.80	137.05	892403.88	0.0000685
3036	53.70	-704.04	127.71	888082.06	0.0000605
3024	44.19	-707.64	118.77	883228.12	0.0000500
3012	39.04	-710.63	110.15	877963.44	0.0000445
3000	39.61	-713.20	101.80	872505.50	0.0000454

Table 6.9: Same as Table 6.7, but for the Region IIIc subcontour.

time	Region IIIa			Region IIIb		
	tilting	stretching	circ. tend.	tilting	stretching	circ. tend.
3294	0.00	0.09	0.03	0.00	3.47	-0.62
3282	0.00	0.04	-0.16	0.00	2.42	-0.28
3270	0.00	0.00	-0.04	0.00	1.66	-0.03
3258	0.00	-0.04	0.05	0.00	1.15	0.06
3246	0.00	-0.08	0.07	0.00	0.80	0.07
3234	0.00	-0.11	-0.01	0.00	0.57	0.06
3222	0.00	-0.15	0.12	0.00	0.42	0.06
3210	0.00	-0.18	0.00	0.00	0.31	0.06
3198	0.00	-0.23	-0.08	0.00	0.23	0.01
3186	0.00	-0.30	-0.12	0.00	0.18	0.12
3174	0.00	-0.39	-0.14	0.00	0.13	0.02
3162	0.00	-0.50	-0.04	0.00	0.10	0.02
3150	0.00	-0.62	0.10	0.00	0.08	0.06
3138	0.00	-0.78	0.02	0.00	0.06	0.07
3126	0.00	-0.95	0.39	0.00	0.05	0.06
3114	0.00	-1.09	0.92	0.00	0.03	0.05
3102	0.00	-1.27	0.56	0.00	0.03	0.06
3090	0.00	-1.54	0.55	0.00	0.02	0.02
3078	0.01	-1.82	1.58	0.00	0.01	0.06
3066	0.02	-2.16	0.81	0.00	0.01	0.05
3054	0.06	-2.74	1.05	0.00	0.01	0.02
3042	0.15	-3.25	2.40	0.00	0.00	0.14
3030	0.48	-4.14	-0.25	0.00	0.00	0.01
3018	1.54	-4.56	3.90	0.00	0.00	0.13
3006	3.96	-3.58	0.40	0.00	0.00	0.03

Table 6.10: Same as Table 6.1, but for Regions IIIa and IIIb.

tendency term is most important positive contribution. However, the expansion of the area of this circuit causes a general decrease in the average vorticity over time. For Region IIIb, there is significant contraction of the circuit near the end of the time period, resulting in the relatively high average vorticity. Tilting is of little significance for Region IIIb because this area remains near the surface.

6.8 Summary

In this chapter we have found a way to represent the material derivative of vertical vorticity on a discrete grid. Essentially the problem becomes that of performing a circulation analysis of an interpolated material contour normalized by the area of the curve. One consequence of this procedure, however, is that the source of vertical vorticity for a grid cell is not necessarily traceable to a single trajectory, in particular the trajectory of the position assigned to the vertical vorticity of the grid cell by an interpolation procedure.

A backwards trajectory analysis was performed on the region of maximum vorticity of Grid 1 in the baseline simulation at 3600 s. A square material contour of 200 points was used for this purpose. Three source regions of parcels were discovered; these regions advect as continuous curves but are connected by tendrils that undergo extreme contraction. One source region is of low-level, high θ_e to the east of the gust front; another consists of downdraft, low θ_e air. The third source region is found to be a combination parcels from the previous two source regions that has had time to diffuse and perform one revolution around the center of vorticity.

The immediate source of the strongest low-level vorticity of the simulation is large-scale stretching (material curve contraction) of parcels already present in the low-level mesocyclone; it is confirmed that not only the streamlines but the trajectories curve cyclonically. The ultimate source of low-level vertical vorticity, however, appears to lie in the long, extended zones connecting the parcels from the two main source regions; this is not unexpected because within these zones lie the major θ_e gradients. These zones undergo extreme contraction as the different θ_e air parcels rotate and combine near the mesocyclone. One region of circulation generation did appear in parcels from the downdraft source region. This would be consistent with the hypotheses of Davies-Jones and Brooks (1993) and Grasso and Cotton (1995) about the downdraft origin of the low-level vertical vorticity.

Past modeling studies using circuits of material contours to investigate the origins of low-level vorticity have found the presence of discrete source regions, in particular one located east of the storm featuring little vertical movement, and another northwest of the storm descending in the downdraft (Wicker and Wilhelmson 1995; Grasso 1996; Finley 1997; Adlerman et al. 1999). It is suggested here that discrete source regions will result from backwards trajectory analyses of even a single grid cell, and that at least to some extent the source regions for parcels can be 'unfolded' into a finite number of continuous curve segments with a common origin, which have since become intermixed by the rotation in the vortex.

There has also been uncertainty expressed in the literature over the sources of near-surface vorticity in trajectory analyses of parcels entering low-level vortices from the east, where there is little of the vertical movement that would be associated with tilting (Wicker and Wilhelmson 1995; Finley 1997). One possible explanation is offered here: the origin of the vertical vorticity of the low-level mesocyclone is not directly related to these parcels, but these parcels are seen to acquire vertical vorticity diffusively, either through explicit model diffusion or the mapping of the trajectories back onto an interpolated material curve. There was no evidence of significant circulation generation for any loop that rose to a height of 62 m from near the surface, except in close proximity to parcels from other regions.

Chapter 7

SENSITIVITY STUDIES

Here we perform a few sensitivity studies to learn more about influences on the evolution of the storm.

7.1 Influence of LCL

The observational studies of Rasmussen and Blanchard (1998) and Markowski et al. (2000) both imply that environments favorable for the generation of strongly negatively buoyant cold pools are not associated with tornadoes, even when they are associated with supercells. The most likely explanation is that the negative buoyancy resists the upward perturbation pressure gradient force that creates the convergence necessary for tornadogenesis. This assumes that the tornado is forced from above in a manner such as the DPE. Because our vortex is formed in an essentially two-dimensional process, it might be expected that this sensitivity would not appear in our simulations.

We performed simulations to test the sensitivity of the vortex generation process to the lifting condensation level (LCL) of the initial sounding, which is the level at which a surface parcel appropriately determined becomes saturated upon adiabatic lifting in the environment. The objective was to test sensitivity to this parameter independently of the CAPE, which determines the energetics of the storm. As a way to nearly fulfill the desire, we lowered the surface pressure of the sounding from the 990 mb of the basic simulation. The CAPE of a sounding is only a function of the LCL pressure, the temperature at the LCL pressure of the parcel, and the temperature profile of the environment above the LCL. In the special case where the potential temperature and mixing ratios are constant with height near the surface, none of these three factors are changed by lowering the surface pressure. However, the physical height of the LCL is lowered, and the wet bulb depression, which is related to the potential evaporative cooling of the low-level air mass, is decreased. The effect is the same as if one raised the level of the surface within the sounding.

In our simulations the sounding is actually slightly unstable in potential temperature, and possesses a noticeable decrease in mixing ratio with height. Thus, simply lowering the surface pressure without changing the rest of our sounding would not be simply equivalent to raising the height of the ground, but would also change the characteristics of the surface parcel and the CAPE. Therefore, when we lowered the surface pressure we also truncated the lowest portion of the potential temperature and mixing ratio profiles up to a height given by 10 m ≈ 0.9 mb.

Figure 7.1 shows a simulation where the surface pressure was lowered from the default 990 mb to 950 mb. We can see the after 3600 s the surface vorticity is approximately the same as for the default simulation. If anything, the maximum vertical vorticity is slightly lower, though the temperature depression of the cold pool is in fact decreased.

It was then realized that there is the question as to whether or not the wind field above $40 \times 10/0.9 = 444$ m should also be truncated. We repeated the 950 mb experiment but this time also truncated the wind field (Figure 7.2). Now the maximum vertical vorticity barely reaches mesocyclonic strength (0.01 s^{-1}), and no closed vortex or pressure depression develops (Figure 7.3 – note the change in vorticity contouring increment).

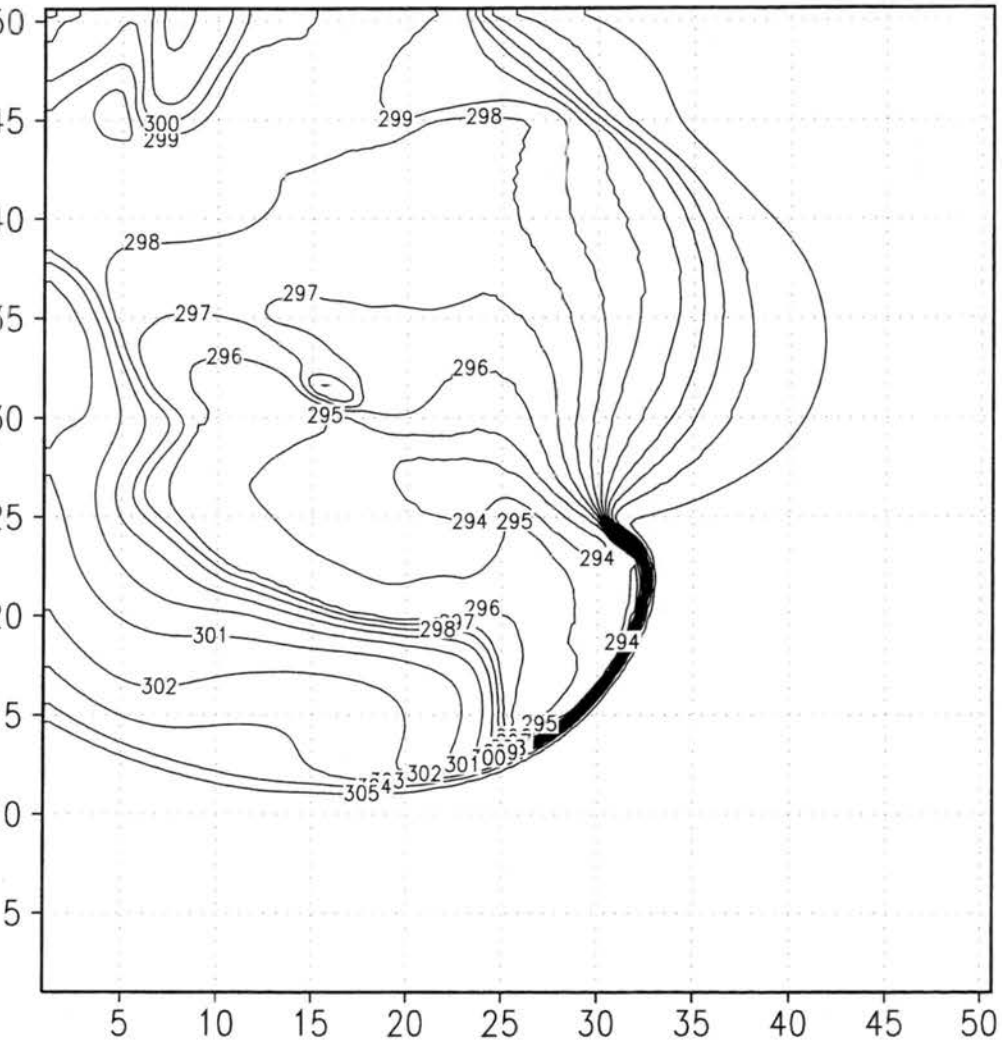

Figure 7.1: Potential temperature (thin contours) and vertical vorticity (thick contours) for 950 mb simulation at 3600 s. Contour increments are 1 K for potential temperature and $0.03\ \mathrm{s}^{-1}$ for vertical vorticity.

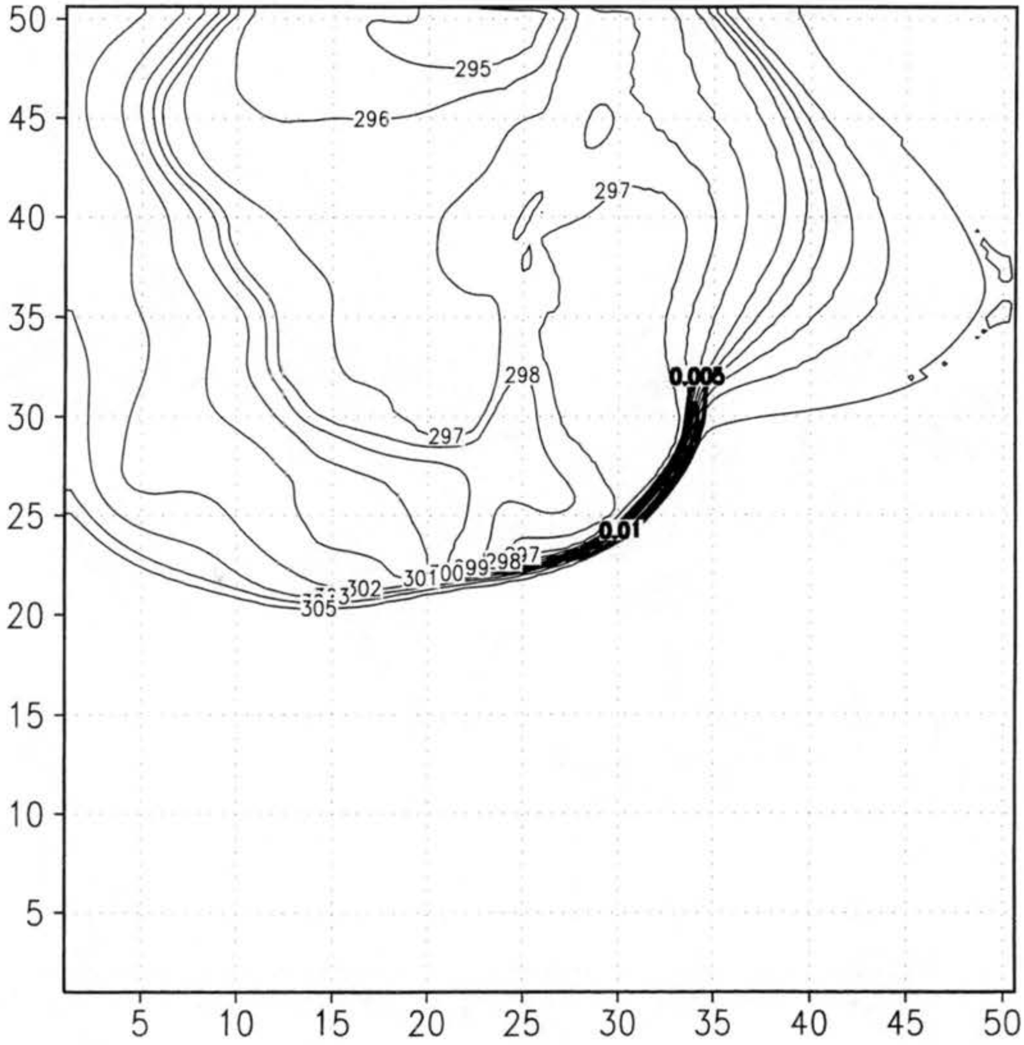

Figure 7.2: Same as Figure 7.1, but with the wind truncated as well. Contour increment for vertical vorticity is 0.005 s^{-1}.

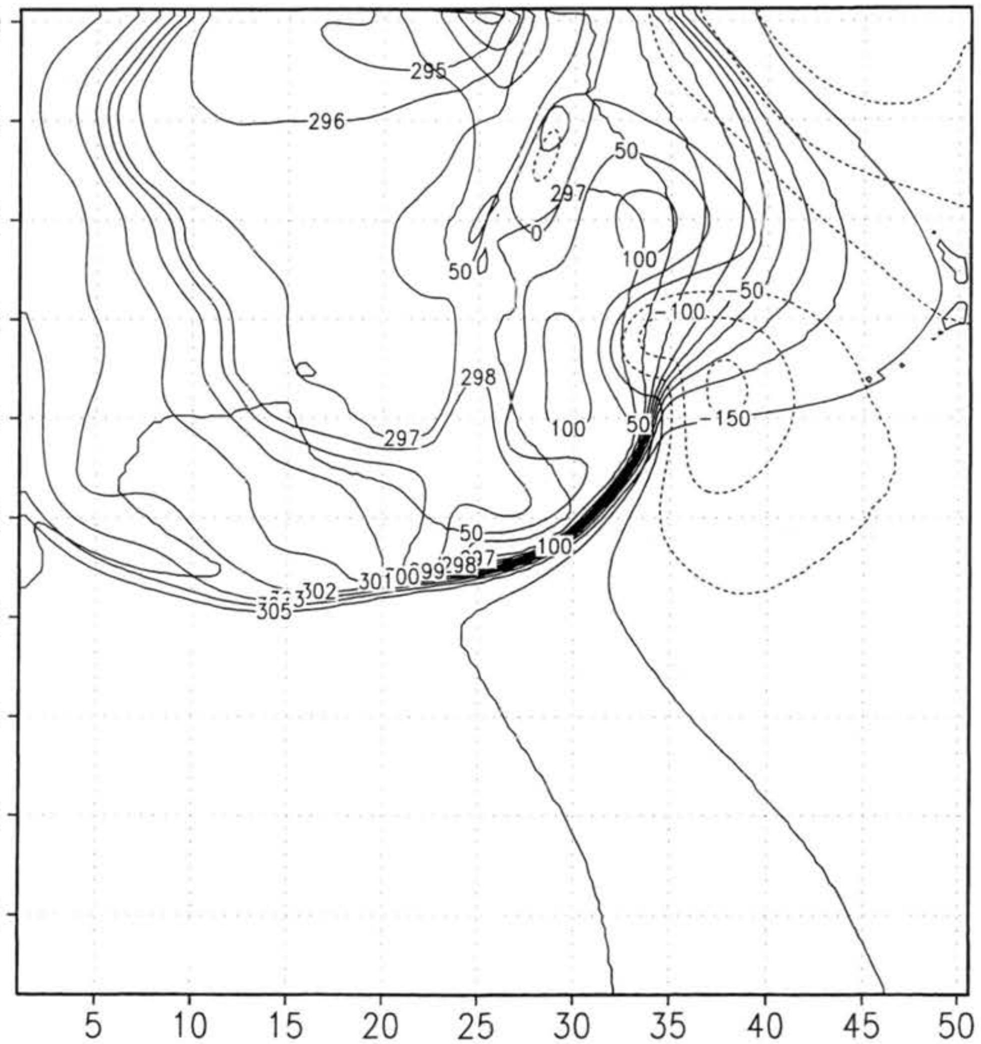

Figure 7.3: Same as Figure 7.2, but showing perturbation pressure (dashed contours) in Pa.

To summarize, we find little sensitivity of vortex evolution to the temperature of the cold pool. To the extent that there is a sensitivity, it is not that suggested by Rasmussen and Blanchard (1998) and Markowski et al. (2000) – our strongest low-level vorticity occurs with the strongest cold pools, due to the enhanced convergence under those conditions (van den Heever 2001). These conclusions were anticipated because of the theorized nature of our vortices. However, it could still be argued that our failure to reproduce the suppression of vertical vorticity by negative vorticity is one of inadequate horizontal resolution with respect to the vertical resolution. So a three-grid simulation was undertaken, with grid spacing on the finest grid down to $55m$.

7.2 Three-grid Simulation

The three-grid simulation contained two nested grids both spawned at 3300 s. The second grid was identical to that in previous sections. The third grid had half the grid spacing as the second grid (55 m), and possessed 130×130 horizontal grid points. Note that for this domain size the vertical and horizontal grid spacings are nearly equal.

The vortex now appears in great detail (Figure 7.4). It can be seen that the vortex has now receded well into the cold pool, but a core of warm air has been entrained into the vortex. The vortex can be seen to possess concentrations of vorticity (Figure 7.5) reminiscent of the secondary vortices of Finley (1997). However, neither the maximum wind speed nor the central pressure deficit are much changed from the two grid simulation, suggesting that both of these are determined by the environment rather than the scale of the vortex (Figure 7.6).

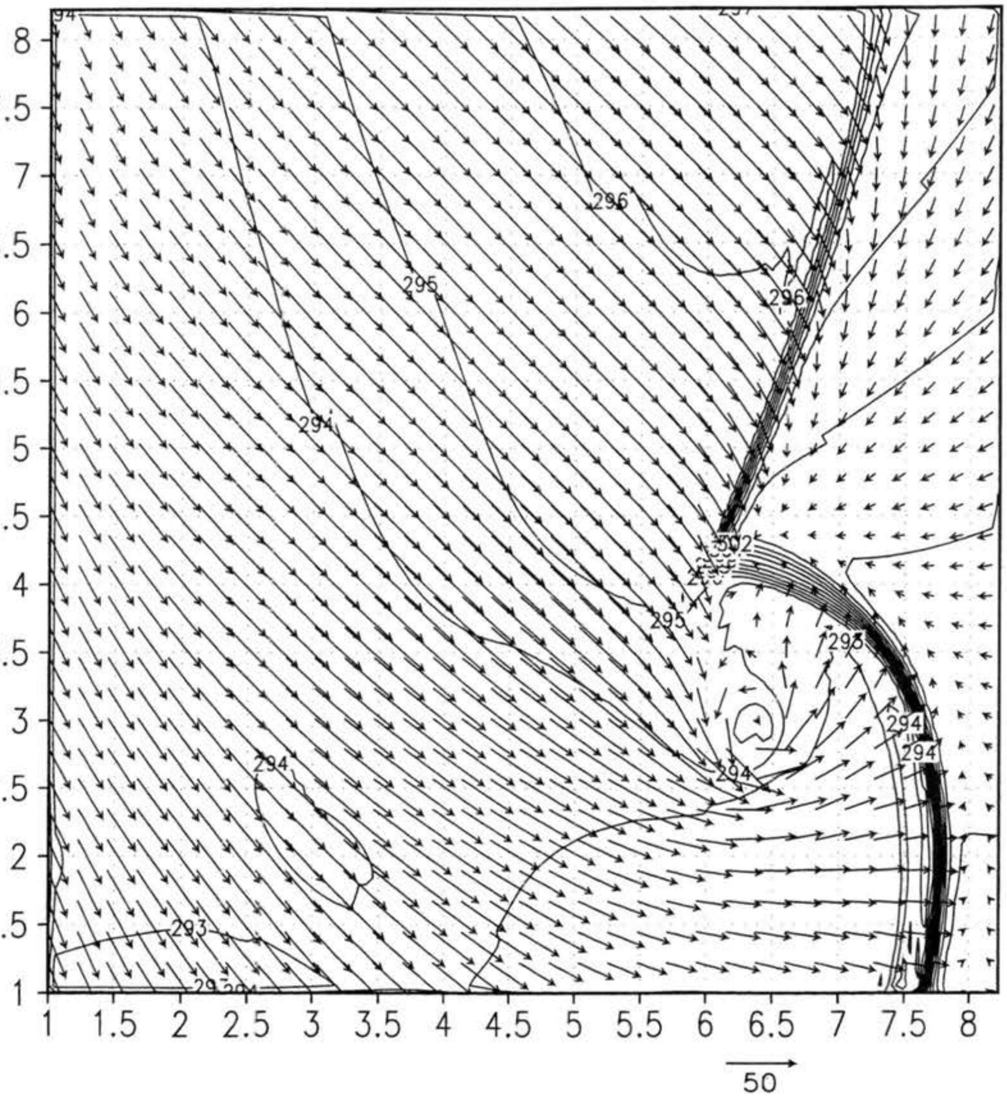

Figure 7.4: Grid-relative horizontal velocity vectors and potential temperature for Grid 3 at 3600 s and 19 m. Contour increment is 1 K. Vector length is in m s^{-1}

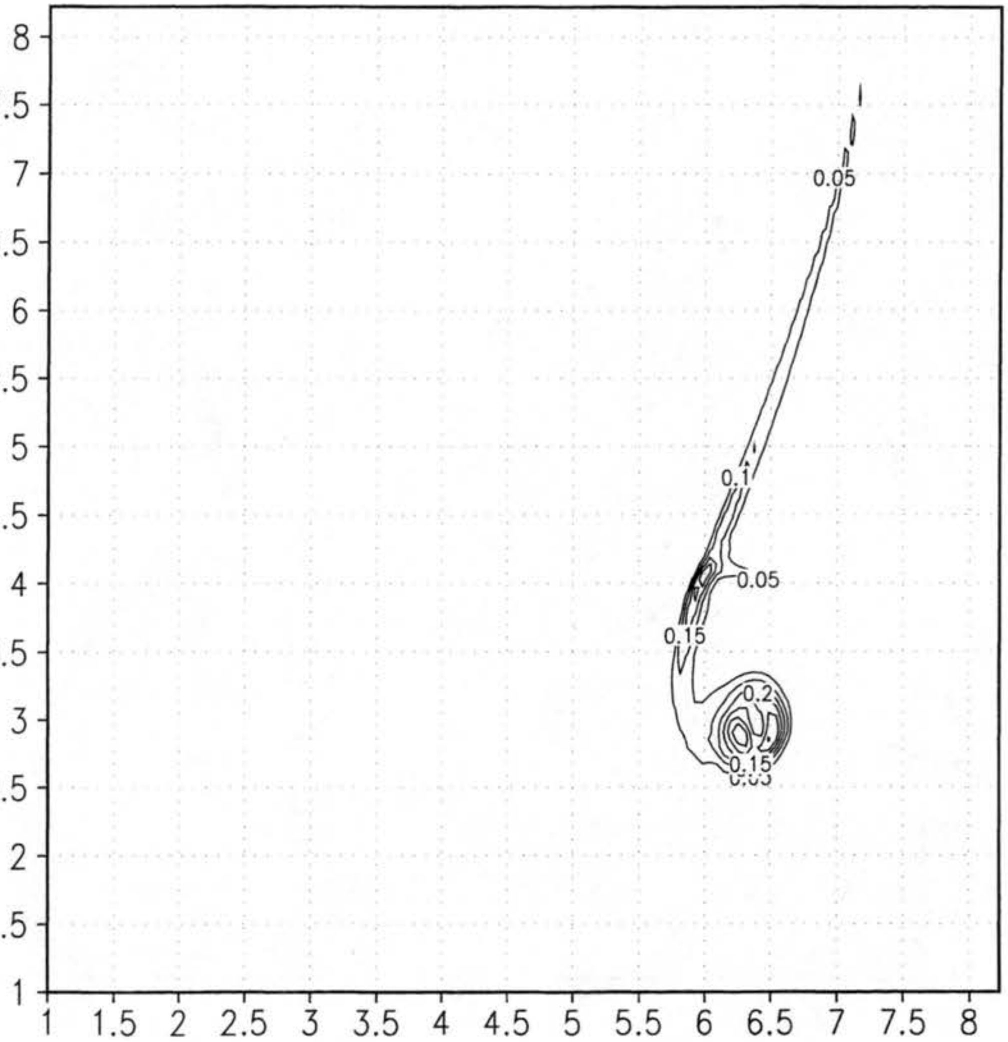

Figure 7.5: Same as Figure 7.4, but showing vertical vorticity contoured every 0.05 s^{-1}.

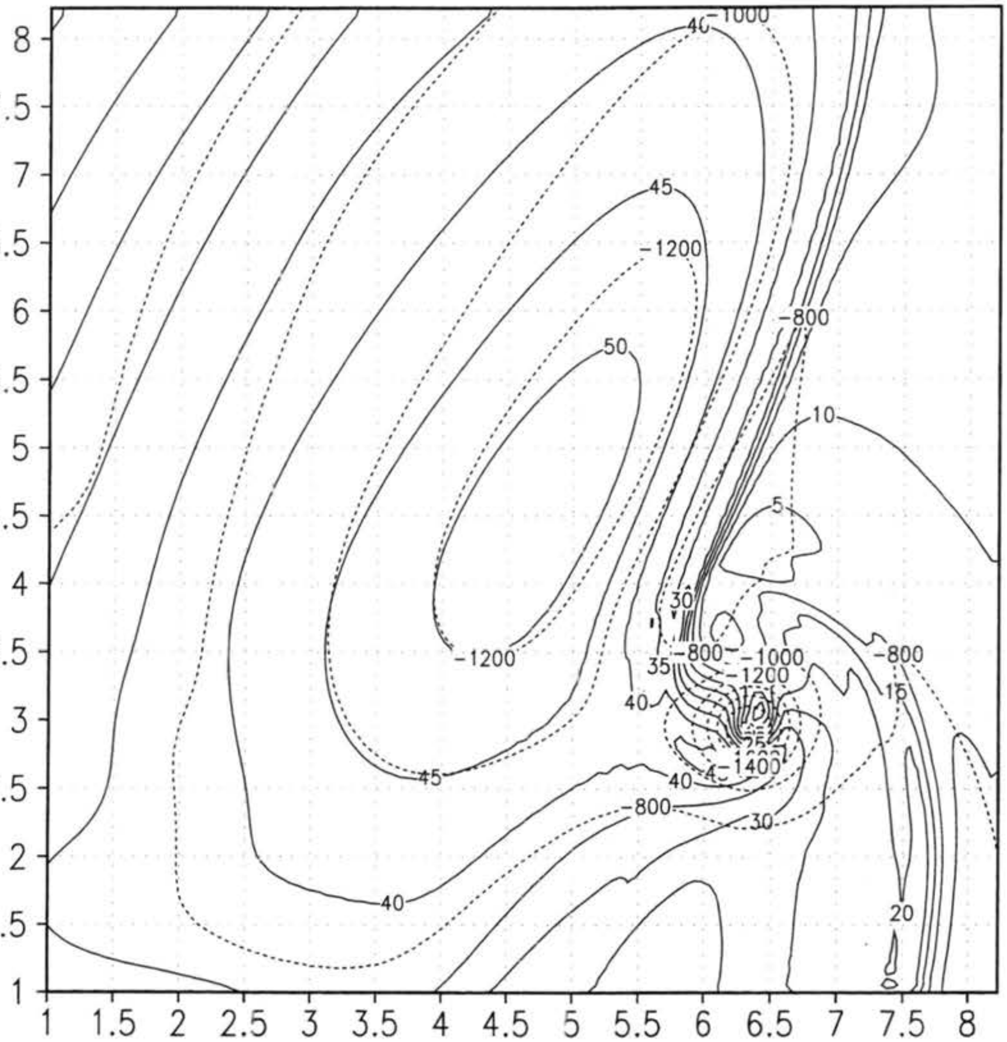

Figure 7.6: Same as Figure 7.4, but showing grid-relative horizontal wind speed contoured every 5 m s^{-1} (solid contours), and perturbation pressure contoured every 200 Pa (dashed contours).

7.3 Tendencies to Convergence

From the description of the evolution of the vortex and the theoretical arguments based on stretched vortex sheet dynamics and barotropic instability, there is certainly a strong indication that the vortex seen in these simulations, despite having vertical continuity in the subcloud layer, is not a manifestation of the dynamic pipe effect, but is essentially a two-dimensional process having more in common with the vortex sheet breakdown modeled by Lee and Wilhelmson (1997a) and observed in NST. Still, the rapidity of atmospheric and model adjustments to changes in pressure can make it difficult to isolate cause-and-effect in the formation of these vortices – that is, does a rapid pressure drop induce the vortex, or does the vortex induce a rapid pressure drop?

We will now attempt to quantify such a distinction. We first return to (2.21) in the following form:

$$\frac{d}{dt}(\boldsymbol{\nabla}\cdot\mathbf{v}) = -\boldsymbol{\nabla}\cdot(\theta_{v0}\boldsymbol{\nabla}\pi') + \frac{\zeta_z^2 - 3\delta^2 - \mathcal{D}^2}{2} - 2\left[\boldsymbol{\nabla}_{\boldsymbol{H}}w\cdot\frac{\partial\mathbf{v_H}}{\partial z}\right] + \frac{\partial B}{\partial z} + \boldsymbol{\nabla}\cdot\mathbf{F}, \tag{7.1}$$

which was formed by taking the divergence of the momentum equations. If we keep separate the divergence of the horizontal momentum and the vertical momentum equations, we can derive two equations:

$$\frac{d}{dt}(\frac{\partial w}{\partial z}) = -\left[\boldsymbol{\nabla}_{\boldsymbol{H}}w\cdot\frac{\partial\mathbf{v_H}}{\partial z}\right] - (\frac{\partial w}{\partial z})^2 - \frac{\partial}{\partial z}(\theta_{v0}\frac{\partial\pi'}{\partial z}) + \frac{\partial B}{\partial z} + \frac{\partial F_z}{\partial z} = G_1 \tag{7.2}$$

$$-\frac{d}{dt}(\frac{\partial u}{\partial x} + \frac{\partial v}{\partial y}) = -\frac{\zeta_z^2 - 3\delta^2 - \mathcal{D}^2}{2} + \left[\boldsymbol{\nabla}_{\boldsymbol{H}}w\cdot\frac{\partial\mathbf{v_H}}{\partial z}\right] + \theta_{v0}\nabla_H^2\pi' - \boldsymbol{\nabla}\cdot\mathbf{F_H} = G_2 \tag{7.3}$$

We will refer to the G_1 and G_2 equations as the horizontal convergence and vertical divergence equations, respectively. The difference $G_1 - G_2$ gives (7.1). In an incompressible model G_1 and G_2 must be made equal; if the momentum or buoyancy fields are such that there is no equality, the perturbation Exner function π' must be assumed to change rapidly until the π' Poisson equation is satisfied. This process causes G_1 and G_2 to become equal. If this final common value is positive, both horizontal convergence and vertical divergence are produced; a negative value indicates the production of horizontal divergence and vertical convergence.

In the compressible model, if G_1 and G_2 are not equal, the acoustic equation, given approximately by (2.23):

$$\frac{\partial \pi'}{\partial t} = -\frac{c_s^2}{\theta_{v0}}(\boldsymbol{\nabla} \cdot \mathbf{v}), \tag{7.4}$$

is activated. For $G_1 > G_2$ there will be a negative tendency in π'. If the gradients of π' are specified at the boundaries, it can be expected that a local region of decreasing π' should be associated with a local region of both increasing $\nabla_H^2 \pi'$ and $\partial^2 \pi' / \partial z^2$. Thus, whenever $G_1 > G_2$ we can expect G_1 to decrease and G_2 to increase and attempt to reach a common value (henceforth referred to as G), assuming that the other forcings stay constant. Because this is an acoustic process, the π' adjustment will occur rapidly.

The formation of a significant vortex in the atmosphere requires the presence of sufficient horizontal convergence to amplify vertical vorticity to large levels. So a necessary precursor to the formation of a vortex is the generation of horizontal convergence, which requires $G > 0$. The occurrence of $G > 0$ requires $G_1 > 0$ and/or $G_2 > 0$. Let us refer to the horizontal convergence generated when $G_1 >> G_2$ as *vertically- forced convergence*, and when $G_2 >> G_1$ as *horizontally-forced convergence*. Note that while convergence is being generated, the vertically-forced case is accompanied by a drop in pressure whereas the horizontally-forced case is accompanied by a drop in pressure. For the vertically-forced case, the immediate cause of the horizontal convergence is the increase in $\nabla_H^2 \pi'$, probably associated with a decrease in π'; in the horizontally-forced case, the positive terms in G_2

induce the horizontal convergence directly. An example of the latter is the convergence zone between two oppositely-surging cold pools, whose source is the convergence of momentum advection in the direction of the momentum; mathematically, the presence of δ in (7.3) induces a further increase in the horizontal convergence.

Once significant convergence is generated, vertical vorticity can rapidly increase. Vertical vorticity creates a negative tendency in G_2, which tends to decrease both the pressure and the horizontal convergence. For the strongest vortices, the reduction in pressure by the vorticity may be enough to induce horizontal divergence and vertical convergence; this can be manifested as a dynamically-induced 'occlusion downdraft' (Klemp and Rotunno 1983) or a two-celled vortex with subsidence in the center (Rotunno 1977). Because both ζ_z and δ have tendency terms proportional to themselves times δ, the interaction between the two can become complicated, as evidenced by the sensitivity of vortex structure to changes in the circulation (Davies-Jones 1986; Lewellen 1993; Nolan and Farrell 1999). If a final steady-state is to be reached, not only the pressure tendency but the convergence tendency must become zero, through suitable adjustment of the pressure and dynamic terms in (7.2) and (7.3). Indeed, in the case of an axisymmetric flow with no circulation, vertically-forced convergence will increase δ in (7.3) to such an extent that the steady-state pressure near the surface along the axis will be increased, not decreased (Rotunno 1978). Nonetheless it remains true that the horizontal convergence present was generated by an instantaneous vertically-induced pressure deficit along the axis.

We can speak of a *vertically-forced vortex* as one that is formed by vertically-forced convergence; a *horizontally forced vortex* is formed by horizontally-forced convergence. Thus a vertically-forced vortex is characterized by a reduction in pressure during the formation of horizontal convergence, a horizontally-forced vortex by an increase in pressure. In a vertically-forced vortex, the vorticity increase is in response to a decrease in the pressure;

in the horizontally-forced vortex, the decrease in pressure is in response to the vorticity increase.

How does this relate to previous analytical models of tornado and vortex formation? In the dynamic pipe effect, the vortex at upper levels is vertically forced by an imposed body force, generally representing buoyancy. At progressively lower levels, the vortex is also vertically-forced, but through the $\theta_{v0}\partial^2\pi'/\partial z^2$ term. The non-DPE vortices of Trapp and Davies-Jones (1997) are also vertically-forced, but occur when buoyancy extends down to the surface, so that the influence of the $\theta_{v0}\partial^2\pi'/\partial z^2$ term is not needed.

The author is not aware of true horizontally-forced geophysical vortex analytical models in the literature. A number of numerical simulations of low-level mesocyclones display what have been termed 'occlusion downdrafts' (Klemp and Rotunno 1983), which are dynamically induced by strong rotation near the surface. This is a manifestation of the vertical convergence/horizontal divergence associated with horizontally-forced vortices near the ground. In Klemp and Rotunno (1983) the strong horizontal convergence needed to generate the low-level mesocyclone is present along the gust front; during the formation of the occlusion downdraft, however, regions of positive w (and also $\partial w/\partial z$ are replaced by regions of negative w.

A related process is found in the numerous barotropic simulations of vortex axisymmetrization, often representing hurricanes (Melander et al. 1987; Montgomery and Enagonio 1998; Kossin and Schubert 2001). Since these barotropic models conserve vertical vorticity (other than by diffusion), the initial presence of the vertical vorticity is not explicitly modeled. However, two-dimensional processes can lead to the formation of a single concentrated vortex, as well as a sudden pressure drop (Kossin and Schubert 2001). The cause of the drop in pressure is the reduction of the $\mathcal{D}^2$ term in (2.26); as previously mentioned, along a one-dimensional shear line ζ_z and $\mathcal{D}$ are equal, but within an axisymmetric vortex with no radial motion, $\mathcal{D}$ is zero. The barotropic axisymmetrization case thus resembles the horizontally-forced vortex in that its formation is due to processes within the horizontal plane, and that the drop in pressure follows the formation of the vortex.

We may thus generalize our definition of a horizontally-forced vortex to include all vortices whose primary concentration process is not due to vertically-forced convergence; for all of these vortices the pressure decrease is a subsequent effect.

7.4 Pressure Forcing in Three-Grid Simulation

If our hypothesis about the mechanism of vortex formation in these simulations is correct, then these vortices clearly are horizontally-forced according to the more general definition. The concentration of the vortex is due to a combination of axisymmetrization, which involves the loss of the $\mathcal{D}$ term, and the uniform plane convergence along the gust front, which exists long before vorticity begins to concentrate there. It was previously argued that convergence along the gust front is horizontally forced. To demonstrate this, suppose that the motion is purely in the x-direction, with velocity U at $x = -\Delta x/2$ and $-U$ at $x = +\Delta x/2$. Let us also suppose that the velocity varies linearly for $-\Delta x/2 < x < +\Delta x/2$. In the absence of horizontal pressure gradient forces, the u-momentum equation within the interval is $\partial u/\partial t = -u(\partial u/\partial x)$; taking the divergence gives:

$$\frac{\partial}{\partial t}\left(\frac{\partial u}{\partial x}\right) = -\left(\frac{\partial u}{\partial x}\right)^2 \tag{7.5}$$

since $\partial u/\partial x$ is constant. Since $\partial u/\partial x$ is given by $-2U/\Delta x$, we obtain

$$\frac{\partial}{\partial t}\left(\frac{\partial u}{\partial x}\right) = -\frac{4U^2}{\Delta x^2}, \tag{7.6}$$

which acts to increase the convergence with time (i.e., the tendency on $\partial u/\partial x$ is negative). Mathematically, this term in the full horizontal convergence equation (7.3) is incorporated into δ and $\mathcal{D}$; physically, we simply have the result that two converging air streams will eventually increase the convergence between them. In the case of the model one of the convergent air streams is that created by the high pressure of the cold pool.

However, we would still like to confirm that there is no vertically-forced convergence during the time that the vortex is concentrating and the pressure is dropping. To accomplish this we will now plot the G_1 and G_2 terms (other than the diffusion terms) for the finest grid of the three-grid simulation. We will examine the simulation at 3480 s, at which time the vortex at 19 m is concentrated but the pressure has not reached its minimum value yet (Figure 7.7). However, this time is typical of the entire Grid 3 simulation period. It can be seen by comparing with Figure 7.6 that the motion of the vortex is to the southeast. We would expect therefore to see a region of positive $G_1 - G_2$ to the southeast of the vortex. This is barely apparent in Figure 7.7, and not related at all to Figure 7.8, which shows G_1. However, we can see a region of decreasing pressure to the southeast of the vortex in Figure 7.9, which plots $-G_2$, although the region is not extensive. So at the lowest model level we have a horizontally-forced pressure drop according to the finite difference representation.

The term containing the dot product of the horizontal w gradient with the vertical horizontal velocity gradient in G_1 will be referred to as the vertical shear term. It can be seen from (7.2) and (7.3) that this term contributes equally but oppositely to the horizontal convergence forcing and the vertical divergence forcing. We can thus argue that the vertical shear term cannot be the ultimate source of either horizontal convergence or vertical divergence. However, a negative value of the vertical shear term unequivocally causes $G_1 - G_2$ to become more positive; thus a negative vertical shear term tends to decrease the pressure, but in manner neither characterizable as vertically-forced nor horizontally-forced. One aspect of the presence of the vertical shear term is that differential vertical advection in the

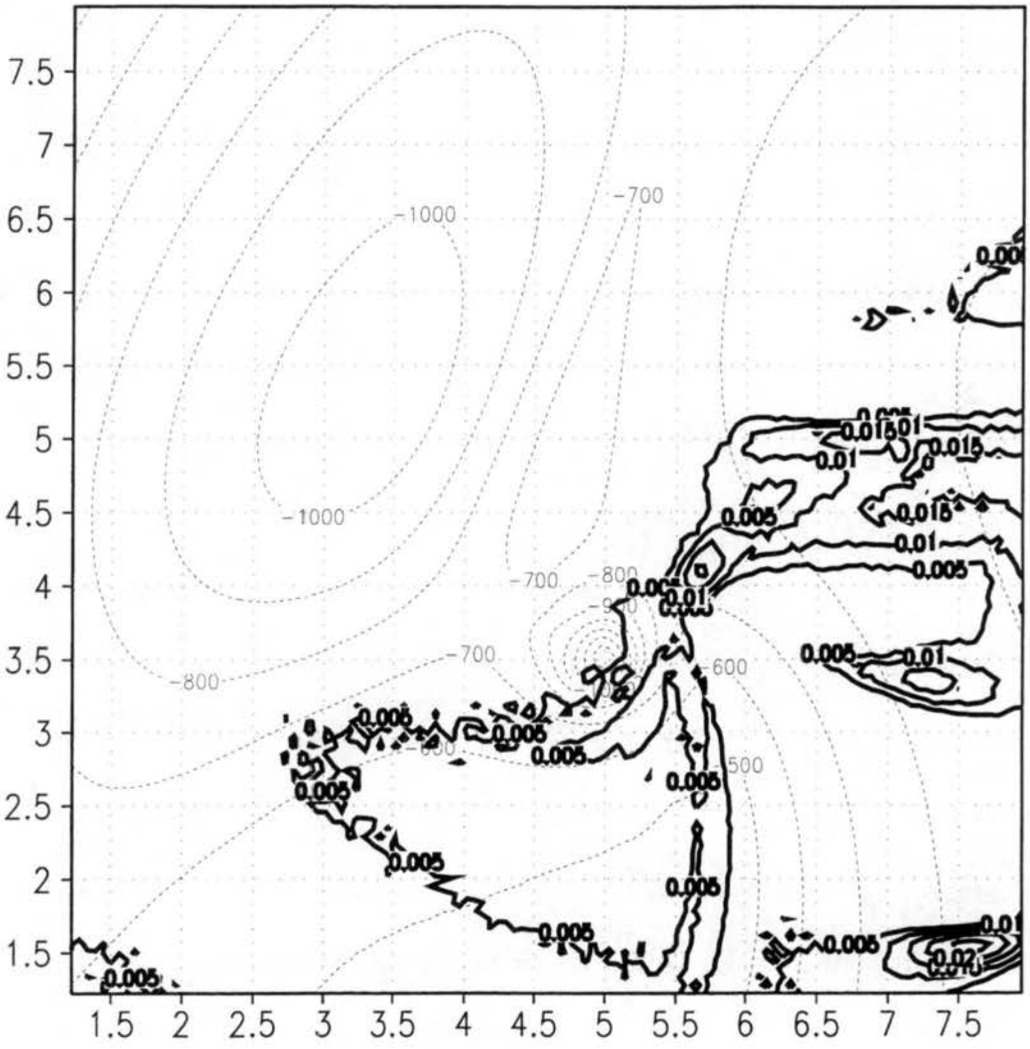

Figure 7.7: Perturbation pressure (thin contours) and $(G_1 - G_2)$ term as defined in the text (thick contours), for 3480 s on Grid 3 at 19 m above surface. Perturbation pressure contour increment is 100 Pa while thick contour increment is $0.005\ \mathrm{s}^{-2}$.

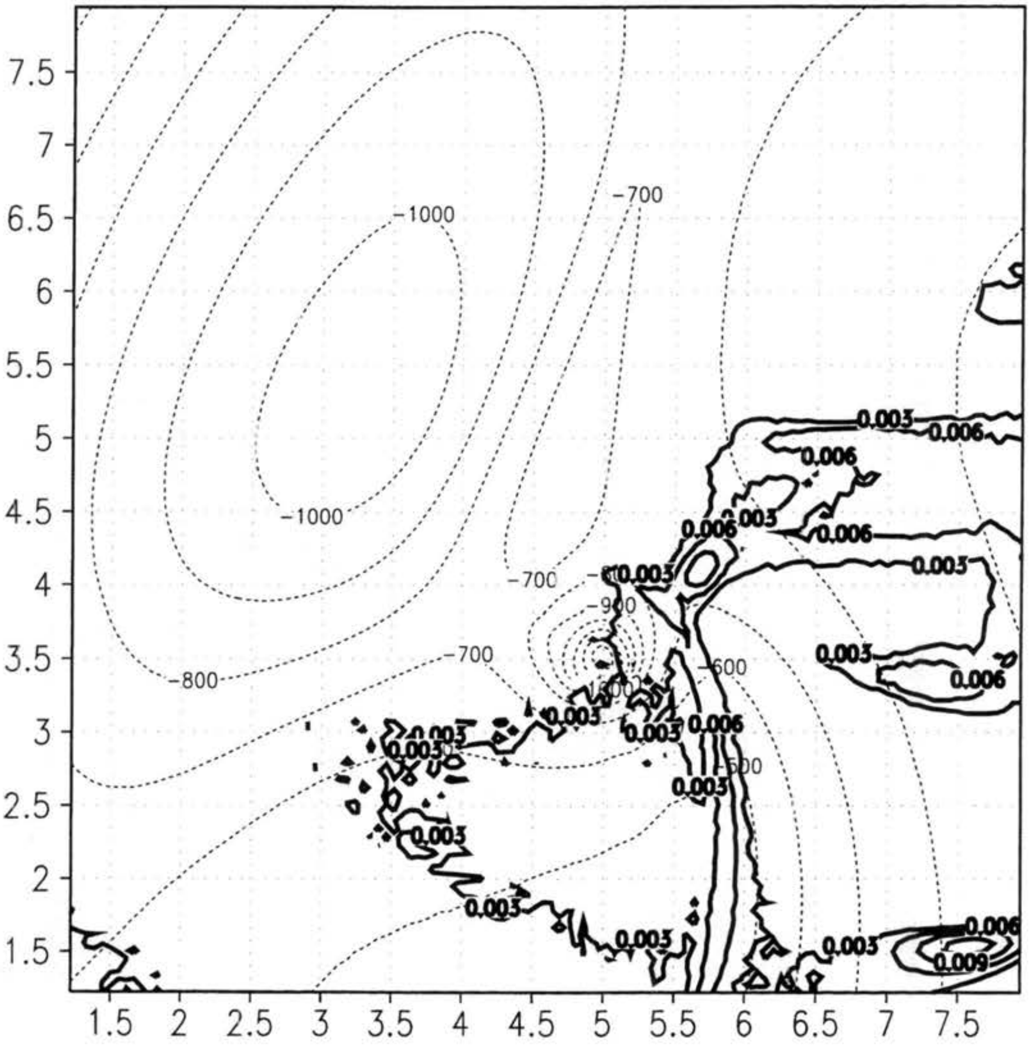

Figure 7.8: Same as Figure 7.7, but for G_1 term. Thick contour increment is 0.003 s^{-2}.

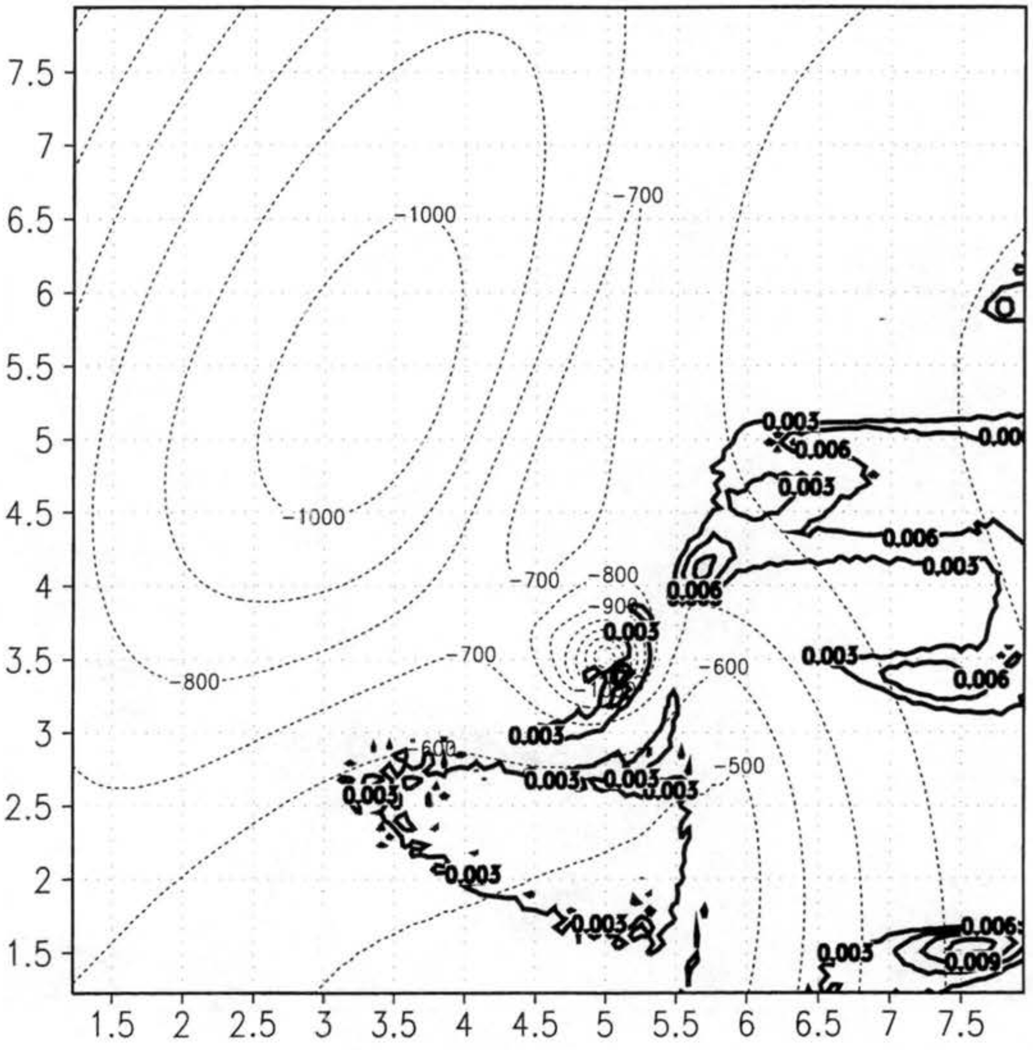

Figure 7.9: Same as Figure 7.7, but for negative of G_2 term. Thick contour increment is $0.003\ \mathrm{s}^{-2}$.

presence of vertical wind shear of the horizontal velocity causes divergence in the horizontal velocity and a low in the pressure field downshear of the region of maximum updraft – a non-linear version of the downshear low induced by convection. Another aspect of the vertical shear term's presence is that differential horizontal advection of the vertical velocity causes divergence in the vertical velocity – which is also associated with low pressure.

From Figure 7.10 it is apparent that the vertical shear term is a major contributor to both G_1 and G_2. In order to determine whether or not the minimum in pressure is being forced vertically or horizontally, however, we should exclude the terms involving the vertical shear from G_1 and G_2. Figure 7.11 shows the sum of the remaining terms in G_1 when G_1 is positive, whereas Figure 7.12 shows the sum of the remaining terms in $-G_2$ when $-G_2$ is positive. (For either of these cases a positive value in the figure indicates a tendency towards lower pressure.) While in neither case are there very extensive areas of negative pressure forcing, it is seen that the negative pressure forcing in the vicinity of the vortex is associated with the terms in G_2. Thus we have evidence that the vortex contains a horizontally-forced pressure deficit at the surface.

At 62 m above the surface, the magnitude of the pressure forcing $G_1 - G_2$ is approximately an order of magnitude greater (Figure 7.13; note increased contour interval). At this level, the vertical shear term is so dominant that G_1 and $-G_2$ are virtually indistinguishable (Figures 7.14 and 7.15). The significance of this unexpected result is not clear at present; it may indicate that the model does not have the resolution to reproduce the core of the vortex adequately, in contrast to the broad region of strong vertical shear in the horizontal velocity near the surface. However, it should be noted that Rotunno and Weisman (2000), examining basically the vertical integral of the G_1 equation (7.2) for a simulation of propagating supercells, found that the vertical integral of a term associated with the vertical shear term (i.e., the $\boldsymbol{v} \times \boldsymbol{\zeta}$ term in the momentum equation) was more important in determining storm

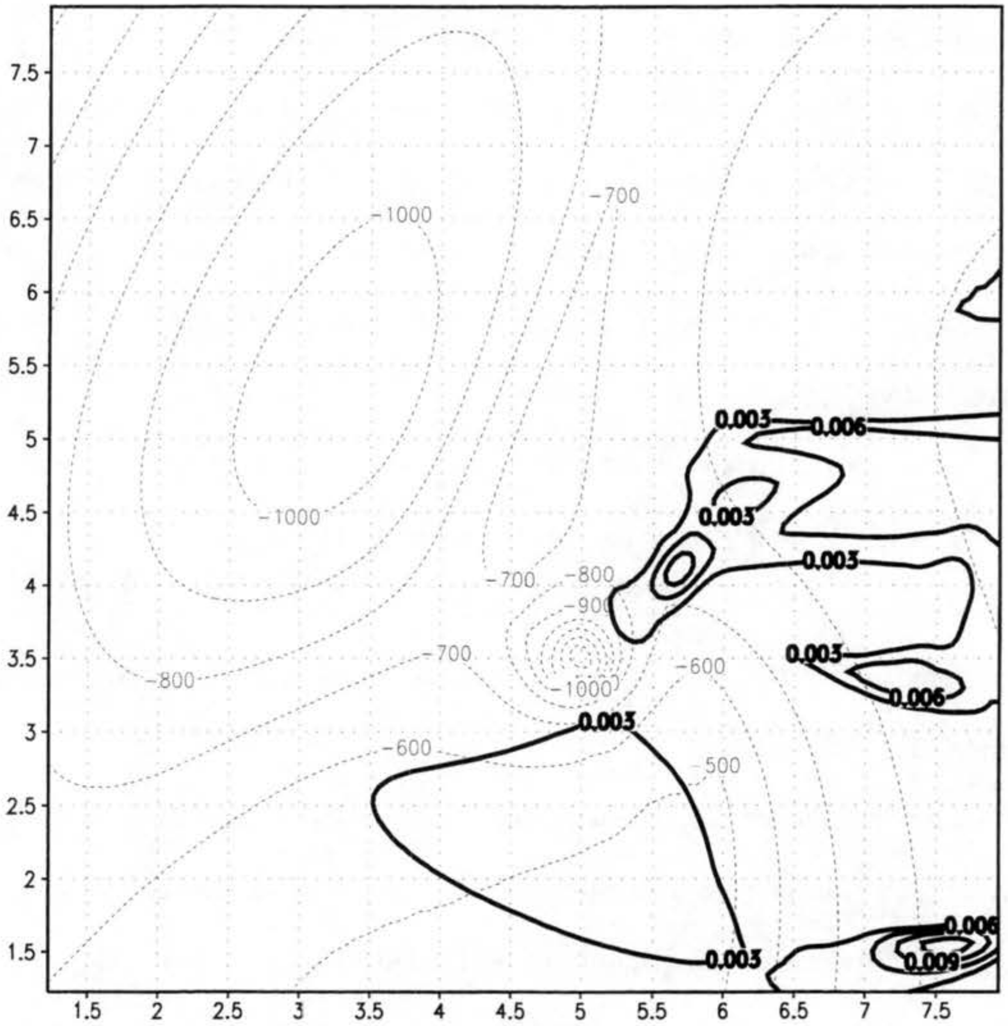

Figure 7.10: Same as Figure 7.7, but for vertical shear term. Thick contour increment is $0.003\ \mathrm{s}^{-2}$.

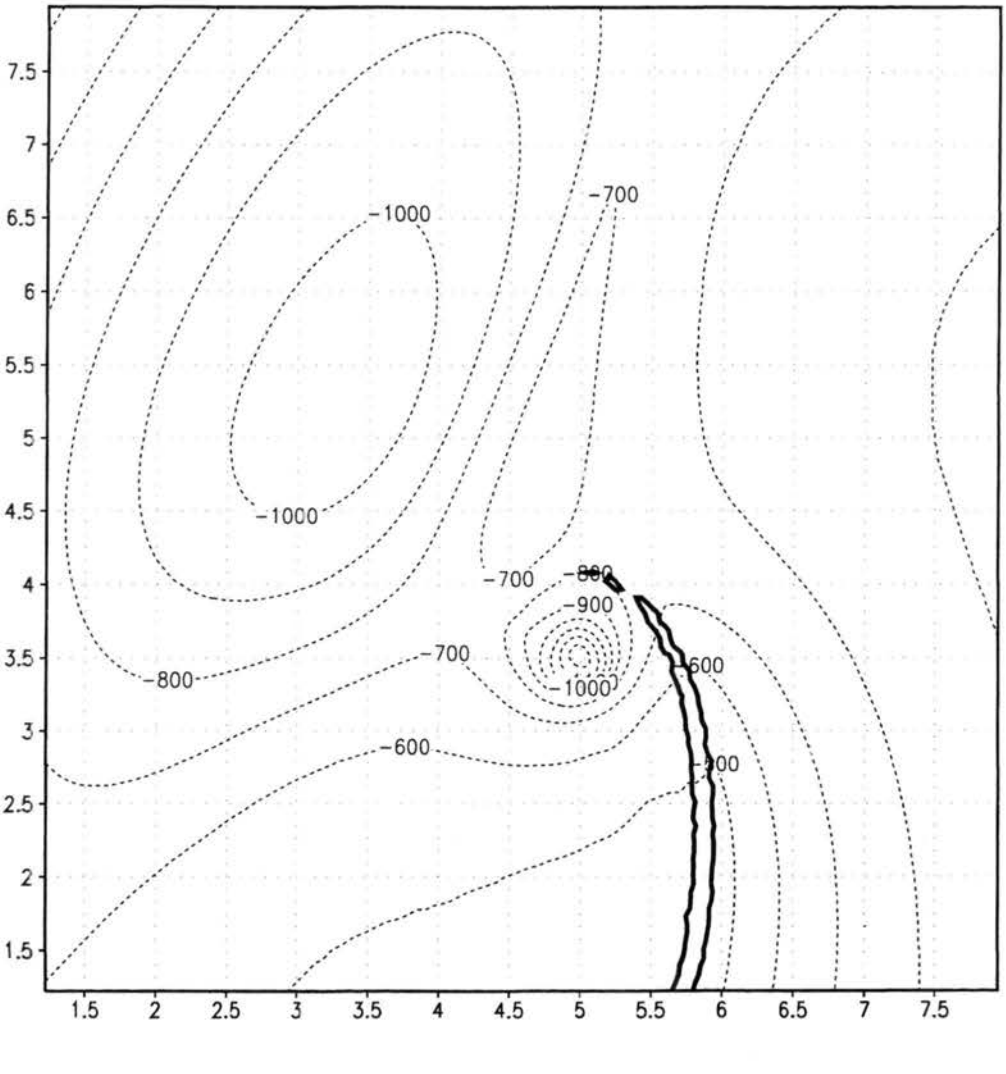

Figure 7.11: Same as Figure 7.7, but for G_1 term, excluding the vertical shear term. Thick contour increment is 0.003 s^{-2}.

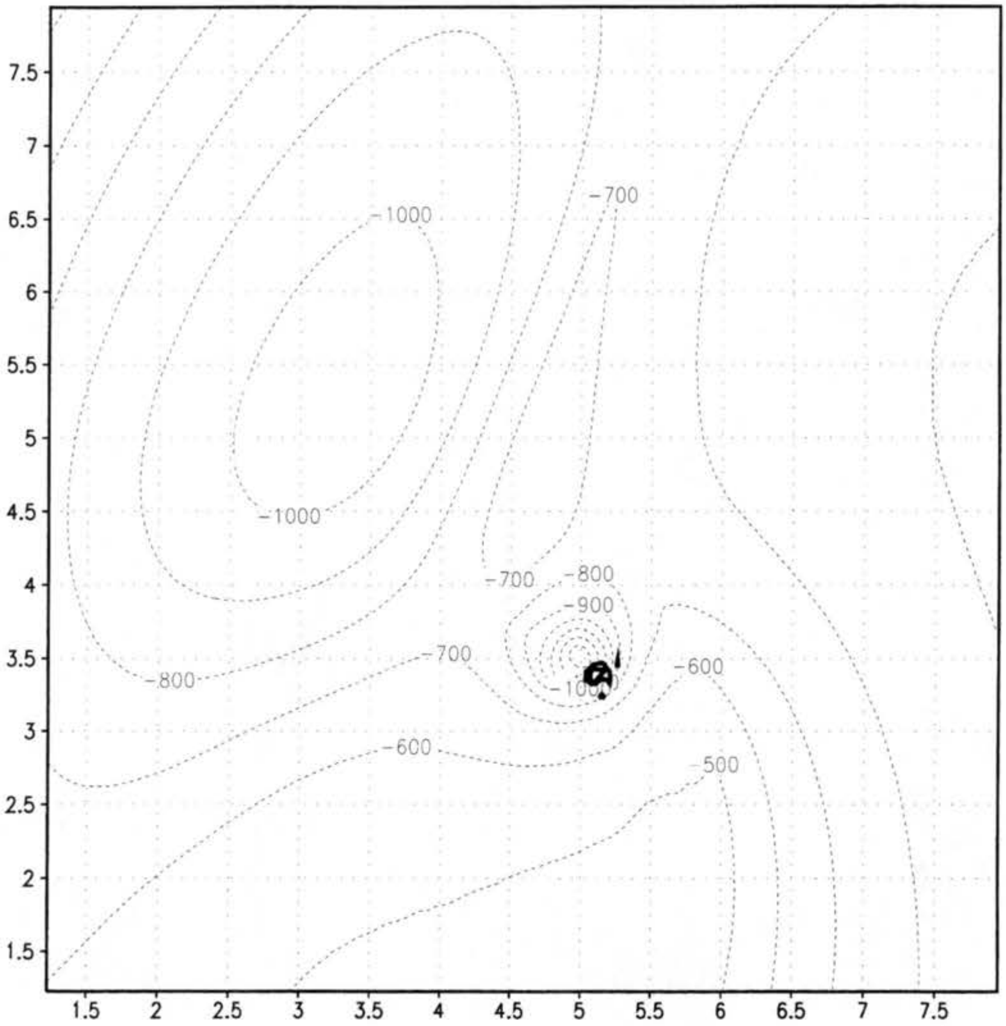

Figure 7.12: Same as Figure 7.7, but for negative of G_2 term, excluding vertical shear term. Thick contour increment is 0.003 s^{-2}.

propagation than the vertical integral of a term associated with $(\partial w/\partial z)^2$ (i.e., the gradient of the Bernoulli function term). Thus, Rotunno and Weisman found that the interaction between gradients in w and the vertical wind shear vector was most important in determining the pressure distribution, just as in this simulation.

When the vertical shear term is excluded, the remainder of both G_1 and $-G_2$ produce regions of negative pressure tendency in the vicinity of the vortex, but the contribution from $-G_2$ is greater (Figures 7.16 and 7.17). In any event, it is clear that the drop in pressure is not associated with a sudden increase in the horizontal convergence tendency, confirming the horizontally-forced nature of the vortex.

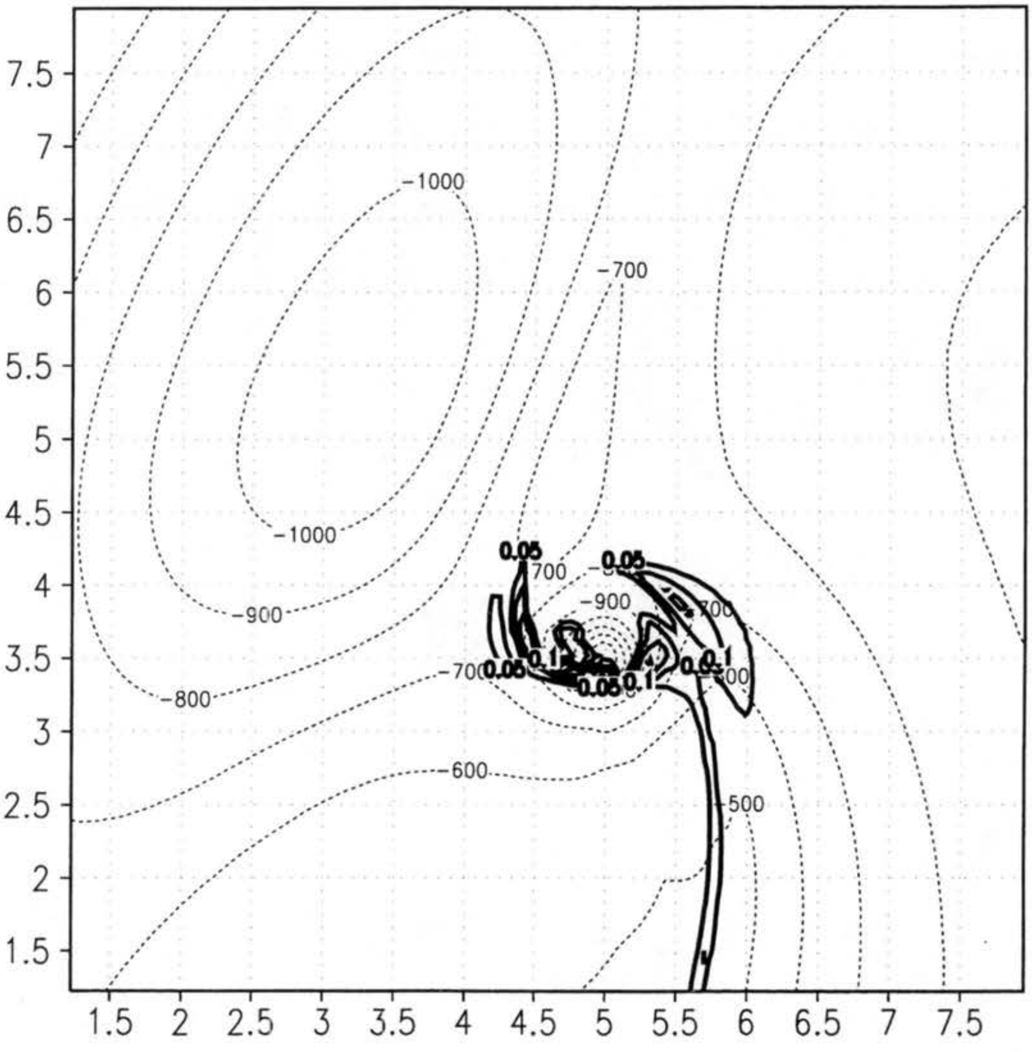

Figure 7.13: Perturbation pressure (thin contours) and $(G_1 - G_2)$ term as defined in the text (thick contours), for 3480 s on Grid 3 at 62 m above surface. Perturbation pressure contour increment is 100 Pa while thick contour increment is $0.05\ \mathrm{s}^{-2}$.

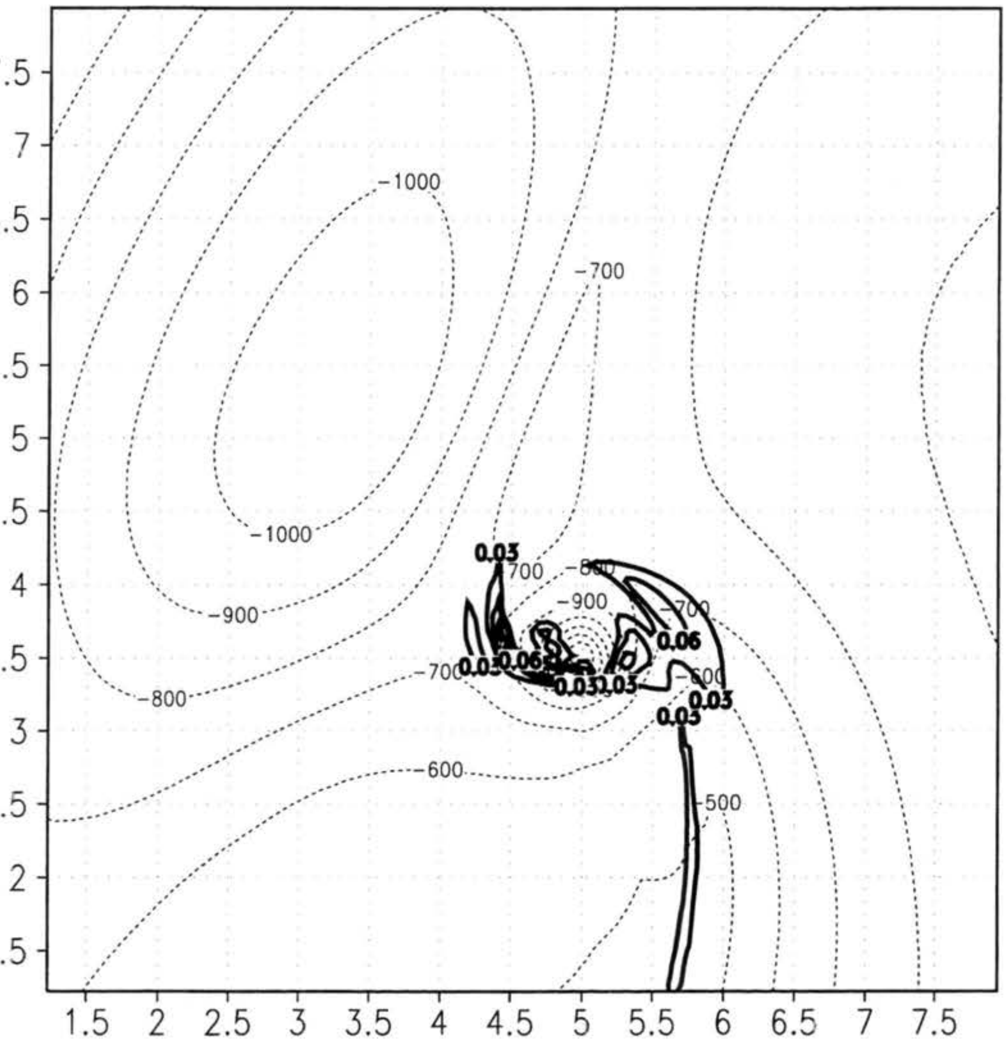

Figure 7.14: Same as Figure 7.13, but for G_1 term. Thick contour increment is $0.03\ \mathrm{s}^{-2}$.

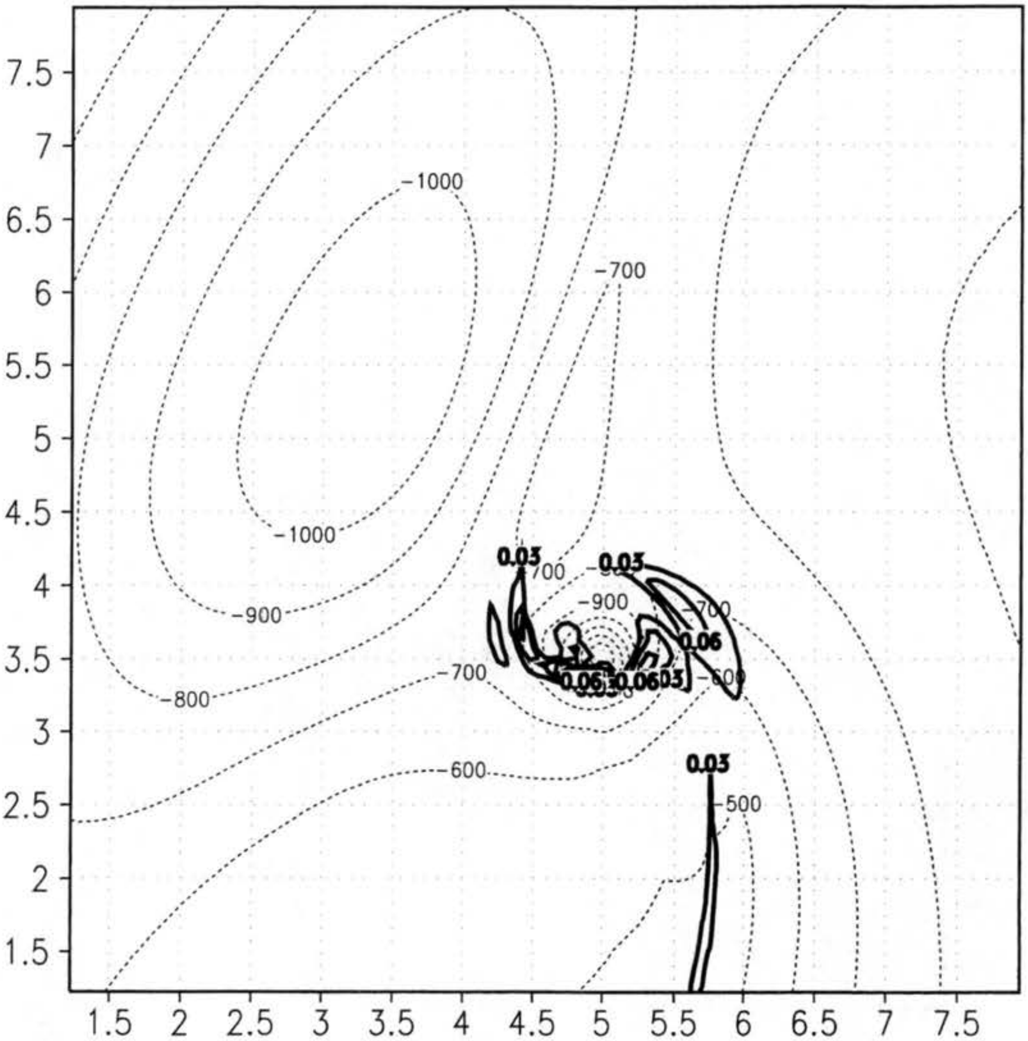

Figure 7.15: Same as Figure 7.13, but for negative of G_2 term. Thick contour increment is 0.03 s^{-2}.

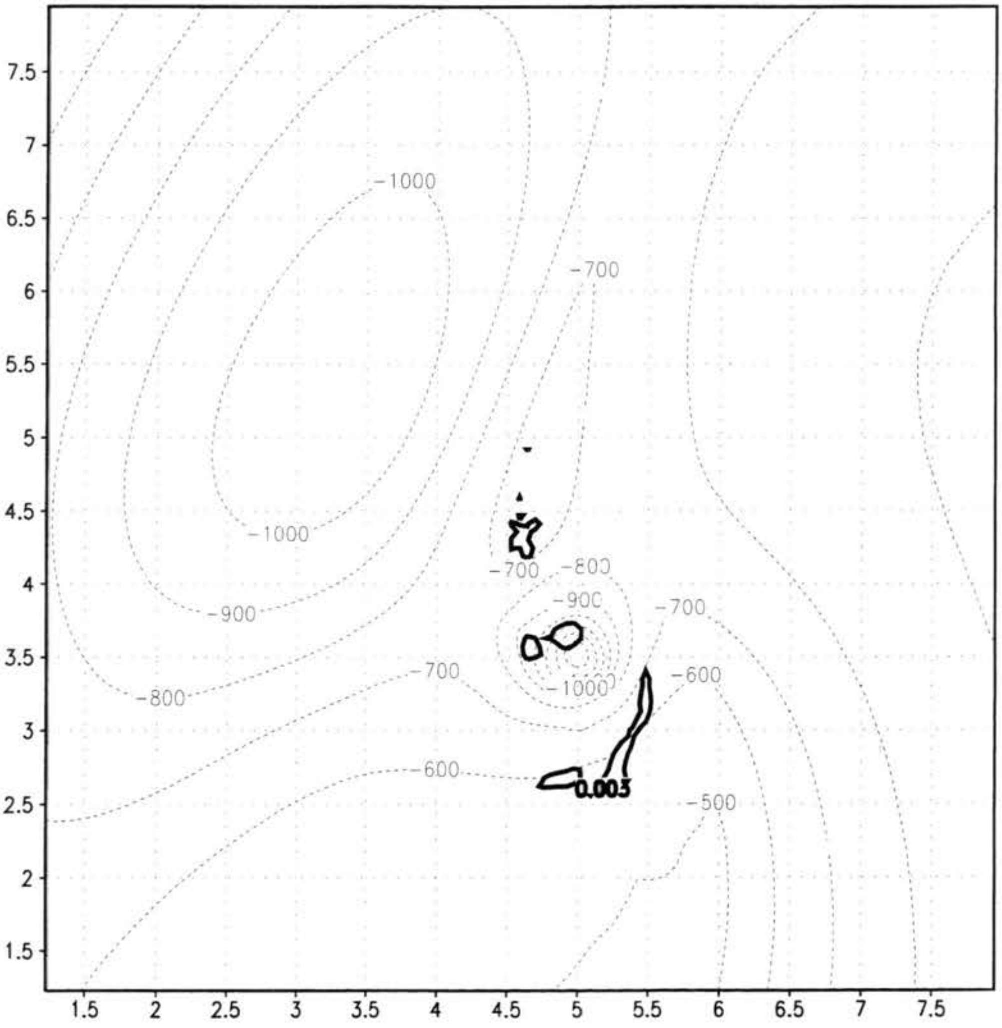

Figure 7.16: Same as Figure 7.13, but for G_1 term, excluding vertical shear. Thick contour increment is $0.003\ \mathrm{s}^{-2}$.

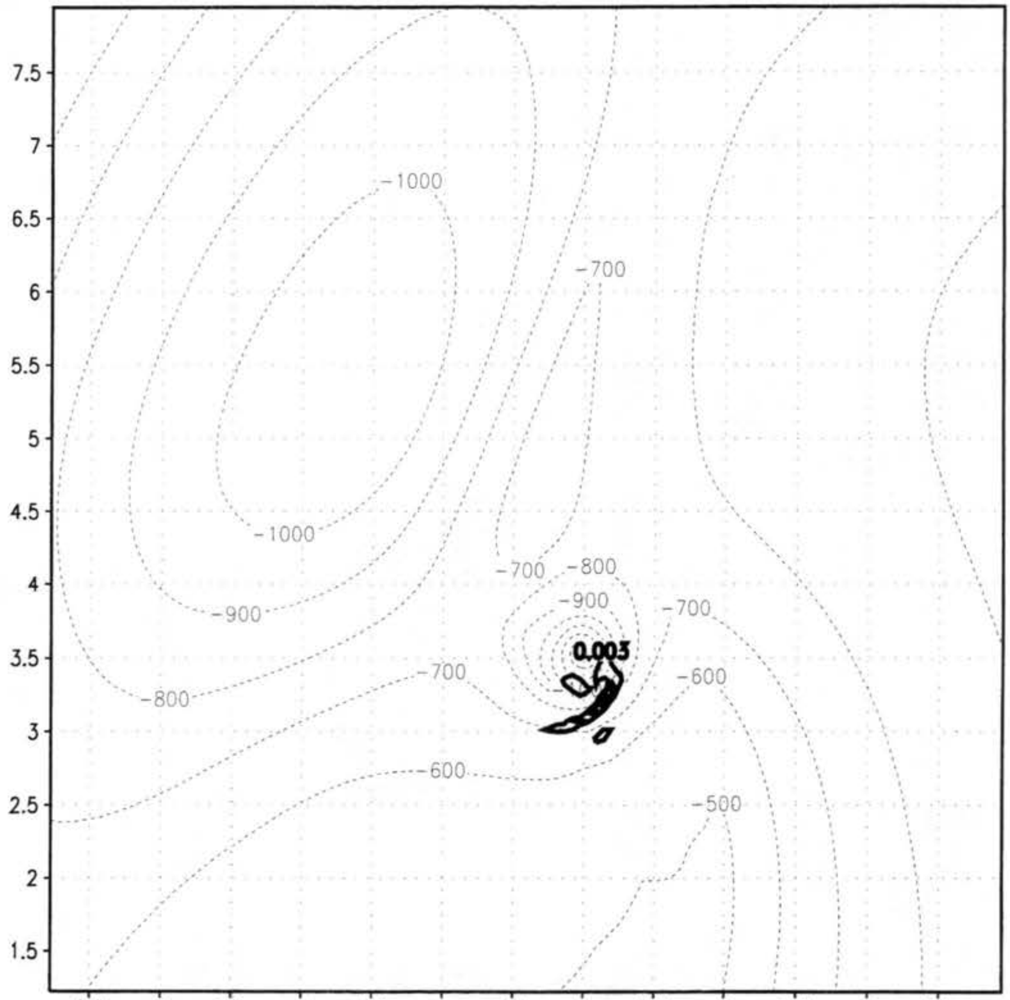

Figure 7.17: Same as Figure 7.13, but for negative of G_2 term, excluding vertical shear. Thick contour increment is 0.003 s^{-2}.

Chapter 8

Summary and Future Work

8.1 Summary

It has been confirmed that modeled supercells can produce concentrated low-level vortices without the introduction of nested grids, though the introduction of nested grids does cause some concentration of tornadic features. There appear to be two distinct stages in the development of the modeled concentrated vortex.

The first stage involves the generation of vertical vorticity along the forward-flank gust front. The picture is very similar to those of Davies-Jones and Brooks (1993) and Grasso and Cotton (1995) in that the vertical vorticity appears to be generated in the baroclinic region associated with a downdraft, and the strongest tilting of horizontal vorticity into the vertical is shown to occur in this region. A circulation trajectory analysis, however, was found to be unable to reveal a unique backward trajectory for the air parcel representing the maximum value of vertical vorticity. The baroclinic zone representing the earliest traceable source of vertical vorticity contracts to a region less than 6 m wide at the location of the maximum strength vortex, and has performed a complete revolution within the baroclinic zone.

The second stage involves the collapse of the low-level vorticity band to a point, as best as can be resolved by the numerical model. The formation of these vortices can occur quite rapidly, on a time scale of minutes, and is accompanied by a rapid decrease of pressure. A Fourier analysis of the components of the circulation budget revealed that the sudden concentration of the vorticity into a discrete vortex is not an axisymmetric process, but is related to the alignment of the axis of maximum radial inflow and the vorticity band. The radial inflow is associated with the convergent flow at the gust front and is predominantly planar. Under normal conditions these two axes would be perpendicular, and the horizontal vorticity flux would only be significant in a narrow region along the gust front. However, a counterclockwise rotation of a portion of the band of vorticity with respect to the axis of plane convergence allows the horizontal vorticity flux from a much more extended region to be converged to a point, the center of rotation of the vorticity band.

The rotation of a portion the vorticity band against the plane convergence is best explained as a manifestation of barotropic instability for a finite-width vortex sheet, based on appearance and on consistency with theoretical predictions of length and time scale. In this respect the vortex appears similar to those that form along shear lines in studies of non-supercell tornadogenesis. One difference here is that the large-scale convergence associated with the gust front allows the formation of discrete centers of vorticity concentration on time scales much smaller than those of purely two-dimensional barotropic instability, given an initial rotation of the vorticity band. Theoretical studies confirm the existence of this mode of vorticity collapse. Sensitivity studies indicate that the vertical momentum equation is secondary to the horizontal wind field in both initiating and determining the strength of the final vortex.

8.2 Relation to Similar Supercell Studies

In the study of van den Heever (2001), supercell simulations using RAMS were performed at 1 km resolution, but otherwise possessed nearly identical model parameters. The intent of that study was to examine the sensitivity of the supercell evolution to mean hail diameter and other microphysical parameters. A key result was that when the mean hail diameter was reduced, the maximum low-level vorticity increased. The cause was attributed to the greater evaporation and melting of the smaller diameter (3 mm) hail, in comparison to the larger diameter (2 cm) hail. The greater evaporation led to more negatively-buoyant downdrafts and greater convergence along the gust fronts, creating a faster exponential increase of low-level vertical vorticity.

This framework is consistent with the low-level mesocyclone being horizontally-forced, as in the current study. As in this study, more negatively-buoyant cold pools were associated with stronger low-level vorticity, in contrast to the findings of the Markowski et al. (2000) observational study. The van den Heever study would suggest that the presence of large amounts of small hail could result in more rapid vortex development by the Neu mechanism. When there is little downdraft evaporative cooling, however, another mechanism would be needed to explain tornadogenesis.

8.3 Relation to Similar Vortex Studies

Most models of tornadogenesis in the literature assume that the final concentration of the low-level mesocyclone into a tornado is vertically-induced, either by buoyant effects (Trapp and Davies-Jones 1997; Lee and Wilhelmson 1997b), or through DPE-induced dynamic pressure forces (Trapp and Davies-Jones 1997). The Markowski et al. (2000) and Rasmussen and Blanchard (1998) observational studies also suggest that tornadogenesis is vertically-forced.

The closest model of tornadogenesis that is not vertically-induced in the literature appears to be that used to explain the misocyclones of Lee and Wilhelmson (1997a). These vortices form by barotropic pooling of vorticity; subsequent vertically-induced convergence created by moist convection converts the misocyclones into tornadoes. In the current study, however, convergence and vertical vorticity generated by the gust front permit a more rapid vortex development, as well as a stronger vortex, than for the misocyclones.

The strong vortices of Grasso (1996) and Finley (1997), which developed in horizontally-heterogeneous environments, were seen to appear first at the surface before being advected to higher levels. This suggests that these vortices are also horizontally-forced. The vortices of Grasso and Cotton (1995) and Wicker and Wilhelmson (1995), also stronger than the vortex of this study, developed in horizontally-homogeneous environments. For these latter two studies, it was suggested that vertical forcing generated the intense vortices.

The necessary conditions for generating the vortex of this study would seem to be quite common in supercells (e.g., strong plane convergence, baroclinic generation of horizontal vorticity), and there does not appear to be any reason that an actual gust-front supercell tornado could not form by this mechanism. However, we have argued that the maximum vortex intensity achievable by this mechanism is not sufficient to account for the strength of powerful supercell tornadoes.

There would appear to be at least four explanations for this discrepancy. One is that the mechanism modeled here has nothing to do with the formation of major supercell tornadoes. Certainly if tornadoes with descending TVSs are associated with the dynamic pipe effect (Trapp et al. 1999) then this first explanation would be the case. Tornadoes with non-descending TVSs tend to form rapidly over their entire depth. Both the vertically-forced non-DPE vortices of Trapp and Davies-Jones (1997) and the vortices of this study involve the existence of convergence prior to vortex intensification; hence both can intensify vortices rapidly along a vertical depth. Therefore, vortices formed by the Neu mechanism may plausibly account for some non-descending TVS weak tornadoes.

A second explanation is that some mechanism such as a near-surface vortex jump (Fiedler and Rotunno 1986; Lewellen 1993; Nolan and Farrell 1999) can intensify the maximum wind speeds of these vortices. It is not clear, however, how this mechanism would operate when the vortex is not vertically forced. Its simulation would also require the incorporation of at least surface drag, and possibly a full no-slip boundary condition.

A third explanation is that a strong vortex can be generated by the Neu mechanism if the vortex can interact with the storm buoyancy or updrafts so that there is some vertically-forced convergence. The resultant vortex would be even more compact, with higher tangential wind speeds. The climatological studies would suggest that vertical forcing is indeed strongly related to tornadogenesis. Furthermore, the Grasso and Cotton (1995) vortex was associated with very strong updrafts near cloud base (over 40 m s^{-1}), and the two main vortices of Wicker and Wilhelmson (1995) were associated with updraft pulses. However, the Grasso and Cotton (1995) vortex was no smaller in scale than the vortex in this study. Thus, if the vertical forcing is the missing factor for producing a stronger vortex, the reason would have more to do with the amount of circulation converged, rather than with the amount of convergence of the same amount of circulation.

A fourth explanation, which is not necessarily exclusive of the third, is that the mesoscale, or even synoptic scale, meteorological fields create large-scale convergence and vorticity fields, and that these fields can serve to concentrate large amounts of circulation on a supercell. This would explain the intensity of the strongest Grasso (1996) vortex, which formed near a dryline, and appeared to be horizontally-forced. It would also be consistent with the Markowksi et al. (1998) climatological study, which found that a preponderance of tornadoes in the VORTEX field project were in close proximity to surface boundaries.

One problem with relating these Neu-like vortices to observed tornadogenesis is that a number of observational studies have emphasized that natural occlusion downdrafts are observed prior to tornadogenesis (Lemon and Doswell 1979; Rasmussen and Straka 1996; Wakimoto et al. 1998; Markowski et al. 2000). If the vortex in this simulation is considered a representation of a tornado, then the occlusion downdraft follows tornadogenesis. This behavior has been found in other numerical simulations as well that have resolved the low-level mesocyclone but not a tornadic vortex (Klemp and Rotunno 1983). Perhaps, then, these Neu-like vortices are most related to intense low-level mesocyclones, which indirectly lead to tornadogenesis by inducing an occluding downdraft that further concentrates vorticity along its perimeter (Wakimoto and Liu 1998). In fact, because the edge of the occluding downdraft should be characterized by strong convergence and a thin ring of vorticity, it may be speculated that a Neu-like process may be important on the scale of the occlusion downdraft perimeter, leading to the formation of the actual tornado.

To summarize: the proposed vortexgenesis process in this study may be relevant to supercell tornadoes, but the formation of a vortex with strong tangential winds requires in addition some combination of the following: vertically-forced convergence interacting with the vortex, mesoscale convergence of circulation into the storm, strong radial convergence associated with the no-slip lower boundary condition, or a secondary Neu-like process that breaks down the vortex ring on the perimeter of the occlusion downdraft.

8.4 Future Work

There is still a lot more work to be accomplished here. The apparent LCL sensitivity of observed tornadoes is an encouraging lead to the tornado forecasting problem, but the proposed physical explanation is still in need of support by modeling studies that explicitly incorporate a realistic supercell. It is suggested that a vertically-forced vortex would be needed to reproduce this effect in a simulation. Thermodynamic sensitivity tests would thus have to be performed with simulations such as Wicker and Wilhelmson (1995) and Grasso and Cotton (1995) where the importance of vertical forcing can be demonstrated.

Of course, the ultimate dream of the mesoscale tornado modeler is to be able to contain an entire supercell and its environment within the grid domain, and simultaneously capture the development of a tornado-scale vortex from the low-level mesocyclone. Because the scales involve range from hundreds of kilometers to a hundredth of a kilometer, the computing challenge is prohibitive at this time. Any tornadic studies will have to involve some plausible idealization of the environment and concentrate on establishing the feasibility of proposed tornadogenesis processes.

The sensitivity of surface drag is another influence that needs to be explored, but one that has proven difficult to address in a mesoscale model. It is possible that a simple predictive turbulent scheme would be needed to address this question adequately. One first-order effect that could be explored by RAMS model simulations would be the difference in near-surface vertical momentum fluxes between the cold pool and the surrounding environment, due to thermal stability. This effect makes the low-level momentum field of the cold pool quite different than what would be expected in the inflow.

Finally, heterogeneity in the model environment should be used to address the origins of the strongest tornadic vortices, in particular the incorporation of mesoscale or synoptic scale boundaries. The first step should be to use an idealized heterogeneous environment, such as a frontal region. The amount of circulation that can be concentrated by such an environment should be investigated. The use of horizontally- heterogeneous environments also permits the incorporation of temporal variability into the simulation, which may be important to the sudden development of low-level mesocyclones and tornadoes.

Appendix A

Divergence Tendency Using π and θ_v

The continuity equation in terms of the mass of the fluid is given by (e.g., Holton 1992):

$$\frac{1}{\rho}\frac{d\rho}{dt} + \boldsymbol{\nabla} \cdot \mathbf{v} = 0. \tag{A.1}$$

so

$$-\boldsymbol{\nabla} \cdot \mathbf{v} = \frac{d}{dt}\left(\ln \rho\right). \tag{A.2}$$

From the ideal gas law $\rho = p/RT_v$, so $\ln \rho = \ln p - \ln R - \ln T_v$, and differentiating gives $d \ln \rho = d \ln p - d \ln T_v$. We can eliminate $d \ln p$ in favor of $d \ln \pi$ through the definition $\pi = c_p (p/p_0)^{R/c_p}$:

$$d \ln \pi = \frac{R}{c_p} d \ln p. \tag{A.3}$$

Also, θ_v can be substituted for T_v by using $\pi \theta_v = c_p T_v$:

$$d \ln \theta_v + d \ln \pi = d \ln T_v \tag{A.4}$$

Thus, substituting into the ideal gas law gives:

$$d \ln \rho = \frac{c_p}{R} d \ln \pi - (d \ln \theta_v + d \ln \pi) = \frac{c_v}{R} d \ln \pi - d \ln \theta_v \tag{A.5}$$

since $(c_p - R)/R = c_v/R$. So, finally, we obtain

$$-\boldsymbol{\nabla} \cdot \mathbf{v} = \frac{c_v}{R}\frac{d \ln \pi}{dt} - \frac{d \ln \theta_v}{dt}. \tag{A.6}$$

Appendix B

Poisson Equation in Rotation-Invariant Form

The incompressible π' Poisson equation is given by (2.24):

$$\nabla \cdot (\theta_{v0} \nabla \pi') = -\left(\frac{\partial u}{\partial x}\right)^2 - \left(\frac{\partial v}{\partial y}\right)^2 - \left(\frac{\partial w}{\partial z}\right)^2 - 2\left[\frac{\partial v}{\partial x}\frac{\partial u}{\partial y} + \frac{\partial w}{\partial x}\frac{\partial u}{\partial z} + \frac{\partial w}{\partial y}\frac{\partial v}{\partial z}\right]$$

$$+\frac{\partial B}{\partial z} + \nabla \cdot \mathbf{F} \tag{B.1}$$

Consider the u and v terms in (2.24):

$$\text{horiz. terms} = -\left(\frac{\partial u}{\partial x}\right)^2 - \left(\frac{\partial v}{\partial y}\right)^2 - 2\frac{\partial v}{\partial x}\frac{\partial u}{\partial y}, \tag{B.2}$$

which are derived from the divergence of the horizontal momentum equations. Using the definitions $\zeta_z = (\partial v/\partial x - \partial u/\partial y)$, $H = (\partial v/\partial x + \partial u/\partial y)$, $\mathcal{T} = (\partial u/\partial x - \partial v/\partial y)$, and $\delta = (\partial u/\partial x + \partial v/\partial y)$, we can rewrite each term in (B.2) as:

$$\text{horiz. terms} = -\left(\frac{\delta + \mathcal{T}}{2}\right)^2 - \left(\frac{\delta - \mathcal{T}}{2}\right)^2 - 2\left(\frac{H - \zeta_z}{2}\right)\left(\frac{H + \zeta_z}{2}\right), \tag{B.3}$$

or

$$\text{horiz. terms} = -\frac{2\delta^2 + 2\mathcal{T}^2 + 2H^2 - 2\zeta_z^2}{4} = -\frac{\delta^2 + \mathcal{T}^2 + H^2 - \zeta_z^2}{2}. \tag{B.4}$$

The quantity $\mathcal{T}^2 + H^2$ is the square of the deformation, $\mathcal{D}^2$. Since δ, ζ_z, and the divergence of the two-dimensional momentum equations are all invariant to rotation in the xy plane, so must be $\mathcal{D}^2$.

Finally, if the fluid is incompressible, then the term $-(\partial w/\partial z)^2$ must be equivalent to δ^2. Combining this term with the two-dimensional terms in (B.1) yields:

$$\boldsymbol{\nabla} \cdot (\theta_{v0} \boldsymbol{\nabla} \pi') = \frac{\zeta_z^2 - 3\delta^2 - \mathcal{D}^2}{2} - 2\left[\boldsymbol{\nabla}_{\boldsymbol{H}} w \cdot \frac{\partial \mathbf{v_H}}{\partial z}\right] + \frac{\partial B}{\partial z} + \boldsymbol{\nabla} \cdot \mathbf{F}. \qquad \text{(B.5)}$$

REFERENCES

Adlerman, E.J., K.K. Droegemeier, and R. Davies-Jones, 1999: A numerical simulation of cyclic mesocyclogenesis. *J. Atmos. Sci.*, **56**, 2045-2069.

Atkins, N.T., M.L. Weisman, and L.J. Wicker, 1999: The influence of preexisting boundaries on supercell evolution. *Mon. Wea. Rev.*, **127**, 2910-2927.

Barnes, S.L., 1970: Some aspects of a severe, right-moving thunderstorm deduced from mesonetwork rawinsonde observations. *J. Atmos. Sci.*, **27**, 634-648.

Barnes, S.L., 1978: Oklahoma thunderstorms on 29-30 April 1970. Part 1: Morphology of a tornadic storm. *Mon. Wea. Rev.*, **106**, 673-684.

Blanchard, D.O., and J. Straka, 1998: Some possible mechanisms for tornadogenesis failure in a supercell. Preprints, *19th Conf. on Severe Local Storms*, Minneapolis, MN, Amer. Meteor. Soc., 116-119.

Bluestein, H.B., 1999: A history of severe-storm-intercept field programs. *Wea. Forecasting*, **14**, 558-577.

Bluestein, H.B., and J.H. Golden, 1993: A review of tornado observations. *The Tornado: Its Structure, Dynamics, Prediction, and Hazards, Geophys. Monogr.*, No. 79, Amer. Meteor. Soc., 319-352.

Bluestein, H.B., J.G. LaDue, H. Stein, D. Speheger, and W.P. Unruh, 1993: Doppler radar wind spectra of supercell tonradoes. *Mon. Wea. Rev.*, **121**, 2200-2221.

Bluestein, H.B., A.L. Pazmany, J.C. Galloway, and R.E. McIntosh, 1995: Studies of the substructure of severe convective storms using a mobile 3-mm wavelength Doppler radar. *Bull. Amer. Meteor. Soc.*, **76**, 2155-2169.

Bluestein, H.B., and A.L. Pazmany, 2000: Observations of tornadoes and other convective phenomena with a mobile, 3-mm wavelength, Doppler radar: The spring 1999 field experiment. *Bull. Amer. Meteor. Soc.*, **12**, 2939-2952.

Brady, R.H.., and E.J. Szoke, 1989: A case study of nonmesocyclone tornado development in northeast Colorado: Similarities to waterspout formation. *Mon. Wea. Rev.*, **117**, 843-856.

Brandes, E.A., 1984: Vertical vorticity generation and mesocyclone sustenance in tornadic thunderstorms: The observational evidence. *Mon. Wea. Rev.*, **112**, 2253-2269.

Brooks, E.M., 1949: The tornado cyclone. *Weatherwise*, **2**, 32-33.

Brooks, H.E., C.A. Doswell III, and R. Davies-Jones, 1993: Environmental helicity and the maintenance and evolution of low-level mesocyclones. *The Tornado: Its Structure, Dynamics, Prediction and Hazards, Geophys. Monogr.*, No. 79, Amer. Geophys. Union, 97-105.

Brooks, H.E., C.A. Doswell III, and R.B. Wilhelmson, 1994: The role of midtropospheric winds in the evolution and maintenance of low-level mesocyclones. *Mon. Wea. Rev.*, **122(1)**, 126-136.

Brown, R.A., L.R. Lemon, and D.W. Burgess, 1978: Tornado detection by pulsed Doppler radar. *Mon. Wea. Rev.*, **106**, 29-38.

Browning, K.A., 1964: Airflow and precipitation trajectories within severe local storms which travel to the right of the winds. *J. Atmos. Sci.*, **21**, 634-639.

Browning, K.A., and R.J. Donaldson, 1963: Airflow and structure of a tornadic storm. *J. Atmos. Sci.*, **20**, 533-545.

Burgers, J.M., 1948: A mathematical model illustrating the theory of turbulence. *Adv. Appl. Mech.*, **1**, 171-199.

Burgess, D.W., and R.J. Donaldson, Jr., 1979: Contrasting tornadic storm types. Preprints, *11th Conf. on Severe Local Storms*, Kansas City, MO, Amer. Meteor. Soc., 189-192.

Burgess, D.W., L.R. Lemon, and R.A. Brown, 1975: Tornado characteristics revealed by Doppler radar. *Geophys. Res. Lett.*, **2**, 183-184.

Burgess, D.W., V.T. Wood, and R.A. Brown, 1982: Mesocyclone evolution statistics. Preprints, *12th Conf. on Severe Local Storms*, San Antonio, TX, Amer. Meteor. Soc., 422-424.

Cai, H., and R.M. Wakimoto, 1998: Comparison between the Garden City tornadic and Hays nontornadic supercells during VORTEX95. Preprints, *19th Conf. on Severe Local Storms*, Minneapolis, MN, 108-111.

Clark, T.L., 1979: Numerical simulations with a three-dimensional cloud model: Lateral boundary condition experiments and multicellular storm simulations. *J. Atmos. Sci.*, **36**, 2191-2215.

Corcos, G., and S. Lin, 1984: The mixing layer: deterministic models of a turbulent flow. Part 2. The origin of the three-dimensional motion. *J. Fluid Mech.*, **139**, 67-95.

Cotton, W.R., and R.A. Anthes, 1989: *Storm and cloud dynamics.* Academic Press, 883 pp.

Darkow, G.L., and D.W. McCann, 1977: Relative environmental winds for 121 tornado bearing storms. Preprints, *10th Conf. on Severe Local Storms*, Omaha, NE, Amer. Meteor. Soc., 413-417.

Davies-Jones, R.P., 1982: Observational and theoretical aspects of tornadogenesis. *Topics in Atmospheric and Oceanographic Sciences: Intense Atmospheric Vortices*, Bengtsson, Lighthill, ed., Springer-Verlag, Berlin, 175-189.

Davies-Jones, R.P., 1984: Streamwise vorticity: the origin of updraft rotation in supercell storms. *J. Atmos. Sci.*, **41**, 2991-3006.

Davies-Jones, R.P., 1986: Tornado dynamics. *Thunderstorm Morphology and Dynamics*, E. Kessler, Ed., University of Oklahoma Press, 411 pp.

Davies-Jones and Brooks, 1993: Mesocyclogenesis from a theoretical perspective. *The Tornado: Its Structure, Dynamics, Prediction, and Hazards, Geophys. Monogr.*, No. 79, Amer. Meteor. Soc., 105-114.

Donaldson, R.J., Jr., 1970: Vortex signature recognition by a Doppler radar. *J. Appl. Meteorol.*, **9**, 661-670.

Doswell, C.A., and D.W. Burgess, 1993: Tornadoes and tornadic storms: a review of conceptual models. *The Tornado: Its Structure, Dynamics, Prediction, and Hazards, Geophys. Monogr.*, No. 79, Amer. Meteor. Soc., 161-172.

Dutton, J.A., 1995: *Dynamics of atmospheric motion.* Dover, 617 pp.

Fawbush, E.J., and R.C. Miller, 1954: The types of air masses in which North American tornadoes form. *Bull. Amer. Meteor.*, **35**, 154-165.

Fiedler, B.H., and R. Rotunno, 1986: A theory for the maximum windspeeds in tornado-like vortices. *J. Atmos. Sci.*, **43**, 2328-2340.

Finley, C.A., 1997: Numerical simulaton of intense multi-scale vortices generated by supercell thunderstorms. Ph.D. dissertation, Colorado State University, 297 pp.

Fleagle, R.G., and J.A. Businger, 1980: *An Introduction to Atmospheric Physics*, 2d. ed. Academic Press, 432 pp.

Forbes, G.S., 1978: Three scales of motions associated with tornadoes. Ph.D. dissertation, University of Chicago, 359 pp.

Fujita, T., 1963: Analytical mesometeorology: A review. *Meteor. Mongr. No. 27*, **5**, 77-125.

Fujita, T.T., 1970: The Lubbock tornadoes: A study of suction spots. *Weatherwise*, **23**, 161-173.

Fujita, T., and H. Grandoso, 1968: Split of a thunderstorm into anticyclonic and cyclonic storms and their motion determined from numerical model experiments. *J. Atmos. Sci.*, **25**, 416-439.

Garrett, R.A., and V.D. Rockney, 1962: Tornadoes in northeastern Kansas, May 19, 1960. *Mon. Wea. Rev.*, **90**, 231-240.

Gill, A.E., 1982: *Atmosphere-Ocean Dynamics*, Academic Press, New York, 662 pp.

Grasso, L.D., 1996: Numerical simulation of the May 15 and April 26, 1991 tornadic thunderstorms. Ph.D. dissertation, Colorado State University, 151 pp.

Grasso, L.D., 2000: The dissipation of a left-moving cell in a severe storm environment. *Mon. Wea. Rev.*, **128**, 2797-2815.

Grasso, L.D., and W.R. Cotton, 1995: Numerical simulation of a tornado vortex. *J. Atmos. Sci.*, **52**, 1092-1203.

Grazulis, T.D., 1993: *Significant Tornadoes 1680-1991: A Chronology and Analysis of Events*, The Tornado Project of Environmental Films, 1326 pp.

Cotton, W.R., and R.A. Anthes, 1989: *Storm and cloud dynamics*. Academic Press, 883 pp.

Grice, G.K., R.J. Trapp, S.F. Corfidi, R. Davies-Jones, C.C. Buonanno, J.P. Craven, K.K. Droegemeier, C. Duchon, J.V. Houghton, R.A. Prentice, G. Romine, K. Schlachter, and K.K. Wagner, 1999: The golden anniversary celebration of the first tornado forecast. *Bull. Amer. Meteor. Soc.*, **80**, 1341-1348.

Guinn, T.A., and W.H. Schubert, 1993: Hurricane spiral bands. *J. Atmos. Sci.*, **50**, 3380-3403.

Haynes, P.H., and M.E. McIntyre, 1987: On the evolution of vorticity and potential vorticity in the presence of diabatic heating and frictional or other forces. *J. Atmos. Sci.*, **44**, 828-841.

Helmholtz, H., 1858: Über Integrale der hydrodynamischen Gleichungen welche den Wirbelbewegungen entsprechen. *Crelles J.*, **55**, 25.

Helmholtz, H., 1868: Über discontinuirliche Flüssigkeits bewegungen. *Monats. Königl. Preuss. Akad. Wiss. Berlin*, **23**, 215-228.

Hill, G.E., 1974: Factors controlling the size and spacing of cumulus clouds as revealed by numerical experiments. *J. Atmos. Sci.*, **31**, 646-673.

Holton, J.R., 1992: *An introduction to dynamic meteorology, 3rd ed.* Academic Press, 511 pp.

Hoskins, B.J., M.E. McIntyre, and A.W. Robertson, 1985: On the use and significance of isentropic potential vorticity maps. *Q. J. R. Meteorol. Soc.*, **111**, 877-946.

Kambe, T., 1983: A class of exact solutions of two-dimensional viscous flow. *J. Phys. Soc. Japan*, **52**, 834-841.

Kelvin, Lord, 1871: Hydrokinetic solutions and observations. *Phil. Mag.*, **42**, 362-377.

Kessler, E., 1970: Tornadoes. *Bull. Amer. Meteor. Soc.*, **51**, 926-936.

Klemp, J.B., and R.B. Wilhelmson, 1978: The simulation of three- dimensional convective storm dynamics. *J. Atmos. Sci.*, **35**, 1070-1096.

Klemp, J.B., and R.B. Wilhelmson, 1978: Simulations of right- and left-moving storms produced through storm splitting. *J. Atmos. Sci.*, **35**, 1097-1110.

Klemp, J.B., and R. Rotunno, 1983: A study of the tornadic region within a supercell thunderstorm. *J. Atmos. Sci*, **40**, 359-377.

Klemp, J.B., R.B. Wilhelmson, and P.S. Ray, 1981: Observed and numerically simulated structure of a mature supercell thunderstorm. *J. Atmos. Sci.*, **38**, 1558-1580.

Kossin, J.P., and W.H. Schubert, 2001: Mesovortices, polygonal flow patterns, and rapid pressure falls in hurricane-like vortices. *J. Atmos. Sci.*, **58**, 2196 - 2209.

Lemon, L.R., and C.A. Doswell III, 1979: Severe thunderstorm evolution and mesocyclone structure as related to tornadogenesis. *Mon. Wea. Rev.*, **107**, 1184-1197.

Lee, B.D., and R.B. Wilhelmson, 1997: The numerical simulation of non-supercell tornadogenesis: Part I: Initiation and evolution of pre-tornadic misocyclone circulations along a dry outflow boundary. *J. Atmos. Sci.*, **54**, 32-60.

Lee, B.D., and R.B. Wilhelmson, 1997: The numerical simulation of non-supercell tornadogenesis: Part II: Evolution of a family of tornadoes along a weak outflow boundary. *J. Atmos. Sci.*, **54**, 2387-2415.

Lee, B.D., and R.B. Wilhelmson, 2000: The numerical simulation of non-supercell tornadogenesis: Part III: Parameter tests investigating the role of CAPE, vortex sheet strength, and boundary layer vertical shear. *J. Atmos. Sci.*, **57**, 2246-2261.

Leslie, L.M., 1971: The development of concentrated vortices: a numerical study. *J. Fluid Mech.*, **48**, 1-21.

Lewellen, W.S., 1993: Tornado vortex theory. *The Tornado: Its Structure, Dynamics, Prediction and Hazards, Geophys. Monogr.*, No. 79, Amer. Geophys. Union, 19-39.

Lewis, P.E., and J.P. Ward, 1989: *Vector Analysis for Engineers and Scientists*. Addison-Wesley, 406 pp.

Lilly, D.K., 1969: Tornado dynamics. National Center for Atmospheric Research Manuscript 69-117, 52 pp.

Lorenz, E.N., 1963: Deterministic nonperiodic flow. *J. Atmos. Sci.*, **20**, 130-141.

Markowski, P.M., E.N. Rasmussen, and J.M. Straka, 1998: The occurrence of tornadoes in supercells interacting with boundaries during VORTEX-95. *Wea. Forecasting*, **13(3)**, 852-859.

Markowski, P., E. Rasmussen, and J. Straka, 2000: Surface thermodynamic characteristics of RFDs as measured by a mobile mesonet. Preprints, *20th Conf. on Severe Local Storms*, Orlando, FL, Amer. Meteor. Soc., 251-254.

McCaul, E.W., Jr., 1993: Observations and simulations of hurricane- spawned tornadic storms. *The Tornado: Its Structure, Dynamics, Prediction and Hazards, Geophys. Monogr.*, No. 79, Amer. Geophys. Union, 97-105.

Melander, M.V., N.J. Zabusky, and J.C. McWilliams, 1988: Symmetric vortex merger in two dimensions: Causes and conditions. *J. Fluid Mech.*, **195**, 303-340.

Meyers, M.P. and W.R. Cotton, 1992: A wintertime orographic quantitative precipitation forecast with an explicit cloud model. Part I: Two-dimensional sensitivity experiments. *J. Appl. Met.*, **31**, 26-50.

Moffat, H.K., S. Kida, and K. Ohkitani, 1994: Stretched vortices – the sinews of turbulence; large Reynolds number asymptotics. *J. Fluid Mech.*, **259**, 241-264.

Montgomery, M.T., and J. Enagonio, 1998: Tropical cyclogenesis via convectively forced vortex Rossby waves in a three-dimensional quasigeostrophic model. *J. Atmos. Sci.*, **55**, 3176-3207.

Montgomery, M.T., and R. Kallenbach, 1997: A theory for vortex Rossby- waves and its application to spiral bands and intensity changes in hurricanes. *Quart. J. Roy. Meteor. Soc.*, **123**, 435-465.

Neu, J.C., 1984: The dynamics of stretched vortices. *J. Fluid Mech.*, **143**, 253-276.

Neu, J.C., 1984: The dynamics of a columnar vortex in an imposed strain. *Phys. Fluids*, **27**, 2397-2402.

Nolan, D.S., 2001: The stabilizing effects of axial stretching on turbulent vortex dynamics. *Phys. Fluids*, **13**, 1724-1738.

Nolan, D.S., and B.F. Farrell, 1999: The structure and dynamics of tornado-like vortices. *J. Atmos. Sci.*, **56**, 2908-2936.

Nolan, D.S., A.S. Almgren, and J.B. Bell, 2000: Studies of the relationship between environmental forcing and the structure and dynamics of tornado-like vortices. Lawrence Berkeley National Laboratory Report LBNL-47554, 65 pp.

Pielke, R.A., W.R. Cotton, R.L. Walko, C.J. Tremback, W.A. Lyons, L.D. Grasso, M.E. Nicholls, M.D. Moran, D.A. Wesley, T.J. Lee, and J.H. Copeland, 1992: A comprehensive meteorological modeling system – RAMSj. *Meteor. and Atmos. Phys.*, **49**, 69-91.

Rasmussen, E.N., and J.M. Straka, 1996: Mobile mesonet observations of tornadoes during VORTEX-95. Preprints, *18th Conf. on Severe Local Storms*, San Francisco, CA, Amer. Meteor. Soc., 1-5.

Rasmussen, E.N., and D.O. Blanchard, 1998: A baseline climatology of sounding-derived supercell and tornado forecast parameters. *Wea. Forecasting*, **4**, 1148-1164.

Rasmussen, E.N., S. Richardson, J.M. Straka, P.M. Markowski, and D.O. Blanchard, 2000: The association of significant tornadoes with a baroclinic boundary on 2 June 1995. *Mon. Wea. Rev.*, **128(1)**, 174-191.

Rasmussen, E.N., J.M. Straka, R. Davies-Jones, C.A. Doswell III, F.H. Carr, M.D. Eilts, and D.R. MacGorman, 1994: Verification of the Origins of Rotation in Tornadoes EXperiment: VORTEX. *Bull. Amer. Meteor. Soc.*, **75**, 995-1006.

Rayleigh, Lord, 1880: On the stability or instability of certain fluid motions. *Proc. Lond. Math. Soc.*, **11**, 57-75.

Rothfusz, L.P., and D.K. Lilly, 1989: Quantitative and theoretical analyses of an experimental helical vortex. *J. Atmos. Sci.*, **46**, 2265-2279.

Rotunno, R., 1977: Numerical simulation of a laboratory vortex. *J. Atmos. Sci.*, **34**, 1942-1956.

Rotunno, R., 1978: A study in tornado-like vortex dynamics. *J. Atmos. Sci.*, **36**, 140-155.

Rotunno, R., 1981: On the evolution of thunderstorm rotation. *Mon. Wea. Rev.*, **109**, 577-586.

Rotunno, R., 1984: An investigation of a three-dimensional asymmetric vortex. *J. Atmos. Sci.*, **41**, 283-298.

Rotunno, R., and J.B. Klemp, 1982: The influence of the shear-induced pressure gradient of thunderstorm motion. *Mon. Wea. Rev.*, **110**, 136-151.

Rotunno, R., and J.B. Klemp, 1985: On the rotation and propagation of simulated supercell thunderstorms. *J. Atmos. Sci.*, **42**, 271-292.

Saffman, P.G., 1992: *Vortex dynamics*. Cambridge University Press, 311 pp.

Schecter, D.A., D.H.E. Dubin, A.C. Cass, C.F. Driscoll, I.M. Lansky, and T.M. O'Neil, 2000: Inviscid damping of asymmetries on a two-dimensional vortex. *Phys. Fluids*, **12**, 2397-2412.

Schlesinger, R.E., 1975: A three-dimensional numerical model of an isolated deep convective cloud: Preliminary results. *J. Atmos. Sci.*, **32**, 934-957.

Schlesinger, R.E., 1980: A three-dimensional numerical model of an isolated thunderstorm. Part II: Dynamics of updraft splitting and mesovortex couplet evolution. *J. Atmos. Sci.*, **37**, 395-420.

Smagorinsky, J., 1963: General circulation experiments with the primitive equations. 1: The basic experiment. *Mon. Wea. Rev.*, **91**, 99-164.

Snow, J.T., and R.L. Pauley, 1984: On the thermodynamic method for estimating maximum tornado windspeeds. *J. Climate Appl. Meteor.*, **23**, 1465-1468.

Straka, J.M., E.N. Rasmussen, and S.E. Fredrickson, 1996: A mobile mesonet for finescale meteorological observations. *J. Atmos. Oceanic Technol.* **13**, 921-936.

Trapp, R.J., 1999: Observations of low-level mesocyclones and attendant tornadogenesis failure during VORTEX. *Mon. Wea. Rev.*, **127**, 1693-1705.

Trapp, R.J., 2000: A clarification of vortex breakdown and tornadogenesis. *Mon. Wea. Rev.*, **128(3)**, 888-895.

Trapp, R.J., and R. Davies-Jones, 1997: Tornadogenesis with and without a dynamic pipe effect. *J. Atmos. Sci*, **54**, 113-133.

Trapp, R.J., E.D. Mitchell, G.A. Tipton, D.W. Effertz, A.I. Watson, D.L. Andra, Jr., and M.A. Magsig, 1999: Descending and nondescending tornadic vortex signatures detected by WSR-88Ds. *Wea. Forecasting*, **14**, 625-639.

van den Heever, S.C., 2001: The impact of several hail parameters on simulated supercell storms. Ph.D. Dissertation, Colorado State University, 265 pp.

Wakimoto, R.M., and C. Liu, 1998: The Garden City, Kansas, storm during VORTEX 95. Part II: The wall cloud and the tornado. *Mon. Wea. Rev.*, **126**, 393-408.

Wakimoto, R.M., and H. Cai, 2000: Analysis of a nontornadic storm during VORTEX 95. *Mon. Wea. Rev.*, **128(3)**, 565-592.

Wakimoto, R.M., C. Liu, and H. Cai, 1998: The Garden City, Kansas, storm during VORTEX 95. Part I: Overview of the storm's life cycle and mesocyclogenesis. *Mon. Wea. Rev.*, **126(2)**, 372-392.

Walko, R.L., 1988: Plausibility of substantial dry adiabatic subsidence in a tornado core. *J. Atmos. Sci.*, **45**, 2251-2267.

Walko, R.L., 1993: Tornado spin-up beneath a convective cell: Required basic structure of the near-field boundary layer winds. *The Tornado: Its Structure, Dynamics, Prediction, and Hazards, Geophys. Monogr.*, No. 79, Amer. Meteor. Soc., 89-95.

Walko, R.L., W.R. Cotton, M.P. Meyers, and J.Y. Harrington, 1995: New RAMS cloud microphysics parameterization. Part I: the single-moment scheme. *Atmos. Res.*, **38**, 29-62.

Weisman, M.L, and J.B. Klemp, 1982: The dependence of numerically simulated convective storms on vertical wind shear and buoyancy. *Mon. Wea. Rev.*, **110**, 504-520.

Weisman, M.L. and C.A. Davis, 1998: Mechanisms for the generation of mesoscale vortices within quasi-linear convective systems. *J. Atmos. Sci.*, **55**, 2603-2622.

Weisman, M.L., and R. Rotunno, 2000: The use of vertical wind shear versus helicity in interpreting supercell dynamics. *J. Atmos. Sci.*, **57**, 1452-1472.

Welander, Pierre, 1955: Studies on the general development of motion in a two-dimensional, ideal fluid. *Tellus*, **7**, 141-156.

Wicker, L.J., 1990: A numerical simulation of a tornado-scale vortex in a three-dimensional cloud model. Ph.D. Dissertation, University of Illinois, 264 pp.

Wicker, L.J., 1996: The role of near surface wind shear on low-level mesocyclone generation and tornadoes. Preprints, *18th Conf. on Severe Local Storms*, San Francisco, CA, Amer. Meteor. Soc., 115-119.

Wicker, L.J., and R.B. Wilhelmson, 1995: Simulation and analysis of tornado development and decay within a three-dimensional supercell thunderstorm. *J. Atmos. Sci.*, **52**, 2675-2703.

Wilhelmson, R.B., and J.B. Klemp, 1981: A three-dimensional numerical simulation of splitting severe storms on 3 April 1964. *J. Atmos. Sci.*, **38**, 1581-1600.

Wurman, J., J. Straka, and E. Rasmussen, 1996: Preliminary radar observations of the structure of tornadoes. Preprints, 18th Conf. on Severe Local Storms, San Francisco, CA, Amer. Meteor. Soc., 17-22.